Ph.D. in ASTRONOMY, ASTROPHYSICS
and SPACE SCIENCE

CYCLE XXXII

COMMUNICATING THE ENERGY: ACCRETION PROPERTIES AND FEEDBACK IN AGN

Andrea Travascio

A.Y. 2019/2020

Supervisor : Enrico Piconcelli

Co-supervisors : Pasquale Mazzotta, Fabrizio Fiore

Coordinator : Paolo De Bernardis

Deputy Coordinator : Nicola Vittorio

CONTENTS

ISTRUZIONI DI LETTURA

La scoperta di un luogo lavorativo, la conquista di un mestiere che ancora non risona nelle tue corde e che mette in luce quel che di te e' lontano dall'equilibrio tanto bramato nell'infinita conoscenza. Questo e' stato per me il percorso di dottorato. La vita, a questo punto, sembra quasi prendere l'iniziativa, e mi regala tre tutori speciali, miei protettori, insegnati e amici, con i quali il mio lavoro sarebbe stato vano, se non fallimentare. Enrico, Angela e Luca, la cui dedizione, passione e accuratezza per i minimi dettagli, ha alimentato in me una coscienza dei limiti e dei traguardi, del significato di ricerca e di qualcosa di piu' del semplice lavoro di gruppo. Mi auguro che i loro sforzi abbiano infuso in me l'ingegno di saper scegliere e apprezzare ogni possibile vetta di arrivo. Per cui devo a loro un grazie speciale, considerandolo come minimo gesto, che non potra' di certo contraccambiare il loro aiuto, direte voi "parzialmente dovuto", ma certamente non aspettato in tale totalita'.

Ogni scelta inoltre e' ardua, nessuno sa cosa vuole dalla vita, e l'inaspettato scorrere di essa rende il tutto cosi' tedioso. Subentra quindi l'esigenza di un pensiero etico che induca ogni persona, dotata di un'esperienza e di una conoscenza il cui limite potrebbe essere per molti uno dei tanti varchi ignoti dell'intelletto umana, a guidare le menti piu' povere e di ridotta esperienza verso un percorso ottimale agli occhi della vita. Devo per questo un ringraziamento a Fabrizio, che insieme ad Enrico, Angela e Luca, ha saputo essere una guida, prendendo a cuore i grandi passi in questo mio percorso, pur se 672.4 km e' cio' che ci separava da due anni ad oggi.

E tra le mille difficolta' di un mondo figurativo che gira, e che si, regala tante prospettive di significati fugaci, ma che ad ogni step sottrae convinzioni e lascia spazio a dubbi, niente poteva essere piu' rincuorante che avere al mio fianco delle persone, a cui ludicamente mi riferiro' come "dottorandi dell'osservatorio". Non mi dilunghero' a farene un elenco. Ognuno sa, si aspetta o immagina, quello che ha portato nella mia vita, i ricordi che ha inframmezzato in questa esperienza. Un'esperienza che e' stata condivisa, intrecciata, ampliata e scossa, e che sara' semplicemente un ricordo insostituibile.

E di questo dottorato resteranno anche due frutti del mio lavoro. Ma questa e' in gran parte menzogna. Mai nessuno fa niente da solo, e se crede cio' allora non e' che *un ingrato. Per questo ringrazio tutti i co-autori, che hanno lavorato al mio fianco, e sono stati un'estensione della mia mente, un supporto ed un prolungamento del mio tempo.*

Ringrazio inoltre i referee della tesi, Roberto Gilli e Francesco Massaro, i quali hanno dedicato il loro tempo alla lettura di questa tesi, migliorandola ed apprezzandola.

E adesso che il dottorato e' concluso, partiro'.. e speranzoso che questo sara' uno dei tanti viaggi, per poi tornare all'origine, arricchito di cio' che adesso non posso esprimere. Partire e' sinonimo di lasciare. E quest'ultima restituisce l'aspra consapevolezza che niente puo' seguire i miei passi se non me stesso. E' per questo che ringrazio i miei amici. E anche qui trovo inutile fornire una lista di nomi, che in questo caso prendono un significato solo per chi ritrova in se' il ruolo di un amico e riconosce in ogni suo passato minimo gesto nei miei confronti un'unicita' e un sostegno. Grazie a voi, che scegliete di condividere insieme a me la vostra vita e di accettarmi per chi sono in ogni istante e chi saro' in ogni luogo. Sono sicuro che chi saro' andra' bene anche a chi ha condiviso con me ogni passata esperienza. Ringrazio quindi la mia famiglia, che ha creduto in me e ha saputo apprezzare ed interessarsi al mio lavoro.

Come gia' e' stato detto, questa tesi che forse sarete in procinto di leggere non nasce solo da me, ma anche dai sacrifici e dal supporto di altre persone, da una condizione di benessere, dalla figura di una guida, dall'amicizia e dall'interesse esterno di chi mi e' sempre stato vicino. Ma ancor piu' ti meraviglierai se ti diro' che questa tesi, per quanto colma di parole e frasi forse vuote, piatte, scientifiche e che solo aspirano all'insegnamento di una disciplina e alla relativa dimostrazione del mio impegno, e' anche frutto dell'amore di una persona. Di chi al mio fianco ha saputo gestire il peggior me, il mio senso di disagio e stress, la mia assenza di autostima, donandomi incondizionato amore e rispetto. Devo quindi anche a Camilla parte del merito. L'amore oggi si e' dottorato in astrofisica e presumo sara' in grado di affrontare tante altre cose.

Odio essere scontato, e concludere questo elogio alla solidarieta' umana con dei ringraziamenti a mia madre e mio padre lo e' in ogni parte del mondo per chi ha la fortuna di avere due persone cosi' speciali da far parte del proprio mondo senza mai pretendere nulla o mai per secondi fini. D'altro canto, e' come vagliare la porta della vita e rendersi conto che e' incomprensibile, questo e' un passo ineluttabile. Diro' semplicemente che ogni cosa da me fatta, detta, studiata, scoperta e quant'altro nasce da loro.

Questa tesi e' dedicata a tutte le persone che hanno gironzolato nei miei pensieri *in questo mio atto di ringraziamenti. Se pero' dovessi fare una dedica ufficiale, direi che andrebbe ai miei nonni Marcello e Delia e alle persone che mi hanno abbandonato, non per loro volere. Mia nonna Luisa, che mi ha lasciato tutto cio' che di piu' bello una nonna puo' lasciare ad un nipote, e mio cugino Alessandro e mia zia Angela venuti a mancare un anno fa. Mi rammarica la loro assenza, e quindi a loro, che hanno avuto sogni, traguardi e ambizioni, dedico i miei.*

So the Universe is not quite as you thought it was. You'd better rearrange your beliefs, then. Because you certainly can't rearrange the Universe.
Cit. Isaac Asimov- The Gods Themselves

EXECUTIVE SUMMARY

Keywords: galaxies: active – galaxies: high-redshift – intergalactic medium – quasars: emission lines – galaxies: halos – galaxies: clusters – galaxies: evolution – galaxies: interactions – galaxies: elliptical and lenticular, cD

This Thesis focuses on investigating the role of nuclear activity in SMBH-host galaxy self-regulated growth. This work is based on an extensive collection of multi-band imaging and spectroscopic data. Indeed, it is now widely accepted that AGN activity can affect different phases of the interstellar medium making mandatory a multi-wavelength approach which combines the study of emitting/absorbing gas at increasing distance from the SMBH. I have studied the relationships among nuclear properties, AGN-driven outflows and host galaxy properties by investigating two specific cases.

The first one aims at understanding if and how the huge radiative output of a hyper-luminous QSO interacts with the circum-galactic medium (CGM) of the host galaxy. This extended reservoir of gas is believed to play a crucial role in the evolution of galaxy across cosmic time, and luminous QSOs are the most promising sources to study energy and matter flows and their coupling from nuclear to circum-galactic scales. Theoretical models indeed suggest that powerful QSOs are ideal targets to study feedback in action in the form of AGN-driven outflows from pc to several kpc scales. While there is a flourishing literature on the detection of cold and ionised outflows affecting the interstellar medium, unambiguous examples of outflows extending well into the CGM are still sparse. The discovery of such winds would therefore be a crucial step forward, providing unprecedented constraints to the expectations of the most popular models of massive galaxy evolution.

The second science case presented in this Thesis regards the formation of the so-called Brightest Cluster Galaxy (BCG). BCGs are the most massive ($M_\star \sim 10^{12} M_\odot$) and luminous ($M_v \approx -23$) galaxies residing at the center of the relaxed, virialized and undisturbed clusters in the local Universe. At low redshift, they appear like red, quiescent, massive and large (up to 100 kpc) elliptical galaxies and they often show radio jets, which are able to affect the gas in the Intra Cluster Medium. On the contrary, observations of galaxy cluster cores at $z>1.4$ do not show the presence of a typical local BCG but are instead characterized by star-forming galaxies (SFGs) with disturbed morphology. Furthermore,

a reversal of the star formation - density relation has been observed in distant clusters, i.e. while at z<1.4 the number of SFGs increases towards the cluster outskirts, at z>1.4 the star formation activity is higher in the core of massive galaxy clusters. Up to now, the processes responsible for the transition between the unquenched and quenched phases in such environments are still unclear and improving our understanding is fundamental not only for explaining the formation of local BCGs but also for both cluster and galaxy evolution. According to many cosmological simulations and semi-analytic models the BCG progenitors form most (~50%) of their mass at z~5. This mass is then assembled at z=1-2, i.e. through major mergers at z>1 and dry mergers at z<1 , to form the final BCG. Based on these models, z~1-2 is a crucial epoch during which we expect a high rate of merger activity among galaxies (the BCG progenitors) in the cores of massive galaxy clusters. This picture has been widely confirmed in high-redshift proto-clusters but remains unclear for galaxy clusters.

Deep multi-band investigations of the central core of a cluster at z~1-2 are indeed mandatory to shed light on the poorly-explored process of assembly of a massive BCG and extreme structure formation process in such a very dense environment. Specifically, the presence of (possibly multiple) AGN and the role of AGN-driven feedback during BGC formation has been largely overlooked so far.

A synopsis of the two main projects carried out during my PhD research work is outlined below.

(I) Studying the so-called *feeding & feedback cycle* of active galaxies at the peak epoch of galaxy assembly and SMBH accretion activity, i.e. 2<z<4, is crucial to improve our understanding of the role and the effects of AGN activity. In order to probe both feeding and feedback at their extremes, the AGN Team at INAF-OAR has undertaken a multi-wavelength program (i.e. the WISSH, WISE/SDSS hyper-luminous, QSOs project) to study the most powerful AGN in the Universe, which happen to shine at these cosmic epochs. The CGM of luminous, high-redshift QSOs is being routinely characterized by sensitive VLT/MUSE integral field spectroscopic data which have recently allowed to routinely detect large baryon reservoirs traced by Lyman alpha emission (the so-called giant Lyα nebulae). I present in Sect. 3 the MUSE observation of J1538+08 at z=3.6. It is an Eddington accreting broad-line QSO included in the WISSH sample that exhibits powerful outflows at all scales both in emission and absorption. I report the discovery of both a very luminous (~$2\times10^{44} erg\ s\ cm^{-2}$), giant (~ 150 kpc) Ly$\alpha$ nebula and an extended (75 kpc) CIV nebula. The Lyα nebula emission exhibits moderate blue-shift (~60 $km\ s^{-1}$) compared with the QSO systemic redshift and a large average velocity dispersion σ_v ~700 $km\ s^{-1}$ across the nebula, while the CIV nebula shows average velocity dispersion σ_v ~ 350 $km\ s^{-1}$. The

Lyα line profile exhibits a significant asymmetry towards negative velocity values at 20-30 kpc south of the QSO and is well parametrised by two Gaussians. The narrower (σ ~470 $km\ s^{-1}$) component traces the bulk of the nebula while the larger one (σ ~1200 $km\ s^{-1}$) is blue-shifted by ~1500 $km\ s^{-1}$. The analysis of the MUSE data of the field surrounding J1538+08 thus reveals the spatial distribution of the CGM and its metal content. The kinematics of the Lyα nebula exhibits clear indication of blue-shifted emission which suggests the presence of an outflow propagating through the CGM over tens of kpc. This work has led to the following paper "*The WISSH QSOs project IV. Outflows and metals in the circum-galactic medium around the hyper-luminous z~3.6 quasar J1538+08*" Travascio et al. (2019a), A&A submitted.

(II) XDCP J0044-2033 is one of the most massive and densest X-ray selected galaxy clusters currently known at redshift z>1.5, whose central galaxy population shows high star formation and strong AGN activity compared to lower-z clusters. A wealth of multi-wavelength photometric and spectroscopic data from radio to X-rays have been collected during the last years to study the galaxy population of the cluster core with unprecedented details at these redshifts (see Sect. 5). Specifically, in the very central region of the cluster (70 kpc × 70 kpc), two galaxy subsystems (Complex A and B) with signature of ongoing merger have been identified and studied with a total of seven confirmed cluster members. These galaxies show perturbed morphologies and two of them, located at the center of each complex, have been found to host luminous, obscured and highly accreting AGN. One of them is also detected in X-ray while the other one and its companions are spatially related to radio emission. These two AGN are among the closest (projected distance of ~35 kpc) AGN pair found at z>1 . Moreover, by analysing the whole cluster, we find that the distribution of the radial velocities of the spectroscopically confirmed cluster members is quite large with values up to ~ 2600 $km\ s^{-1}$ and a velocity dispersion of σ ~1500 $km\ s^{-1}$, higher than expected from the velocity dispersion - temperature relation. Finally, the cluster velocity dispersion profile, compared to the dark matter one, suggests the presence of merging substructures in the central core and of a filament, entering the cluster, at large radii. The observations of high star formation, merger signatures and nuclear activity in the core of XDCP0044-2033 suggest that all these processes concur in shaping the nascent BCG. According to our data, XDCP0044-2033 could form a typical massive galaxy of $M_{*} \sim 10^{12}\ M_{\odot}$ in a time scale of few Myrs. Such galaxy could then be quenched by AGN-driven feedback thus leaving a massive elliptical BCG, as observed in the local Universe. This work has led to the following paper "*BCG assembly and AGN activity in the XDCPJ0044.0-2033 core*" Travascio et al. (2019b) A&A submitted.

1. AGN PHYSICS AND FEEDBACK

The term Active Galactic Nuclei (AGN) refers to an accreting Super-Massive Black Hole (SMBH) hosted in the center of a galaxy (Salpeter, 1964). These SMBHs exhibit typical masses of $10^6 - 10^9 M_\odot$. Because of the large amount of energy released in this accretion process, AGN are among the brightest astrophysical sources in the Universe, exhibiting luminosities of $\simeq 10^{42} - 10^{48}\ erg\ s^{-1}$. Moreover, their emitted radiation can cover the whole electromagnetic spectrum, ranging from radio to gamma-rays. Interestingly, the AGN radiative output can exceed the binding energy of the host galaxy and have a large impact on the galaxy and the surrounding environment. Specifically, AGN can power winds, outflows and radio jets, which are able to deposit energy, momentum and metals on pc-to-kpc scales.

This chapter provides a review of the observed properties of AGN and how the AGN feedback impacts the surrounding medium and the galaxy evolution.

1.1 Physics of the BH accretion

During the AGN phase the accretion of matter onto a BH produces a huge amount of luminosity. This latter is originated by the conversion of a fraction of the gravitational potential of the falling matter. For example, assuming that a BH accretes at the rate $\dot{M}_{acc}$, it should emit a bolometric luminosity given by the following equation:

$$L_{bol} = \eta \dot{M}_{acc} c^2 \tag{1.1}$$

where c is the speed of light and η is the mass-to-energy conversion efficiency, that is the conversion of the gravitational potential into radiation. In order to have an estimation of a typical value for η, we shall consider an element of matter of mass m_{acc} falling toward the BH at distance r. It will have a potential energy U given by the equation:

$$U = \frac{G m_{acc} M_{BH}}{r} \tag{1.2}$$

and, if converted into radiation, it has the following luminosity:

$$L_{bol} \simeq \frac{dU}{dt} = \frac{G M_{BH}}{r} \frac{dm_{acc}}{dt} = \frac{G M_{BH} \dot{m}_{acc}}{r} \tag{1.3}$$

Comparing the Eq.(1.1) with the Eq.(1.3) the accretion efficiency is:

$$\eta \simeq \frac{GM}{rc^2} = \frac{R_s}{2r} \tag{1.4}$$

in which $R_s = 2GM/c^2$ is the BH Schwarzschild radius. Assuming r=5R_s, where the most of the optical-UV continuum radiation is expected to originate (Peterson, 1997), then $\eta \simeq 0.1$, which means that the mass is converted into energy with an efficiency of 10%. Considering a rotating BH (Kerr metric) the mass-to-energy conversion can reach 47% of efficiency (Thorne, 1974).

1.1.1 *The Eddington limit*

When the mass is flowing towards the BH it undergoes a radiative pressure acting against the free fall. This involves the existence of a limit on the luminosity and mass accretion rate of a BH, called Eddington limit. The latter is reached when the attractive gravitational force acting on an electron-ion pair balances with the repulsive force due to radiation pressure. Assuming a spherical symmetry, the electrons will undergo a radiative force of the photons emitted by the AGN, which is equal to:

$$F_{rad} = \frac{L_{bol}\sigma_T}{4\pi r^2 c} \tag{1.5}$$

where σ_T is the scattering Thomson cross section, while the gravitational force, by neglecting the one acting on the electron, is simply given by the formula:

$$F_{grav} = \frac{GM_{BH}m_p}{r^2} \tag{1.6}$$

Thus, we can derive the Eddington luminosity by equating the gravitational force (eq.1.6) to the radiation one (eq.1.5):

$$L_{Edd} = \frac{4\pi GM_{BH}m_p c}{\sigma_T} \simeq 1.3 \times 10^{38}\frac{M_{BH}}{M_\odot}\ erg\ s^{-1} \tag{1.7}$$

If the luminosity exceeds the Eddington limit, the radiative pressure will dominate, sweeping away the gas and preventing further BH accretion. The Eddington accretion rate is then defined as:

$$\dot{M}_{Edd} = \frac{L_{Edd}}{\eta c^2} \tag{1.8}$$

An additional commonly used value related to the Eddington luminosity is the Eddington ratio (λ), which indicates the relative BH accretion rate and it is defined as:

$$\lambda = \frac{L_{bol}}{L_{Edd}} \tag{1.9}$$

where $\lambda = 0.1$ is the typical value used to discern between low and high accretion rate.

1.1.2 Accretion disk and energy release

In the scenario in which the energy is released through the BH accretion, the gas needs to lose angular momentum, which is transported outwards by processes such as tidal torques, major and minor mergers and instability of the disk (e.g. bars, spiral waves). These act on large scales (>100 pc), while on shorter distances (< 1 pc) the magneto-rotational instability seems to play a crucial role in driving gas accretion (e.g. Hernquist, 1989; Barnes & Hernquist, 1991; Hernquist & Mihos, 1995; Bournaud et al., 2005; Balbus & Hawley, 1991).

Shakura & Sunyaev (1973) proposed a theory for the accretion disc (α-disk model), according to which an optically thick and geometrically thin accretion is present, and the viscosity (ν) between the neighbouring layers of the disk allows angular momentum transport. The spectral energy distribution emitted from the accretion disk consists of multiple black body (BB) components with different temperatures as a function of the radius r. These effective temperatures are given by the following formula:

$$T_{eff} \simeq 6.2 \times 10^5 \left(\frac{\eta M_8}{\lambda}\right)^{-1/4} \left(\frac{r}{R_s}\right)^{-3/4} K \tag{1.10}$$

This equation shows that the peak of the temperature decreases as the BH mass increases.

An alternative disk model consists of an optically-thin and geometrically-thick accretion disk, in which the mass accretion rate is low (i.e. Radiatively Inefficient Accretion Flows; Narayan & Yi, 1994). Such accretion mode is unable to efficiently cool the falling gas and non-radiative mechanisms are able to transport energy and momentum outwards through collimated radio jet.

1.2 Structure and physics of an AGN

1.2.1 AGN taxonomy

The AGN taxonomy is originated by observational evidences of AGN with different features at different wavelengths.

1. **Optical/UV.** Observations in Optical and UV bands allow the distinction between Seyfert galaxies (Seyfert, 1943), i.e. active galaxies with $L_{bol} < 10^{46} erg\ s^{-1}$ and absolute B magnitude $M_B > -23$, and the Quasi-Stellar Objects (QSOs Schmidt & Green, 1983) with $L_{bol} > 10^{46} erg\ s^{-1}$ and $M_B < -23$ (Véron-Cetty & Véron, 2003). Seyfert galaxies are usually spiral galaxies exhibiting high surface brightness nuclei, strong high-ionisation lines and weak absorption lines due to stellar population of the host galaxy. The latter is easily detectable and discernible from the nuclear emission

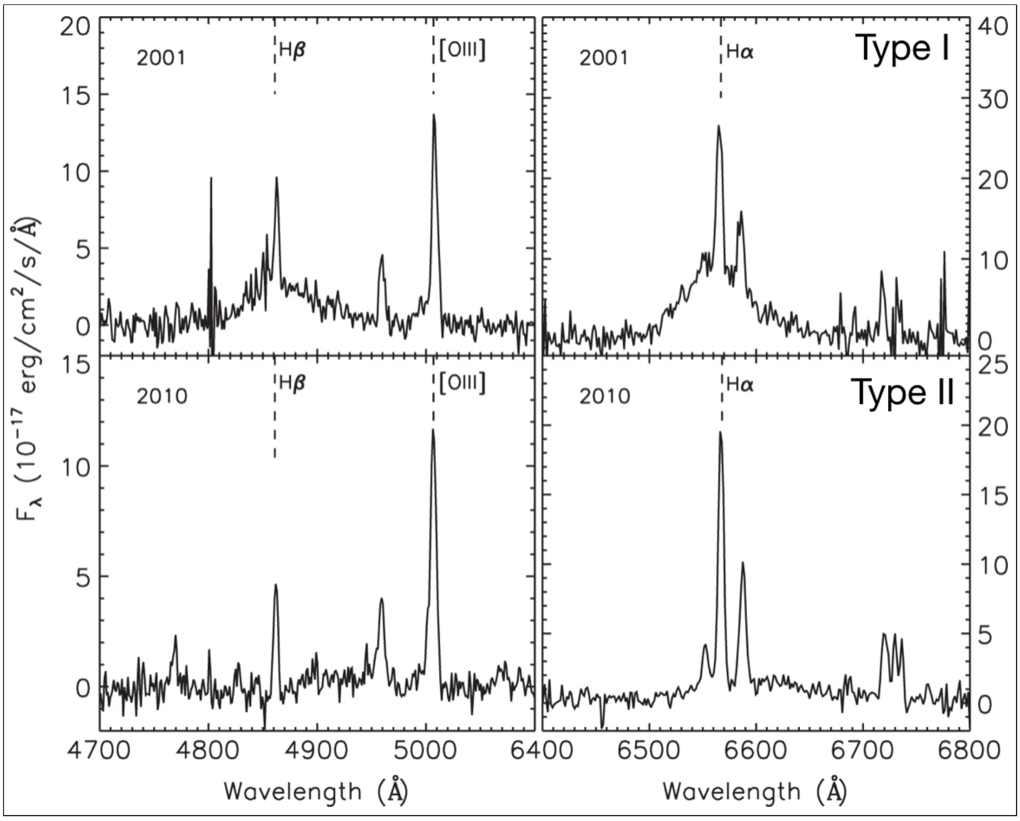

Figure 1.1: Zoom-in of the Hα and Hβ emission lines in two spectra derived by stacking 2000 type I AGN (top panel) and 2010 type II AGN (bottom panel) spectra, in which the continuum (power-law) and host galaxy component have been subtracted (LaMassa et al., 2015).

if compared to the QSOs. The so-called "Type I" AGN show permitted, broad ($FWHM > 2000\ km\ s^{-1}$) emission lines together with the permitted and forbidden narrow ($FWHM < 1000\ km\ s^{-1}$) emission lines (Ramos Almeida & Ricci, 2017, and references therein). The most prominent permitted broad/narrow emission lines are Hα, Hβ, Hγ, Lyα, CIV and MgII, while the typical forbidden narrow emission lines are [OIII], [OII], [NII] and [SII]. On the other hand, the Type II AGN show only narrow emission lines. The broad emission spectral lines are emitted in the so-called Broad Line Region (BLR), while forbidden and narrow emission lines are emitted in the so-called Narrow Line Region (NLR). The properties of these two regions will be discussed in the Sect. 1.2.2. Fig. 1.1 reports two examples of spectra, which are obtained by stacking 2000 SDSS (top panel; Type I) and 2010 BOSS (bottom panel; Type II) spectra and by subtracting the power-law continuum and galaxy components (LaMassa et al., 2015). Fig. 1.2 shows an UV/optical spectrum created by stacking 2200 type I QSO

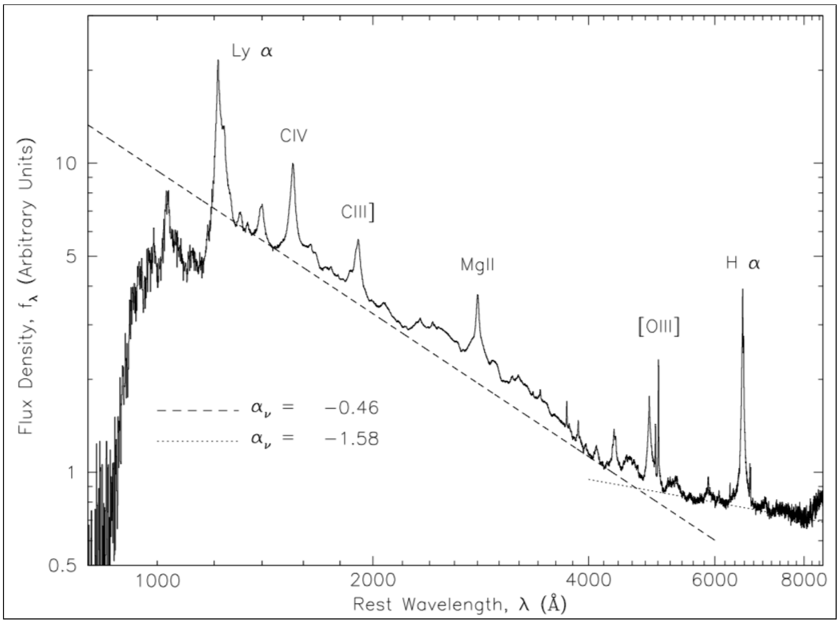

Figure 1.2: Composite QSO spectrum obtained by stacking 2200 SDSS spectra of type-I QSOs (Vanden Berk et al., 2001).

SDSS spectra (Vanden Berk et al., 2001). The UV and Optical continuum are modelled by power laws with spectral index $\alpha = -0.46$ and -1.58, respectively. The intensity of the emission lines ratios is useful to distinguish Seyfert II galaxies from other galaxy types (e.g., HII regions). Indeed, the strength of different lines is a function of the ionising continuum and is connected to the emitting object features. Therefore, the Baldwin et al. (1981) (BPT) diagram (see Fig. 1.3) is used to discern Seyferts or QSOs (showing larger $[OIII]\ \lambda5007\ /\ H\beta$ values), from HII regions and Low Ionisation Nuclear Emission Regions (LINERs) galaxies, which are galaxies exhibiting prominent low ionisation lines as [OI] λ6300, [SII] $\lambda\lambda$6548 6853, [NII] $\lambda\lambda$6716 6731 and [OII] λ3727.

2. **X-ray.** The X-ray emission is ubiquitous in AGN and it appears to be most variable (Elvis et al., 1978). AGN with $L_{[2-10]keV} > 10^{44}\ erg\ s^{-1}$, $L_{[2-10]keV} \sim 10^{42} - 10^{44}\ erg\ s^{-1}$ and $L_{[2-10]keV} < 10^{42}\ erg\ s^{-1}$ are classified as high, moderate and low luminosity AGN, respectively. The X-ray spectrum of an AGN is characterised by a power-law continuum with a slope of ~1.7-2 (Piconcelli et al., 2005). Type II AGN shows an X-ray spectrum with a curvature in the soft portion (i.e. <2-3 keV) due to the presence of absorption along our line of sight, typically associated to the dusty torus. Fig 1.4 shows two X-ray spectra of NGC 1365 obtained from Suzaku observations performed on different moments, highlighting the extreme spectral changes and the

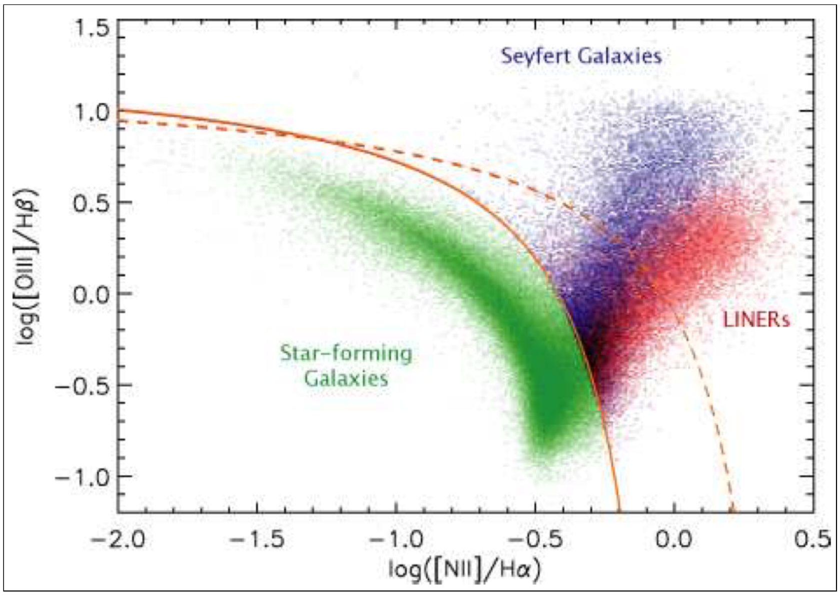

Figure 1.3: BPT diagram of the emission-line flux ratio $NII\lambda6584$Å/ Hα versus the ratio $[OIII]\lambda5007$Å/ Hβ for all the galaxy in the by Kauffmann et al. (2003b). BPT diagram is useful to distinguish the star-forming galaxies (green), LINERs (red) and Seyfert type-II galaxies (blue). The solid (Kauffmann separator) and dashed (Kewley separator) curves represent the AGN / star-burst galaxies separation.

rapid variability of the X-ray spectrum ($\sim 10\ h$). Indeed, its configuration changes from Compton Thin ($N_H \sim 10^{23} cm^{-2}$; black and blue points) to Compton Thick ($N_H > 10^{24} cm^{-2}$; red points). The high variability suggests that in this source the obscuration of X-ray emission is due to the high-velocity clouds located close to the AGN with column density $> 10^{24} cm^{-2}$ and velocity $\sim 1000\ km\ s^{-1}$ (Risaliti et al., 2007).

3. **Radio.** According to the radio-optical ratio parameter $R_{r-o} = F_{5\ GHz}/F_B$, the AGN can be classified in radio-quiet QSOs, with $R_{r-o} < 10$, and radio-loud QSOs having $R_{r-o} > 10$ (Kellermann et al., 1989). Recently, Padovani (2017) introduced a new classification based on the presence of a further criteria and, more specifically, in jetted and non-jetted features. The radio jetted AGN are mainly observed with two different configurations (Fanaroff & Riley, 1974): Faranoff-Riley I (FRI) and Faranoff-Riley II (FRII). FRI AGN exhibit a luminosity $L_{178\ MHz} < 2 \times 10^{32} erg\ s^{-1}$ and a radio emission decreasing rapidly with the distance from the galaxy center, where the spectra are steeper, as an indication of an old age of the radiating particles. These are usually associated to luminous, massive elliptical galaxies in the center of galaxy clusters, in which the presence of diffuse hot gas (i.e. intra-cluster medium) can distort the radio structures through ram pressure. On

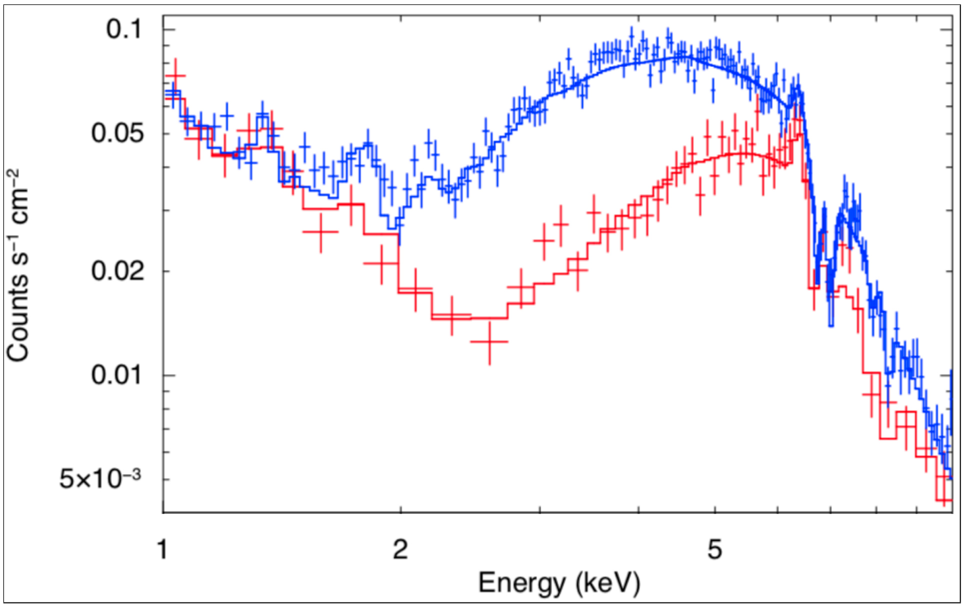

Figure 1.4: X-ray spectra of the Seyfert galaxy NGC 1365 (Risaliti et al., 2007) derived by Suzaku observations obtained in different intervals of 10 ks. This spectral variability suggests the presence of absorption clouds with $N_H \geq 10^{24}\ cm^{-2}$ over BLR scales.

the other hand, the FRII AGN are associated with spheroidal galaxies and show prominent extended radio jets with brighter lobes than FRI at large distances and evidence of hot-spots. Moreover, FRII radio-galaxies exhibit $L_{178\ MHz} > 2 \times 10^{32} erg\ s^{-1}$. An example for both a FRI and a FRII radio galaxies is reported in Fig. 1.5 (Tadhunter, 2016).

1.2.2 The AGN unified model

Antonucci (1993) introduced the "unified model" in order to justify the observed AGN taxonomy. This model outlined by Antonucci (1993) and Urry & Padovani (1995) claims that the line of sight with respect to a specific AGN structure can explain the AGN taxonomy. This model therefore envisages an almost unique AGN structure, which will be described in this section (Fig. 1.6). The presence of a molecular, dusty and toroidal structure surrounding the accretion disk on parsec scales, plays a fundamental role in this AGN unified model, because it is able to block our view of the emitting gas (i.e. accretion disk and BLR emitting clouds) from the central AGN. Moreover, it is also needed to explain the polarisation of the scattered broad emission lines.

The torus allows us to explain Type I and Type II AGN dichotomy. Indeed, the high broadening of the emission lines observed in the type I AGN (see Sect.1.2.1) is explained with the high dispersion velocity of the emitting gas driven by the

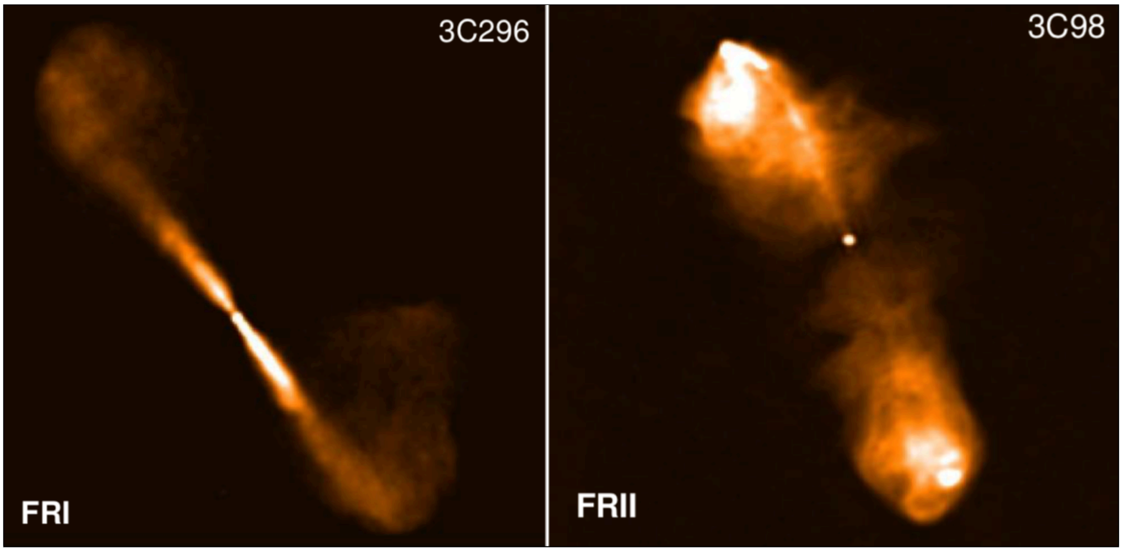

Figure 1.5: The Fanaroff-Riley classifications of radio AGN. *Left panel*: FRI is a jet-dominated radio AGN in which the jets decelerate on scales of hundred of pc to kpc. *Right panel*: FRII is a lobe-dominated radio AGN in which the jets are moderately relativistic and supersonic from the nucleus to the hot-spot. Figures from Tadhunter (2016)

gravitational effects of the central BH. Therefore, the broad, permitted emission lines are likely released from cold ($T \sim 10^4 K$) and dense ($n_e > 10^9\ cm^{-3}$) clouds, close ($\sim$ 1 pc) to the BH, i.e. from the BLR (Krolik et al., 1981). On the other hand, the narrow emission lines have to be emitted from regions not affected by the BH gravity (> 100 pc scales) and with low density ($\sim 10^{3-5} cm^{-3}$), i.e. the NLR. This low density is necessary to explain the presence of forbidden emission lines, which can easily be suppressed by collisions, as indeed happens in the BLR.

According to this configuration, a type II AGN is observed if the torus is located along the line of sight and obscures the BLR, allowing us to only detect the only narrow emission lines.

On the other hand, the presence of a radio emission cannot be explained with the angular position of the line of sight with respect to the axial-symmetry structure of the AGN, but it is rather an intrinsic property of the AGN, probably dependent on the accretion mode of the central BH. However, the angle of view can probably change the properties observed for radio AGN. For example, the Blazars are radio AGN whose collimated jet is aligned to the observer line of sight. Such a interpretation is able to explain many blazars properties, like the high luminosity, high polarisation, superluminal motions of the jets, and high variability (Madejski & Sikora, 2016).

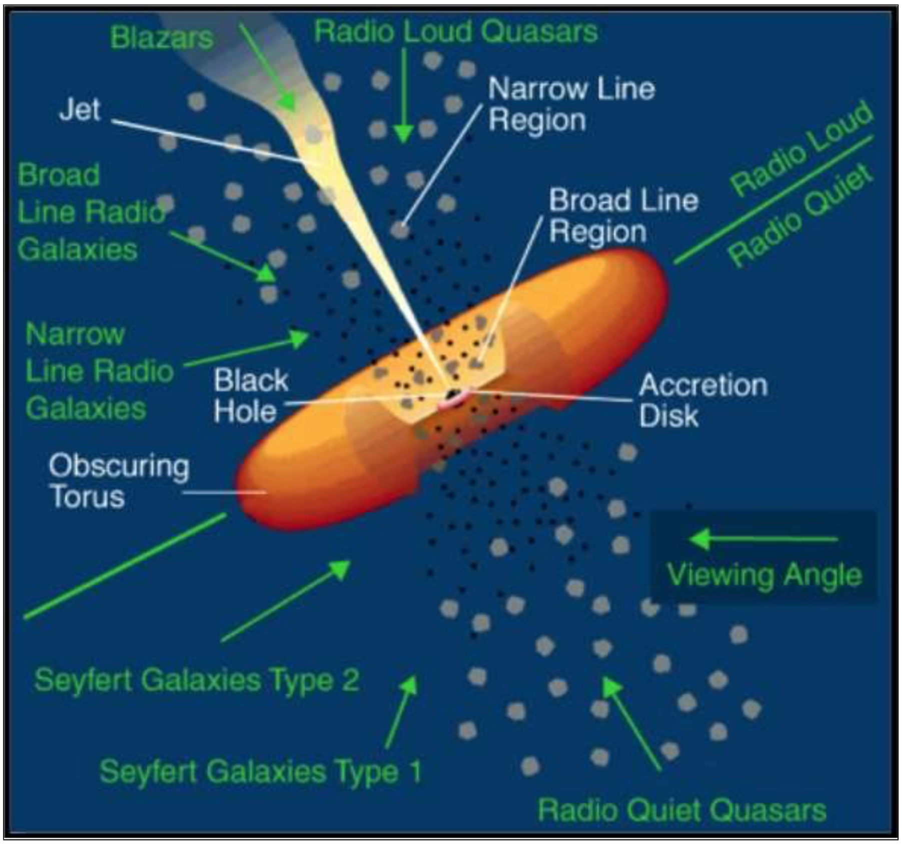

Figure 1.6: Unified AGN model proposed by Urry & Padovani (1995). It is able to explain the AGN taxonomy in terms of different viewing angles with respect to the torus.

1.2.3 Black hole mass estimation

Under the assumption that the broadening of the BLR emission lines depends on the BH gravitational potential, the properties of these lines are an excellent proxy to derive the BH mass through the virial theorem:

$$M_{BH} = \frac{f R_{BLR} v_{BLR}^2}{G} \tag{1.11}$$

where f is a parameter which depends on the geometry of the BLR and v_{BLR} is the velocity of the BLR clouds, derived from the Full Width at Half Maximum ($FWHM$) of a broad emission line, at distance R_{BLR}. Observations with high spatially resolution and sampling allow us to obtain very good estimations of the BH mass through the reverberation mapping technique (Peterson, 2004; Ferrarese & Ford, 2005). The latter allows us to derive the structure of the BLR and the BH mass directly from the motions induced by the gravitational force on the surrounding gas. This method requires some assumptions, i.e:

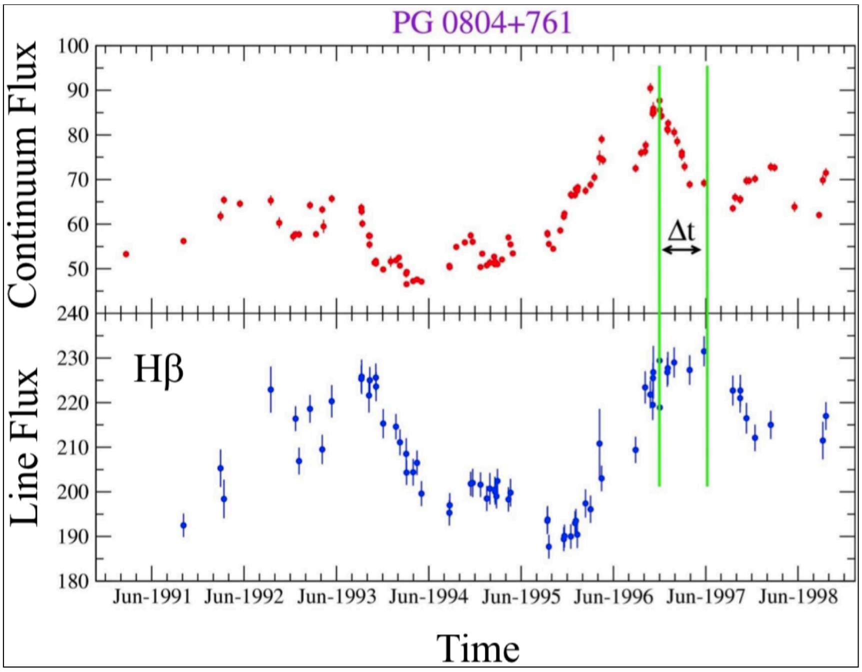

Figure 1.7: Variation of the optical continuum (top) and Hβ emission line (bottom) flux as a function of the time for the AGN PG 0804+761 (Kaspi et al., 2000).

- the continuum emission occurs at a distance from the central BH shorter than the BLR emission one;

- a simple relation between optical and ionising continuum;

- and that the delay time between the variation of the emission line and of the ionising continuum is due to the differences in the light travel time.

Under these conditions the variation of the continuum luminosity is investigated, as well as the BLR response to the variation (see Fig 1.7). The delay to this variation depends on the distance from the central source as $t = R(1 + cos\theta)/c$, where θ is the angle between the observer's line of sight and the line connecting the AGN with the position of the cloud. The distance of the clouds emitting emission lines can be therefore estimated.

To estimate the BH mass from the formula (1.11) is necessary to measure the velocities of these clouds, which are derived by the width of the emission lines, i.e. the velocity dispersion, in the spectrum of a type I AGN. BH masses in distant AGN (in which the reverberation mapping is not applicable) can be obtained by the single epoch method (Vestergaard, 2002). The latter reproduces the virial

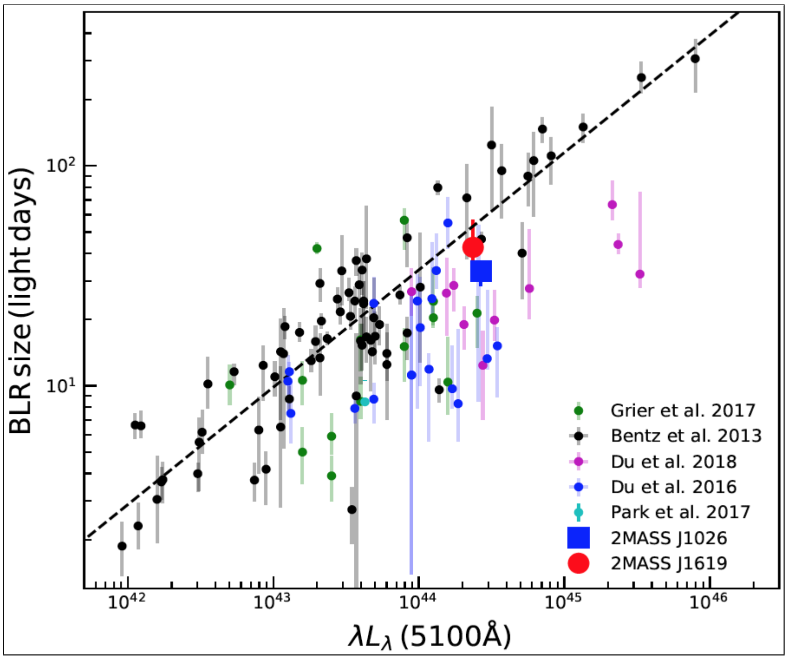

Figure 1.8: BLR size versus monochromatic luminosity at 5100 (L_{5100}) Å relation obtained by recent AGN samples (Rakshit et al., 2019). The dashed line represents the best-fit relation obtained by Bentz et al. (2013).

equation (1.11) by combining information about the $FWHM$ of the BLR lines, the radius-luminosity relations, which are derived by the reverberation mapping methods, and the calibration coefficients. Indeed, reverberation mapping experiments show existence of correlations between clouds distance from the BH and continuum luminosity. Fig. 1.8 reports an example of a relation between BLR size and monochromatic luminosity at 5100 Å ($R_{BLR} \propto L_{5100}^{\alpha_{line}}$) for different AGN samples (see Rakshit et al., 2019, for details). All this information is combined in following formula:

$$M_{BH} = \frac{f\, R_{BLR} FWHM_{obs}^2}{G} \tag{1.12}$$

where G is the gravitational constant and f is a virial factor associated to the geometry, inclination angle and kinematics of the BLR. The formula (1.12) can be also written as follows:

$$Log(M_{BH}/M_\odot) = a + b \times Log\left(\frac{FWHM}{10^3 km\ s^{-1}}\right) + c \times Log\left(\frac{L}{10^{44} erg\ s^{-1}}\right) \tag{1.13}$$

Different broad emission lines have been used to derive the mass of the BH, e.g. Hα, Hβ, CIV, MgII, by assuming different (a, b, c) values for each line. The

Hβ emission line is the most suitable in the reverberation mapping and several authors (Kaspi et al., 2000; Bentz et al., 2013) found a relation between $R_{H\beta}$ and the monochromatic luminosity at 5100 Å (L_{5100}) in the form of $R_{H\beta} = \alpha l_{44}^{\beta}$, with $l_{44} = L_{5100}/10^{44}\ erg\ s^{-1}$. In the simple scenario in which (i) the photo-ionisation is the main mechanism of line emission; (ii) the ionising source is isotropic; (iii) its luminosity (L_{ion}) is proportional to L_{5100} and (iv) it is emitted from a source with size smaller than the distance between BLR clouds and the central BH, then the relation is $R_{H\beta} \propto L_{5100}^{1/2}$, based on the ionisation parameter $U \sim L_{ion}/R_{H\beta}^2 n_e T$.

Some studies confirm that the widths of Hα and MgII lines strongly correlate with those of the Hβ (Greene & Ho, 2005; Shen et al., 2008), while such a correlation is not observed with the CIV emission line width (Shen & Liu, 2012), probably due to the presence of outflows (Vietri et al., 2018). Furthermore, Greene & Ho (2005) found a new method, still based on the virial mass system, to estimate the BH mass by exploiting the broad $H\alpha$ emission line. They found a correlation between $L_{H\alpha}$ and L_{5100}, by assuming that the L_{5100} is a good proxy of the continuum that powers the emission lines, as follows:

$$L_{H\alpha} = (5.25 \pm 0.02) \times 10^{42} \left(\frac{L_{5100}}{10^{44}\ erg\ s^{-1}} \right)^{1.157 \pm 0.005} \tag{1.14}$$

and finally they obtained the virial mass dependent only from the Hα:

$$M_{BH} = 2.0^{+0.4}_{-0.3} \times 10^6 \left(\frac{L_{H\alpha}}{10^{42}} \right)^{0.55 \pm 0.02} \times \left(\frac{FWHM}{1000\ km\ s^{-1}} \right)^{2.06 \pm 0.06} M_{\odot} \tag{1.15}$$

1.3 AGN host-galaxy co-evolution

1.3.1 Scaling relations

Quiescent SMBHs are found in the center of local spheroidal galaxies and many authors suggested a past AGN activity for these objects (Lynden-Bell, 1969). Observational evidences report tight correlations between the SMBH mass and some properties (i.e. luminosity, mass and velocity dispersion) of the galactic bulges for local galaxies. Kormendy & Richstone (1995) firstly reported the existence of a $M_{BH} - M_{bulge}$ correlation, with a constant slope $M_{BH}/M_{bulge} \approx 10^{-3}$. Furthermore, a robust relation between M_{BH} and stellar velocity dispersion (σ) has also been reported (Shankar et al., 2016). Fig.1.9 (a) shows the $M_{BH} - \sigma$ relation derived by van den Bosch (2016), based on a sample of 230 galaxies, including a wide variety of types (i.e. from dwarf to giant elliptical galaxies), and on different methods of M_{BH} measurements. The grey lines represent the best-fit (solid line) and once (dashed line) and three (dotted line) times the intrinsic scatter. The accuracy of M_{BH} measurements is crucial to estimate these

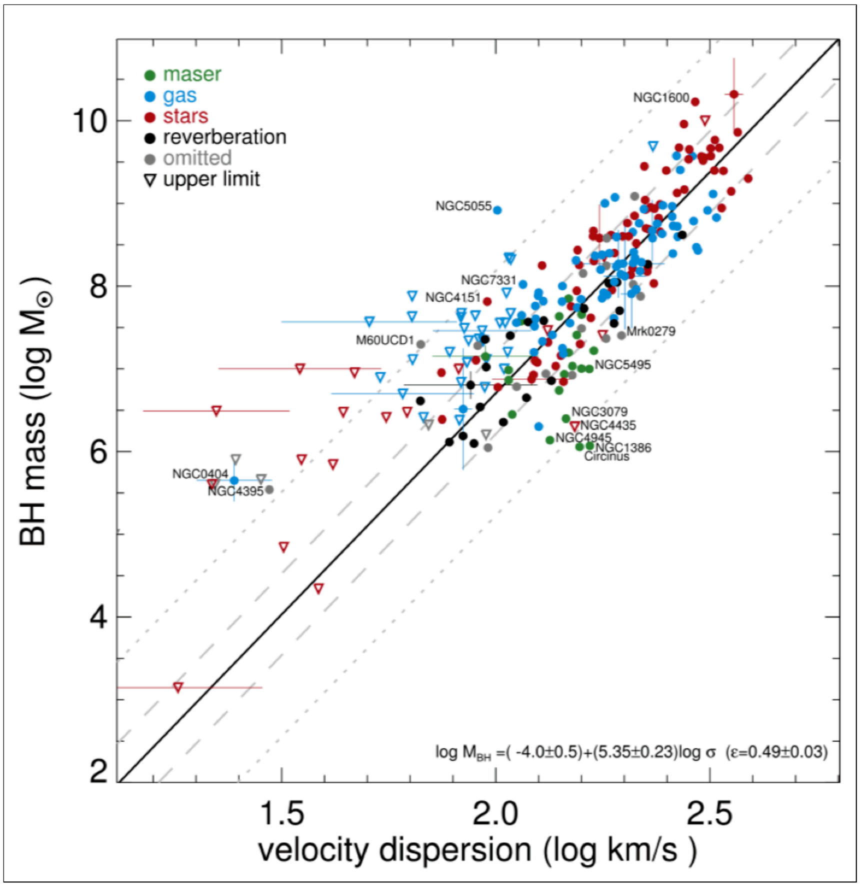

Figure 1.9: Correlation between BH mass and stellar velocity dispersion of the galactic bulge, i.e. $M_{BH} - \sigma$ relation (van den Bosch, 2016). The black line is the best-fit obtained from the analysis of 230 different type of galaxies, whose different colors indicate different measurements of the BH mass. Triangles represent upper limit values. The grey dashed and dotted lines indicate one and three times intrinsic scatter, respectively.

scaling relations with low intrinsic scatters (see Sect. 1.2.3). Fig. 1.9 shows the $M_{BH} - \sigma$ relation obtained with the BH masses derived through spatially resolved kinematics of gas (Marconi et al., 2001), stars (van der Marel et al., 1998) and masers (Kuo et al., 2011), showing a very low intrinsic scatter (Gebhardt et al., 2000).

1.3.2 Cosmic evolution of star formation and BH accretion

Boyle & Terlevich (1998) revealed a similar trend for the evolution of the cosmic star formation (SF) and BH accretion history (Marconi et al., 2004). The latter can be related to the cosmic evolution of the AGN bolometric luminosity function. Indeed, the Soltan argument (Soltan, 1982) claims that the integration of

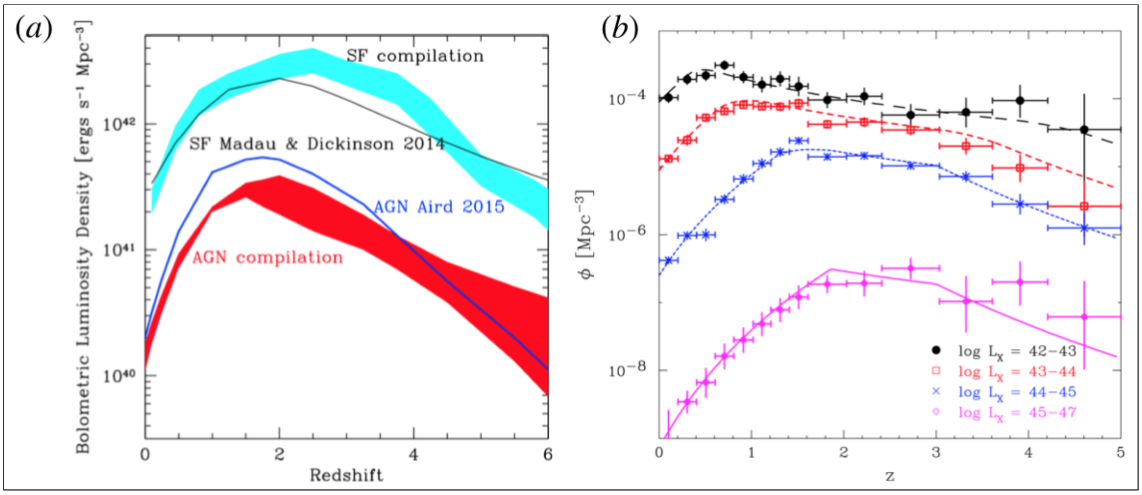

Figure 1.10: *Panel a*: evolution of the AGN bolometric luminosity density (Fiore et al., 2017). The red band represents the AGN L_{bol} function computed from a collection of X-ray luminosity functions with $L_X = 10^{42} - 10^{45} erg\ s^{-1}$ by using the bolometric correction by Marconi et al. (2004). The cyan band reports the average UV luminosity density, which is linearly correlated with the SFR density. The blue and black lines indicate the AGN and SFR luminosity density function estimated by Aird et al. (2015) and Madau & Dickinson (2014), respectively. *Panel b*: AGN comoving number of density as a function of redshift in four X-ray luminosity bins (Ueda et al., 2014).

L_{Bol} will be equivalent to the density of mass accreted on BHs, at each redshift, if we assume an accretion efficiency (η), i.e:

$$\rho_{BH}(z) = \frac{1-\eta}{\eta c^2} \int L\phi(L,z)dL \tag{1.16}$$

The bolometric luminosity function is typically derived assuming a bolometric correction (k_{band}). The latter is derived thanks to AGN surveys and is applied to X-ray, Optical, UV and IR luminosity functions to determine total energy of the AGN output from a monochromatic luminosity ($L_{bol} = k_{band} \times L_{band}$). The survey completeness due to the selection effects and sensitivity (Hopkins et al., 2007; Merloni & Heinz, 2013) and the estimation of the bolometric corrections (Runnoe et al., 2012) represent the main issues to obtain the real AGN bolometric luminosity function.

The X-ray 2-10 keV AGN surveys offer a highly efficient method to detect the AGN over a wide range of luminosity and redshift, thanks to their strong penetrating power and little contamination from host galaxy (Brandt & Hasinger, 2005). Nevertheless, this method fails to detect heavily obscured ($N_H > 10^{24}$ cm^{-2}) Compton-thick AGN, which represents $\sim 30-40\%$ of the local AGN (Risaliti et al., 1999; Gilli et al., 2007). In turn, heavily Compton-thick AGN can be

detected through IR surveys (Levenson, 2014), which are sensitive to the emission of dusty torus in AGN. However, to avoid large numbers of false detections due to galaxy contamination, IR surveys require the support of optical/UV surveys or spectroscopy (Spinoglio & Malkan, 1989), as it is hard to separate dusty AGN emission from starburst galaxies.
Several authors collected multi-wavelength observations of AGN in order to estimate bolometric corrections (Ueda et al., 2014, and reference therein), but many difficulties are encountered while calculating these corrections. In particular, it is important to avoid including contaminating emissions from the host galaxy and it is necessary to consider the variability of the monochromatic luminosity, which increases the intrinsic error in estimating the bolometric correction.

The bolometric luminosity function at a given redshift that emerges from several works (Shankar et al., 2009; Fiore et al., 2017) is described as follows:

$$\frac{d\phi}{d\,log(L)} = \frac{\phi_*}{[(L/L_*)^{\gamma_1} + (L/L_*)^{\gamma_2}]} \tag{1.17}$$

Fig. 1.10 (a) shows the evolution of the AGN bolometric luminosity density (red band) reported in Fiore et al. (2017) and obtained from the X-ray luminosity function by using the bolometric correction in Marconi et al. (2004). This is compared to the SF luminosity density (cyan band) of galaxies as derived by Santini et al. (2009) and Gruppioni et al. (2015). Interestingly, this result highlights the similar evolution of the star formation rate (SFR) and AGN activities, as well as BH accretion by suggesting a likely BH-host galaxy co-evolution.

The second crucial aspect in our understanding the AGN-galaxies co-evolution is represented by the so-called "downsizing". The latter refers to the anti-hierarchical evolution of both the luminosity of the AGN and the SFR of the galaxies. Indeed, SF history of massive galaxies peaks at higher redshift than the low mass galaxies one (Cowie et al., 1996). Similarly, Fig. 1.10(b) reports the AGN comoving number density versus the redshift, as a function of four 2-10 keV luminosity bins, and shows that the number density of the most X-ray luminous AGN peaks at higher redshift ($z \sim 2-3$) than the low luminosity ($L_{[2-10]keV} \sim 10^{43} - 10^{44} erg\ s^{-1}$) ones (Ueda et al., 2014).

Summarising, both scaling relations and the evidence for similar evolution of SFR and BH accretion lead to the conclusion that the AGN activity has a crucial role in the galaxy formation and evolution (Silk & Rees, 1998; Fabian, 1999; King, 2003).

1.3.3 Energy budget of SMBH

It is worth comparing the radiative energy liberated during the growth of a SMBH with the host-galaxy parameters, once $M_{BH} \sim 2 \times 10^{-3} M_{bulge}$ is assumed.

The energy released during the BH accretion event is indeed able to exceed the binding energy of the host galaxy bulge (see Fabian 2012 and references therein). The latter is given by the following formula:

$$E_{bulge} \propto M_{bulge}\sigma^2 \sim 10^{-6} M_{bulge} c^2 \left(\frac{\sigma}{300\ km\ s^{-1}} \right)^2 \tag{1.18}$$

where M_{bulge} is the mass of the bulge and σ is the stellar velocity dispersion. On the other hand, the energy released by the BH accretion, assuming energy-to-mass conversion efficiency of $\simeq 0.1$, is the following:

$$E_{BH} = 0.1 M_{BH} c^2 \sim 2 \times 10^{-4} M_{bulge} c^2 \tag{1.19}$$

Under the assumption that stellar velocity dispersion of galactic bulge reach maximum values of 300 $km\ s^{-1}$, the 1% of the energy produced by the AGN is enough to unbind the bulge of the galaxy.

1.3.4 Quenching star formation in massive galaxies

The theory of the structure formation in ΛCDM cosmology provides a galaxies mass function (see Mukhanov et al., 1992, for review). At the same time, observations provide the galaxy luminosity function (Schechter, 1976). To obtain the observed galaxy mass function it is necessary to assume a M/L ratio. The comparison between the theoretical (solid black line) and observed (green band) galaxies mass function reports inconsistencies (Fig. 1.11 (a)) for both low and high mass galaxies, which are less than expected. This discrepancy between theory and observations suggests low efficiency of small and large DM structures in forming stars within them. Such SF ineffectiveness for low mass galaxies is easily explained thanks to the energy released by starburst and/or supernovae (SNe) in the form of winds, which are able to remove the fuel in low potential wells (Stinson et al., 2010). Similarly, high mass galaxies need to have critical processes capable to stop the SF, by removing or heating of the gas reservoir.

The need of such a process is also the conclusion reached by observing the color evolution of the galaxy population. In fact, in the local Universe the galaxy population exhibits a clear bi-modality (Kauffmann et al., 2003a). The local galaxy population is divided in (i) blue star-forming galaxies discs or irregular (late type), characterised by small stellar mass (M_*) and low stellar surface mass density (μ_*), and (ii) "red" and massive, elliptical or lenticular, galaxies (early type) exhibiting low SF, large stellar mass and high μ_* (Heckman & Best, 2014). Some works (e.g., Brinchmann et al., 2004; Salim et al., 2007) showed that the blue star-forming galaxy population is distributed on a SFR vs M_* linear relation, named the star-forming main sequence or "blue cloud", while the red and dead massive galaxies populate a region called "red sequence" (Fig. 1.11 (b)).

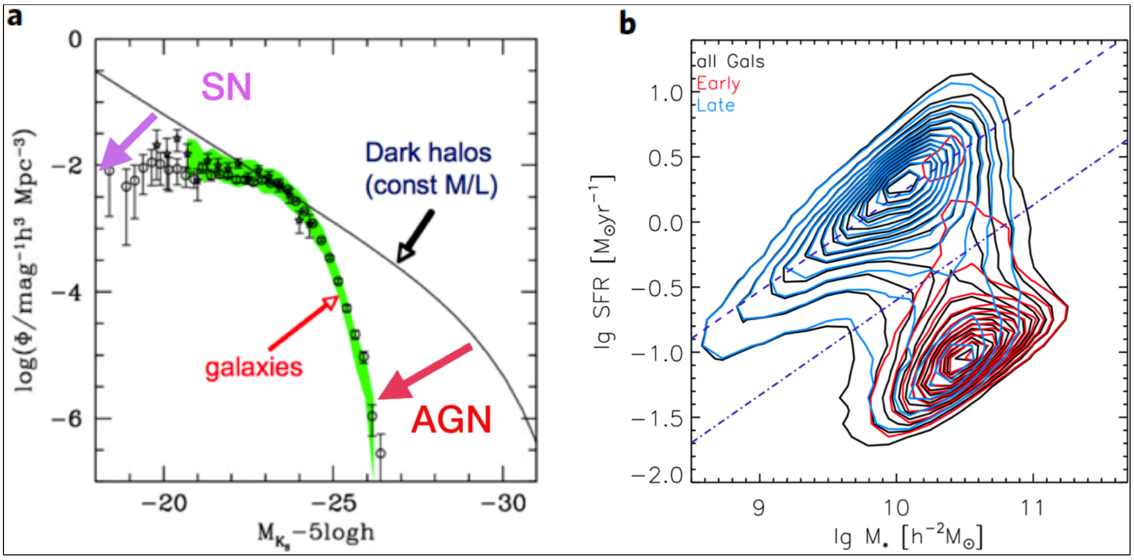

Figure 1.11: *Panel a*: Role of feedback in modifying the mass function of the galaxies (circles) computed by the observed luminosity function of the galaxies (Benson et al., 2003). Solid black line reports the theoretically mass function of the galaxies obtained by the standard cosmological ΛCDM model (White & Frenk, 1991). *Panel b*: distribution of local galaxies in the $log\ SFR$ - $log\ M_*$ diagram, where M_* is the stellar mass. Red and blue contours show the distribution of early-type and late-type galaxies, respectively. Black contours indicate the galaxies of all morphologies. The purple dashed line indicates the highest density region (i.e. the Main Sequence), while the purple dashed-dotted line is the lowest density region and it is used to separate the Main Sequence and the quenched galaxy population. Figure from Liu et al. (2019).

The behaviour of the local star-forming galaxies, in which the specific SFR (sSFR=SFR/M_*) is correlated with the M_* as sSFR∝ $M_*^{-0.1}$, suggests that the most massive galaxies are now forming a lower fraction of their stellar mass (Peng et al., 2010). Moreover, the blue cloud population dominates at z>1 (Wolf et al., 2003) and remains approximately constant from z=1 to z=0, while the number of density of red and dead galaxies increases as the redshift decreases. These pieces of evidence imply that massive star-forming galaxies (blue cloud) have to undergo a rapid evolution, in which their SF quench and become red sequence galaxies. The SMBH energy output is invoked as one of the possible mechanisms to stop and prevent the SF in these massive galaxies.

1.4 QSO mode feedback: outflows

Several theoretical models of galaxy evolution (e.g. Di Matteo et al., 2005) invoke mechanisms which are able to heat the gas on large scales (>>1 kpc), quench star formation and deposit metals on the surrounding environment (Gebhardt et al., 2000). The most popular scenario predicts that the winds produced by the accretion onto the BH in the galactic centers can be responsible for both mechanisms (e.g. Morganti, 2017) . The properties of these winds, as well as the effects of their interaction with the surrounding environment, are very dependent on the BH accretion mode. Currently, two different AGN feedback modes have been proposed, which are associated to a different level of the accretion rate (Fabian, 2012; Harrison, 2017):

- **Radiative(QSO)-mode feedback** is associated to most luminous AGN, which are characterised by a high accretion rate ($\lambda_{Edd} \geq 0.01$) of gas from an optically thick geometrically-thin disk. In this case the AGN radiative output is able to launch very powerful radiatively-driven winds, whose properties will be extensively discussed in the the following.
- **Radio(Jet)-mode feedback** is a associated to SMBHs which have a low accretion rate ($\lambda_{Edd} < 0.01$) of hot gas typically observed in the center of galaxy clusters. The energy is released under the form of radiatively inefficient radio jets, which can reach very large scales, i.e. beyond the virial radius of the galaxy.

Focusing on the QSO-mode feedback, radiation-driven outflows can be detected in the form of broadened and Doppler-shifted emission/absorption lines in QSO spectra. Outflowing gas has been ubiquitously revealed in luminous AGN, in different phases (i.e. ionised, neutral, atomic and molecular) at different distances from the QSO (i.e. sub-pc, pc and kpc scales), see Cresci & Maiolino (2018) and references therein. It is possible to derive physical quantities such as maximum velocity v_{max}, mass outflow rate $\dot{M}_o$ and kinetic power $\dot{E}_{kin}$, by adopting different assumptions. Maximum velocity can be estimated as follows:

$$v_{max} = |v| + 2\sigma^{broad} \tag{1.20}$$

where σ^{broad} is the velocity dispersion measured of the broad line and v is the velocity shift with respect to the QSO systemic redshift.
The mass outflow rate is given by:

$$\dot{M}_o = \frac{3 \times v_{max} \times M_o}{R_o} \tag{1.21}$$

Specifically, $\dot{M}_o$ is the instantaneous outflow rate of the gas at the R_o, M_o is the total mass of the outflow and R_o is the radius at which the outflow rate is computed. Finally, the kinetic power of an outflow can be computed as follows:

$$\dot{E}_{kin} = \frac{1}{2}\dot{M} v_{max}^2 \tag{1.22}$$

In the following, a brief review of the most relevant outflows discovered at different scales from a QSO is reported.

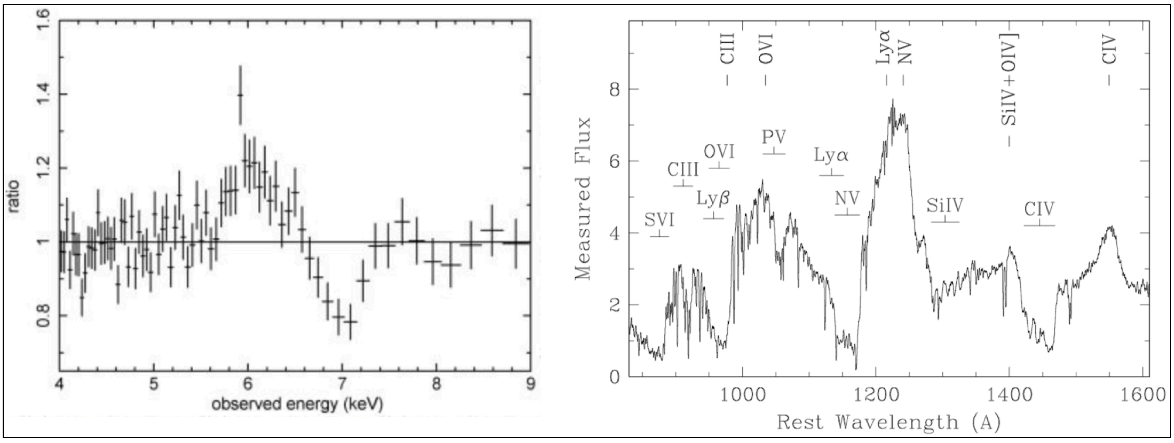

Figure 1.12: *Left Panel*: Fe K profile of PG 1211+143, resembling a P Cygni profile characteristic of an outflow, with both emission and blue-shifted absorption components (Pounds & Reeves, 2009). *Right Panel*: HST spectrum of PG 1254+047 at the rest-frame wavelengths exhibiting broad absorption lines labelled above the spectrum.

(A) **Nuclear winds**

Blue-shifted absorption lines in the UV and X-ray spectrum of AGN reveal the presence of massive and ionised outflows close to the SMBH (~few pc), in the region dominated by the SMBH gravitational field. Thanks to the high sensitivity and good spectral resolution of XMM-Newton and Chandra space telescopes, it has been possible to detect the presence of Ultra Fast Outflows (UFOs) in the X-ray spectrum of local AGN (Tombesi et al., 2010). These are powerful ($E_{kin} \sim 0.1\ L_{bol}$) and relativistic ($\sim 0.1 - 0.4c$) winds of highly ionised gas with high column density ($N_H \simeq 10^{22}$–$10^{24}\ cm^{-2}$), probed at sub-pc scales (~0.01-0.1 pc; Crenshaw et al., 2003; Tombesi et al., 2012) traced by blue- and/or red-shifted and highly ionised Fe K absorption lines (at energies >7 keV), usually associated to FeXXV-XXVI K-shell resonant absorption Fig. 1.12.

Theoretical studies (King, 2010) proved that the observed high ionisation of the outflowing material could be due to the intense radiation from the accretion disk, suggesting a direct link to it. UFOs can bring outward a significant amount of energy, momentum and mass, which are deposited on the surrounding medium. Moreover, their mass outflow rates can be compared with accretion rate and, therefore, affect SMBH growth.

Furthermore, winds with lower velocity ($v \sim 100 - 1000\ km\ s^{-1}$), smaller column densities ($N_H \simeq 10^{20} - 10^{22.5}\ cm^{-2}$) and less ionised (ionisation parameter $-1 \leq log[\frac{\xi}{erg/s/cm^2}] \leq 3$) than UFOs have been found in ~50% of the X-ray spectra of type 1 AGN (Piconcelli et al., 2005). They are called warm absorbers (WAs) and revealed by the presence of absorption lines (i.e. OVII, OVIII, Ne IX, Fe M-shell) in the $\sim$ 0.3 - 2 keV energy band (Kaspi et al., 2001). The location of WAs can also be constrained by widths and blueshifts of these line, assuming they are approximately virial. This implies a location near ~1 pc for a 10^6 $M_\odot$ SMBH. Their origin and the launching mechanisms are still debated. These WAs may represent thermally-driven outflowing gas from the torus (Blustin et al., 2005) or magnetically-driven winds from the accretion disk (Fukumura et al., 2010). A recent model by (King & Pounds, 2014) suggests that WAs can be the result of radiation-driven UFOs halted by collisions with the host galaxy interstellar medium

Outflows with velocities up to ~0.2 c (Hewett & Foltz, 2003) close to the SMBH (i.e. >0.1 pc) are also revealed by the detection of broad absorption lines (BALs) in UV of AGN spectra, which are also blue-shifted with respect to the systemic of AGN (Gibson et al., 2009). Fig. 1.12(b) shows an example of the HST spectrum of the BAL QSO PG1254+047, which exhibits many intrinsic broad absorption lines, i.e. physically related to the AGN. BALs can be associated to high ionisation metals (C IV, S IV, N V, O VI) and/or low ionisation metals (Mg II, Al III).

Several works found a fraction of BAL in the SDSS survey AGN population of $f_{BAL} \sim 15$ % (Reichard et al., 2003; Gibson et al., 2009). These authors adopted the CIV Balnicity Index (BI>0) as criterion to identify BAL AGN, where BI is defined by Weymann et al. (1991) as follows:

$$BI = \int_{3000}^{25000} (1 - \frac{f(v)}{0.9}) C \, dv \tag{1.23}$$

in which the parameter C is the unity over contiguous wavelength layers of at least 2000 $km\ s^{-1}$. Interestingly, Bruni et al. (2019) found that the fraction of BAL AGN in the population of hyper-luminous AGN with $L_{bol} > 10^{47} erg\ s^{-1}$ is about two times higher than the typical fraction observed in the entire AGN population. Furthermore, BALs in luminous QSOs exhibit the largest maximum velocities (defined in Eq. 1.20) and the highest values of BI (Fig. 1.13). These findings suggest that an high L_{bol} favours the BAL wind acceleration.

Finally, Elvis (2000) suggests a unifying structure for the inner regions of QSOs (see Fig. 1.14), which is able to explain (i) the broad emission lines observed in all the QSOs; (ii) the BALs observed in ~15% of QSOs and (iii) ionised outflows seen in NALs in UV and X-ray spectra of half of AGN. He proposes the funnel-shaped thin shells of warm gas winds arise vertically from the accretion disk with velocities comparable with the broad emission lines. The AGN radiation accelerates these winds radially and bends them to a cone angle of ~60° from the QSO axis, accounting for BAL features with a covering factor of 10-20%. If the observer line of sight is at larger angle

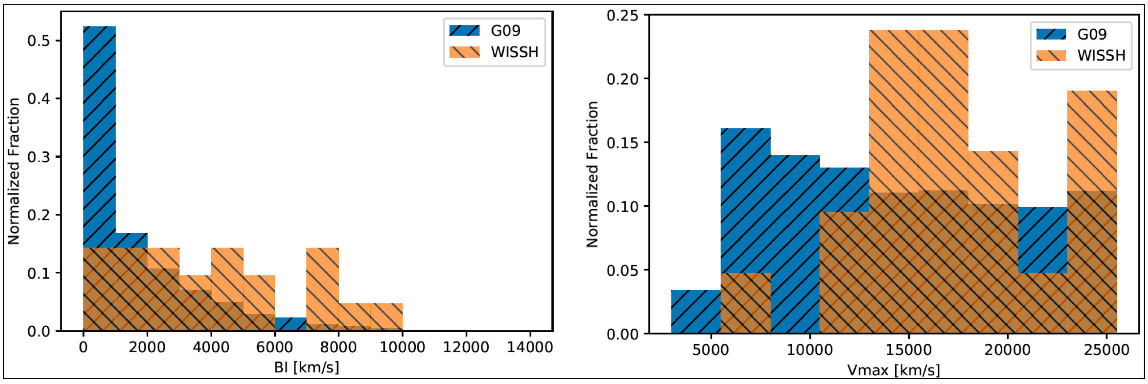

Figure 1.13: Distribution of BI (*left panel*) and maximum velocity (*right panel*) of the CIV in hyper-luminous QSOs (WISSH QSOs sample; Bischetti et al., 2017) and BAL QSOs from the Gibson et al. (2009) sample (Bruni et al., 2019).

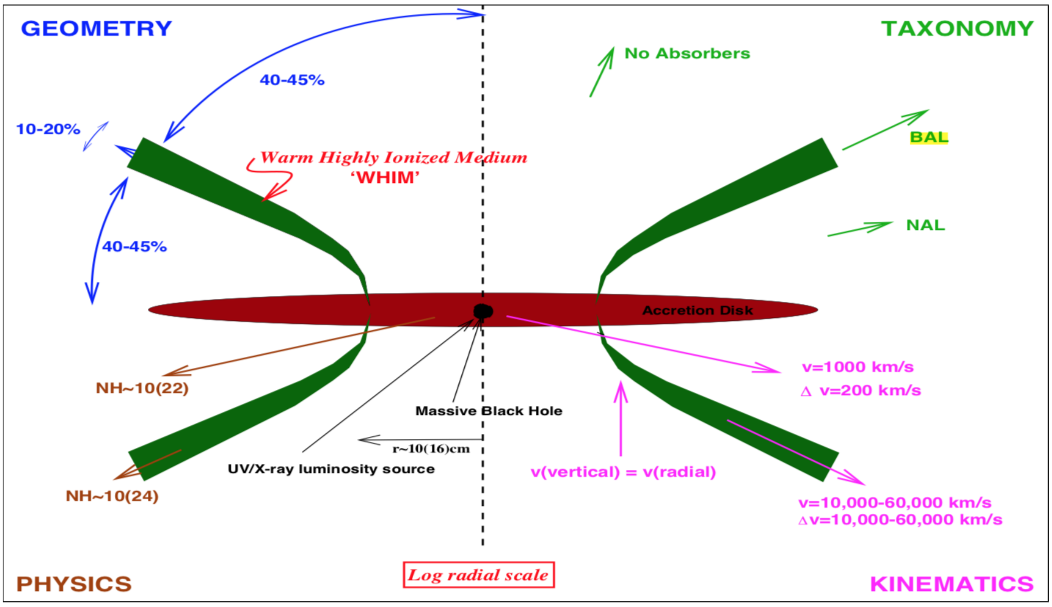

Figure 1.14: Unified internal structure of QSOs proposed by Elvis (2000). The four quadrants illustrate as the geometry, taxonomy, physics and kinematics of outflowing gas vary according to the angle of the observer's line of sight. See text for details.

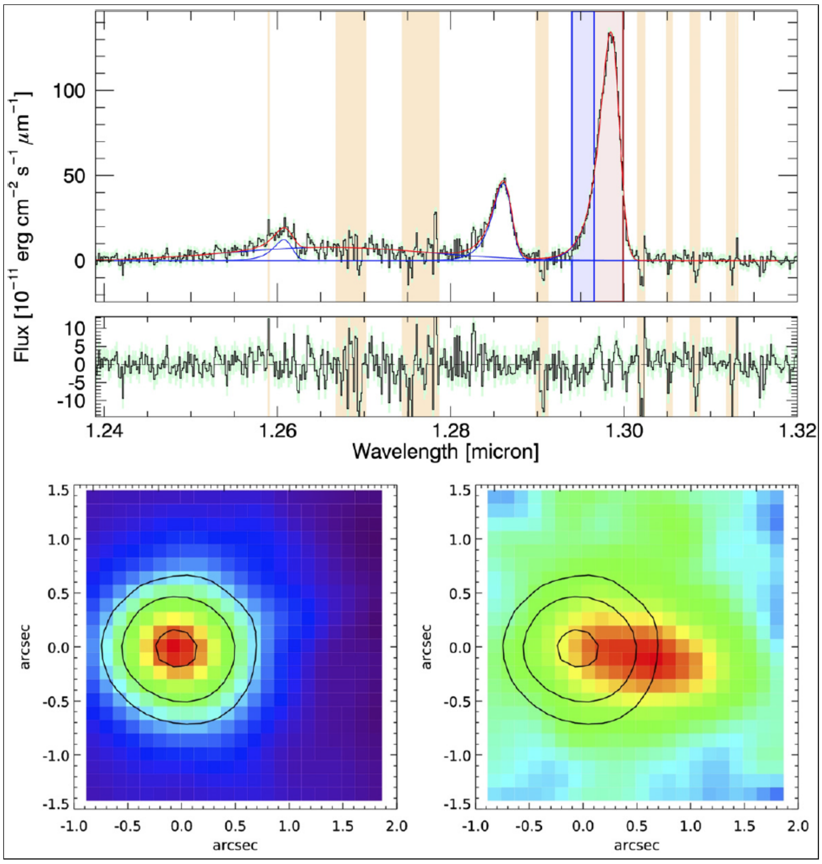

Figure 1.15: Spectrum of XID2028 QSO (Cresci et al., 2015), integrated in a region of 1"×1" of SINFONI IFU data. The red and blue shaded areas cover the spectral region collapsed, corresponding to the [OIII] emission line, whose images are shown in the lower panels. It can be noted that by collapsing the red area covering the emission line core, a point source results. On the other hand, the image obtained from the collapse of the [OIII] wing (i.e. the outflow) exhibits a conical shape with an offset from the peak of the quiescent [OIII] emission.

with respect to the QSO axis then NAL are viewed, otherwise for smaller angle with respect to the QSO axis no absorber is seen (see also Risaliti & Elvis, 2010). Fig. 1.14 shows the typical angles (top-left), the taxonomy (top-right), the typical kinematics of the outflows (bottom-right) and the column density expected for the nuclear winds (bottom-left), as a function of the line of sight.

(B) Galactic-scale outflows

Investigations of different gas phases (i.e. ionised, neutral, atomic and molecular) revealed presence of outflows on large scales, i.e. >10-100 kpc.

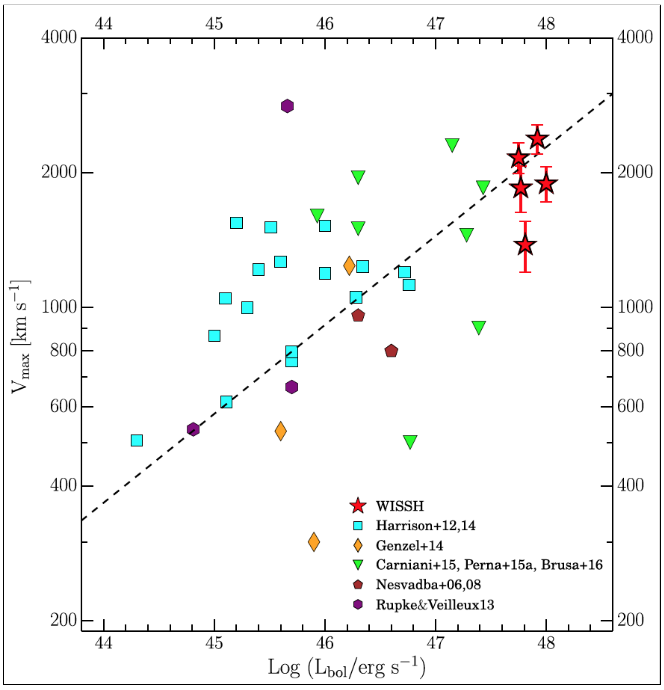

Figure 1.16: Maximum velocity of outflowing [OIII] gas as a function of the bolometric luminosity L_{bol} of different type of AGN reported by the literature (see Bischetti et al., 2017, and references therein). The dashed line represents the relation $L_{bol} \propto v_{max}^5$ (with arbitrary normalization) expected for energy conserving winds (see Costa, 2014).

Spatially resolved spectroscopy provided by integral-field unit (IFU) observations allows us to identify large-scale outflows, estimate velocity, map their morphology and, therefore, determine $\dot{M}_o$ and E_{kin}. The [OIII]λ5007 is a good proxy for large-scale ionised outflows, as it is a forbidden emission line, which needs to be emitted in low density regions (i.e. NLR) not to be suppressed by collisional de-excitations, as happens in the BLR (Bennert et al., 2002; Swinbank et al., 2006; Nesvadba et al., 2006).

The [OIII] emission line profiles observed in luminous AGN usually exhibits a broad and blue-shifted component revealing the presence of an extended outflow, whose velocity dispersion reflects the outflow kinematics. Fig. 1.15 reports an example of an [OIII] outflow detected by Cresci et al. (2015) with velocity of ~1500 $km\ s^{-1}$ and a distance from the BH of ~13 kpc, as clearly shown from the morphology of the spatially resolved [OIII] wing emission. A correlation between [OIII] outflow properties and AGN bolometric luminosity (L_{bol}) is observed. Figs. 1.16 and 1.17 are taken from Bischetti et al. (2017) and show the v_{max}, $\dot{M}_o$ and $\dot{E}_{kin}$ of ionised outflows as a function of the L_{bol} for some samples of outflows powered by

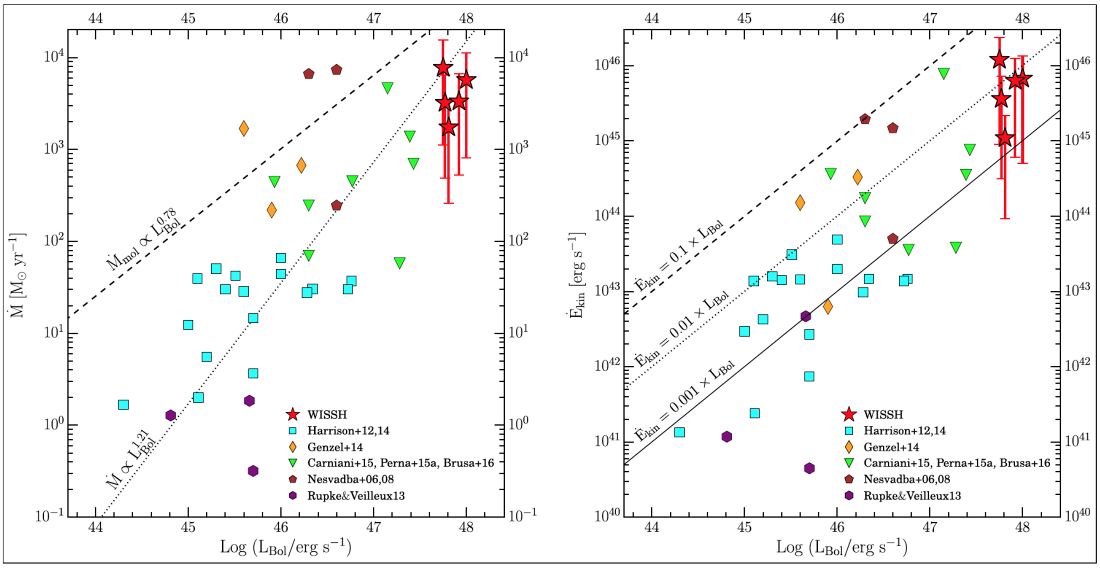

Figure 1.17: *Left panel*: mass rate of ionised [OIII] outflows as a function of L_{bol} of AGN. Dotted (dashed) line represents the best-fit relation derived for ionised (molecular) outflows. *Right panel*: kinetic power of ionised [OIII] outflows as a function of the AGN L_{bol}. Dashed, dotted and solid lines indicate $\dot{E}_{kin}/L_{bol}$ values of 10%, 1%, and 0.1%, respectively. Figures from (Bischetti et al., 2017).

different type of AGN (e.g. obscured X-ray AGN, high-z radio galaxies, hyper-luminous AGN). Specifically, Fig.1.16 shows that ionised outflows follow a $L_{bol} \propto v_{max}^5$ relation, as expected for energy conserving winds (see Sect. 1.5). Moreover, it is worth noting that most luminous AGN seem to exhibit the largest maximum velocities, as well as kinetic power and mass rate values (1.17). These two findings emphasize the role of the AGN in powering these kpc-scale ionised outflows.

Furthermore, outflows extending on galactic scales have been also observed through the study of the molecular and atomic phases traced by some prominent emission/absorption lines such as CO (Feruglio et al., 2010; Cicone et al., 2012; Bischetti et al., 2019a), OH (Fischer et al., 2010; Veilleux et al., 2013; Stone et al., 2016), H_2 (Rupke & Veilleux, 2013) and [CII] Cicone et al. (2015); Bischetti et al. (2019b). According to these observational evidences, the molecular gas is a good proxy for extended kpc-scale outflows, exhibiting a typical mass outflows rate ranging from 100 to 1000 $M_\odot\ yr^{-1}$ and velocity up to ~1000 $km\ s^{-1}$.

One of the first detection of molecular outflow was reported in Mrk231 by Feruglio et al. (2010) and it was discovered through a CO(1-0) transition line showing a broad and shifted component (red dotted line in Fig. 1.18).

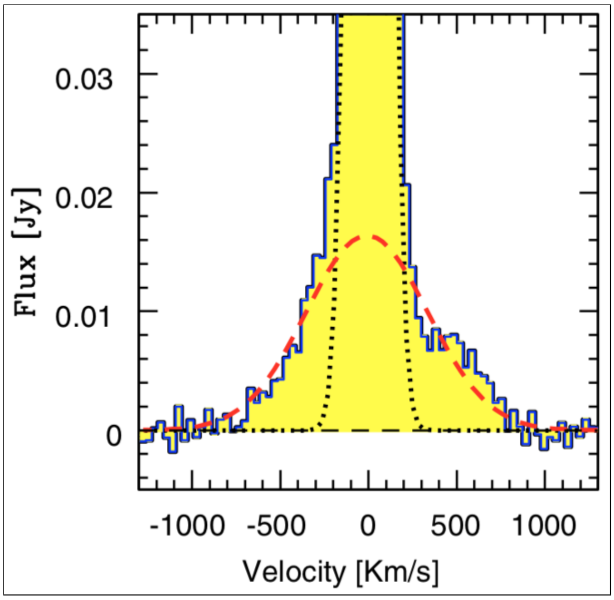

Figure 1.18: Zoom of CO(1-0) emission line in the spectrum of Mrk231 (Feruglio et al., 2010). The line exhibits broad wings (dashed red line) which provide a clear indication of the presence of molecular outflow.

This outflow exhibits a velocity of ~1000 $km\ s^{-1}$ and a mass outflow rate ~ 700 $M_\odot\ yr^{-1}$. For the same object Feruglio et al. (2015) show also molecular CO(2-1) outflow reaching a distance of 1 kpc from the AGN. They found a decrease of the $\dot{M}_o$ and a flat v_{max} profile as the distance from the AGN increases. This suggests a decrease of either the average density (ρ) or the filling factor of the outflow, as the distance from the AGN increases. In this scenario, once the density of the gas is reduced, UV photons could photo-dissociate the CO molecular gas, turning it into atomic gas (e.g. [CII], [NII]), which would continue to expand on few tens kpc scales. Indeed, Cicone et al. (2015) detected a [CII]158μm outflow exhibiting velocity ~1400 $km\ s^{-1}$, with a maximum projected radius from the AGN of ~30 kpc (Fig. 1.19). Moreover, this finding seem to suggest that outflows can even interact with gas at several kpc scales, i.e. Inter-Stellar Medium (ISM) and beyond. However, the coupling between AGN driven winds from different outflowing gas phases and Circum-Galactic Medium (CGM) is still not well understood.

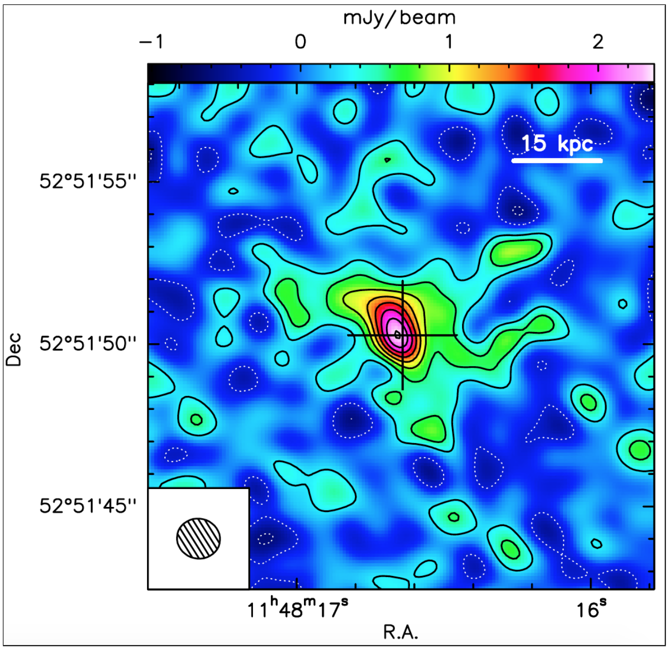

Figure 1.19: Map of the continuum-subtracted [CII] emission from the z=6.41 QSO SDSSJ1148+5251 (black cross), integrated within velocities range from -1400 to 1200 $km\ s^{-1}$ (Cicone et al., 2015). The contours are shown in steps of 3σ ($\sigma \simeq 0.26\ Jy\ beam^{-1}\ km\ s^{-1}$). The beam is shown in the left-bottom corner ($\simeq$ 1.3" × 1.2").

Many AGN exhibit cold molecular and neutral gas outflows with mass outflow rates exceeding the host galaxy SFR, suggesting that these outflows can affect the host galaxy evolution (e.g. Feruglio et al., 2013; Cicone et al., 2015; Fluetsch et al., 2019). For example, Bischetti et al. (2019a) investigated the mechanism of molecular large-scale outflow expansion and their impact on the host-galaxy. Specifically, they analysed the CO(3-2) molecular emission in PDS456, which is the most luminous ($L_{bol} \simeq 10^{47}\ erg\ s^{-1}$) radio quiet AGN at low redshift ($z \sim 0.18$), exhibiting a nuclear (0.01 pc from the AGN), fast (~0.3c), and quasi-spherical UFO expanding with a kinetic power of 20-30% of the L_{bol} (Nardini et al., 2015; Luminari et al., 2018). Bischetti et al. (2019a) found a CO(3-2) molecular outflow showing a complex morphology as shown in Fig. 1.20, in which multiple outflowing clumps are observed. The values of the total mass of the molecular gas ($M_{mol} \simeq 2.5 \times 10^9 M_{\odot}$) and mass rates of these outflowing components ($\dot{M}_{out} \sim 290\ M_{\odot}\ yr^{-1}$) suggest a possible scenario of SF quenching due to the AGN-driven outflow, in which the gas reservoir in PDS456 should depleted in a short time of $\tau_{dep} \sim M_{mol}/\dot{M}_{out} \simeq$8 Myr.

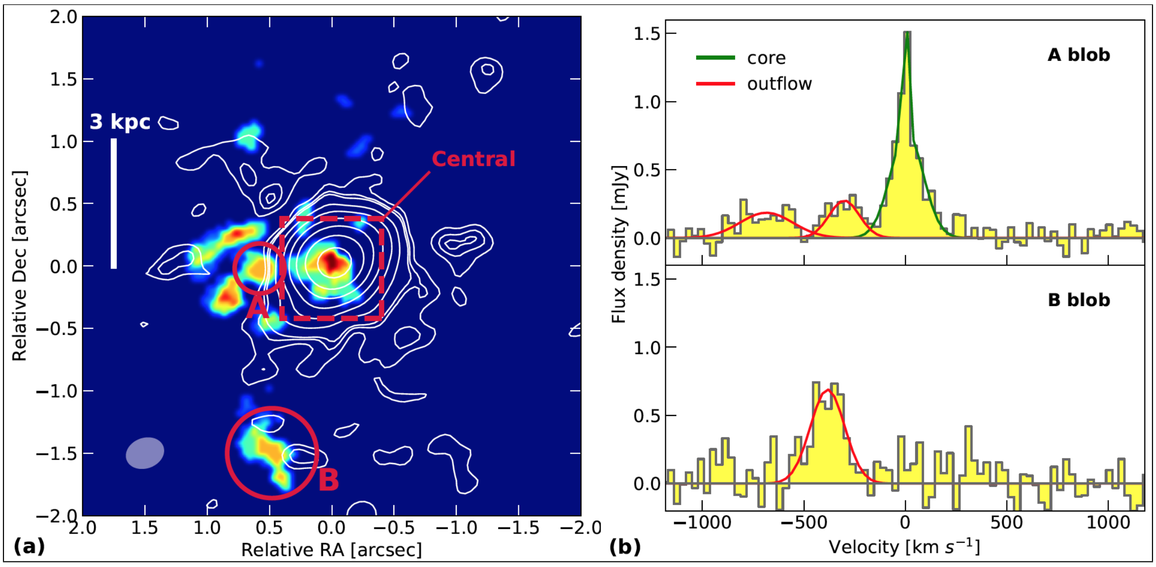

Figure 1.20: The molecular outflow in PDS456 as seen by ALMA (Bischetti et al., 2019a). *Panel a*: velocity integrated map of the blue-shifted CO(3-2) emission obtained by integrating the emission at $> 3\sigma$ in a velocity range of 120 $km\ s^{-1}$. White contours show the systemic CO(3-2) emission. *Panel b*: CO(3-2) spectra of the outflowing clumps A and B. Green curve in the spectrum indicates the systemic of the QSO.

Fiore et al. (2017) collected multi-wavelength observations of 94 AGN up to z$\sim$ 2.5, showing outflows in different gas phases. They explored the correlation between the AGN and ionised, molecular, BAL and X-ray outflows properties. Fig. 1.21a shows a correlation between $\dot{M}_o$ and L_{bol} for both molecular ($\dot{M} \propto L_{bol}^{0.76\pm0.06}$) and ionised outflows ($\dot{M} \propto L_{bol}^{1.29\pm0.38}$). The ratio between molecular and ionised mass outflow rates decreases with the AGN bolometric luminosity, therefore the importance of ionised outflows increases with the luminosity of the AGN. L_{bol} correlates with the $\dot{E}_{kin}$ (Fig. 1.21b): specifically, ionised gas, X-ray absorbers and BALs exhibit values $\dot{E}_{kin}/L_{bol} \simeq 0.1-10\%$, while molecular gas exhibits $\dot{E}_{kin}/L_{bol} \simeq 1-10\%$. Fig. 1.21c shows a correlation between L_{bol} and v_{max} for ionised+molecular outflows and UFOs, in which the v_{max}^{UFO} and $v_{max}^{ion-mol}$ ratio is about constant ($\sim$ 40 – 50) at each L_{bol}, implying that the gas mass involved in galaxy scale outflows could be $\sim$ 2000 times larger than the one involved in nuclear winds. Finally, $\dot{P}_{mol}/\dot{P}_{rad}$ versus v_{max} reported in Fig. 1.21d sheds light on the outflow driving mechanism of the different gas phases. In Sect. 1.5 two mechanisms will be introduced in details: energy- and momentum-driven. The first (second) one occurs when the shocked gas cannot (can) cool efficiently during its expansion, so that is able to transfer the most of energy (ram-pressure) to the contact gas. According to the predictions of King (2003),

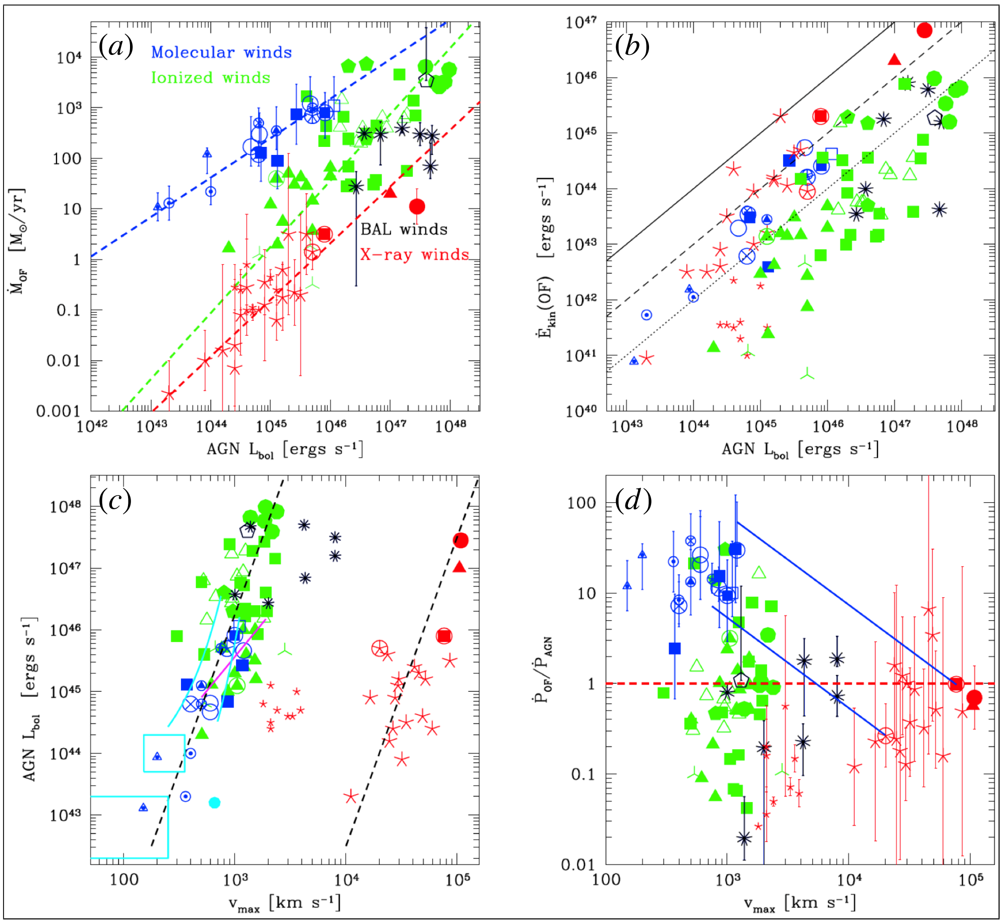

Figure 1.21: AGN bolometric luminosity as a function of the mass rate (*a*), kinetic energy (*b*) and maximum velocity (*c*) of multi-phase outflows. Panel (*d*) reports the wind momentum load ($\dot{P}_{mol}/\dot{P}_{rad}$) as a function of the maximum velocity of multi-phase outflows. Multi-phase outflows consists of molecular (blue), ionised (green), BAL (black) and X-ray (red) winds (see Fiore et al., 2017, for more details).

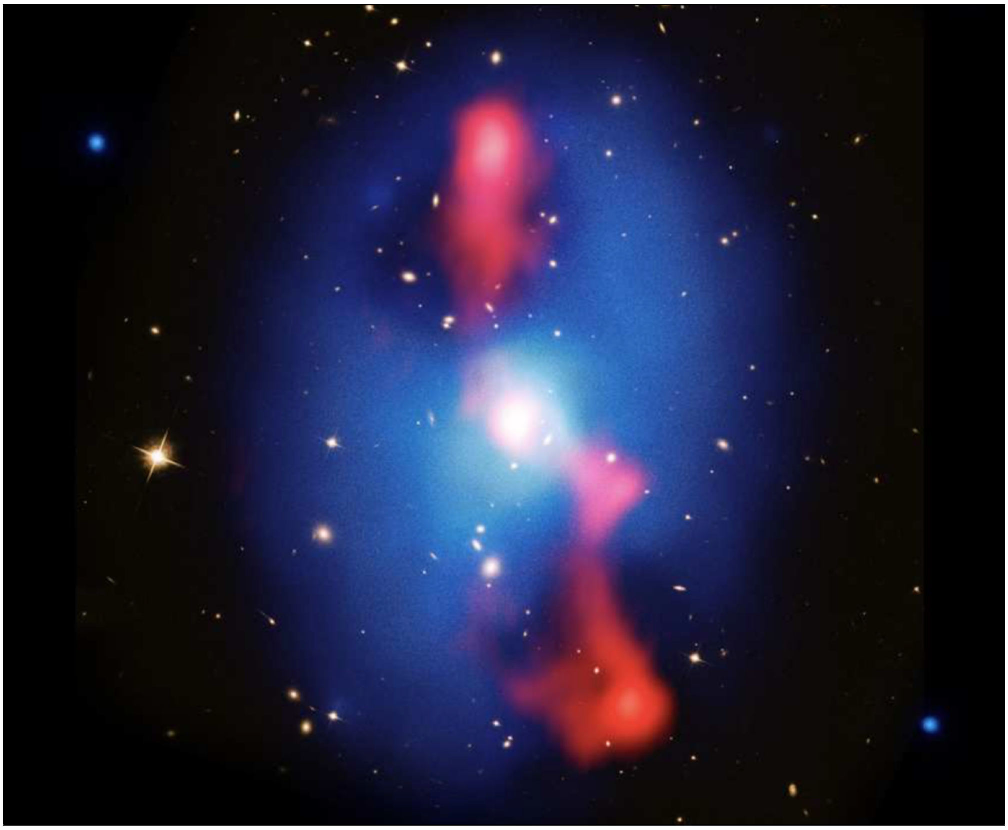

Figure 1.22: HST image (800 $kpc \times 800$ kpc) of the galaxy cluster cool core MS 0735+7421 (Gitti et al., 2012). Blue and red superposed colors represent the Chandra X-ray and the Very Large Array 330 MHz radio images, respectively. Radio emission shows the morphology of radio jets, which shock the ICM, by producing giant X-ray cavities observed with Chandra data.

the momentum flux of the wind normalised to the AGN radiative momentum output ($\dot{P}_{mol}/\dot{P}_{rad}$) allows the distinction between these two mechanisms. In particular, Fiore et al. (2017) found that molecular and several ionised winds show $\dot{P}_{mol}/\dot{P}_{rad} > 1$ (energy-conserving), while BALs and X-ray absorbers winds exhibit $\dot{P}_{mol}/\dot{P}_{rad} \sim 0.01 - 1$ (momentum conserving).

1.4.1 Radio-mode AGN feedback

Direct observations of the radio-mode AGN feedback on large scales are obtained thanks to the detection of cavities and shock fronts produced in the X-ray emitting gas (Fabian et al., 2000). Indeed, the collimated jet transports kinetic energy, which is dissipated by shocks through the interaction with the ICM (Blanton et al., 2009). The jets from AGN can be able to inflate massive bubbles of hot X-ray emitting gas that proceed to rise buoyantly through the ICM. Jet-inflated bubbles do work on the ICM by exciting shocks, turbulence and sound waves. Fig. 1.22 shows an example of radio jets morphology and shocked X-ray cavities in the galaxy located in the cluster core MS 0735+7421.

Radio-mode feedback is typically observed in very massive, elliptical galaxies (i.e. the brightest cluster galaxies) placed in local galaxy cluster cores. As main effect, the radio jet of these objects has to heat the ICM through one or more mechanisms, e.g. cavity heating, shock heating and convection or turbulence (Gitti et al., 2012, and references therein). Such heating is hence required to explain the so called "cooling flow problem" (Fabian, 1994). This problem is linked to the physics of the diffuse gas in galaxy cluster, which is expected to have a cooling time shorter than the Hubble time (Fabian & Nulsen, 1977) in the densest (i.e. central) region. According to this expectation, we should observe a great amount of cold inflow gas accumulating in molecular clouds and forms stars. However, this is not observed.

The radio-mode AGN feedback appears to be responsible for heating the ICM and depositing, energy and entropy. The heating prevents further condensation of the ICM, leading to the AGN shutting off and allowing the ICM to cool again. Thus, the balance of radiative cooling and AGN heating provide an efficient mechanism to regulate the temperature of the ICM. Moreover, recent observational evidences have shown that radio jets also can interact with the ISM on large (McNamara & Nulsen, 2012) and small (Morganti et al., 2013) scales, by accelerating high velocity and massive atomic and molecular outflows (Cicone et al., 2014).

1.5 Acceleration and propagation of outflows beyond the host galaxy

In the scenario suggested by the standard cosmological model ΛCMD, the formation of the large scale structures starts with the growth of fluctuations of matter through the gravity, forming DM halos which collapse and reach the virial equilibrium and are distributed in a network of sheets and filaments forming a "cosmic web" structure.

The study of absorption lines in spectra of luminous background QSOs, has revealed the presence of heavy metals of $Z \sim 10^{-3} - 10^{-2}\ Z_{\odot}$ in the cosmic web filaments (Cowie et al., 1995; Schaye et al., 2003). Outflows driven by supernovae and, in particular, AGN can be energetic enough to overcome the gravitational binding energy of the galaxies and deposit metals in the Inter-Galactic Medium (IGM). Therefore, the high metallicity of the IGM strongly requires that AGN driven outflows interact with large scale environment, beyond the virial radius of galactic halos.

Direct observations of extended radiative outflows at distances > 15 kpc, i.e.

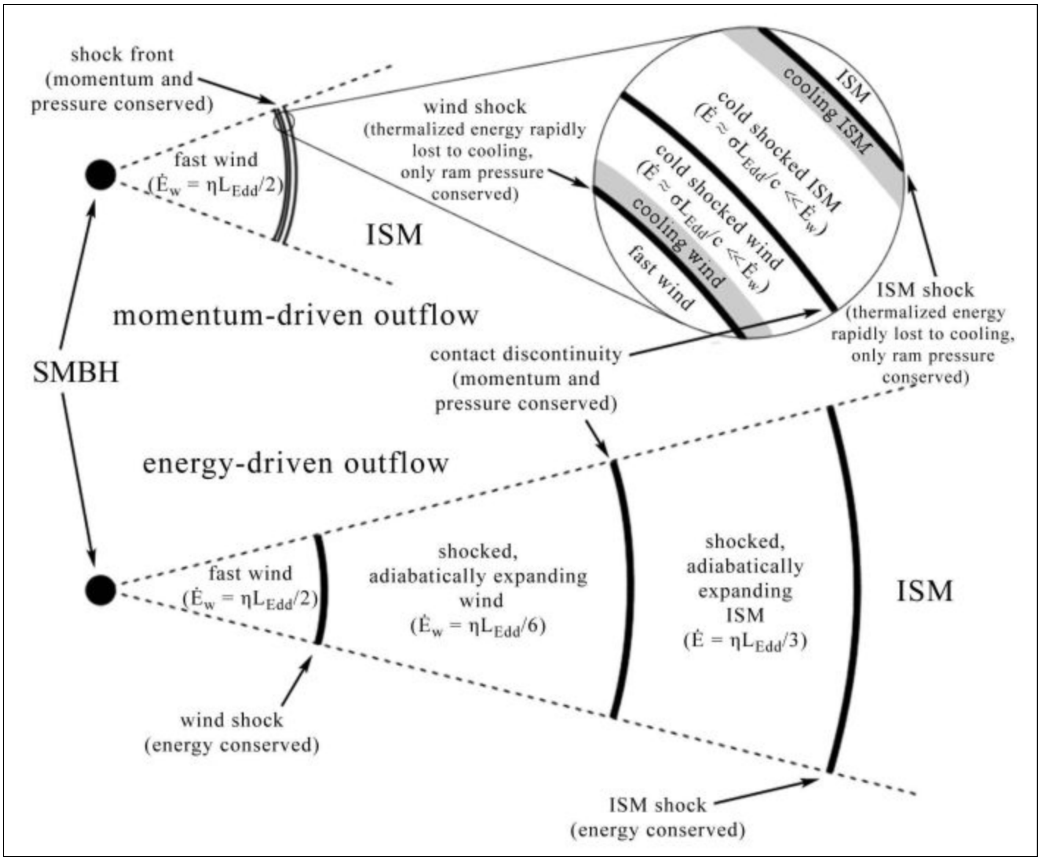

Figure 1.23: Diagram of momentum- (top) and energy- (bottom) driven outflows, showing the effects of their interaction between winds and ISM, and the energy and momentum transfer King & Pounds (2015).

beyond the ISM of the host galaxy, are scarce (Alexander et al., 2010; Maiolino et al., 2012). Reporting some examples, Tremonti et al. (2007) analysed 14 post-starburst galaxies at $z \simeq 0.6$ and detected MgII outflows with $v \simeq 500-2000\ km\ s^{-1}$ reaching distances of $\sim 100\ kpc$. Holt et al. (2008) found jet-driven outflows spatially extended up to 20 kpc in a sample of 14 compact radio sources. Cicone et al. (2015) detected an [CII] outflow extended on about 30 kpc scales in a $z \sim 6.4$ AGN. These studies provide evidences of gas phases moving outwards the host galaxies, leading to the idea that this could affect CGM and IGM (see Sect. 2).

In order to understand the coupling between SMBH energy output and the ISM and the CGM is essential to demonstrate whether AGN-driven outflows are able to reach such large scales. Specifically, outflows from luminous AGN can be either in the energy-conserving or in the momentum-conserving regime (King, 2003). In the interaction between nuclear wind and ISM, the first is slowed in an inner reverse shock, heating the shocked gas up a temperature of $\sim 10^{11} K$ and

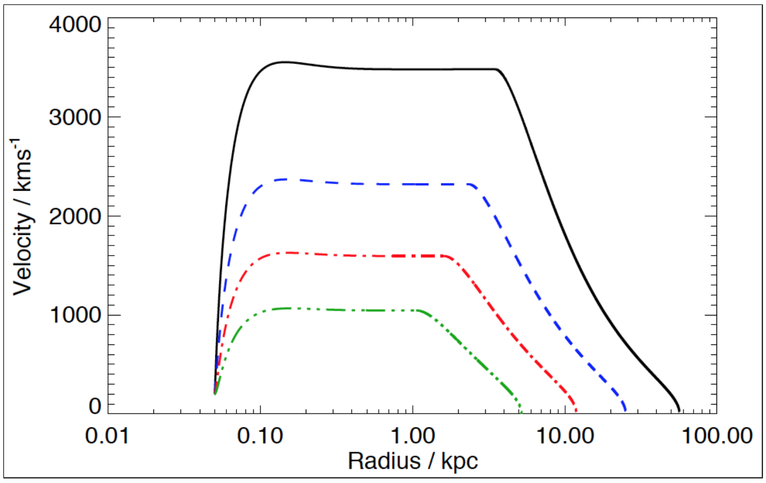

Figure 1.24: Numerical solutions of the full equation of the motion by King (2011), showing the trend of the outflow velocity (V) with the radius (R) and at different average gas fractions as $f_g = 3 \times 10^{-3}$ (black), 10^{-2} (blue), 3×10^{-2} (red) and 10^{-1} (green), assuming $R_0 = 50$ pc and V_0 =200 $km\ s^{-1}$ as initial conditions.

moving it outwards. This shocked gas injects energy and momentum into the ISM depending on its cooling time with respect to the outflows time scale (Zubovas & King, 2012). In the momentum-conserving regime, the hot shocked gas is highly compressed in the so-called contact discontinuity region and cools efficiently, communicating its ram pressure to the host ISM. Conversely, the energy-conserving regime occurs when the hot shocked gas does not cool and expands adiabatically, communicating most of the wind kinetic energy to the ISM. The energy-driven case is much more violent than the momentum-driven one. Indeed, in the second case the shocked gas can transfer only a part of the mechanical luminosity $L_{wind} \simeq 0.05 L_{Edd}$ to the surrounding gas, so that it cannot exceed the bulge binding energy and stop the BH accretion (Fig 1.23; top). In the energy-conserving case, according to the calculations made by King (2011), a large amount of bulge mass can escape from the galaxy. King (2011) consider an Eddington wind ($\dot{M}_{out} = \dot{M}_{Edd}$) with velocity $\simeq 0.1c$ and reverse shock temperature of $\simeq 1.6 \times 10^{10}$ K, expanding in an isothermal atmosphere. In this model, the gas can lose energy through Compton and free-free scatters (Fig 1.23 bottom). The rate of energy lost depends on the radiation density, which decreases as r^{-2}, so that the cooling time increases as r^2, while the flow time increases as r. Therefore, on one hand, close to the BH the cooling time (t_c) is expected to be shorter than the momentum-driven flow time (t_f) . On the other hand, at radii larger than the typical cooling radius ($r_C \simeq 500 M_8^{1/2} \sigma_{200} pc$) the flow is expected to be energy-driven ($t_c > t_f$) (King, 2003, 2005). Once the SMBH stops to grow up at t_{acc}, the shock pattern keeps on using the residual pressure to drive the outflows on larger scales and it persists for a time (t_{stall}) given by:

$$t_{stall} \simeq \left(\frac{v_e}{\sigma}\right)^2 t_{acc} \tag{1.24}$$

where σ is the velocity dispersion of the ambient medium and v_e the constant velocity of the pattern shock after the QSO switch off. If the shocked pattern reaches the virial radius (R_V) of the galaxy before stalling (at R_{stall}), then it will be likely that the shocked gas escapes from the galaxy (King, 2011). Therefore, in order to have outflows escaping from the galaxy the following condition should be satisfied:

$$R_V > R_{stall} \tag{1.25}$$

with $R_V = \sigma/7H$ where, $H = H_0 h(z)$ with H_0 the Hubble constant and $h(z)$ gives the redshift dependence. At the same time, the SMBH accretion time should be:

$$t_{acc} > 1 \times 10^8 \left(\frac{\eta_{0.1} f_g}{f_c}\right)^{2/3} \left(\frac{\sigma}{200\ km\ s^{-1}}\right)^{2/3} yr \tag{1.26}$$

where f_g and f_c are the fraction of the gas before and after the removing of the bulge mass and $\eta_{0.1} = \eta/0.1$ is the accretion efficiency. Fig. 1.24 shows the trend of the velocity with the radius obtained by numerical solutions, in which the equation of the motion by King (2011) are included. In the specific case of the black solid line, outflows can reach distances from the AGN of ~ 60 kpc. Therefore, outflows could be able to affect very distant environment, as required by the observations of CGM/IGM metallicity.

2. CIRCUM-GALACTIC MEDIUM OF AGNS

The Circum-Galactic Medium (CGM) is a multiphase gas located around a galaxy exhibiting complex kinematics and a wide range of ionisation potential energy, both in the cold ($T \sim 10^4 - 10^{5.5}\ K$) and in the hot phase ($T > 10^6\ K$).

According to the current standard cosmological ΛCDM model, the total Universe consists of ~5% of baryons, synthesised during the Big Bang, and the ~27% of DM (Planck Collaboration et al., 2016). The cosmological simulations of the formation of large scale structures predict that the final disposition of both DM and baryonic structures will look like a "cosmic web" of sheets and filaments (e.g, Springel, 2005; Frenk & White, 2012). At the intersection of the filaments there are over-densities of DM with $\delta = \Delta\rho/\bar{\rho} > 100$, with $\bar{\rho}$ the average density of the Universe showing a typical size of ~100-300 kpc in case of galaxies. The cool and diffuse gas within these over-density regions is the CGM. However, a net separation between CGM and the gas gravitationally bound to the central galaxy (i.e., the ISM) is not well defined (typically ~15 kpc). In turn, these formation regions of galaxies or groups, are connected with each other by cold ($T \sim 10^4 - 10^5$K) gas filaments structures (i.e. the IGM), which trace low density regions ($\delta < 100$) of the cosmic web (Martin, 2019). Recently, a warm-hot ($T > 10^5$K) intergalactic medium (WHIM) phase has been also observed (Nicastro et al., 2018).

The IGM and CGM gas was detected for the first time thanks to the study of a set of absorption lines (i.e. the Lyα forest) in the spectra of luminous background high-z QSOs (Gunn & Peterson, 1965; Lynds, 1971). These absorption lines represent neutral hydrogen absorbers along the line of sight between the observed and the background source. In particular, narrow absorption lines with column density $N_H < 10^{17.3} cm^{-2}$ are due to the IGM, while the broader ones associated to $N_H > 10^{17.3} cm^{-2}$ trace the gas in collapsed and virialized DM halos (i.e. ISM and/or CGM; Fumagalli et al., 2011).

Therefore, the diffuse gas on large scales traces the growth of non-linear structures and contains a large amount of the total baryonic matter of the Universe. Moreover, it acts as reservoir from which the galaxies can supply themselves via accretion processes. Mapping the distribution and analysing the physical and kinematics CGM properties is crucial to investigate the formation of the cosmic web structure and the baryonic processes involved in the galaxy evolution.

In this chapter, I will focus on the properties of the CGM around luminous

QSOs in the framework of the so-called *feeding & feedback cycle*. Such a cycle can be partially explored through the analysis of the metallicity and kinematics of the CGM, in particular, via the study of the Lyα emission.

2.1 The CGM as venue of the feeding and feedback processes

The theory of the galaxy evolution has several problems that do not match with observations (see Tumlinson et al., 2017, for details). Specifically, three of them are reported below:

- how do galaxies sustain the observed star formation over a Hubble time?
- What quenches galaxies?
- How do galaxies loose metals produced in their stars?

These problems are also clearly related to our poor understanding of the physical properties and evolution of the CGM, which is the interface between galaxies and the IGM. In other words, it is a playground of processes such as accretion from the IGM, galaxy interaction, winds and outflows and recycling outflows. Specifically, these processes are incorporated in the so called feeding & feedback cycle of galaxies assuming that each galaxy undergoes active phase(s) (Springel et al., 2005; Croton et al., 2006; Somerville et al., 2008). Fig. 2.1 shows a picture, taken from (Tumlinson et al., 2017), representing the summary of the processes which can happen in this cycle of complex interactions between inflowing (blue), outflowing (orange) and recycling (magenta) gas.

2.1.1 Accretion processes

In the feeding and feedback cycle, the accretion phase is crucial to feed galactic SF and the central BH. Several mechanisms are able to destabilise the gas, driving massive inflows towards galactic nucleus, e.g. minor and major mergers, secular processes. Moreover, semi-analytic models and cosmological hydrodynamical simulations (see Stewart, 2017, and reference therein) stressed the importance of the filamentary IGM gas to feed galaxies. In this scenario two cases are envisaged:

- In the "**hot mode**" **accretion**, the cooling time is larger than the free fall time ($t_c > t_{ff}$), so that the gas shock-heats to the virial temperature ($\sim 10^6 K$) of the DM halo and contracts very slowly, eventually fragmenting. Finally, the gas cools and collapse is into the center of the DM halo and form stars.

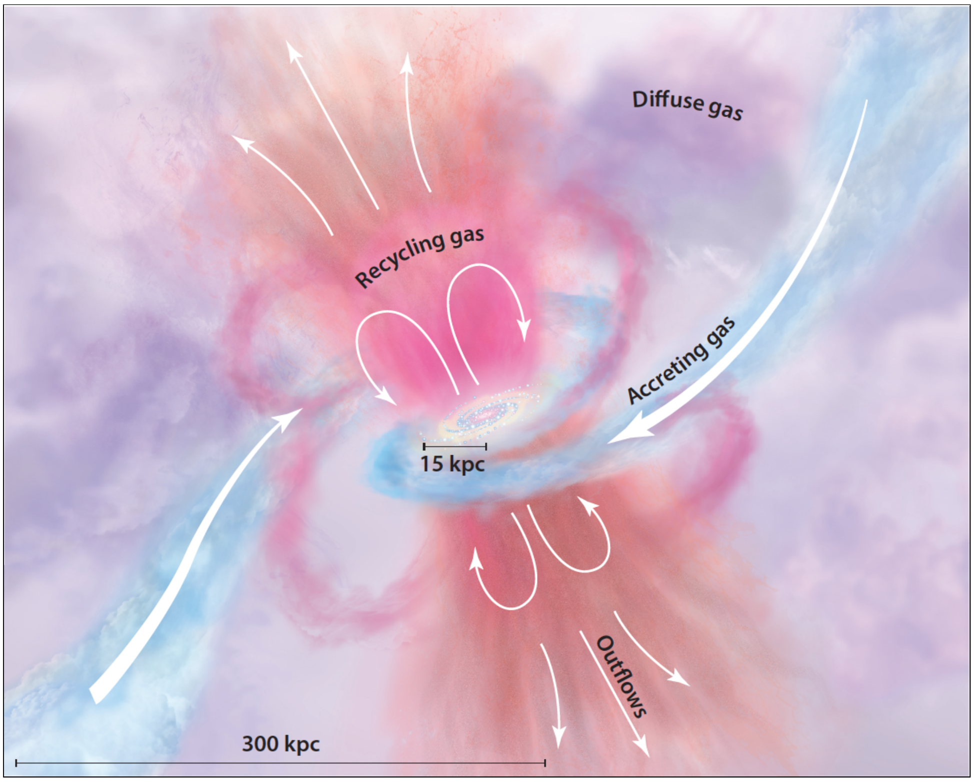

Figure 2.1: A cartoon view of the feeding and feedback processes in the CGM. The red central bulge and the gaseous disk of the galaxies are fed by blue filamentary accretion from the IGM. Outflows are shown to emerge from the disk in pink and orange. A portion of the ejected gas is recycling. The diffuse gas halo in varying tones of purple includes gas that is likely contributed by all these sources and mixed together over time (Tumlinson et al., 2017).

- In the "**cold mode**" **accretion**, cold streams, coming from the IGM, could quickly penetrate the virial radius of the galactic halo and maintain a cooling time shorter than the shock-heating timescale (Hobbs et al., 2015), leading to an efficient SF in the galactic center. Moreover, such accretion mode leads to the formation of large spiraling gas structures exhibiting complex morphologies and kinematics. These rotating structures conserve the angular momentum produced in the early epochs by tidal torques.

Cold mode accretion seems to be important in star-forming galaxies within galactic halos with $M_{halo} < M_{cr} = 5 \times 10^{11} M_{\odot}$. Instead, the hot phase accretion becomes dominant in passive galaxies at $z < z_{cr}$ ($z_{cr} \approx 2 - 3$) within DM halos above critical mass $M_{halo} \sim M_{cr}$ (see Dekel & Birnboim, 2006, and references therein). However, the cold mode may in some cases coexist with the hot mode even above the critical mass, especially at $z > z_{cr}$ (Kereš et al., 2005). This suggests that the inefficiency of the cold gas accretion from the CGM can contribute to the quench of the SF in massive galaxies at low-z.

A large amount of gas is expected to cross the CGM, probably leaving signs of its transition. Unfortunately, direct observational evidences of inflowing gas are very hard to acquire and still sparse so far. This is probably due to the very low covering fractions of these accretion streams, which make difficult to separate them from static gas and galactic outflows (Faucher-Giguère, 2011).

The main method to probe the properties of accretion gas is based on the comparison between the observed properties of the CGM gas and the expectations of cosmological simulations. Specifically, observations of metal poor absorbers exhibiting rotational patterns, with low column density, could be a clue of the presence of cold gas accretion (Ribaudo et al., 2011), while higher metallicities may represent outflows, recycled gas, mergers and accretion, acting all together. However, only indirect indications of accretion gas have been found up to date. At moderate redshifts, several studies (e.g., Bouché et al., 2016; Bowen et al., 2016) detected absorbers co-rotating with the galactic disk, along the major axis of the galaxy, exhibiting angular momentum higher than the galactic disk one. These evidences are in agreement with the massive and extended structures, showing inflowing disk-like kinematics, predicted by models (e.g., Stewart, 2017). At higher redshift, kinematic studies based on emission lines of the CGM gas reveal large-scale rotation structures consistent with the typical structures of cold gas accretion modelled by simulations (e.g., Prescott et al., 2015; Arrigoni Battaia et al., 2018a).

2.1.2 Feedback and Recycling processes

The amount of cold gas accreting onto the galaxy from the surrounding environment ensures new fuel to create stars and to feed the central BH, triggering the AGN phase. Consequently, supernovae and AGN driven winds will be ejected (Hopkins et al., 2008). Observational evidences, e.g. metals in the CGM and IGM and low fraction of baryons in massive galaxies (Gonzalez et al., 2013; Ford et al., 2014; Turner et al., 2016), strongly suggest galactic winds as mechanism (i) to deposit energy, momentum and metals on the surroundings, (ii) to efficiently remove the gas from the ISM of massive galaxies, affecting the properties of the large scale gas and shutting down further accretion.

A big issue concerns the mass-metallicity relation in galaxies. Indeed, by exploring the galaxy metallicity distribution, a problem arises: the stars seem to produce less metals than what was expected. This is known as the "missing metals problem" (see Tumlinson et al., 2017, and references therein). These "missed metals" observed in the CGM (e.g. Hennawi & Prochaska, 2007), and galactic outflows (possibly generated by AGN activity) have therefore been invoked as some of the possible mechanisms to transport these metals outwards large scales. However, direct evidence of large-scale metal-rich outflows are still lacking. Moreover, some complications in studying the exchange of metals between galaxy and CGM arise from the possible fate of outflows. The latter could either to slow down until to join the warm-hot CGM (Davé et al., 2001), or produce cold gas clouds (in the case of efficient cooling), or to reverse the trajectory and re-accrete onto the galaxy (i.e. the recycling winds; see Oppenheimer et al., 2010). Therefore, recycling processes increase the complexity of the study of the metallicity distribution in these systems. As an example, IGM gas could be induced to mix with these metal-rich recycling outflows, loosing its distinctive metal-poor appearance.

Finally, zoom-in cosmological simulations found that the pristine gas accreting onto the galaxy from the IGM for the first time represents the dominant component of the CGM at high-z. Nevertheless, the fraction of gas due to recycling processes increases at low redshifts and becomes comparable to the fraction of the pristine gas accretion at $z \approx 0$ (van de Voort, 2017). In agreement with these results, Ford et al. (2014) found that the majority (~60%) of SF at z=0 is fuelled by recycled gas, that was in the CGM a billion years before.

2.2 Exploring the feeding and feedback cycle via metallicity

The properties of the CGM gas can be explained by the following processes:

- accretion from IGM to CGM of pristine gas
- ejection of high-metallicity gas from galaxy to CGM
- accretion of metal rich gas, belonging to old or recent outflows, from CGM and/or IGM towards the galaxy ISM

Therefore, the physical properties of the CGM (i.e. metallicity, kinematics, ionisation state) as a function of the time, depend on the complex interaction of inflows and outflows (Shen et al., 2012). In particular, the study of the fate of metals in CGM provides critical clues about the contribution of these processes.

Most of the works published studied the metallicity distribution through absorption lines in luminous background QSOs in order to determine how metals in CGM change over cosmic time (Wotta et al., 2019; Lehner et al., 2019). With the advent of the Cosmic Origins Spectrograph (COS), mounted on HST, there have been many progresses in our understanding of the CGM metallicity distribution at z<1 (Green et al., 2012). Indeed, HST/COS allowed to have a good spectral resolution and high sensitivity to survey the low-z CGM without any metallicity bias. Specifically, the COS-Halos survey has been built on a selection of HI column density (N_{HI}) and metal lines (e.g. CIV, MgII, OVI), thus avoiding bias in the metallicity distribution of these absorbers and being sensitive at high or low metallicities (Tumlinson, 2012). Moreover, the distinction in column

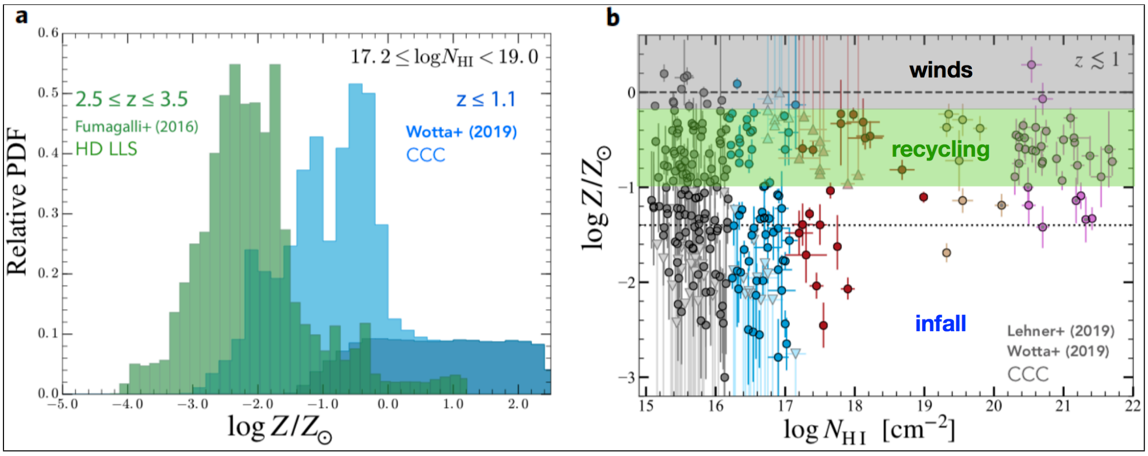

Figure 2.2: *Panel a*: Evolution of the probability distribution functions of the metallicity distributions of the absorbers at z≤ 1 with $17.2 < Log[N_H/cm^{-2}] < 18.5$ as reported by (Lehner et al., 2019). *Panel b*: Metallicity versus column density at z≤ 1 obtained from a large compilation of surveys (Lehner et al., 2019).

density is useful to recognise the different structures of the Universe, i.e. CGM ($Log[N_{HI}/cm^{-2}] > 14.5$) and IGM ($Log[N_{HI}/cm^{-2}] < 14.5$) (Lehner et al., 2019).

Concerning the "missing metals problem" (see Sect. 2.1.2), Gallazzi et al. (2008) found that a fraction of 25%(40%) of metals is locked in disc-dominated (early-type) galaxies at z=0. However, if the metal budget in the CGM out to 150 kpc is also taken into account, the fraction of metals at z=0 increases up to 50%. The contribution of AGN feedback, stellar winds, tidal stripping, ram pressure and mergers processes could therefore reduce the discrepancy between a low metal content in galaxies and their star formation history (Tumlinson et al., 2011).

Fig. 2.2a reports an exhaustive overview for the evolution of the metallicity in the CGM gas, with column density $17.2 < Log[N_{HI}/cm^{-2}] < 19.0$, as a function of two different epochs (Lehner et al., 2019). At high redshifts (2.5<z<3.5) the distribution is almost unimodal, exhibiting a peak centered at $Log[Z/Z_{\odot}] \simeq -2.5$, suggesting a high contribution of the accretion of metal-poor ($Log[Z/Z_{\odot}] < -2$) IGM gas to populate the CGM at this epoch. At z< 1.1 the CGM gas shows a higher average metallicity and two metallicity peaks emerge. Such a double peak fully agrees with the distinction between low metallicity, due to the accretion of the pristine IGM, and high metallicity gas ($Log[Z/Z_{\odot}] > -1$), which is a signature of gas previously ejected from the galaxy. However, the absence of intermediate values suggests a poor mix of these two phases (Hafen et al., 2016).

The $Log[Z/Z_{\odot}]$ vs $Log[N_{HI}/cm^{-2}]$, distribution in Fig. 2.2b shows that low density regions ($Log[N_{HI}/cm^{-2}] < 18$) at z<1, have both low and high metallicities, which are poorly mixed. The presence of metal-enriched gas in density regions with $17.2 < Log[N_{HI}/cm^{-2}] < 18$ confirms a metals contamination in the CGM (Johnson et al., 2015). On the other hand, focusing on the very low density regions ($16.2 < Log[N_{HI}/cm^{-2}] < 17.2$), the excess of metal-poor gas implies a low enrichment of metals in the IGM at z<1. Moreover, the lack of metal-poor gas in high density regions suggests that the CGM gas at low redshift is typically always metal-rich, i.e. polluted by outflows or by metal-rich IGM gas. However, some papers (Berg et al., 2019; Chen et al., 2019) report the presence of poor-metal gas in high density regions of the CGM, suggesting the strong contribution of the accretion of pristine gas from the IGM and an efficient mix with the CGM gas. As observed in zoom-in simulations, the accreting gas should be metal-poor with relative low column density ($Log[N_{HI}/cm^{-2}] < 17.2$; points in the "infall" region in Fig. 2.2b). Very high metallicity values are likely associated to regions affected by metal-rich galactic winds (grey area in Fig. 2.2b), while lower metallicity regions (green area in Fig. 2.2b) could be populated by a mix of pristine and ejected gases, where wind recycling occurs (Lehner et al., 2019; Wotta et al., 2019).

The vast majority of published works present results about the CGM around galaxies, without distinguishing AGN and no-AGN. However, it is widely accepted that every galaxy undergoes AGN activity during its lifetime (Marconi et al., 2004). The CGM around AGN is more likely to be detected during its metal-enriching phase due to ejection of cool and/or warm gas cloud streams from AGN. In order to explore this scenario, Prochaska et al. (2014) (and subsequent works) started the Quasar Probing Quasar (QPQ) project, selecting pairs of QSOs and investigating the CGM around z∼ 2, foreground QSO, through the spectral analysis of the background one. They revealed a high fraction of cool gas in the CGM of QSOs, and the presence of metals, i.e. CII, CIV and MgII, on a range of distances from 39 kpc to 1 Mpc. Specifically, massive halo structures around QSOs appear to be traced by CIV structures which look patchy and exhibit covering fraction quickly decreasing beyond 100 kpc (Landoni et al., 2016). The detection of metals up to large distances from the galaxy imply the importance of a cooperation of outflows and recycling winds (Tripp et al., 2011).

2.3 Studying the CGM emission

The most efficient way to probe the CGM structure is by investigating the transitions of the hydrogen, which is more than 70% of the ordinary matter in the Universe. In particular, the strongest HI line is the Lyα λ1215.67 Å ($h\nu_{Ly\alpha} \simeq 10.2\ eV$). The optical depth at line center is proportional to the probability that the HI will absorb a Lyα photon (cross section) times the column density and gives an estimation of the number of scattering experienced by Lyα photons. It can be written as:

$$\tau(Ly\alpha) = 8 \times 10^{4} \left(\frac{15\ km\ s^{-1}}{b} \right) \left(\frac{N_H}{10^{17.2} cm^{-2}} \right) \left(\frac{\lambda}{912 \text{Å}} \right)^{3} \tag{2.1}$$

where b is the Doppler broadening parameter. Eq. (2.1) shows that the Lyα optical depth is large even for low N_H, implying that HI clouds are transparent to the Lyα photons only for very low column density $Log[N_H/cm^{-2}] < 14$ (Draine, 2011).

2.3.1 Mechanisms for Lyα emission of the CGM

(A) **Fluorescence**

Spatially extended sources are usually characterised by the Surface Brightness (SB), defined as the flux per unit of solid angle (see Fig. 2.3a). In this case, the SB of an extended Lyα source at redshift z, is:

$$\frac{Flux}{\Omega} = \frac{d_A^2(z) Flux}{dA} = \frac{d_A^2(z)}{dA} \frac{Luminosity}{4\pi d_L^2(z)} = \frac{\epsilon_{Ly\alpha} L}{4\pi (1+z)^4} \tag{2.2}$$

where the solid angle is defined as $d\Omega \equiv dA/d_A^2(z)$, in which $d_A(z)$ is the angular diameter distance and it is related to the luminosiy distance, i.e. $d_L(z)$, by the formula $d_L(z) = d_A(z)(1+z)^2$. Finally, the luminosity that we detect from dA depends on the length of the cylinder (L) and the Lyα emission per unit volume ($\epsilon_{Ly\alpha}$), i.e. $Luminosity = \epsilon_{Ly\alpha} \times dA \times L$.

The main Lyα emitting process associated to diffuse and cold gas is the "fluorescence Lyα emission". This emission is expected to have a minimum SB of $\approx 10^{-20}\ erg\ s^{-1}\ cm^{-2}\ arcsec^{-2}$ (Rauch et al., 2008), reaching values of the order of $\approx 10^{-18}\ erg\ s^{-1}\ cm^{-2}\ arcsec^{-2}$ around luminous QSOs (Cantalupo et al., 2012). In this scenario, a central source photo-ionises the CGM gas. Specifically, the QSO UV photons, interacting with the surrounding neutral hydrogen, trigger the emission of Lyα photons through two main processes: recombination and collisional excitation (Cantalupo et al., 2005). The first one happens when an electron is captured by a HII atom, ionised by a UV photon, ending up in a quantum state (n, l) with $n > 2$. From this state, a Lyα photon can be produced through a downward cascade from the transition 2p → 1s (see Fig. 2.3b) with a fraction of recombination which is slightly temperature dependent. In the second process, the neutral hydrogen atom can be excited through collisions with free electrons. In this process the thermal energy of the electron is converted into radiation. In this case the highly efficient emission depends on the relative velocities of the two particle populations, i.e. on the temperature. Furthermore, in the scenario of photo-ionised gas from a central source

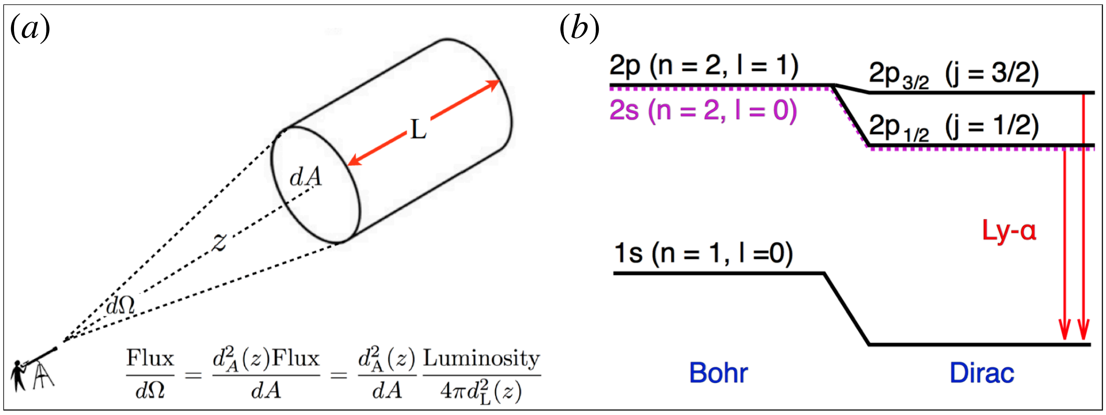

Figure 2.3: *Panel a*: cartoon of the geometry adopted to compute the $SB_{Ly\alpha}$ of an extended source emitting by recombination at redshift z (Dijkstra, 2017). *Panel b*: Lyman α transition that occurs in a ionised hydrogen atom (HII) through the recombination of an electron from the orbital level n=2 to the n=1 orbital. This recombination allows a Lyα photon emission at the wavelength $\lambda \sim 1216$ Å.

emitting a ionising luminosity ($L_{\nu_{LL}}$), it is possible distinguish two regimes (Hennawi & Prochaska, 2013):

- **Optically thick**: the gas is optically thick ($N_H >> 10^{17.2} cm^{-2}$) and the ionising continuum is not intense enough to highly ionise all the gas. In this case the cool gas acts like a mirror and converts ~66% of the ionising luminosity into Lyα photons (Cantalupo et al., 2005). Therefore, the $SB_{Ly\alpha}$ will be related to the ionising luminosity as follows:

$$SB_{Ly\alpha} \propto f_C L_{\nu_{LL}} \tag{2.3}$$

  where f_C is the covering factor of the cool gas in the halo.

- **Optically thin**: the gas is optically thin ($N_H << 10^{17.2} cm^{-2}$) and $L_{\nu_{LL}}$ is strong enough to maintain the gas highly ionised. Therefore, the $SB_{Ly\alpha}$ depends only on the physical properties of the gas (i.e. volume density n_H, column density N_H), and the relation can be written as:

$$SB_{Ly\alpha} \propto n_H N_N \tag{2.4}$$

(B) **Resonant scattering**
Lyα photons emitted by the central AGN undergo frequent resonant scattering by hydrogen atoms in the ground state and the final spectrum can be affected by complex radiative transfer effects. Lyα photons have a random walk in position and frequency due to the many scatters, which depends on the medium properties (e.g. column density, clumpiness, extension of the

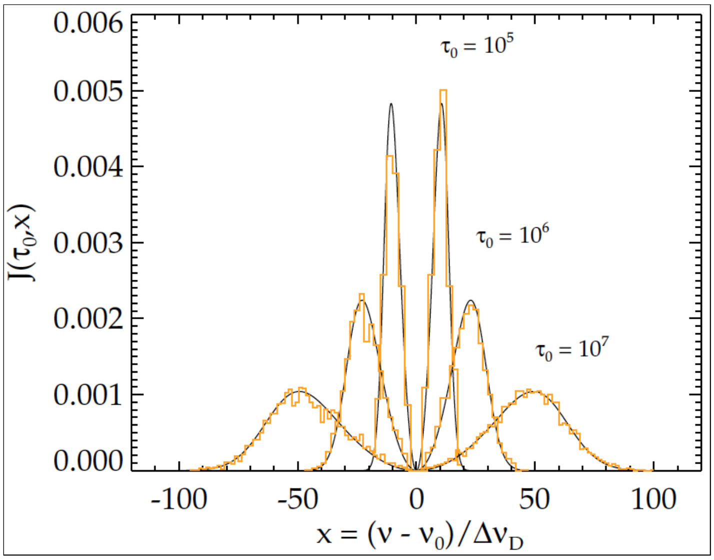

Figure 2.4: Three Lyα line profiles due to the resonant scattering of Lyα photons from a uniform spherical, static HI gas shell with total line-center optical depths $\tau_0 = 10^5$, 10^6 and 10^7, surrounding a source. The axis $x = (\nu - \nu_0)/\Delta\nu_D$ reports the shift in frequency around the Lyα line center ν_0, where $\Delta\nu_D = \nu_0 v_{th}/c$ is the thermal width and v_{th} is the thermal velocity (Dijkstra, 2017).

hydrogen cloud). Once the frequency is far from the resonant frequency the photon can escape the system, leading to a double-peak of the Lyα emission line profile (Fig .2.4; see Dijkstra 2017 for a review). Moreover, Fig. 2.4 shows that larger optical depths of the Lyα photons in the line-center lead to a larger distance between the two peaks, because most of the Lyα photons will undergoes more scatters, thus increasing its frequencies further from the center of the line before being able to escape. Moreover, the two peaks exhibit a similar intensity if the frequency of the Lyα photon has an equal chance of increasing and decreasing during the random walk process. This depends very much on the configuration and kinematics of the system. In particular, the only gas kinematics with respect to the emitting source can lead to Lyα profile changes.

For example, in the case of an expanding and homogeneous sphere surrounding the continuum source, the Lyα photons coming from the source will appear at higher energy than 1216 Å. They will be closer to the center of the Lyα line than the lower energy photons. Thereby, shorter wavelength photons (i.e. emission peak on the left in Fig. 2.5) will be scattered more easily with respect to the lower energy photons (i.e. emission peak on the right). As a consequence, a fraction of the photons that, in the case of a static gas would populated the peak on the left, will migrate on the peak

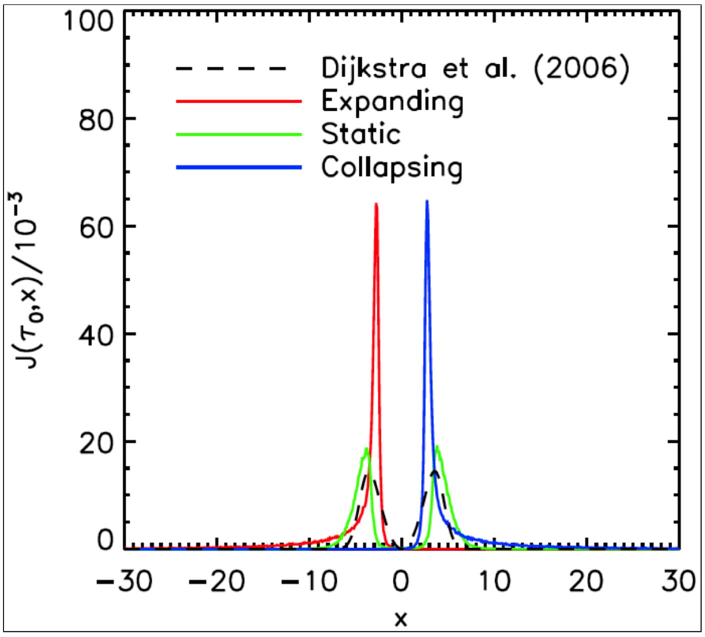

Figure 2.5: Three Lyα emission line profiles due to the only contribution of resonant scattering produced by isothermal ($T = 10^4 K$) and homogeneous sphere of gas with N_{HI} from the center to the edge of $2 \times 10^{18} cm^{-2}$, which undergoes isotropic contraction (blue) or expansion (red), so that the maximum velocity at the edge of the sphere is $v = \pm 200\ km\ s^{-1}$. The profile obtained by Dijkstra et al. (2006) through simulations (green) and analytic solutions (black) for a static sphere with $N_H \sim 2 \times 10^{18}\ cm^{-2}$ are also shown. Figure from Dijkstra (2017)

at lower energy (which will become the dominant one). In conclusion, the Lyα profile emerging from this ideal case will be the red one in Fig. 2.5. In the case of a collapsing gas shell the blue spectrum in Fig. 2.5 is obtained. However, the dusty gas distribution can also play a crucial role in the definition of the Lyα line profile by absorbing and reprocessing Lyα photons.

(C) **Shock winds powered by outflows**
An additional origin of the Lyα emission can be related to the collisional excitation powered by shock due to galactic outflows powered by AGN and supernovae. Main signatures of this process are large width of the Lyα line ($\sim$ 1000 $km\ s^{-1}$) and the presence of associated extended metal-line (e.g. CIV, HeII) emission (e.g., Allen et al. 2008; Arrigoni Battaia et al. 2015b).

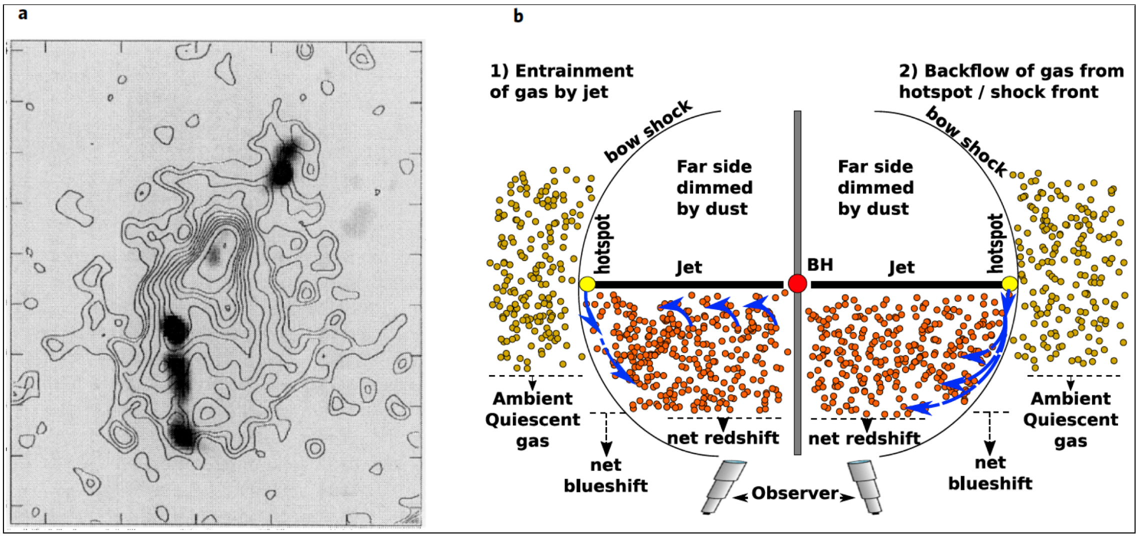

Figure 2.6: *Panel a*: NB-image of the Lyα nebula around the HzRG 1243+036, detected by van Ojik et al. (1996). The black contours indicate the Lyα emission with the 8.3 GHz VLA map in grey-scale superimposed. *Panel b*: scheme representing two scenarios which aims to describe the kinematics observed for the Lyα nebula around MRC 0943-242 (Silva et al., 2018). The AGN driven radio jet expands itself up to the hot spot (yellow circle), where it is stopped by the ISM pressure. The radio plasma cools and spreads along the blue arrows, leading to the observation of blue-shifted emission lines of warm ionised gas with large velocity dispersion, close to the hot spot. Beyond the bow shock, narrow emission lines are observed. The radio jet entrains the ISM gas along its velocity vector, so that the gas appears to be redshifted. The second scenario is similar to the first, but the radio plasma that moves away from the hot spot is immediately dragged by the radio jet, which allows us to observe the same redshifted gas component in the central region.

2.4 Giant Lyα nebulae around AGN: early results

2.4.1 Lyα nebula around High-z Radio Galaxies

The first Lyα nebulae were mostly detected around high-z radio galaxies (HzRGs) at z> 2, through narrow band (NB) -imaging and slit-spectroscopy observations (Heckman et al., 1991). HzRGs are z≥2 AGNs exhibiting extended radio jets and these are the probable progenitors of elliptical galaxies (Best et al., 1998) surrounded by a large amount of pristine gas. HzRGs are surrounded by an extended (~150 kpc), massive ($M_{gas} \sim 10^8 - 10^{10}\ M_{\odot}$) and luminous ($L_{Ly\alpha} \sim 10^{43} - 10^{45}\ erg\ s^{-1}$) Ly$\alpha$ nebulae (Fig. 2.6a), whose morphology are aligned with the radio jet directions (van Ojik et al., 1996).

The gas emission lines which are spatially correlated with the radio source show high velocity dispersions (FWHM≥ 1000 $km\ s^{-1}$ Villar-Martín et al., 1999).

These probably indicate shocked gas which is accelerated by outflows reaching higher velocities than the velocity escape of the system (Villar-Martín et al., 2006). Therefore, shock ionisation by radio jets seems provide a large contribution to the extended Lyα emission around HzRGs. Fig. 2.6b reports two scenarios predicted for the Lyα nebula around MRC 0943-242, showing interaction between radio jets and ISM/CGM (Silva et al., 2018). Lyα nebulae around HzRGs consists of some regions with low SB and quiescent kinematics (FWHM<1000 $km\ s^{-1}$), which are beyond the radio cocoon, when the ISM does not interact with radio jets. On the other hand, blue-shifted emission lines exhibiting high FWHM are observed spatially correlated with the hotspots, where the radio jet is stopped by the ISM pressure. Finally, the central warm and ionised gas, emitting narrow and red-shifted emission lines, is interpreted as gas dragged by the radio jets. As shown in Fig. 2.6b, theoretical models predict that a fraction of the gas is available for accretion onto SMBH (e.g. redshifted emission lines), thus supporting the radio activity for $\sim 10^8\ yr$ (see Silva et al., 2018, and references therein).

2.4.2 Cosmic web: Enormous Lyα nebulae around multiple radio-quiet QSOs

As mentioned in Sect. 2, the cosmological ΛCDM model predicts that the matter is distributed in a cosmic web structure, consisting of sheets, filaments and potential wells in which a large amount of gas and galaxies are located. The Lyα nebulae are large baryon reservoirs in the densest parts of the cosmic web (i.e. intersections of cosmic filamentary structures), associated to regions in which massive galaxies form or multiple galaxies live (Prescott et al., 2015). For example, HzRGs are believed to be the site of proto-clusters, given the presence of multiple galaxies close to them (Venemans et al., 2007). Enormous (>200 kpc) structures of Lyα emission (ELANe) have been rarely detected (~1% of the Lyα nebulae detected so far; Arrigoni Battaia et al. 2019). The first two reported cases were the Slug nebula (Cantalupo et al., 2014) and the Jackpot nebula (Hennawi et al., 2015). The Slug (Fig. 2.7a) is an extended (~460 kpc) and luminous ($\sim 10^{45}\ erg\ s^{-1}$) nebula around the z≃2.3 radio-quiet QSO UM827 and its AGN companion. It was discovered with the Low Resolution Imaging Spectrometer (LRIS) at the Keck-I telescope. The enormous Lyα Slug nebula represents a large amount of cool gas, which is extended well beyond the virial radius of UM827, and it is associated to a cosmic web filament between two AGNs, with SB $> 10^{-17}\ erg\ s^{-1}\ cm^{-2}\ arcsec^{-2}$ for hundred of kpc. The Jackpot ELAN (Fig. 2.7b) is associated to four close AGNs at z~2, exhibiting maximum projected distance of ~330 kpc and luminosity $L_{Ly\alpha} \sim 2.1 \times 10^{44}\ erg\ s^{-1}$. Jackpot nebula shows extreme kinematics and metal-enriched gas (i.e. SiII, CII, SiIII, CIV, SiIV).

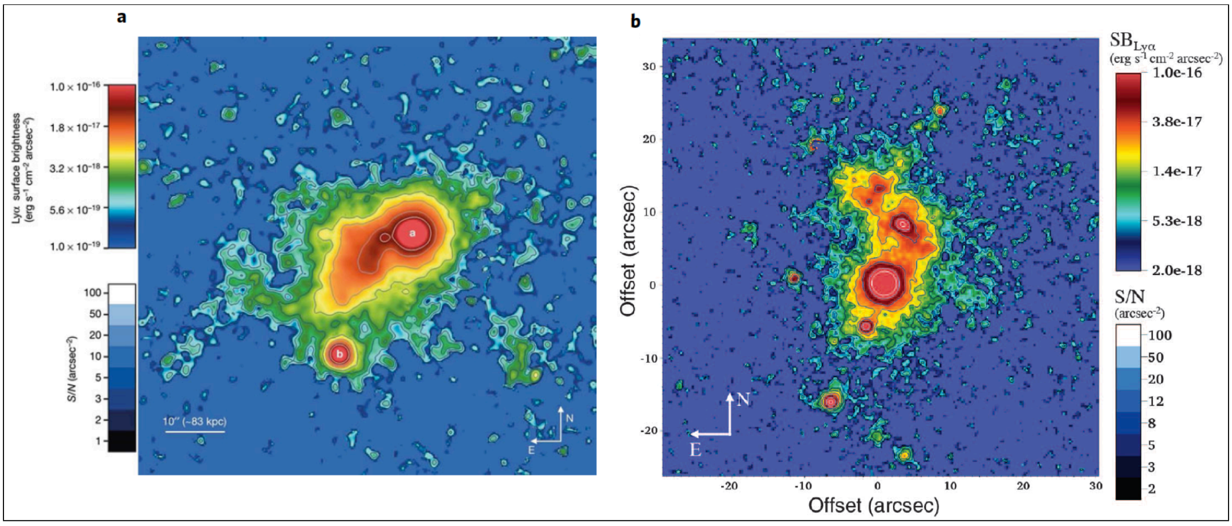

Figure 2.7: Narrow-band images of the enormous Lyα nebulae: the Slug Nebula (*a*; Cantalupo et al. 2014) and the Jackpot nebula (*b*; Hennawi et al. 2015) observed with Keck/LRIS instruments (V-band) with and exposure time of 10h and 3h, respectively. These are spatially correlated with multiple AGN at z≈2, and exhibit maximum projected distances and luminosities of 460, 330 kpc and 2×10^{44}, 10^{45} $erg\ s^{-1}$, respectively. These represent large reservoirs of cool gas tracing the filaments and potential wells belonging to the cosmic web structure.

The rarity of these systems seems to suggest they are associated to proto-clusters and trace giant structures of cool gas in the location of clustering galaxies (e.g. Lyα emitters, AGNs), which could be the progenitors of the large structures (e.g. galaxy clusters, groups, massive galaxies) in the local Universe.

Finally, Wisotzki et al. (2018) obtained a very interesting result thanks to the powerful of the Multi Unit Spectroscopic Explorer (MUSE; Bacon et al. 2010) instrument, mounted on the Very Large Telescope (VLT). Indeed, they found a low SB Lyα emission ($SB^{1\sigma}_{Ly\alpha;\ lim} \sim 5 \times 10^{-21}\ erg\ s^{-1}\ cm^{-2}\ arcsec^{-2}$) with a projected sky coverage of ~100%, surrounding the faint galaxies at 3<z<6 (Fig. 2.8). This finding underlines even more the importance of extended Lyα emissions to probe the distribution of the biggest and elusive component of the baryonic cosmic matter distribution.

2.5 The advent of spatially resolved spectroscopy

The first detections of Lyα nebulae were obtained by imaging observations with narrow-band filters or slit-spectroscopy. The detection rate of Lyα nebulae around radio-quiet QSOs was only of 10%. This is due to limits of these observational

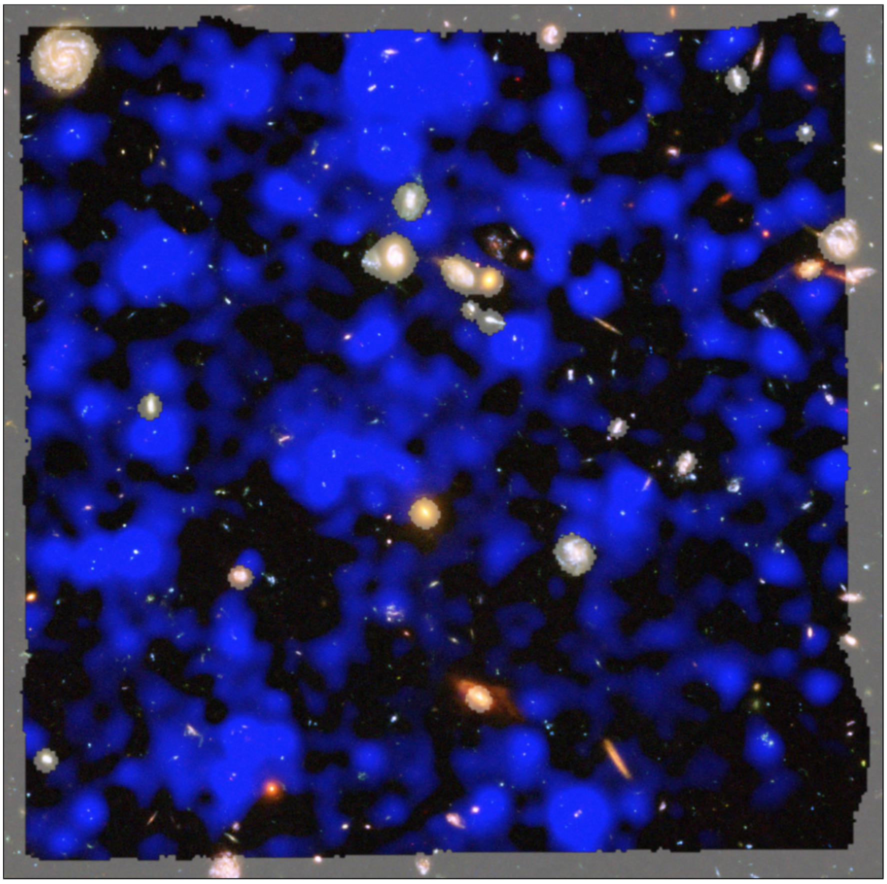

Figure 2.8: Map of the noise-free, seeing-corrected models of the distribution of the Lyα emission (blue shade) covering a large fraction of the sky from z~3 to 6 (Wisotzki et al., 2018). It is obtained by very long MUSE exposures (mean integration time of 10h) in the Hubble Deep Field South and Hubble Ultra Deep Field.

techniques. The main problem in using NB-imaging for detecting Lyα nebulae is represented by "filter losses" (Borisova et al., 2016), which depend on the inability to predict where the line is, given the inaccuracy to estimate the systemic redshift of the QSO. Moreover, a narrow filter could create problem in detecting a kinematically broad nebula, causing the loss of some emission. On the other hand, slit spectroscopic allows us to analyse the complete kinematics of the Lyα emission profile, but in a small region ("slit losses"). This can be a big problem due to the asymmetry that the Lyα nebulae usually exhibit (Cai et al., 2019). Another problem is the one concerning the subtraction of the Point Spread Function (PSF) associated to the central source (i.e. the QSO) in order to remove the contribution of the QSO emission and detect the much fainter nebular emission ("PSF losses"). Indeed, by NB imaging data is very difficult to estimate the QSO

PSF (and it is basically impossible by long slit-spectroscopy).

Integral Field Spectrographs (IFS) recently mounted on 8-10 meter telescopes, e.g. VLT and Keck, allowed to explore the diffuse gas on CGM scales around bright AGN at z=2-4. Specifically, their combination of 3D spectroscopy and high resolution is fundamental in the estimation and removal of the QSO PSF.

For example, the VLT/MUSE instrument (Bacon et al., 2010) provides spatially resolved spectroscopy data, in which each pixel has an associated spectrum. It provides a large Field of View (FoV $1' \times 1'$), high spatial (pixel scale 0.2”/pixel) and spectral ($R \sim 3000$) resolution and high sensitivity ($SB_{2\sigma} \approx 10^{-18}\ erg\ s^{-1}\ cm^{-2}\ arcsec^{-2}$ with an exposure time of $\sim 1\ hr$) in a spectral range of 4500-9000 Å. This instrument has been the first to significantly improve our capability in detecting and studying giant Lyα nebulae around radio-quiet QSOs (Borisova et al., 2016).

The Keck Cosmic Web Imager (KCWI) instrument ($\lambda = 3950 - 4800$ Å), mounted on the Keck II telescope, has also provided a great contribution to the discovery of Lyα extended emission surrounding AGN at z≃2 (e.g. Cai et al., 2019). Specifically, KCWI allows us to have a field of view of $16''.8 \times 20''$ with spatial resolution of $\approx 0.7''$ and spectral resolution of $R > 4000$, by reaching a SB limit of $\sim 10^{-18}\ erg\ s\ cm^{-2}\ arcsec^{-2}$ with exposure times of $2hr$.

2.6 Lyα nebulae observed by IFU around radio-quiet QSOs

2.6.1 *Samples of Lyα nebulae around AGN with IFU data*

Borisova et al. (2016) (hereafter B16) collected a sample of Lyα nebulae around 17 radio-quiet QSOs and 2 radio-loud QSOs at 3<z<4, observed by VLT/MUSE with 1h of exposure. These Lyα nebulae exhibit luminosities $L_{Ly\alpha} = 10^{43} - 4.4 \times 10^{44}\ erg\ s^{-1}$ and a large range of sizes (i.e. ~120 - 320 kpc) and morphologies (Fig. 2.9). Specifically, the circular nebulae have smaller sizes (~100 kpc) than the nebulae showing filamentary structures.

Another larger sample of Lyα nebulae discovered by MUSE is the QSO MUSEUM[1] sample (Arrigoni Battaia et al., 2019, hereafter AB19). It consists of 61 QSOs at 3.03<z<3.46 (Fig. 2.10) and is characterised by different radio-loudness, i.e. 39 radio-quiet QSOs, 15 radio-loud QSOs and 7 radio unclassified QSOs. AB19 found that Lyα nebulae around radio-quiet and radio-loud QSOs show no differences in morphology and size. Also the AB19 sample show that larger Lyα nebulae are more asymmetrical. The asymmetry in this case is quantified by the parameter α, which is the ratio between the semi-minor axis b and

---

[1] *Quasar Snapshot Observations with MUse: Search for Extended Ultraviolet eMission*

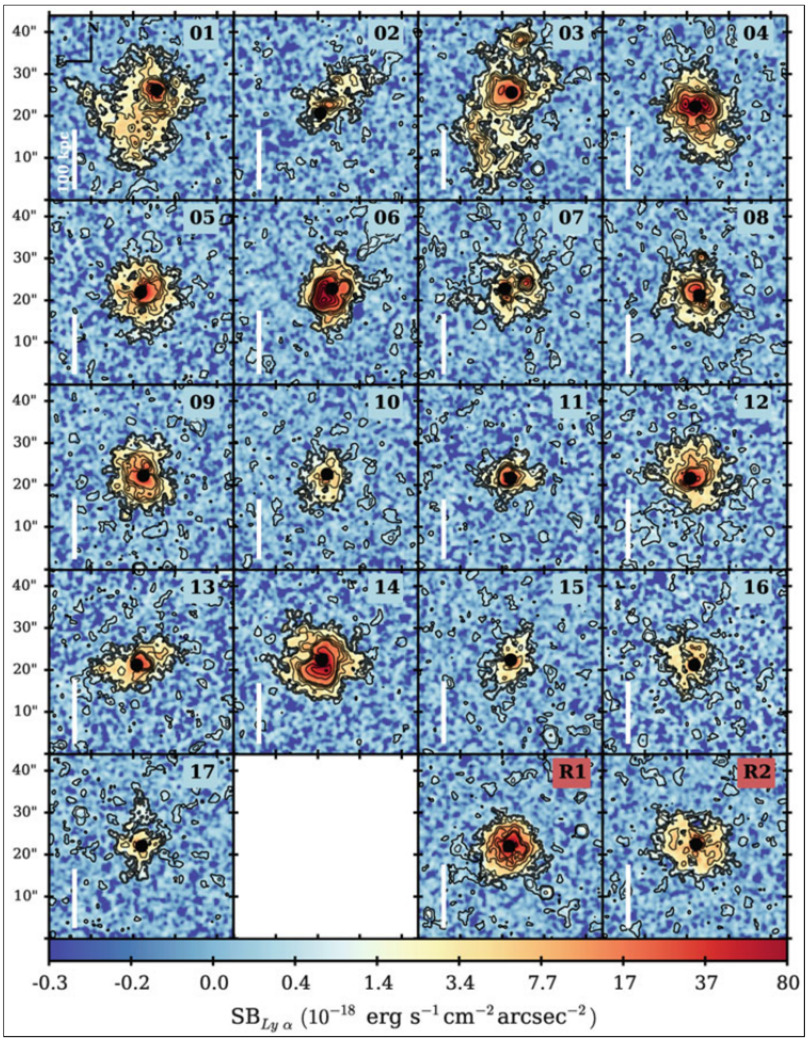

Figure 2.9: Surface brightness maps, i.e. optimally extracted pseudo-NB images from MUSE observations, of Lyα nebulae around 17 radio-quiet QSOs and 2 radio-loud QSOs (i.e., R1 and R2), shown after the PSF and continuum subtraction (Borisova et al., 2016). The black dots mark the QSO positions. The black thin contours indicates the region with SNR levels = 2, $4+\Delta\times6$ ($\Delta = 0, 1, 2, \ldots$), while the thick contours correspond to a SB $\sim 10^{-18}$ $erg\ s^{-1}\ cm^{-2}\ arcsec^{-2}$.

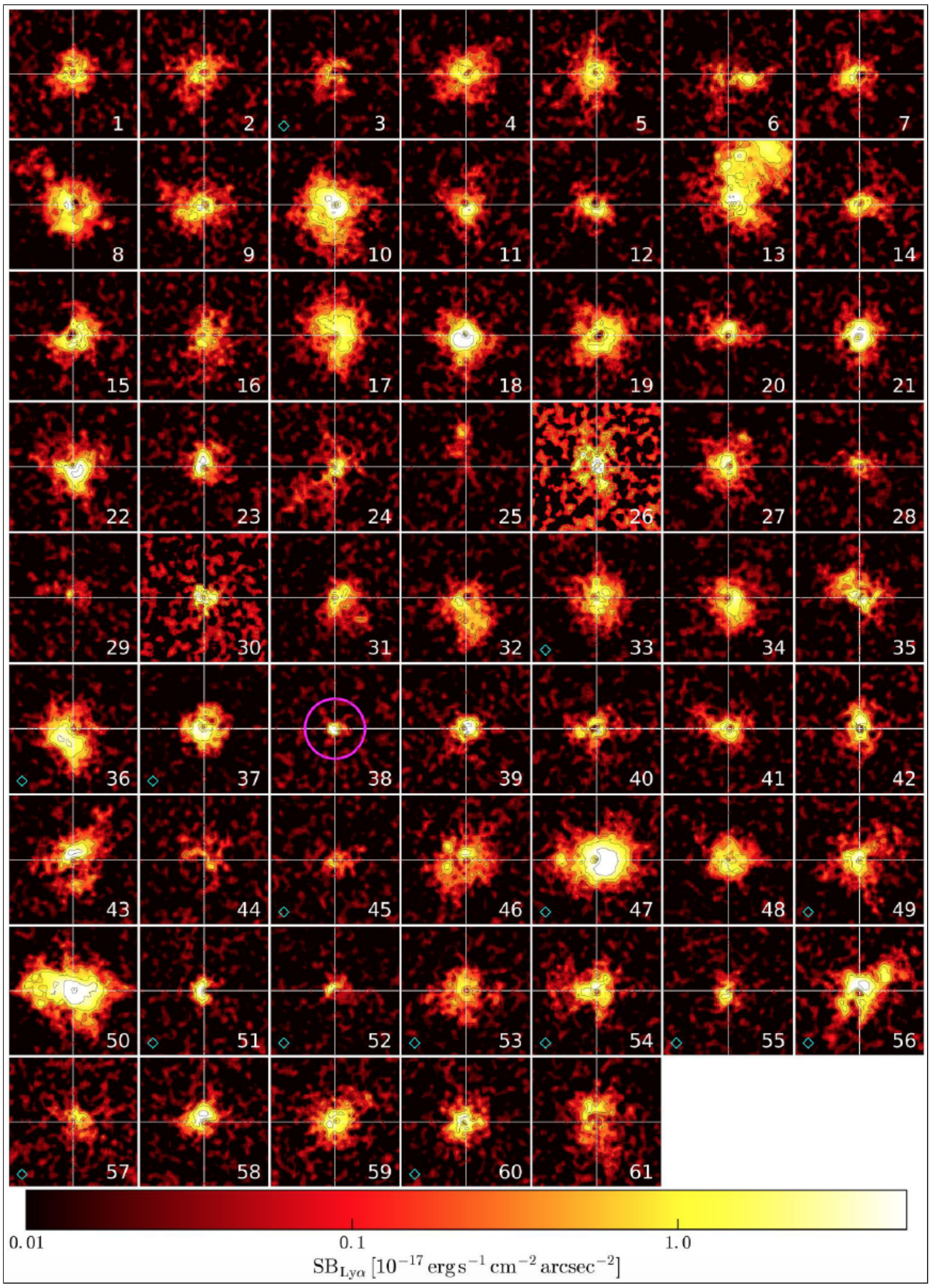

Figure 2.10: Collection of 61 SB maps of Lyα nebulae around AGN belonging to the QSO MUSEUM sample (Arrigoni Battaia et al., 2019). Each map shows 230 kpc×230 kpc centered on the QSO position after the PSF and continuum subtraction. Thin contours report the SNR levels of ~2, 4, 10, 20 and 50. Radio-loud QSOs are indicated with a cyan diamond in the bottom-left corner. The magenta circle with radius 50 kpc is shown on the image with ID 38.

semi-major axis a, i.e:

$$\alpha = \frac{a}{b} = \frac{1 - \sqrt{Q^2 + U^2}}{1 + \sqrt{Q^2 + U^2}} \tag{2.5}$$

where Q and U are the Stokes parameters computed via the flux weighted second order moments (M), as follows:

$$Q = M_{xx} - M_{yy} \ , \qquad U = 2M_{xy} \tag{2.6}$$

Furthermore, AB19 compared the properties of Lyα nebulae observed with IFU data around radio-quiet QSOs at z~3 with those observed through the NB technique around 15 radio-quiet QSOs at z~2.They found that the NB-discovered Lyα nebulae exhibit fainter luminosities than the IFU-detected one, and suggested that the cool gas mass at z~3 is larger than that at z~2. However, this comparison is based on heterogeneous techniques in the detection of the nebulae. Cai et al. (2019) (hereafter C19) reported Keck/KCWI IFU observations of Lyα nebulae (Fig. 2.11) in a sample of 16 ultra-luminous QSOs at 2.1<z<2.3. The addition of this sample, together with the B16 and AB19 Lyα nebulae samples, is crucial to investigate the evolution of their properties at 2<z<4. The first evidence is that z~ 2 nebulae show a stronger field to field variation, as reported in Fig. 2.11. Indeed, some Lyα nebulae show a maximum projected size >150 kpc, while others have sizes <100 kpc. Moreover, C19 found that the most of Lyα nebulae around QSOs at z≈2 appear more asymmetric than the nebulae at z≈3. Indeed, the median value of α for the z=3 AB19 sample is ~0.71, while that of the C19 sample is ~0.54. C19 suggest that the morphology evolution of Lyα nebulae can be correlated with the halo morphological merger fraction increasing from z=3 to z=2 (Conselice et al., 2008). Therefore, the higher rate of merger activity may lead to a larger nebula asymmetry.

Fig. 2.12 reports a comparison between circular-averaged SB profiles of nebulae around different types of object (e.g., radio-quiet QSOs at z~2 and z~3, Lyα emitters and Lyman break galaxies), which are detected with different techniques (i.e., IFU and narrow-band). These SB radial profiles are corrected for the redshift dimming and re-scaled at z=2.3. The comparison between the median SB radial profiles of B16 (purple points), AB19 (orange points) and C19 (red area) samples, with error bars that denote the 25% and 75% percentile of the Lyα SB, shows that the profiles at z≈3 are a factor of ~2-3 higher than that at z≈2 radio-quiet QSOs. C19 suggest that the main reason of this evolution probably is that Lyα emitting clouds around z~2 QSOs have a lower covering factor than those at z~3. Indeed, they found that the covering factor of the Lyα emitting clouds at z~3 is 2.7 times larger than at z~2. On the other hand, the SB of the Lyα nebula at z~2 could be intrinsically fainter than the one at z~3, suggesting a lower gas density at this epoch. However, C19 found that the density of the cool gas has only a little evolution from z=3 to z=2, which cannot explain the evolution of the SB emission. This conclusion is drawn under the assumption that the

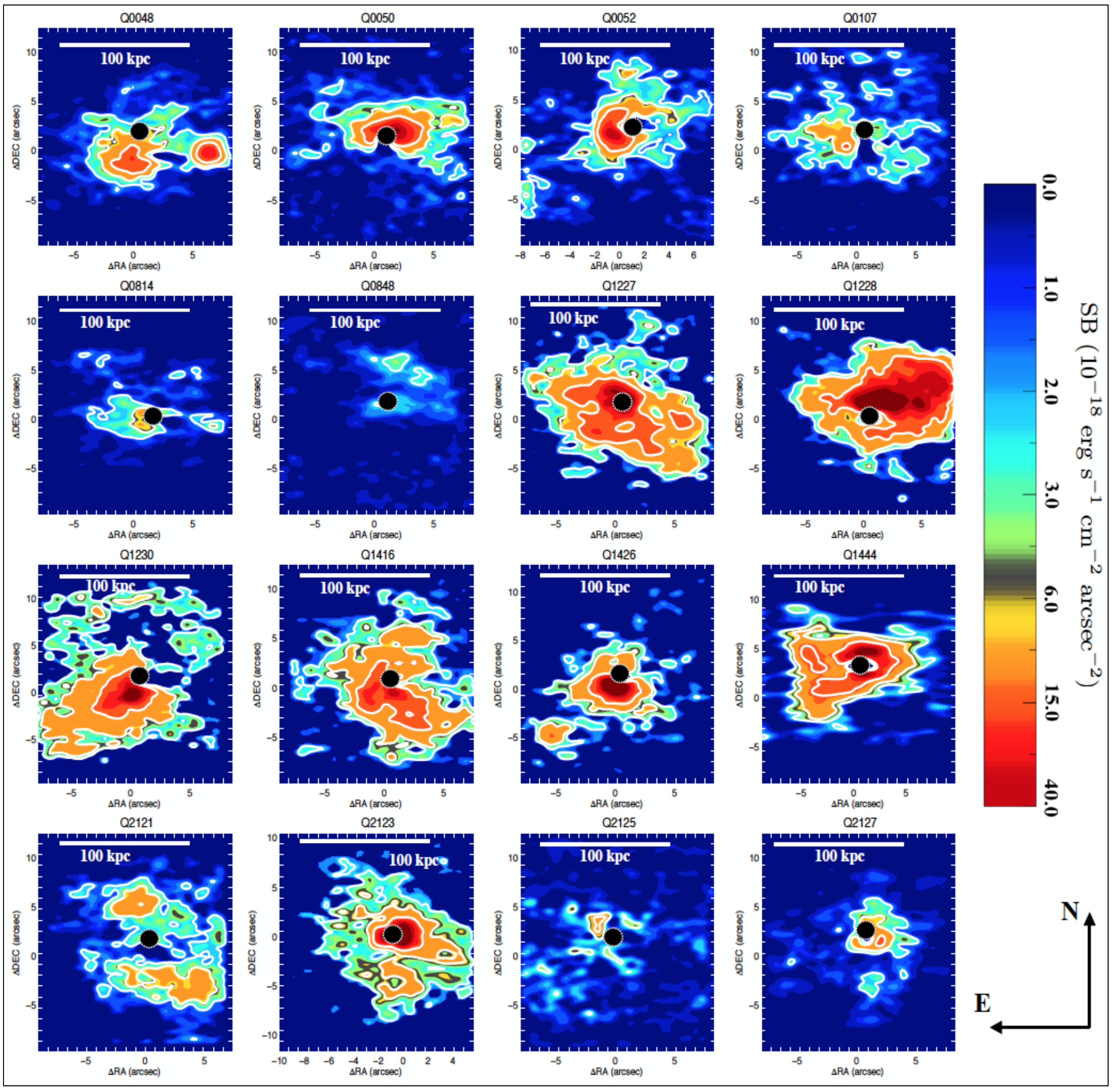

Figure 2.11: Optimally extracted images (16"×20") of Lyα nebulae surrounding radio-quiet QSOs after the PSF and continuum subtraction of KCWI data-cubes (Cai et al., 2019). White contours indicate 2, 5 and 10 σ of the SB, with $\sigma_{SB} = 5 \times 10^{-19}\ erg\ s^{-1}\ cm^{-2}\ arcsec^{-2}$.

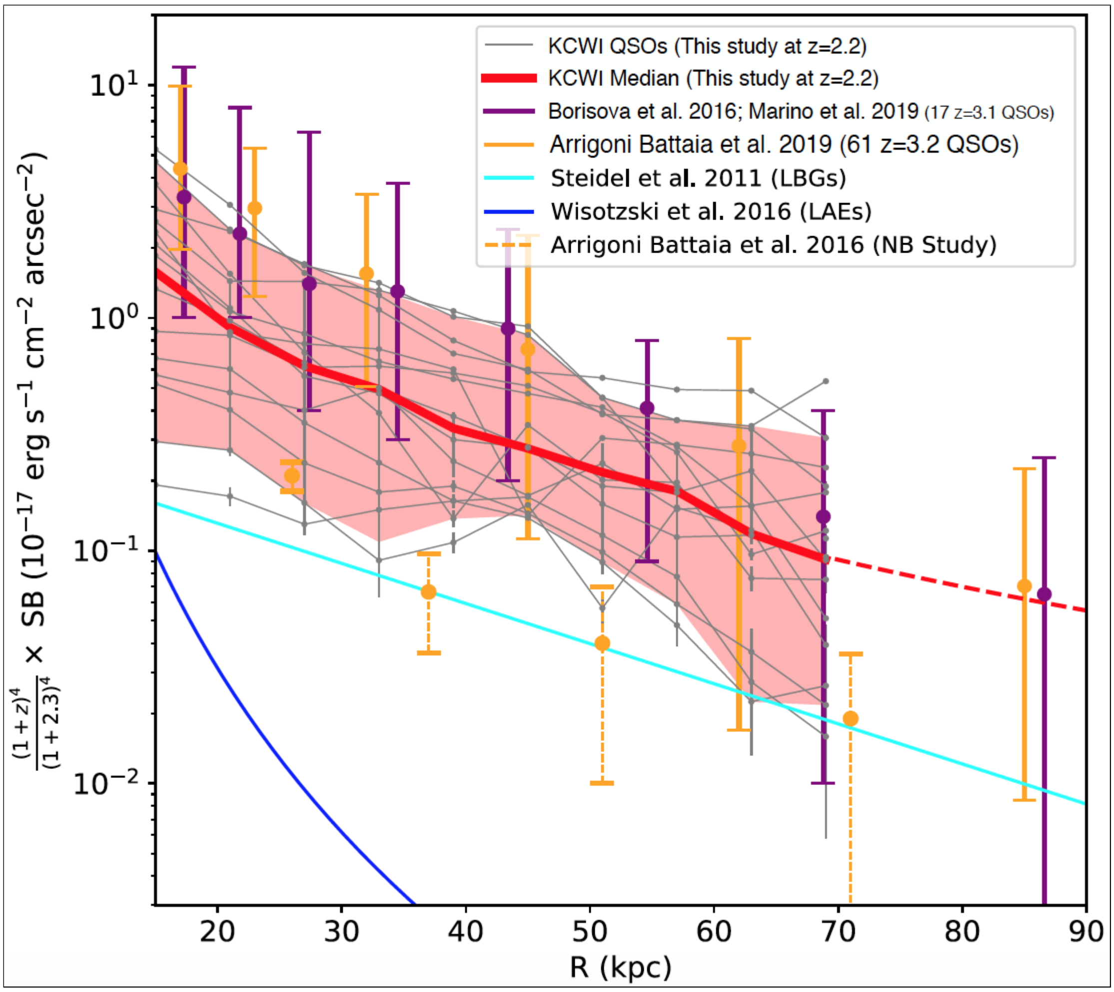

Figure 2.12: Circular average $SB_{Ly\alpha}$ radial profiles around different sources (i.e., QSOs, Lyman break galaxies, Lyman emitters galaxies). The grey lines are the SB radial profiles of each individual nebula belonging to the KCWI sample of C19, while the red line+area represent the median and the error bars, respectively. All error bars show the 25 and 75 percentile. All the radial profiles have been corrected for the redshift dimming and re-scaled at z=2.3. The purple and orange symbols report the median profiles and errors for Marino et al. (2019) and Arrigoni Battaia et al. (2019), respectively. The orange points with the dashed lines represent the median $SB_{Ly\alpha}$ radial profile computed by Arrigoni Battaia et al. (2016) using a NB filter. Finally, cyan and blue lines mark the median $SB_{Ly\alpha}$ radial profiles for the LBGs and LAEs sample by Steidel et al. (2011) and Wisotzki et al. (2016), respectively.

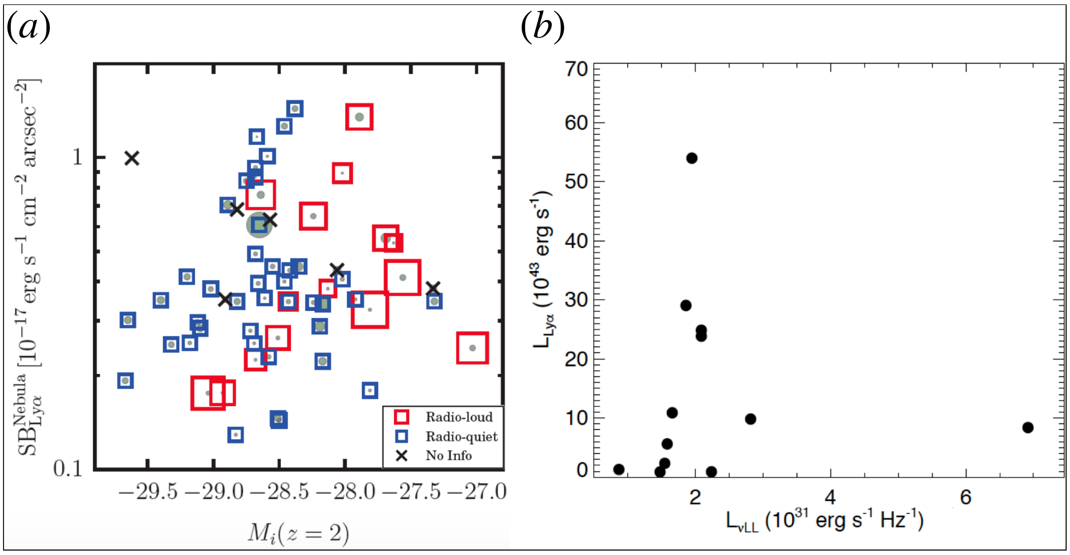

Figure 2.13: *Left panel*: Absolute i-magnitude, normalised at z=2, of the radio-loud (red squares), quiet (blue squares) and not-classified (black crosses) QSOs belonging to the AB19 VLT/MUSE sample, versus the average Lyα SB of the respective nebulae. *Right panel*: ionising luminosity of the radio-quiet QSOs belonging to the C19 Keck/KCWI sample versus the total Lyα nebular luminosity (Cai et al., 2019).

favoured origin of the Lyα emission of these nebulae is the optically thin photo-ionisation. Furthermore, the decrease of Lyα emission from z≈3 to z≈2 can also be the consequence of a decrement of the cool gas penetration in massive halos (i.e. the "cold mode" accretion; see Sect. 2.1.1). Indeed, simulations by Dekel et al. (2009) found that the threshold mass of the QSO halo beyond which it is dominated by hot gas is $10^{13}M_\odot$ at z = 3 and $10^{12}M_\odot$ at z = 2. Therefore, for the same halo mass, lower redshift QSO halos have a higher fraction of hot gas, as well as a less significant cool gas penetration. Furthermore, Fig. 2.12 shows that Lyα nebulae SB of Lyman break (Steidel et al., 2011) and Lyα emitter galaxies (Wisotzki et al., 2016) are fainter than that powered by AGN.

Concerning on the origin of these Lyα nebulae, in the optically thick photo-ionised scenario (see Sect. 2.3.1) the observed SB is expected to increase with the increasing ionising luminosity of the central source. However, the two panels in Fig. 2.13, reported by AB19 (left; M_i versus $SB_{Ly\alpha}$) and C19 (right; $L_{L\nu_{LL}}$ versus $L_{Ly\alpha}$) for their samples do not show a clear correlation between the Lyα luminosity and the QSO ionising luminosity. This result implies that a fully optically thick regime cannot be the cause of the Lyα emission of the diffuse cool gas around AGN and suggests that the extended Lyα emissions in AB19 and C19 are powered by recombination and resonant scattering in a optically thin medium.

2.6.2 Kinematics of Lyα nebulae

The kinematics of the Lyα nebulae in B16, AB19 and C19, is investigated by mapping the first (velocity) and second (dispersion) moment of the flux distribution with respect to the centroid of Lyα profile (Figs. 2.14 and 2.15). Velocity maps indeed allow us to reveal kinematic patterns of the diffuse CGM gas (e.g. rotation, inflows and outflows). However, complex radiative transfer effects can contribute to the Lyα emission and complicate the interpretation of the kinematics of these nebulae. Fig. 2.14 shows velocity maps of six Lyα nebulae belonging to the samples of B16 (a), AB19 (b) and C19 (c). Most of the velocity maps does not show evidence for clear dynamical patterns, as shown in the right side of the all panels in Fig. 2.14. On the other hand, largest nebulae (shown in the left side of each panel) usually exhibit rotation kinematics patterns, resembling disk-like structures over hundreds of kpc. These kinematics structures are an indication of the presence of spiraling motions, possibly suggesting gas inflow in agreement with the simulations (e.g., Stewart et al., 2013). Velocity maps range from -450 $km\ s^{-1}$ to 450 $km\ s^{-1}$, in agreement with the radial velocities expected in the gravitational field of a DM halo of an AGN (White et al., 2012) Fig. 2.15 shows, for each sample (i.e. B16, AB19 and C19), the velocity dispersion maps of the same targets presented in Fig. 2.14. A common result of these three studies is that Lyα nebulae around radio-quiet QSOs exhibit average velocity dispersions of $\sigma < 400\ km\ s^{-1}$. These values are consistent with gravitational motions expected in a typical DM halo ($M_{halo} \sim 10^{12.5} M_{\odot}$) hosting an AGN at z$\simeq$2-3 (White et al., 2012). Moreover, Prochaska & Hennawi (2009) found similar velocity dispersions in absorption lines in the CGM around z=2 QSOs.

Fig. 2.16 reports the velocity dispersion maps of a Lyα nebula around two radio-loud QSOs belonging to the B16 and AB19 samples. Remarkably, B16 found that Lyα nebulae around radio-loud QSO exhibit high velocity dispersions values ($\sigma > 400\ km\ s^{-1}$; left panel Fig. 2.16), which are consistent with the values observed around HzRGs, probably associated with the interaction between radio jet and gas (see Sect. 2.4.1). On the other hand, AB19 found radio-loud QSOs showing relatively quiescent Lyα nebulae (right panel Fig. 2.16), similar to those observed around radio-quiet QSOs (Fig. 2.15b). A possible cause of these different results could be that the radio-loud QSOs belonging to the AB19 sample are, on average, 2.4 magnitudes fainter than the ones in the B16 sample. In this case, AB19 suggest the three following scenarios:

- winds in radio-loud QSOs could be driven by the AGN radiation rather than by a jet;
- winds couple more efficiently with CGM gas around more luminous AGN;
- more powerful winds (or jets) are triggered in higher luminous radio-loud QSOs for a longer time.

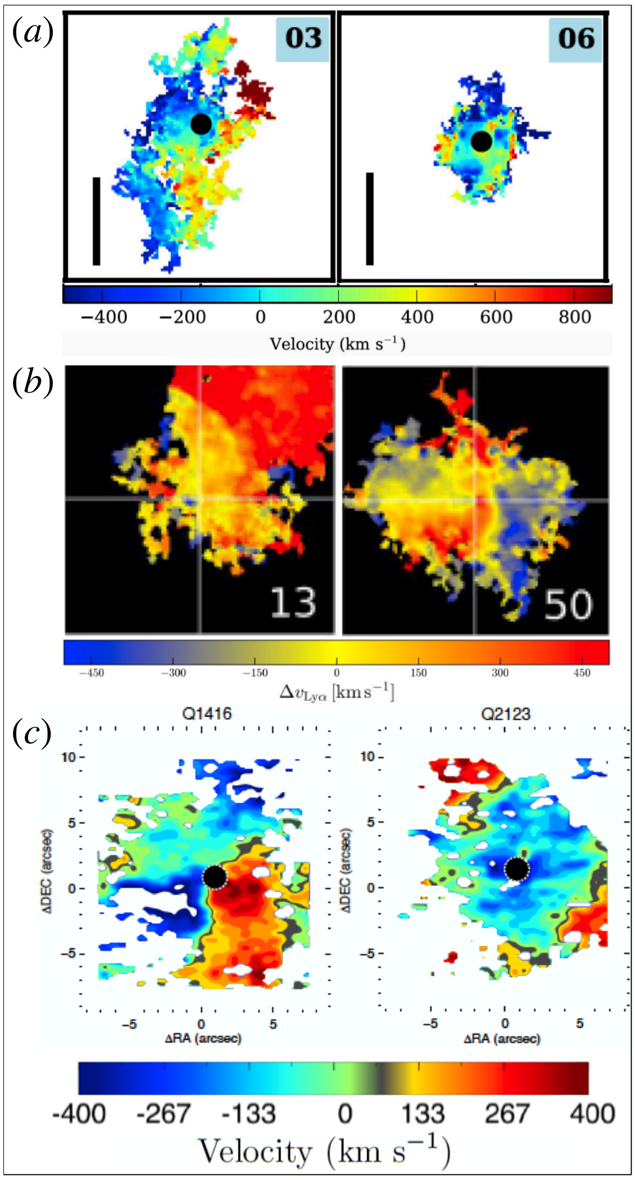

Figure 2.14: Velocity maps computed as first moment of the flux distribution with respect to the flux-weighted velocity centroid. The three panels report two examples of velocity maps of Lyα nebulae around radio-quiet QSOs belonging to the sample of B16 (a), AB19 (b) and C19 (c). The left plot in each panel show a giant Lyα nebula exhibiting a rotation kinematics pattern. The right plot reports a smaller Lyα nebula without a clear kinematic pattern.

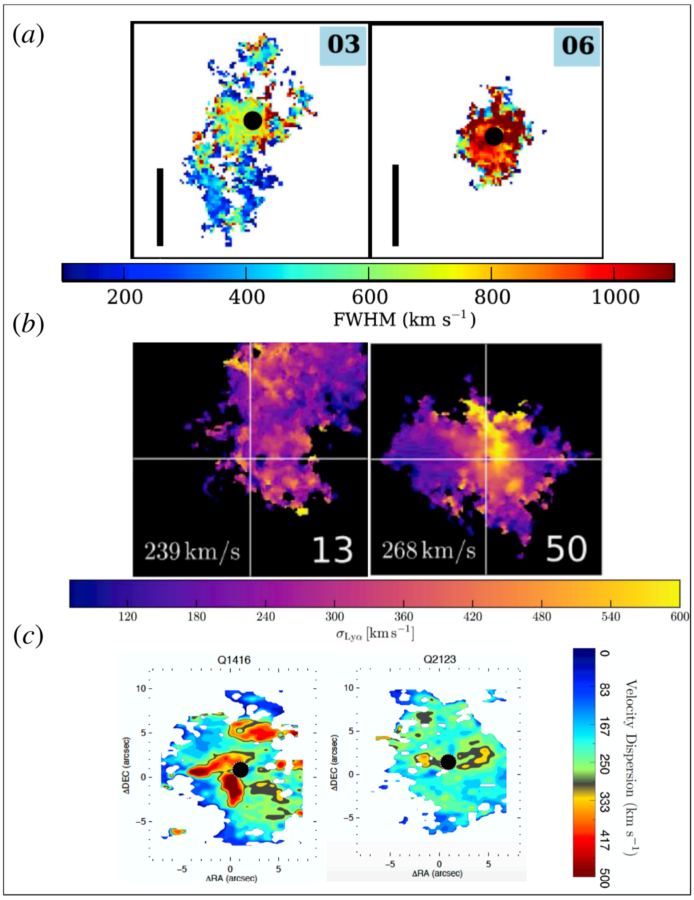

Figure 2.15: FWHM (2.355×σ; *Panel a*) and velocity dispersion (σ; *Panel b*,*c*) maps computed as the second moment of the flux distribution. Each panel shows 2 velocity dispersion maps of Lyα nebulae around radio-quiet QSOs belonging to the B16, AB19 and C19 samples, also shown in Fig. 2.14.

Surprisingly, B16 found a Lyα nebula around a hyper-luminous ($L_{bol} \simeq 10^{47.5} erg\ s^{-1}$) radio-quiet QSO (#6; in the middle panel in Fig. 2.15a), with a high velocity dispersion ($\sigma > 400 km\ s^{-1}$), as found around the radio-loud QSOs in the same sample. Therefore, such a high velocity dispersion of the emitting gas in CGM is not an exclusive feature of nebulae around radio-loud QSOs. This conclusion suggests that other mechanisms, in addition to the interaction with radio jets, can affect the gas on these large scales (e.g., mergers, radiative AGN driven outflows, stellar winds).

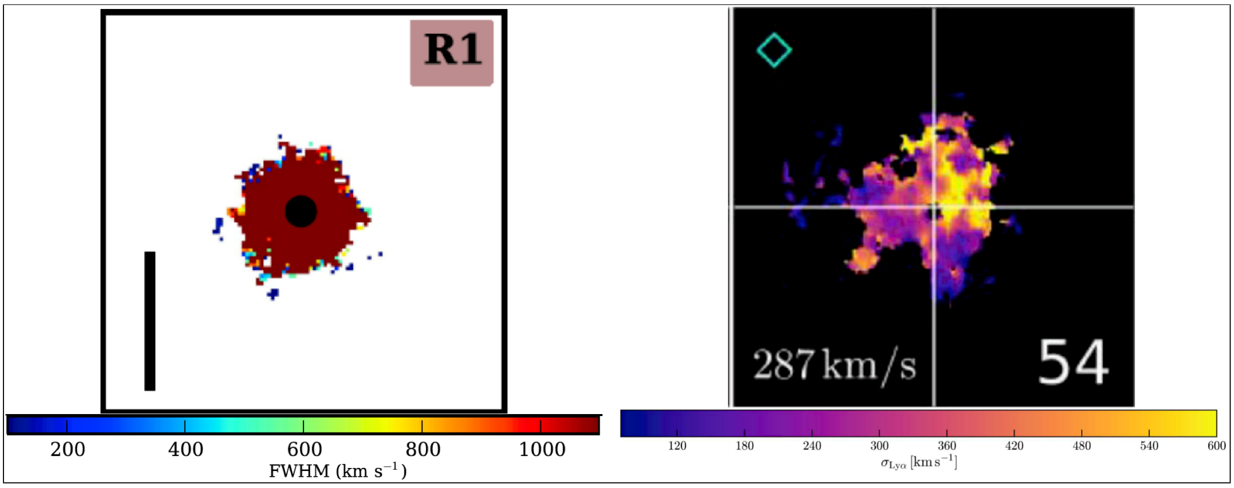

Figure 2.16: FWHM (2.355×σ; left) and velocity dispersion (σ; right) maps of Lyα nebulae around radio-loud QSOs belonging to the B16 and AB19 samples.

2.7 Detection of CIV and HeII nebulae

The wide spectral region of the new IFU instruments offers the possibility to detect giant nebulae from other transitions in addition to Lyα. Specifically, CIVλ1549Å and HeIIλ1640Å are among the strongest UV emission lines, after the Lyα transition. The ratios CIV/Lyα and HeII/Lyα are useful to constrain the properties of the diffuse gas (e.g. ionisation parameter, density, metallicity) and its emission mechanism, assuming photo-ionisation and shock models (e.g., Allen et al., 2008; Arrigoni Battaia et al., 2015a).

The presence of a CIV nebula, suggests the presence of metal enriched gas in the CGM. Prochaska et al. (2014) already found a high covering factor of the CIV clouds around QSO at z=2 up to over hundreds of kpc away, from the study of absorption lines. These high metallicity of the CGM could be a signature of galactic outflows or merger activity (Ford et al., 2014; Turner et al., 2016). However, CIV is a resonant line, although effects of resonant scattering are less pronounced than Lyα ones due to its lower density. Therefore, the detection of an extended non-resonant HeII emission is crucial to accurately trace the morphology and kinematics pattern of the CGM gas and estimate the contribution of the resonant scattering in Lyα and CIV emission. Accordingly, if diffuse HeII and Lyα emission share the same extension, this means that the resonant scattering mechanism is not relevant for the Lyα emission. Moreover, CIV and HeII emission lines have different main emission mechanisms: the first one is mainly powered by collisional excitation, therefore the CIV emission is strongly dependent on the temperature and ionisation parameter, while the second one is mainly due to the fluorescence mechanism through recombination and its ionisa-

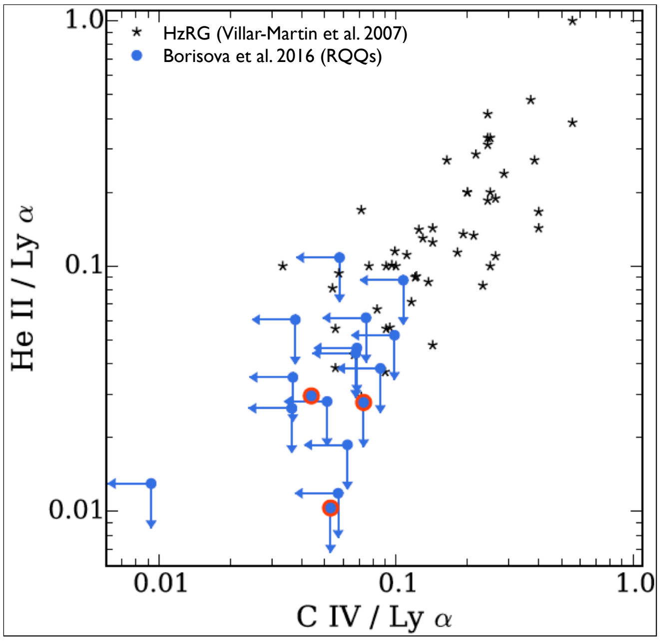

Figure 2.17: Line ratio diagram CIV/Lyα vs HeII/Lyα for the gas nebular emission in the CGM around two distinct populations: HzRGs (black stars) and radio-quiet QSOs (circles) from B16. Blue circles represent upper limits (2σ) on CIV/Lyα and HeII/Lyα emission in b16. Red circles indicate marginal ($\sim 2.5\sigma$) CIV or HeII detection in Borisova et al. (2016).

tion parameter[1] peaks at U≃-2 (Arrigoni Battaia et al., 2015a). Finally, the CIII] emission is very dependent both on the ionisation parameter and metallicity (Erb et al., 2010). Therefore, if used in combination of CIV and HeII it provides an excellent tool to accurately constrain the physical properties of thew CGM.

Fig 2.17 reports a CIV/Lyα vs HeII/Lyα line ratios obtained for Lyα nebulae around HzRGs (Villar-Martín et al., 2007c), and their radio-quiet QSOs. B16 highlight that Lyα nebulae around radio-quiet QSOs seem to follow a different trend (in the line ratio diagram) compared to those surrounding HzRGs, suggesting possible different origin for the nebulae in these populations. However, this result is based on upper limit values for CIV and HeII nebulae around radio-quiet QSOs. Significant extended CIV and HeII nebular emission has been revealed in ELANs. Specifically, MAMMOTH-1 is an ELAN, spatially correlated with a overdensity of radio-quiet QSOs and LAEs at z≈2.32 (Cai et al., 2017b; Arrigoni Battaia et al., 2018b). This nebula exhibits a projected size of ~440 kpc and luminosity $L_{Ly\alpha} \simeq 5 \times 10^{44}\ erg\ s^{-1}$. Cai et al. (2017b) detected extended CIV, HeII and CIII] emissions (>30 kpc) by using LBT/MODS slit-spectroscopy observations (Fig. 2.18a). All emission line profiles exhibit a double-peak. The latter, if observed for the only Lyα line might be due to resonant scattering ef-

---

[1] *it is defined as the ratio of the ionising luminosity to the volume density of hydrogen atoms:* $U = L_{\nu_{LL}}/n_H$

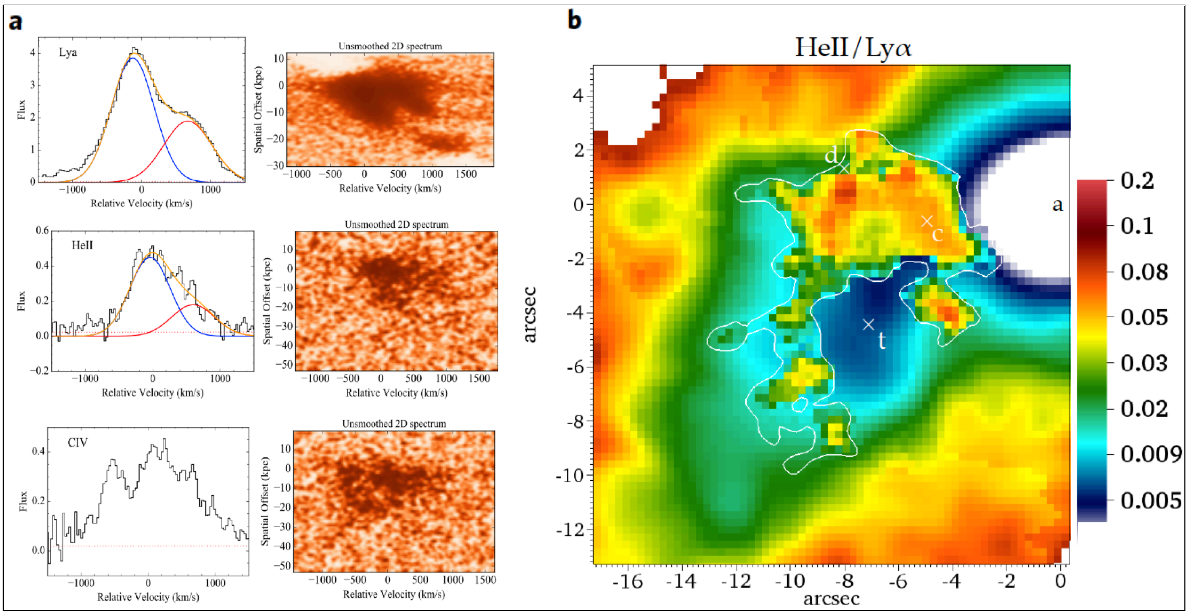

Figure 2.18: This figure reports two examples of extended CIV and HeII emission associated to two enormous Lyα nebuae. *Panel a* shows three spectra + 2D spectra of the Lyα, HeII and CIV emission lines of the extended nebular system, MAMMOTH-1, in the LBT/MODS observations (Cai et al., 2017b). All spectra exhibit a double-peak due to the kinematics of the CGM gas. The upper limit of the extension for HeII and CIV emission, depending on the width of the slit, is 31 and 33 kpc, respectively. *Panel b* shows the HeII/Lyα map observed in the Slug nebula through VLT/MUSE observations with the SB. The region outside the white contours indicates 1σ upper limit un an aperture of 0.8" × 0.8" and spectral width of 3.75 Å (Cantalupo et al., 2019). The white crosses mark the position of the quasar ("a"), of the Lyα emitting sources at the same redshift of the nebula ("c" and "d") and of the bright tail of the Lyα nebula ("t").

fects, but since the HeII also shows this double peak, it could be related to the kinematics. Indeed, Cai et al. (2017b) found that the presence of asymmetry of emission lines, metals in the CGM and the CIII]/HeII vs CIV/HeII and CIV/Lyα vs HeII/Lyα ratios, are consistent with photo-ionisation and shock-heating models (Arrigoni Battaia et al., 2015a), indicating presence of outflows over CGM scales. The ELAN Slug, also exhibits metal-line diffuse emission on large scale. Cantalupo et al. (2019) found an extended (maximum extension of ~100 kpc) HeII nebula associated to the faint continuum of a detected source (C source in Fig 2.18b). Fig. 2.18b reports the HeII/Lyα ratio showing a net confinement of the HeII emission which can be explained as a different distance of the nebula in that region (see Cantalupo et al., 2019, for details).

3. OUTFLOWS AND METALS IN THE CGM AROUND THE HYPER-LUMINOUS Z∼3.6 QSO J1538+08

Description: *During the last years, Lyα nebulae have been routinely detected around high redshift, radio–quiet QSOs thanks to the highly sensitive VLT/MUSE integral field spectrograph. Constraining their physical properties is crucial for our understanding of the circum-galactic medium environment and its role both as a repository for intergalactic and galactic baryons and venue for feeding and feedback processes. The most luminous QSOs are privileged test-beds to study these processes, given their large ionising flux and their expected high masses of host dark matter halo. We aim at characterising the rest-frame ultraviolet emission lines in the circum-galactic medium around a hyper-luminous, broad-line, radio-quiet QSO exhibiting presence of powerful outflows at nuclear and host galaxy scales. We analyse VLT/MUSE observations of the* $z\sim$ 3.6 *QSO SDSS J153830.55+085517.0 (*$L_{bol} = 6\times10^{47}$ *erg* s^{-1}*) and perform a search for extended emission to characterise its extent, geometry, emissivity, kinematics and metal content.*

3.1 J1538+08 from the WISSH QSO sample

SDSS J153830.55+085517.0 (hereafter J1538+08) is a hyper-luminous ($L_{\rm bol} \approx 6\times10^{47}$erg s^{-1}) and BAL QSO at $z_{\rm QSO} = 3.567^{+0.003}_{-0.002}$ based on Hβ (Vietri et al., 2018). Fig. 3.1 reports the QSO spectrum of J1538+08 extracted from an aperture with radius of 3 arcsec from the MUSE data-cube. This QSO belongs to the WISSH sample (Bischetti et al., 2017), i.e. WISE-SDSS selected hyper-luminous QSOs at z∼2-4.5. The WISSH QSOs are characterized by powerful winds from nuclear (Vietri et al., 2018; Bruni et al., 2019) to kpc scales (Bischetti et al., 2017) and, hence, are ideal laboratories for a detailed study of the effects of the AGN activity on kinematics and metal content of the CGM.

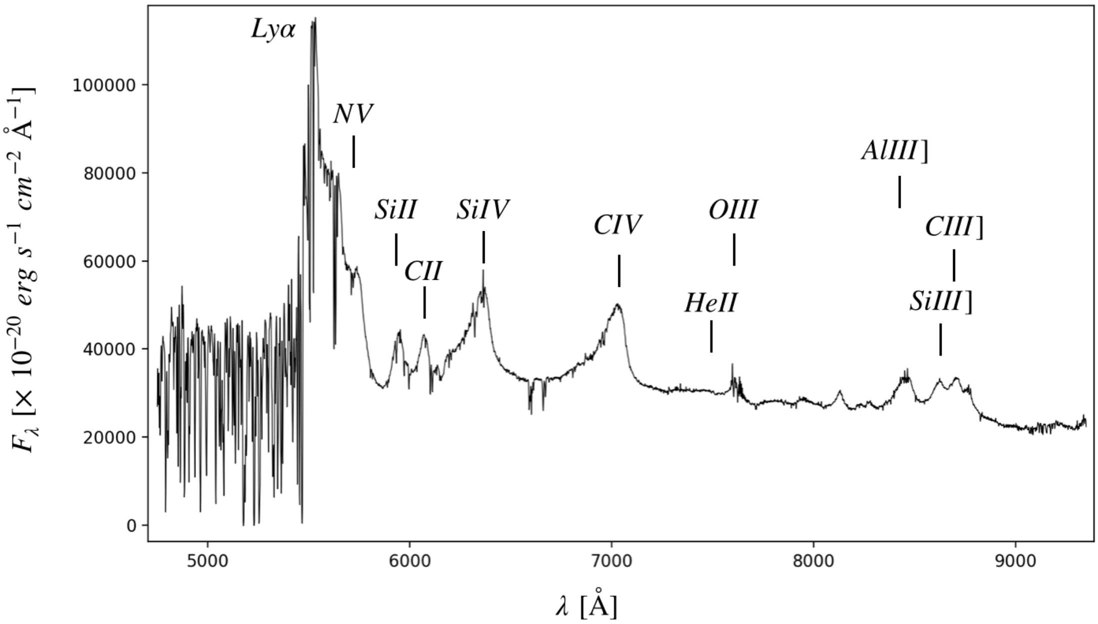

Figure 3.1: MUSE spectrum ($\lambda \sim 4700 - 9400$ Å) of the QSO J1538+08 extracted from a circular region with a radius of 3 arcsec.

3.2 Data Reduction

J1538+08 was observed with MUSE on July 26 2017 as part of the ESO program ID 099.A-0316(A) (PI F. Fiore). The observation consists of 4 exposures of 1020 sec each, for a total integration time of 1 h and 8 minutes. Each exposure was rotated by 90 degrees with the addition of a small dithering. The average seeing was $\approx$ 0.9 arcsec. The data reduction was performed by using the ESO MUSE pipeline (EsoRex v. 3.12.3; Weilbacher et al., 2014) and the code `CubExtractor` (details for which we will used the CubeFix, CubeSharp and CubEx recipes). We followed a procedure similar to that reported in B16, which has been described in more detail by Cantalupo et al. (2019). We briefly summarize the main steps in the following:

- we used the ESO MUSE pipeline. For each exposure we applied bias subtraction, corrected for flat-fielding, twilight and illumination. Finally, we applied a wavelength, geometry and astrometric calibration.
- we used `CubeFix` to apply a more accurate flat-fielding correction in each datacube by using the continuum and the emission lines of the sky as calibrators. This procedure consists in deriving the correction factors to be applied to each IFU and its elements in order to have coherent values of

the sky on the whole FOV and allows to perform a wavelength and flux dependent correction. The continuum of the sources need to be iteratively masked to minimize the self-calibration errors;

- We performed a correction of the sky line spread function by `CubeSharp` procedure which adopts a flux-conserving sky-substraction method based on the (see Cantalupo et al., 2019).
- Then `CubEx` was used to obtain more refined science datacubes and the associated variances. The standard ESO pipeline can indeed underestimate the propagated variance (Bacon et al., 2017). Therefore, the pipeline variance is propagated during the execution of the `CubEx` packages and is rescaled by a constant factor to match the empirical spatial variance estimated from the cube for each wavelength layer (see Borisova et al., 2016, for details). The final datacube is a median stack (with 3σ-clipping) of the single datacubes derived from each exposure.

Finally, we notice that during the data reduction with the `CubExtractor` code, we accounted for the presence of a saturated bright (Vega magnitude $V \simeq 9.7$) star at the edge of the MUSE field of view contaminating large part of the field in each exposure. In the flat-fielding and sky-subtraction, we indeed masked the stellar emission and the bleed trails up to a distance of 16 arcsec from the quasar where this contribution starts to become negligible for our purposes (see Sect. 3.4.3 for further details).

3.3 Nebulae detection methodology

We performed the identification and extraction of the nebulae in the final datacube with the `CubExtractor` package. We first removed the quasar Point Spread Function (PSF) with the `CubePSFSub` task, by masking the expected spectral regions having an extended emission in order to avoid any contamination in the PSF estimation. This recipe estimates the quasar PSF empirically at each wavelength layer from a pseudo-NB image. In our case, each pseudo-NB image was computed with a spectral width of ±150 pixels which corresponds to ±188 Å. The estimated PSF was rescaled to its flux in each wavelength layer image and then subtracted. The PSF normalization was derived by assuming that the central pixels, within a region of $1'' \times 1''$, are quasar dominated. Furthermore, we removed the continuum emission of any source within the MUSE FOV by means of a fast median-filtering approach using the `CubeBKGSub` task (see Cantalupo et al. 2019 for further details).

The diffuse emission search was performed on the PSF- and continuum- subtracted datacube with the `CubEx` recipe. The latter allows to detect and extract extended sources, by applying a connected labeling component algorithm.

The key input parameters of this algorithms are N_{min}^{vox} and SNR_{th}, which define the minimum number of connected voxels and the Signal to Noise Ratio (SNR) threshold of the extended emission to be searched, respectively. `CubEx` returns astrometric, photometric and spectroscopic information of the extended nebular emissions, and generates both a three-dimensional mask (3D-mask), which defines the datacube elements (i.e. voxels) belonging to the all detected nebulae, and a three dimensional SNR cube. Once the nebula is detected and extracted, `Cube2Im` task allows to create three data products by using the only voxels of the PSF- and continuum- subtracted datacube defined in the 3D-mask: (i) the SB map, i.e. an "optimally extracted image" derived by applying the 3D-mask to the datacube and by collapsing at each spaxel the contribution of the nebula voxels above the chosen SNR_{th}; (ii) a map of the velocity distribution obtained as the first moment of the flux distribution ; (iii) a map of the velocity dispersion (σ_{v}) which is derived as the second moment of the flux distribution. All these data products were smoothed with a Gaussian-kernel of σ = 2 pixels (0.4 arcsec). We computed the SNR map from the pseudo-NB image obtained by collapsing the wavelength range (i.e. the layers) in which the extended emission was detected to have an estimation of the variance distribution of the SB map. Then we associated a SNR value to each pixel, where the noise is the mean of the standard deviations derived in several background regions with size $1'' \times 1''$. The SNR map was finally smoothed with a Gaussian-kernel of σ= 2 pixels, to be consistent with the smoothing of the maps produced by `Cube2Im`.

Throughout this chapter we adopt a cosmology with $\Omega_\Lambda = 0.68$ and $H_0 = 67.4\, km\, s^{-1} Mpc^{-1}$ (Planck Collaboration et al., 2018), for which 1 arcsec corresponds to ~7.4 kpc at the QSO redshift. All the errors are quoted at 1σ significance and all flux-weighted quantities are computed in regions with signal to noise ≥3, unless otherwise stated.

3.4 Detection and properties of nebulae

We searched for nebulae around J1538+08 traced by typical CGM UV transitions, such as Ly$\alpha\lambda$1215 Å, NVλ1240 Å, SiIVλ1397 Å, CIVλ1549 Å, HeIIλ1641 Å and CIII]λ1909 Å. In the following we describe the properties of the detected extended nebular emissions.

3.4.1 Lyα nebula

We found a Lyα nebula consisting of ~55000 connected voxels by using SNR_{th} = 2.5 and N_{min}^{vox} = 10000 pixels. This nebula exhibits a maximum angular extension of ~20 arcsec. At the redshift of the QSO this corresponds to ~150 kpc. The line emission integrated over the entire nebula spans a maximum wavelength range

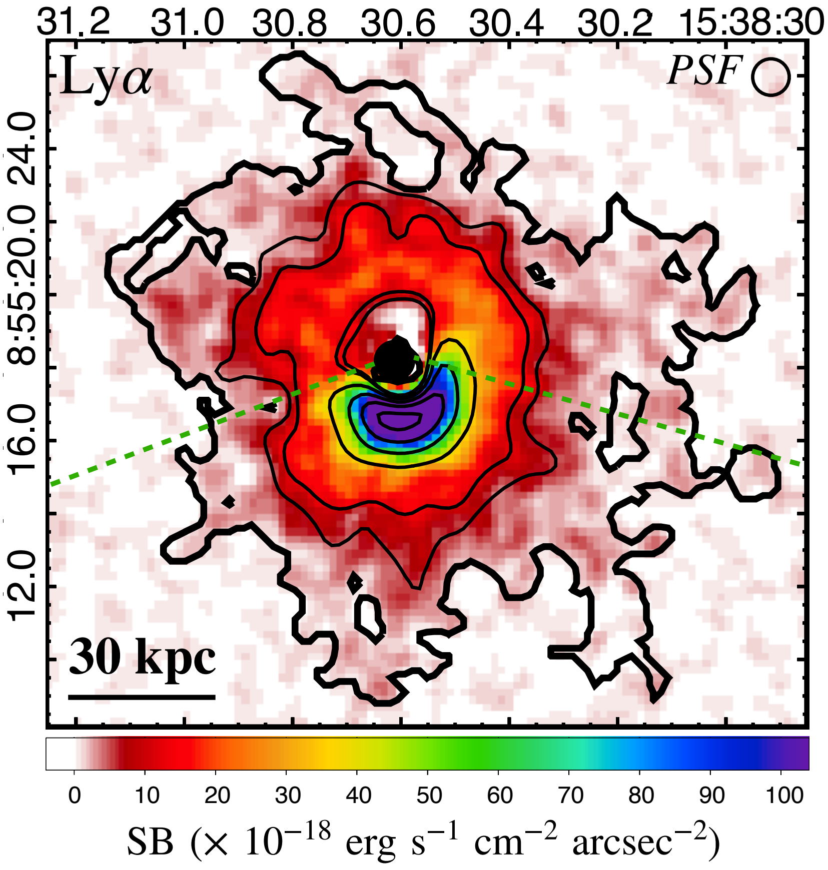

Figure 3.2: Optimally extracted SB map of the Lyα nebula. The QSO position is marked by a black dot. The thick black contour corresponds to the two-dimensional projection of the boundary of the nebula from the 3D-mask. It indicates a SB level of ~ 10^{-18} $erg\ s^{-1}\ cm^{-2}$. The thin black contours indicate SNR levels 3, 5, 15, 25, 35, 45 extracted from the SNR map. The wavelength layer at the Lyα profile peak is used to report the background fluctuations in the image. On the top-right corner the circle indicates the size of the FWHM of the instrument PSF. The green dashed lines delimit the nebula in two regions (southern and northern) relative to the QSO position from which radial profiles have been computed (see Fig. 3.4).

of ~ 95 Å (~ 5000 $km\ s^{-1}$) and shows a peak at $\lambda^{Neb}_{Ly\alpha} = (5543.8 \pm 1.8)$ Å measured through a Gaussian fit[1]. This corresponds to a redshift of $z^{Ly\alpha}_{Neb} = 3.563 \pm 0.002$.

Fig. 3.2 shows the SB map of the Lyα nebula. The reported background consists of a single layer of the data-cube corresponding to the central wavelength of the spectral range of the 3D-mask (white region in Fig. 3.3). The thick contour represents the projected boundary derived from the 3D-mask which encloses the detected nebular emission with $SNR > 2.5$. The thin contours displays the

---

[1] *Throughout the paper we used the scipy function "curve_fit", developed on python software, to fit the spectra.*

Table 3.1: Physical properties of the detected nebulae.

	Lyα	CIV
λ^{a}_{cen} [Å]	5543.8 ± 1.8	7064.7 ± 1.8
z^{b}_{Neb}	3.563 ± 0.002	3.561 ± 0.001
Size^{c} [kpc]	~150	~75
Spectral width ^{d} [Å]	~ 95	~42
$d^{peak,e}_{Neb}$ [kpc] ± 3.7 kpc	10.4	15.1
$d^{cen,e}_{Neb}$ [kpc] ±3.7 kpc	5.7	13.7
α^{g}	~0.72	~0.62
ϕ^{h} [degree]	~62	~11
Flux^{i} [$\times 10^{-16}$ $erg\ s^{-1}\ cm^{-2}$]	17.8±0.1	0.77 ± 0.03
Luminosity^{l} [$\times 10^{43}$ $erg\ s^{-1}$]	20.55 ± 0.16	1.00 ± 0.03
$\bar{\sigma}^{m;\ Ly\alpha}_{v}$ [$km\ s^{-1}$]	732 ± 84	301 ± 138
$\bar{\sigma}^{m;\ CIV}_{v}$ [$km\ s^{-1}$]	560 ± 15	455 ± 55

Notes: ^{a} Line peak wavelength from the Gaussian modelling of Lyα and CIV nebulae spectrum. ^{b} Redshift of the nebulae corresponding to λ_{cen}. We used as Lyα and CIV λ rest-frame 1215 Å and 1549 Å, respectively. ^{c} Maximum projected physical size derived from the 3D-mask. ^{d} Spectral width within which the nebula is detected (from 3D-mask). ^{e} Distance from the QSO position to the SB peak of the nebula. ^{f} Distance from the QSO position to the flux weighted centroid of the nebula. ^{g} Asymmetry parameter, i.e. the ratio between the semi-minor and semi-major axis of the SB map. ^{h} Position angle East of North of the major axis of the SB map. ^{i} Total flux derived from the SB maps (Figs. 3.2 and 3.5). ^{l} Total nebula luminosity. ^{m} The first value reports the spatially averaged flux-weighted dispersion measured from the dispersion map (see Section 3.4.4) of the Lyα and CIV, respectively. The second value is derived from the Gaussian fit of the total nebula spectrum.

SNR levels derived from the SNR map. The morphology of the extended nebular emission is approximately circular. We computed the flux weighted centroid shift (d^{cen}_{Neb}), the peak displacement (d^{peak}_{Neb}), the asymmetry (α) and the position angle East of North (ϕ) of the nebula. The first two quantities are reported relative to the QSO position, while the remaining ones are estimated from the Stokes parameters as in AB19 (see Table 3.1). The Lyα nebula exhibits a maximum SB value of $\sim 10^{-16}$ $erg\ s^{-1}\ cm^{-2}$ and a total luminosity of $L_{Ly\alpha} \simeq (2.06 \pm 0.02) \times 10^{44}$ $erg\ s^{-1}$. Fig. 3.3 shows the comparison between the Lyα spectra of the QSO and the nebula normalised to their peak emission. The QSO spectrum was extracted from an aperture of radius 3 arcsec, while the nebula spectrum was obtained from the PSF- and continuum- subtracted data-cube by summing the spectral

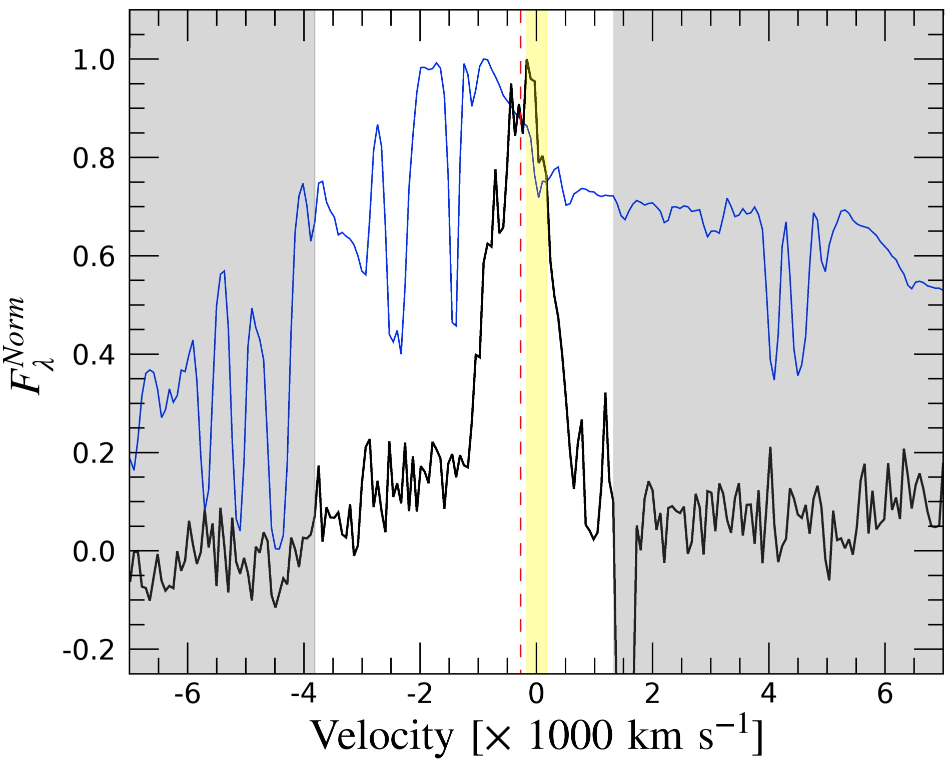

Figure 3.3: Black and blue lines are the nebula and QSO spectrum, respectively. These Lyα line spectra are reported in velocity space relative to the z_{QSO} and they both are normalised to their peak. The white region reports the spectral range of the 3D-mask. The red dashed vertical line marks the peak wavelength of the Lyα line derived through Gaussian modelling. The yellow area indicates the 1σ uncertainty of the systemic redshift of the QSO (Vietri et al., 2018). The absorption line at ~1500 $km\ s^{-1}$ is a sky feature which could not be appropriately removed by the algorithm `CubePSFSub`.

contribution of all the spaxels belonging to the nebula, i.e. the region enclosed in the black thick contour shown in Fig. 3.2. The x-axis reports the velocity relative to the z_{QSO}. The white region in the plot corresponds to the spectral width where the nebula was detected (i.e. the maximum spectral extent of the 3D mask; see also Table 3.1). The red dashed line marks the peak of the Lyα profile of the nebula, modelled with a Gaussian component and with a constant term for the continuum, within a range of ±500 Å (±27000 $km\ s^{-1}$) from the line peak. This peak appears to be broadly consistent with the z_{QSO} (yellow area in Fig. 3.3).

Fig. 3.4 reports the circularly averaged radial SB profile of the nebula (black data points) corrected for residual background due to the bright star located at the edge of the MUSE field of view. The profile is extracted from the pseudo-

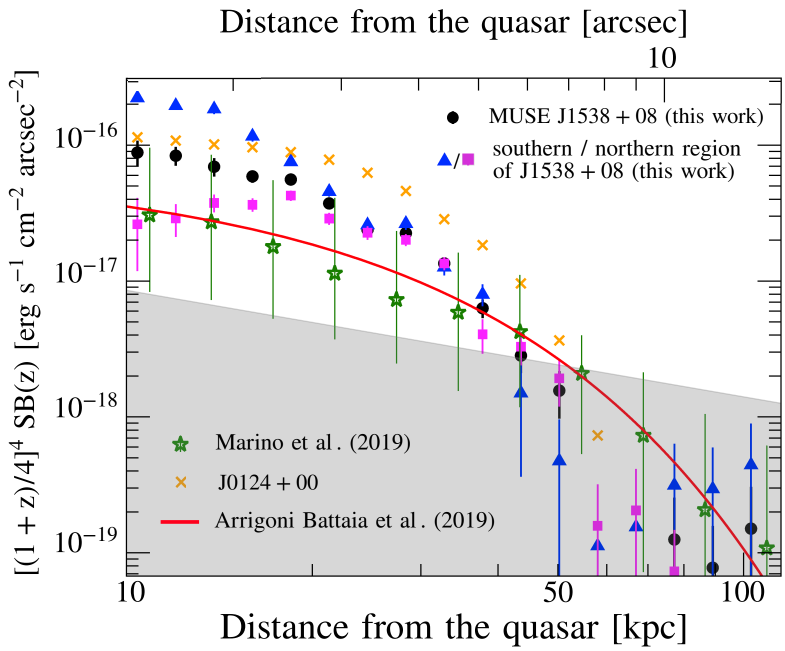

Figure 3.4: Lyα SB radial profile (black circles) of the pseudo-NB image. The points represent bins of SB measured in concentric annuli centered on the QSO position and their errors indicate the 16th and 84th percentile (corresponding to 1σ for a Gaussian distribution). The bin width is chosen to be uniformly spaced in a logarithmic scale. The blue triangles and magenta squares show the radial profiles measured in the southern and northern region, respectively (see Fig. 3.2). The red curve is the modelled average radial profile of the AB19 QSO sample. We also include the average radial profile of the Lyα nebulae of the sample of B16 recalculated by Marino et al. (2019) (the error bars represent the 25th and 75th percentiles). We report as orange crosses the radial profile of the high velocity dispersion nebula detected by B16 around the WISSH QSO J0124+00. All the radial profiles are corrected for the cosmological dimming effects and re-scaled at z=3 (i.e. $[(1 + z)/4]^4 \times SB(z)$). The grey shaded area indicates the 2σ Poissonian noise relative to the rescaled profiles of the Lyα nebula around J1538+08 (see Section 3.4.1 for details).

NB image in concentric annular regions centered on the QSO position. The grey area indicates the 2σ Poissonian noise associated with the SB profile[2]. The radial profile was compared with the average radial profiles reported by B16 and AB19. All the SB radial profiles in Fig. 3.4 are corrected for the cosmological $(1 + z)^4$ SB dimming factor and re-scaled at z=3 for comparison. We also reported the rescaled profile of the nebula around the WISSH QSO J0124+00, which was identified by B16 as the brightest and most peculiar in their sample in terms of

---

[2] *The Poissonian noise was estimated as the average value of the standard deviations within background regions* 1" × 1" *of the pseudo-NB divided by the square root of each annulus area.*

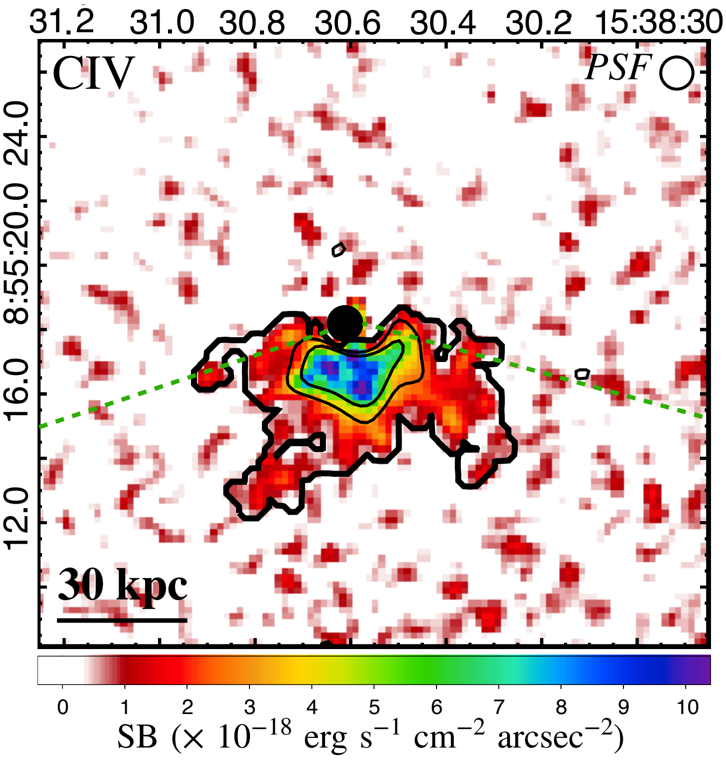

Figure 3.5: Optimally extracted SB map of the CIV nebula. The black dot, the contours and the dashed green lines have the same meaning of Fig. 3.2. Thin contours reports levels of $SNR = 3$ and 5.

sharp-peaked morphology and large velocity dispersion. We noticed a SB excess at 10-20 kpc which extends out to 40 kpc relative to the B16 and AB19 average profiles. This behaviour is somewhat similar to the one reported for the radial profile of J0124+00.

In order to further investigate the excess of emission, we computed radial profiles in two regions: a southern one containing the SB peak and a northern one without it. These regions are delimited by the green dashed lines in Fig. 3.2 which have been traced in order to include both the Lyα SB peak and the CIV nebula (see Fig. 3.5). The comparison between these profiles, reported in Fig. 3.4, shows that the peak emission in the SB image, contained in the southern region profile (blue data points), is responsible for the SB excess exhibited by the circularly average radial profile at 10-20 kpc. Nonetheless the northern region exhibits a profile at 20-40 kpc similar to the southern region, with an excess compared with the average profiles reported for the B16 and AB19 samples.

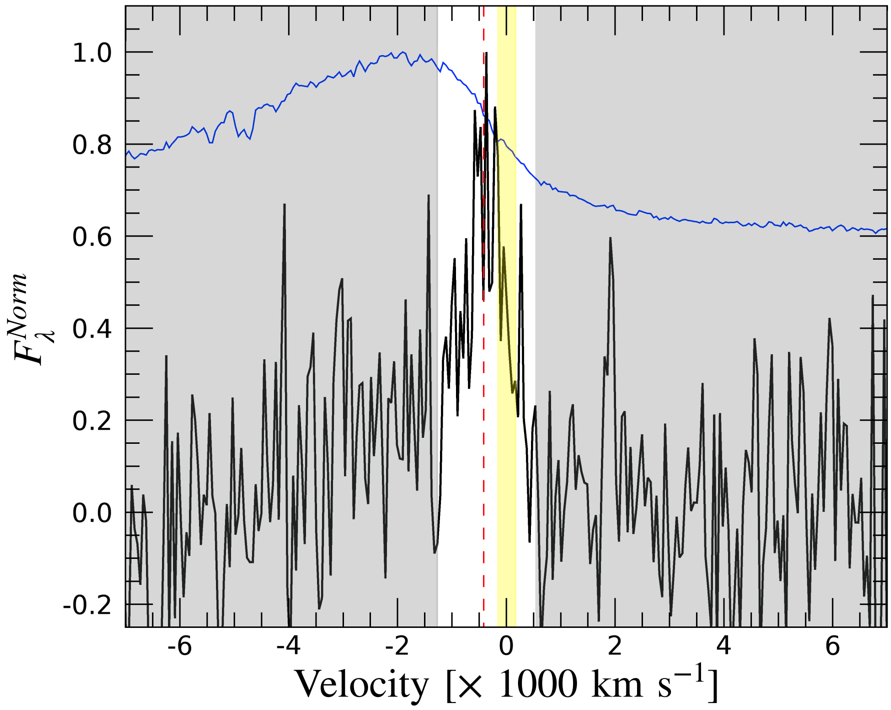

Figure 3.6: CIV line spectra, reported in velocity space relative to the QSO rest-frame, of the nebula (black) and QSO (blue) normalized to their peak emission. The details of the plot are the same as reported in Fig. 3.3

3.4.2 CIV nebula

We scanned the data-cube searching for diffuse emission in additional transitions typically found in the CGM. The only extended emission detected at good significance level is traced by the CIV line. Given its typically lower emissivity compared with the Lyα we started our search by setting SNR_{th} =2.5 and N_{th}^{vox} =10000 and then progressively lowered the latter parameter by steps of 1000 voxels until the extended emission was detected. We found that the N_{th}^{vox} = 4000 was required to detect the nebula.

The SB map of the CIV nebula is shown in Fig. 3.5. This nebula, consisting of 4700 voxels, is much smaller than the Lyα nebula, with a maximum angular extension of ~ 10 arcsec, which corresponds to a projected physical size of ~75 kpc. It is almost completely contained in the southern region in which the Lyα exhibits its peak emission (see Fig. 3.2) and exhibits an asymmetric morphology with α = 0.62. The peak of the SB_{CIV} is located roughly at the same position of the $SB_{Ly\alpha}$ peak and it is estimated to be at a distance of 7.5 to 15 kpc from the QSO position. The value of the SB peak (~ 10^{-17} $erg\ s^{-1}\ cm^{-2}$) and the

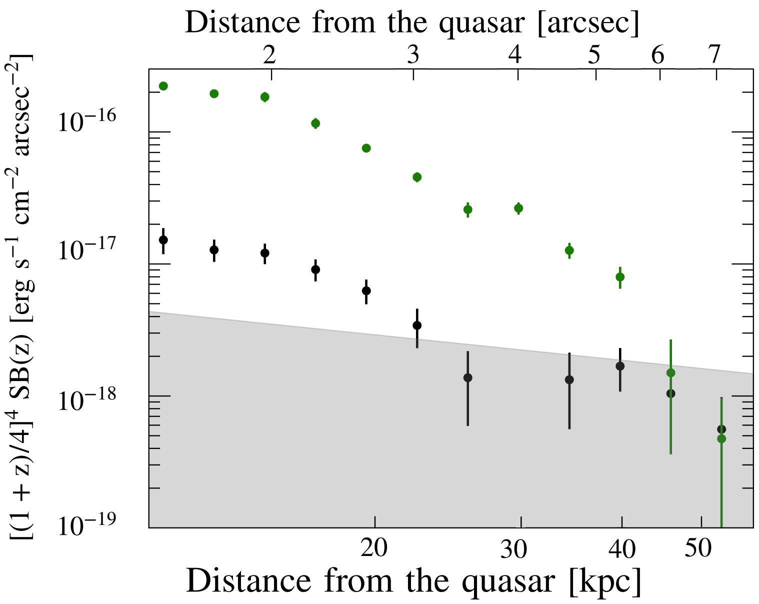

Figure 3.7: SB radial profile of the CIV nebula (black) extracted in the southern region (see Fig. 3.5). The SB profile for the Lyα nebula, extracted in the same region, is also reported in green. These SB profiles have been rescaled for SB cosmological dimming similarly to what has been done in Fig. 3.4. For other details refer to the caption of Fig. 3.4.

luminosity of the CIV nebula ($L_{CIV} \simeq 9.33 \pm 0.33 \times 10^{42}$ $erg\ s^{-1}$) are one order of magnitude lower than those measured for the Lyα nebula.

Fig. 3.6 shows the comparison between the spectrum of the CIV nebula and the QSO one. The CIV nebula was detected in a relatively smaller spectral range ($\sim$ 2000 $km\ s^{-1}$) than the spectral region of the Lyα nebula ($\sim$ 5000 $km\ s^{-1}$). Through a Gaussian modelling of the line (similarly to the one performed for the Lyα), we found that the CIV line peaks at $\lambda_{CIV}^{Neb} = 7064.7 \pm 1.8$ Å. This corresponds to a redshift of $z_{Neb}^{CIV} = 3.561 \pm 0.001$, i.e. in good agreement with the Lyα nebula one. We computed the SB radial profile of the CIV (Fig. 3.7) centered in the QSO position from the southern region. The emission of the nebula is higher than the 2σ Poissonian SB limit up to a distance of ~20 kpc from the QSO. For comparison, we also reported the Lyα radial profile computed in the same region.

3.4.3 *Stellar contamination*

Fig. 3.8 reports the image of the MUSE FOV obtained by collapsing the spectral region of the Lyα- (left) and CIV- (right) nebula in the PSF- and continuum-subtracted datacube. The upper-left corner in each image represents the region contaminated by the luminous star, which has been masked during the data reduction. A visual inspection reveals no residual contamination at the nebula position. We performed a more quantitive estimation by measuring the average flux in concentric annular regions centered on the star and we found no significant stellar contamination on the nebular emissions. The average background was estimated in concentric annuli with respect the center of the star, by excluding both the regions clearly contaminated by the star and the nebular regions. We estimated the radial gradient of the residuals with respect to the star position and the percentages of the maximum contribution of these residuals to the nebular emissions, which are the 8% and 4% for Lyα- and CIV-nebula, respectively.

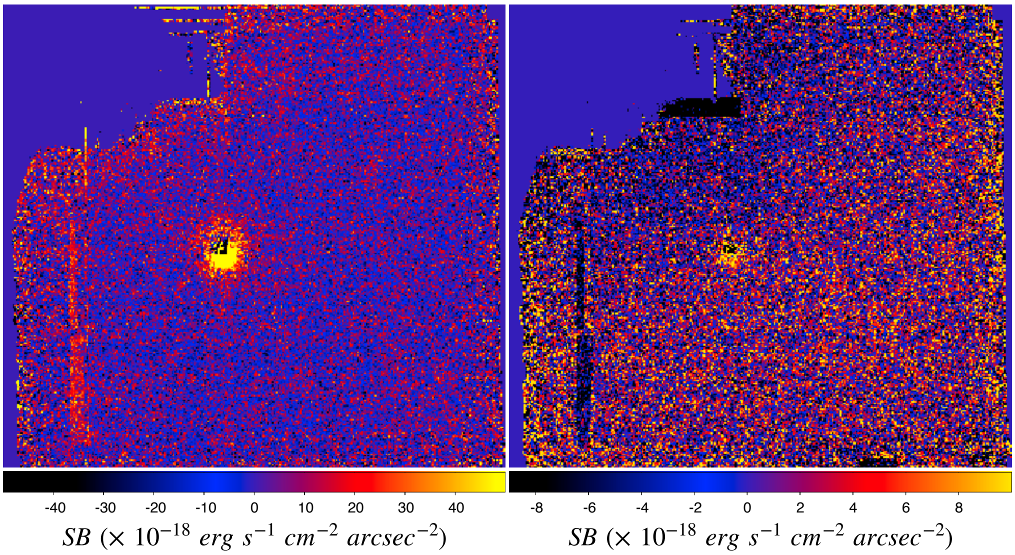

Figure 3.8: Pseudo-NB images obtained by collapsing the final PSF- and continuum subtracted cubes in the spectral regions of Lyα (right panel) and CIV (left panel) nebula, respectively. The homogeneous blue area on the upper-left corner represents the mask applied to the exposures during the data reduction, in order to mask the star in the field of view.

3.4.4 Kinematic properties of the nebulae

Figs. 3.9 and 3.10 show the velocity maps for Lyα and CIV nebula, respectively. In each figure we reported the velocities relative to the nebula (z_{Neb}; left panel) and z_{QSO} (right panel) rest-frame, respectively. Compared with the Lyα nebula rest-frame, we do not see significant structure indicative of bulk motion or clear separation between red/blue-shifted gas components. Almost the entire Lyα nebula exhibits velocities spanning ~ -1000 km s^{-1}.

We investigated the radial velocity profile of the Lyα nebula to assess a possible trend with the distance from the QSO. Specifically, we extracted spectra from the PSF- and continuum- subtracted data-cube in each annular region used for

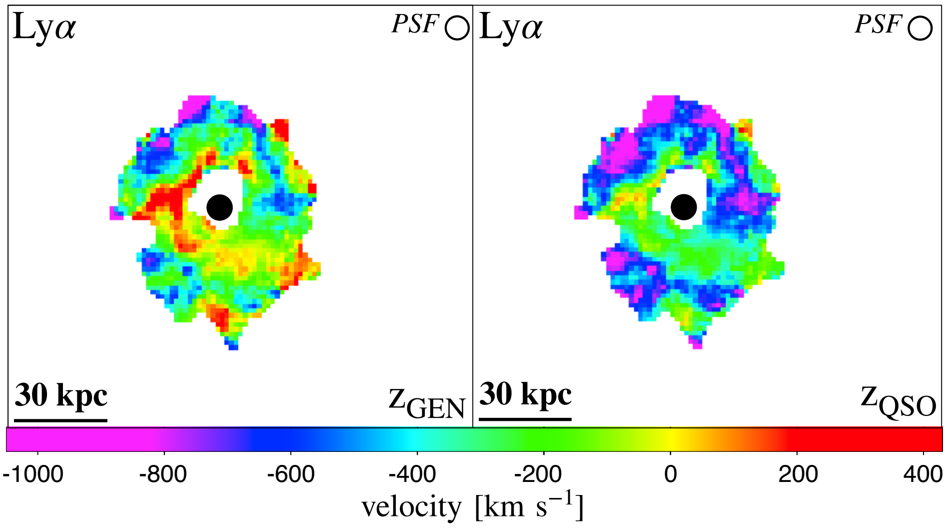

Figure 3.9: Flux-weighted velocity maps relative to the Lyα peak of the whole nebula (left) and to the QSO systemic redshift (right). Figures show only regions with $SNR \geq 3$. The black dot indicates the QSO position.

the SB radial profiles (see Fig. 3.4). For each spectrum, we modelled the Lyα emission line with a Gaussian profile. Fig. 3.11 shows the radial distribution of the best-fit velocities relative to the z_{Neb}. The velocity profile exhibits a constant value around $\sim 100-200\ km\ s^{-1}$ up to 15 – 20 kpc. There is an apparent decline of the velocity down to $-200\ km\ s^{-1}$ at larger radii (20-30 kpc).

The flux-weighted velocity dispersion maps for Lyα (left panel) and CIV nebula (right panel) are shown in Fig. 3.12. In the case of Lyα, the dispersion reaches values up to $\sigma_v \sim 1000\ km\ s^{-1}$, with no clear significant radial gradient.

In order to better investigate the trend of the dispersion of the Lyα emission with the distance from the QSO, we computed the radial dispersion profile using the same methodology adopted for the velocity profile (see red points in Fig. 3.11). The profile exhibits σ_v around $\sim 500\ km\ s^{-1}$ up to $\sim 15-20$ kpc and increases up to $\sigma_v \sim 900\ km\ s^{-1}$ at ~ 25 kpc from the QSO. The profiles could only be accurately computed until 40 kpc since the line profile modelling at larger distances is completely unconstrained. Therefore, the values in the map at distances larger than ~40 kpc from the QSO must be considered with caution.

3.4.5 CIV/Lyα and HeII/Lyα line ratios

We computed a total flux CIV/Lyα ratio of 0.06 ± 0.01. This agrees with the approximate values of 0.04 – 0.08 previously estimated for some tentative ($\sim 2.2\sigma - 2.8\sigma$) detections in B16. Similarly our result, these values were obtained by estimating the total flux of the voxels associated to the Lyα 3D-Mask shifted

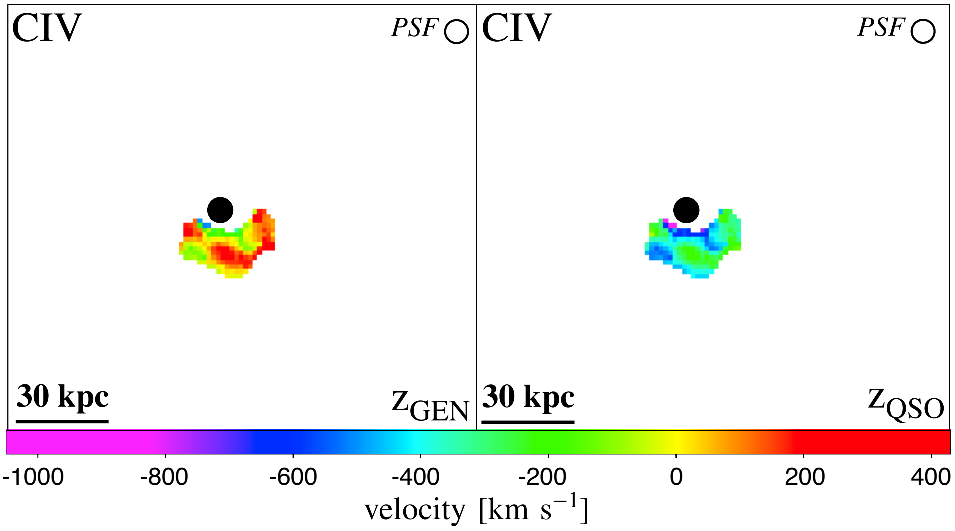

Figure 3.10: Velocity maps of the CIV extended structure. As in Fig. 3.9 the right panel shows the velocity relative to the CIV peak emission line of the nebula, while the right panel is derived assuming as reference the QSO systemic redshift. Figures show only regions with SNR ≥3.

at the wavelength of the CIV corresponding to z_{Neb}, divided by the total flux of the Lyα nebula (reported in Table 3.1). This procedure avoids the bias due to aperture effects (i.e. different extensions for different line emissions) and provides a conservative estimate if, as expected, the Lyα nebula is the brightest and more extended one.

The CIV/Lyα ratio map reported in Fig. 3.13 is the ratio of the SB maps over the regions with $SNR>3$ in both the Lyα and CIV nebula. The spatial distribution of the ratios is not constant and, on average, shows larger values in the external regions (> 30 kpc) where, however, the SNR is low. The median value of the CIV to Lyα ratio directly computed in the CIV/Lyα map is $0.08^{+0.11}_{-0.04}$. A consistent value is obtained by computing the average of the map values weighted with the SNR values of both Lyα and CIV nebula.

While extended HeII emission is commonly observed around high-redshift radio galaxies (e.g. Wilman et al. 2000, Villar-Martín et al. 2007a), only 6% of the radio-quiet QSOs in the B16 sample show HeII diffuse emission. No HeII emission is found around J1538+08. We inferred a 2σ upper limit to the HeII/Lyα ratio of > 0.02 by applying the same Lyα 3D-mask shift procedure used to obtain the total flux CIV/Lyα ratio. These CIV/Lyα and HeII/Lyα ratios could be used to understand the mechanisms powering the observed Lyα nebula, i.e. QSO photoionisation, shocks and/or collisional excitation (i.e. cooling). Because of the detection of relatively bright extended CIV, we can rule out cooling due to gravitational accretion as the powering mechanism of this nebula. However, it is notoriously difficult to disentangle photoionisation models from shock models

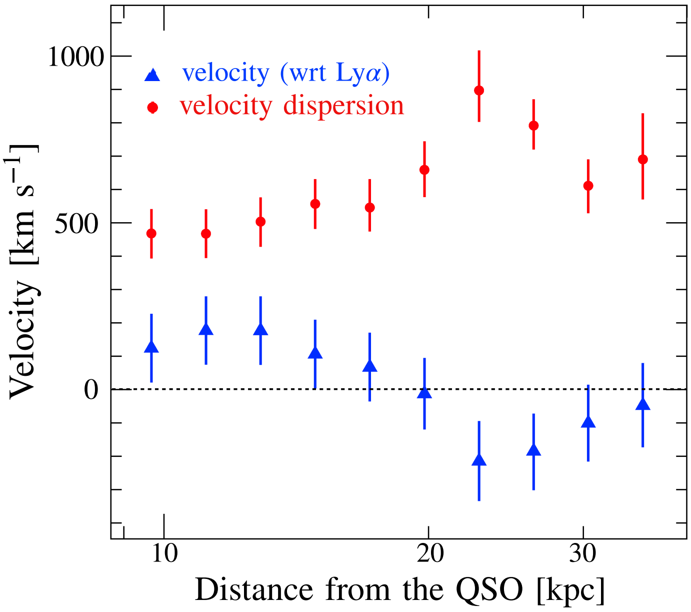

Figure 3.11: Radial profile of velocity (blue triangles) and dispersion (red circles) derived from Gaussian modelling of the Lyα profile extracted in concentric logarithmic spaced annular region centered on the QSO position.

in a HeII/Lyα vs CIV/Lyα ratio (Arrigoni Battaia et al., 2015b). Nevertheless, photoionisation models usually do not predict lower levels of HeII/Lyα with respect to CIV/Lyα (e.g. Humphrey, 2019). On the contrary they predict ratios of the same order for the two transitions. This is because these two line emissions have similar ionisation energies 64.5 eV for CIV and 54.4 eV (4 Ryd) for HeII. On the other hand, shock models (Allen et al., 2008) do show cases in which the HeII/Lyα ratio is lower than the CIV/Lyα ratio. Indeed, according to shock+precursors models presented by Allen et al. (2008) and Arrigoni Battaia et al. (2015a) for the origin of extended nebular emission, the values of CIV/Lyα and HeII/Lyα inferred from our analysis are consistent with a shock propagating at 200-300 $km\ s^{-1}$ in a $n_H \sim 10 - 100\ cm^{-3}$ gas or with a faster >1000 $km\ s^{-1}$ shock in a denser, $n_H > 100\ cm^{-3}$, gas. We caution that such models are approximate as they do not take into account the complex radiative transfer of the Lyα emission.

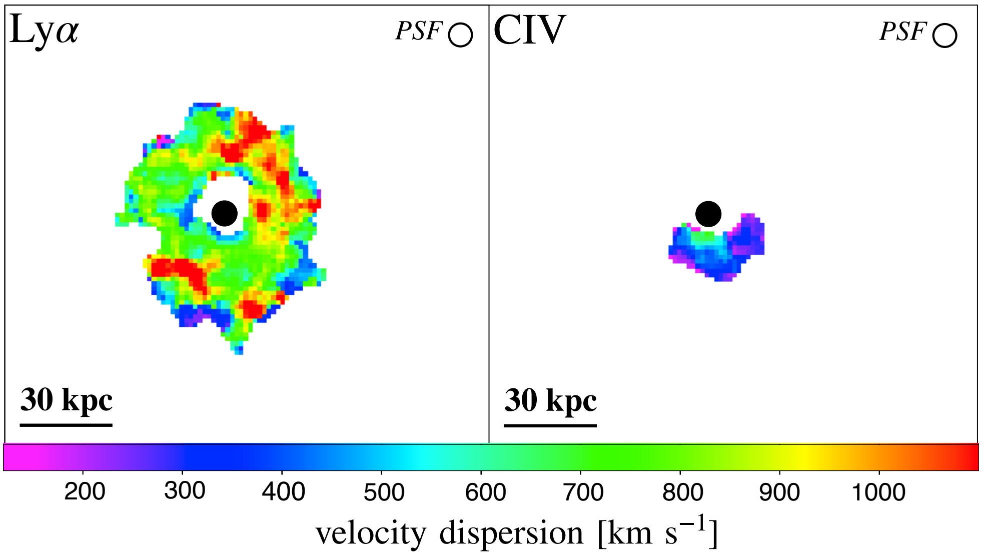

Figure 3.12: Flux-weighted velocity dispersion maps for Lyα (left) and CIV (right) nebular emission with $SNR \geq 3$. The standard deviation derived from the MUSE spectral resolution at the observed position of the Lyα and CIV is $\approx 70\ km\ s^{-1}$.

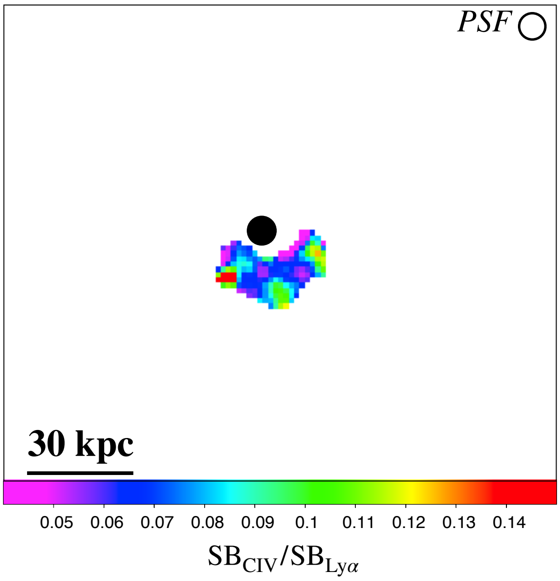

Figure 3.13: Map of the CIV/Lyα SB ratio associated with regions of CIV and Lyα nebulae at $SNR > 3$.

3.5 Discussion

3.5.1 Surface brightness and morphology of the nebulae around J1538+08

We have reported the discovery of a Lyα nebula around the hyper-luminous radio-quiet QSO J1538+08, which exhibits a projected size of ~150 kpc and a luminosity of $L_{Ly\alpha} \sim 2 \times 10^{44}$ $erg\ s^{-1}$. Previous MUSE studies at similar redshifts (i.e. z~ $3-4$) and exposures (0.75-1 hours) reported Lyα nebulae around similarly luminous radio-quiet QSOs (B16) or sources with slightly lower L_{bol} (AB19). The Lyα nebula around J1538+08 exhibits a maximum projected size which is similar to the average value (~ 150 kpc) for the B16 and AB19 samples[1]. The $SB_{Ly\alpha}$ radial profile of our nebula, shown in Fig. 3.4, exhibits a projected distance from the QSO at a SB of ~ $10^{-18} erg\ s^{-1}\ cm^{-2}\ arcsec^{-2}$ (i.e. ~ 50 kpc), which is similar to the one inferred from the average profiles from B16 and AB19. This behaviour seems to be independent from the luminosity of the QSO. However, notice that the SB at this distance coincides with the level of the 2σ Poissonian noise of the image and therefore deeper observations are needed in order to verify this claim.

The flux-weighted centroid shift and the asymmetry measured for the Lyα nebula around J1538+08 are close to the median values reported in AB19, i.e. 8.3 kpc and 0.71 respectively. The luminosity of our Lyα nebula is one of the highest measured so far (i.e. among the 10% brightest sources of the B16 and AB19 samples) and is comparable to the luminosity of known ELANe (Cantalupo et al., 2014; Hennawi et al., 2015; Cai et al., 2017a; Arrigoni Battaia et al., 2018b, AB19).

Interestingly, some WISSH quasars are included in the B16 (J0124+00, J1621-00), AB19 (J0125−10, J0947+14) and Cai et al. (2019) (J2123−00). The size and luminosity of the Lyα nebulae detected around them appear to be heterogeneous (see Fig. 3.14), suggesting that the properties of these nebulae have no simple dependence on the similar, large quasar radiative output (i.e. $L_{bol} > 10^{47}$ erg s^{-1}).

We checked for possible dependencies on the radio-quiet QSOs bolometric and 2500 Å luminosities (derived from Spectral Energy Distribution modelled by Duras et al. 2017 and Duras et al. in prep.) to verify if the nuclear radiative output could affect the properties of the Lyα nebula around the WISSH QSOs considered here. No significant trend with luminosity was observed, confirming the result reported by AB19 for a larger sample of QSOs.

The CIV nebula revealed around J1538+08 is one of the first extended (75 kpc) structure detected at high significance (5σ)[2] and spatially mapped around a radio-quiet QSO. This provides a clear indication of a metal enriched medium

---

[1] *We excluded from the comparison Lyα blobs, enormous Lyα nebulae and nebulae surrounding radio-loud QSOs.*

[2] *This value represents the integrated SNR computed for the extended CIV emission line.*

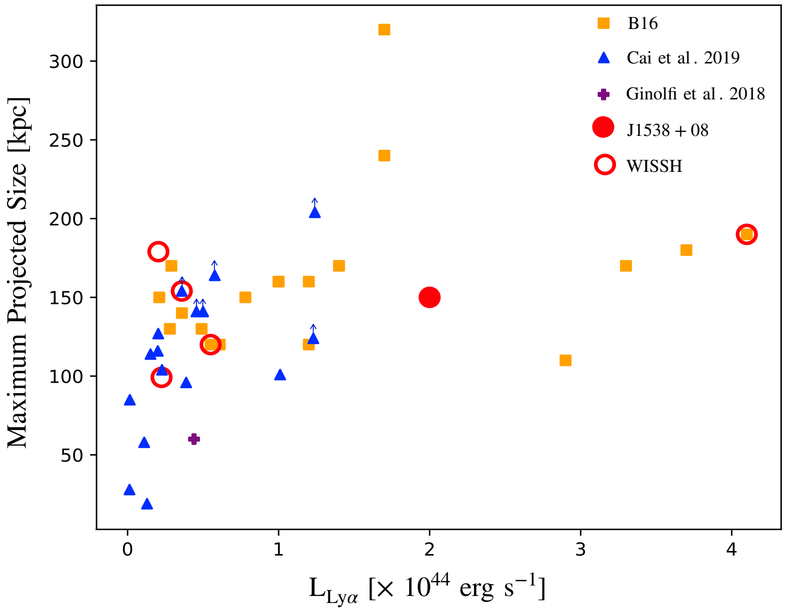

Figure 3.14: Maximum projected size versus luminosity of the Lyα nebulae around quasars from the B16 (orange squares), Cai et al. (2019) (blue triangles) and Ginolfi et al. (2018) (purple cross). WISSH quasars are marked with an additional red circle. We also show the two WISSH quasars included in the AB19 sample. For these sources AB19 do not report the maximum projected size, therefore we plot the maximum distance from the quasar spanned by the Lyα emission within the 2σ isophote multiplied by a factor of two (empty red circles).

(i.e. non-pristine) around this QSO. The luminosity of this nebula ($L_{CIV} \simeq 10^{43} erg\ s^{-1}$) is comparable to those measured in high-redshift radio galaxies at similar redshift (Villar-Martín et al., 2007a). Compared with other CIV nebulae, the one revealed around J1538+08 shows a striking difference in term of asymmetry relative to the central QSO (e.g. Villar-Martín et al., 2007b; Silva et al., 2018). Interestingly the ratio between the SB radial profiles of the Lyα and CIV reported in Fig. 3.7 (i.e. in the southern wedge containing the SB Lyα peak and the CIV nebula) is a factor of ~10 and is constant up to ~ 25 kpc (i.e. the distance where the Poissonian noise starts to be dominant in the CIV nebula). This evidence and the spatial co-location of the SB peaks of the two nebulae suggest that they could be tracing the same gas and, hence, triggered by the same mechanism. Deeper observations would hopefully reveal CIV emission tracing the same structure we are seeing for the Lyα at larger scales.

3.5.2 Kinematics

From the velocity maps of the Lyα and CIV nebula (Figs. 3.9 and 3.10) no coherent kinematic structures possibly hinting at bulk motions and rotations are detected. Interestingly, a large fraction of the Lyα nebula exhibits negative velocities. Indeed the percentages of $SNR > 3$ pixels with negative velocity are 79^{+9}_{-10}% and > 87% adopting z_{Neb} and z_{QSO}, respectively[3]. A similar trend is shown also for the CIV velocity map (Fig. 3.10) which exhibits more than the 97% of pixels with SNR>3 and with negative velocities relative to the z_{QSO}. On the other hand, we did not measure a significant fraction of the CIV nebula pixels with negative velocities with respect to the z_{Neb}.

B16 and AB19 report the velocity of the flux-weighted centroid of the Lyα emission relative to the z_{QSO}. Our Lyα nebula has a centroid with a negative velocity of $v \approx -247 \pm 178$ $km\ s^{-1}$. Even considering the uncertainties of z_{QSO} the centroid shows negative velocity at 3σ. The great majority of the Lyα nebulae detected by MUSE shows positive values, i.e. 75% and 100% of the sample for AB19 and B16, respectively.

Notice, however, that the difference in velocity may be due to an inaccurate determination of the QSO systemic redshift. Indeed B16 and AB19 estimate the z_{QSO} from CIV emission lines with a luminosity dependent correction for the expected shift (Shen et al., 2016). This correction has an estimated uncertainty of 415 $km\ s^{-1}$. Accounting for uncertainties, the velocity distribution of AB19, which span a range of $v = [-2000, +5980]$ $km\ s^{-1}$ ($v_{median} = 782$ $km\ s^{-1}$), can be consistent at $\sim 2\sigma$ level with no bias. In case of B16 sample, the $v = [+959, +4011]$ $km\ s^{-1}$ ($v_{median} = 1821$ $km\ s^{-1}$) velocity range still remains heavily biased towards significantly positive values. The WISSH QSOs included in these samples do not exhibit a statistically significant preference towards positive or negative values of the velocity shifts. Specifically, while the Lyα nebulae around J0124+00, J1621−00 and J0947+14 show $v \sim 1000 - 4000$ $km\ s^{-1}$, the Lyα nebulae surrounding J0125−10 has a negative velocity ~ -2000 $km\ s^{-1}$.

Regarding the velocity dispersion, we measured from the dispersion map a spatially average value $\bar{\sigma_v} \approx 733 \pm 85$ $km\ s^{-1}$ (see Table 3.1). This is a factor of two larger than those measured around the QSOs of B16 and AB19 samples, which span the range $\sigma_v \approx [200, 400]$ $km\ s^{-1}$. Although few Lyα nebulae around radio-quiet QSOs exhibit $\bar{\sigma_v} \gtrsim 500$ $km\ s^{-1}$ (namely the WISSH QSO J0124+00 in the B16 sample and the J1605-01 by Ginolfi et al. 2018), such velocities are however still lower than the value reported for the Lyα nebula in J1538+08, which agrees with the reported $\sigma_v \gtrsim 600$ $km\ s^{-1}$ values for high-redshift radio galaxies (van Ojik et al., 1997; Villar-Martín et al., 2003; Humphrey et al., 2006; Silva et al., 2018). As for the CIV nebula we computed a maximum value of ~ 600 $km\ s^{-1}$

---

[3] *The velocity errors have been estimated by considering the spectral resolution and the uncertainties on the Lyα peak reported in Table3.1.*

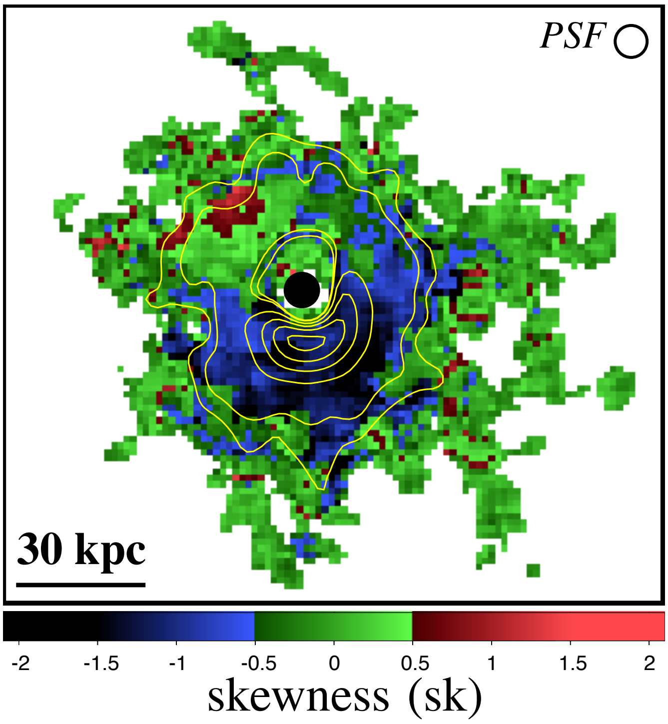

Figure 3.15: Skewness map of the line profile of the Lyα nebula. Contours reports SNR levels as described in Fig. 3.2.

in correspondence of its SB peak and an average value of $\bar{\sigma_v} \sim 355 \pm 137\ km\ s^{-1}$ (see Table 3.1).

Interestingly, the dispersion map of the Lyα nebula around J1538+08 reports several discrete and compact regions with very high $\sigma_v \approx 1000\ km\ s^{-1}$ at an average distance from J1538+08 of 20-30 kpc (see Fig. 3.12). These high σ_v regions could be due to turbulence generated by continuum or line-emitting active sources at z_{Neb}. We verified that no continuum source in the MUSE field of view is associated to high-σ_v values within the Lyα nebula. Furthermore, similarly to AB19, we then used `CubExtractor` to search for Lyα emitters by setting $SNR_{th} > 5$ and $N_{min}^{vox} = 50$. We did not detect any source within the nebular emission. We only found a source at z~ 3.560 at a projected distance from the QSO of $\sim 250\ kpc$ (RA= 15:38:28.7, Dec= +8:55:00.80) and flux of $\simeq 3.5 \times 10^{-16} erg\ s^{-1}\ cm^{-2}$.

3.5.3 Evidence of an outflow reaching the CGM

The profile of the Lyα emission extracted from the entire nebula and reported in Fig. 3.3 exhibits a blue tail which can be modelled by an additional component with negative velocity. With the aim of exploring the spatial distribution of this blue tail component, we mapped the asymmetry of the Lyα emission line profile by using the skewness estimator (sk). The skewness map is obtained as third moment of the flux distribution according to the following formula:

$$skewness = \frac{\sum_{i,j,k}^{3D-Mask} \mathrm{Residuals}^3_{\mathrm{i,j,k}} \times \mathrm{F_{i,j,k}}}{M_2^{3/2} \times \sum_{i,j,k}^{3D-Mask} F_{i,j,k}} \tag{3.1}$$

where $\sum_{i,j,k}^{3D-Mask}$ is the sum on each voxel defined in the 3D-Mask, $\mathrm{F_{i,j,k}}$ is the flux from the datacube with PSF and continuum subtracted and $\mathrm{M_2}$ is the second moment of the flux distribution, defined as:

$$\mathrm{M_2} = \frac{\sum_{\mathrm{i,j,k}}^{\mathrm{3D-Mask}} \mathrm{Residuals}^2_{\mathrm{i,j,k}} \times \mathrm{F_{i,j,k}}}{[\sum_{\mathrm{i,j,k}}^{\mathrm{3D-Mask}} \mathrm{F_{i,j,k}}]^2 - [\sum_{\mathrm{i,j,k}}^{\mathrm{3D-Mask}} \mathrm{F^2_{i,j,k}}]} \tag{3.2}$$

We found a banana shaped region with skewness values $sk < -0.5$ (blue regions in Fig.3.15) which overlaps the region of high SB and the spatial distribution of the discrete high-σ_v clumps reported in Fig. 3.12. We verified that other regions do not exhibit skewness at significant levels (i.e. mostly symmetric and low SNR line profiles). The Lyα spectrum extracted from spaxel with $sk < -0.5$ and $SNR \geq 3$ resulted to be clearly asymmetric (Fig. 3.16). We fitted it with two Gaussian components and an additional constant term to account for the background. The two Gaussian components exhibit different width, with the broad ($\sigma_v \sim 1170 \pm 260$ km s^{-1}) component blue-shifted by $v_{shift} = 1520 \pm 360$ km s^{-1} compared with the narrow one ($\sigma_v \sim 470 \pm 70$ km s^{-1}, see Table 3.2). Such a dispersion is typical of Lyα nebulae around high-z radio-quiet QSOs (e.g. B16, AB19). The centroid of the narrow component corresponds to a redshift of z~ 3.565 ± 0.001, which is consistent with z_{QSO}. The blue-shifted broad component provides a tantalizing evidence for the presence of outflowing gas reaching a projected distance of 20-30 kpc from the QSO, i.e. in the CGM surrounding J1538+08. In the framework of the shock+precursors model (see Sect.3.4.5), if we assume that the $v_{shift} \sim 1520$ km s^{-1} is the velocity of the shock, then the emitting gas is required to be at high densities ($n_H > 100$ cm^{-3}). Deeper observations and more refined shock models for the CGM emission are needed to confirm this first order estimate.

The overlap between the high negative skewness ($sk < -0.5$) region (where we detected the outflowing gas) and the regions where we reported high velocity dispersion ($\sigma_v \sim 1000$ km s^{-1}) in the Lyα nebula, suggests that the σ_v values could likely be affected by the presence of the outflow component. Notice that the inspection of the v and σ_v radial profiles reported in Fig. 3.11 shows a sudden increase of the velocity dispersion up to $\sigma_v \sim 900$ km s^{-1} at distance of ~ 20 kpc. This high-σ_v may be affected by the presence of the outflow component and

Table 3.2: Properties derived from the two-component Gaussian fit of the Lyα nebula spectrum extracted from the region with negative skewness values (see Sect. 3.5.3 and Fig. 3.15 for further details).

Components	narrow	broad
λ_{cen} [Å]	5546.3 ± 1.3	5518.3 ± 6.5
σ_v $[km\ s^{-1}]$	470 ± 70	1170 ± 260
Flux[a] [$\times 10^{-16}$ erg s^{-1} cm^{-2}]	7.4 ± 0.7	2.7 ± 0.9
v^b_{shift}	$(1520 \pm 360)\ km\ s^{-1}$	
v^c_{max}	(3860 ± 870) km s^{-1}	
χ^2/dof	402/366	

Notes: [a] Integrated fluxes of the narrow and broad Gaussian components. [b] Velocity offset between the positions of the broad and narrow components; [c] Maximum velocity of the blue-shifted, broad component defined as $v_{max} = v_{shift} + 2\sigma_v$, where σ_v is the dispersion derived for the broad component.

hence by an incorrect parametrisation of the line profile by a single Gaussian component.

We tried to test this hypothesis by recomputing the radial profile (reported in Fig. 3.11) of the v and σ_v of the Lyα profiles by using a two-component Gaussian modelling. Unfortunately, v and σ_v could not be constrained as the SNR of the broad Lyα line in each bin is too low. Deeper MUSE observations are needed to verify the presence of a broad and blue-shifted component over the entire Lyα nebula and assess if the CIV nebula also shares the same kinematics.

Given the resonant nature of the Lyα transition, complex radiative transfer models accounting for the velocity field, density structure of the nebula and the geometry of the radiation field are needed in order to properly interpret the properties derived by the Lyα line profile fitting (e.g. Cantalupo et al., 2005; Gronke & Dijkstra, 2016). It is worth noting that the presence of an expanding shell surrounding the QSO, assuming a spherical symmetry and isotropic geometry of the photo-ionising radiation field, may produce an asymmetric double peak profile in which the blue-ward component is strongly suppressed (Verhamme et al., 2006; Laursen et al., 2009; Steidel et al., 2010; Chung et al., 2019). This would provide support for the hypothesis of an outflowing nebula whose two components of the Lyα profile are associated with the same expanding gas. Notice that in this simple model (i.e. symmetric, homogeneous and isotropic gas distribution) the main peak component is always on the red side compared with the systemic redshift of the nebula. Assuming that $z_{QSO} \equiv z_{Neb}$, our Lyα nebula does not show such a similar red line component (see Fig.3.16). To test the nature of this pu-

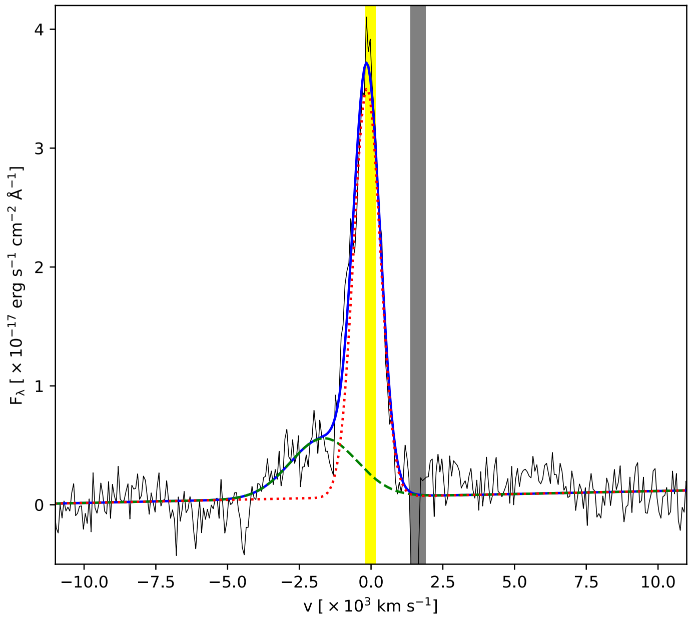

Figure 3.16: Lyα spectrum extracted from the nebula region with $sk < -0.5$ and $SNR > 3$ and modelled (blue solid line) by two Gaussian components (red dotted and green dashed lines). Interestingly, the broad ($\sim 1170\ km\ s^{-1}$) wing is blue-shifted of $\sim 1520\ km\ s^{-1}$ from the narrow component. The grey area is not considered in the modelling as it includes a region contaminated by a sky feature. The yellow region reports the $\pm 1\sigma$ uncertainty on the z_{QSO}.

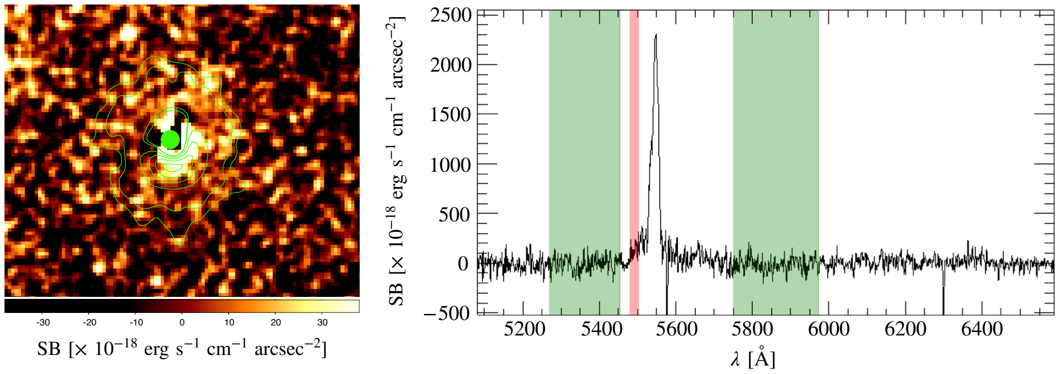

Figure 3.17: Pseudo-NB image of the blue tail emission (left panel) and spectrum extracted from the PSF- and continuum- subtracted data-cube, by selecting the only spaxel belonging to the nebula with SNR>5 (right panel). The pseudo-NB is obtained by collapsing the spectral region of the blue tail (red area in right panel) and by subtracting the continuum estimated in spectral regions without line features (green areas in right panel).

tative outflow in the context of an asymmetric, inhomogeneous gas distribution, MUSE observations with higher SNR are needed along with an alternative determination of z_{QSO} (i.e. from the CO line) and more accurate radiative transfer models.

Fig. 3.17 (left) reports the pseudo NB image computed on the red region (see right panel) in the Lyα blue tail. It shows an asymmetric shape with respect to the QSO position and it is spatially associated with the peak of the SB observed in the Lyα nebula. The asymmetric shape rules out that the blue tail emission is due to a residual QSO Lyα emission after the PSF subtraction. Indeed, the latter would exhibits a symmetric shape around the QSO position. Furthermore, we found that the typical PSF subtraction residuals are three times weaker than the blue tail emission.

4. AGN ACTIVITY IN HIGH-Z GALAXY CLUSTER CORES

This chapter aims to outline the main properties of galaxy clusters and the contribution of AGN activity to the evolution of the most massive galaxies in high-z galaxy cluster cores. The latter are the densest environments in the Universe, where the combination of hot gas and high-density of galaxies boost merger activity which, in turn, affects and accelerates the evolution of galaxies.

4.1 Local galaxy clusters: general properties

Galaxy clusters are the largest bound dark matter (DM) structures of the Universe, in which complex baryonic processes occur (see Kravtsov & Borgani 2012 for a review). The standard ΛCDM cosmological model predicts a hierarchical scenario (Bond et al., 1991) for the formation and evolution of large-scale structures in an expanding Universe. In this scenario, large galaxy clusters are formed by mergers of smaller collapsed structures, i.e. galaxies or groups of galaxies. This prediction is partially confirmed by observational evidences of substructures that experience highly energetic ($E_{kin} \sim 10^{64} erg$) merger events (e.g., Sarazin 2001; Russell et al. 2010).

Galaxy clusters mainly consist of DM (80% of the total mass; Blumenthal et al., 1984) and with a significant percentage of baryonic matter under the form of galaxies (~5%) and diffuse gas (~15%), (White & Fabian, 1995; Spergel et al., 2003).

- **Dark matter**. Zwicky (1933) firstly predicted the presence of DM in galaxy clusters. By analysing 800 galaxies belonging to the Coma galaxy cluster, noted a large scatter of their velocities (~2000 $km\ s^{-1}$). He computed the Coma mass through the virial theorem, i.e. under the assumption that a relaxed system reaches the equipartition between its kinetic and potential energy, discovering that this mass was larger than the total mass computed through the luminosity of the 800 cluster galaxies. The mass excess confirmed the presence of additional not visible matter in galaxy clusters, i.e. DM. Many works attempted to reproduce the profile distribution of the DM halo in galaxy clusters (Dubinski & Carlberg, 1991; Navarro et al., 1995).

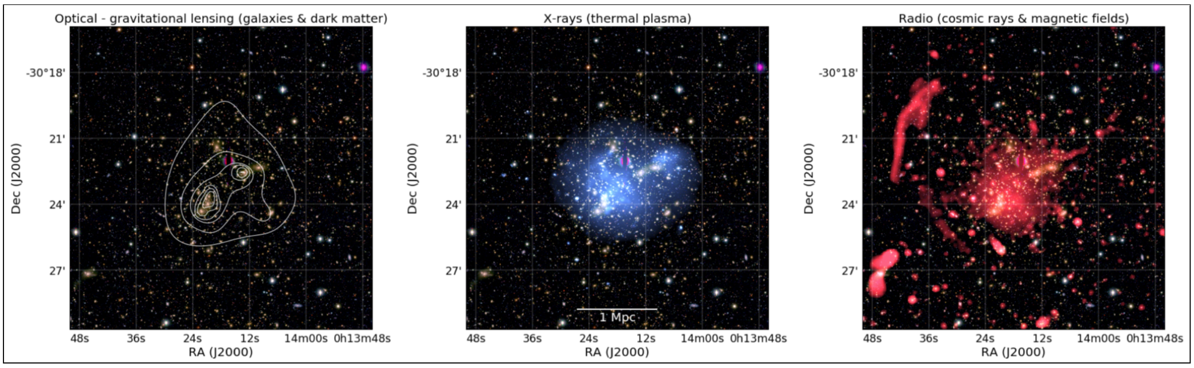

Figure 4.1: Galaxy cluster Abell 2744 (van Weeren et al., 2019). *Left panel*: optical emission (Medezinski et al., 2016) with white contours indicating the mass surface density derived from a weak lensing analysis (Lotz et al., 2017). *Middle panel*: blue color shows the thermal X-ray emission due to the ICM. *Right panel*: VLA-detected radio emission at 1-4 GHz in red.

Currently, the most used form to describe the DM density distribution is the NFW profile (Navarro et al., 1995), which is the following:

$$\rho_{NFW}(r) = \frac{4\rho_s}{\frac{r}{r_s}(1+\frac{r}{r_s})^2} \tag{4.1}$$

where r_s is the scale radius and ρ_s is the DM density within the scale radius.

- **Intra-Cluster Medium**. A diffuse (density $n \sim 10^{-2} - 10^{-4} cm^{-3}$) baryonic component, i.e. the Intra Cluster Medium (ICM), resides inside galaxy clusters. The ICM is hot ($T \sim 10^7 - 10^8$K) and was discovered for the first time in the Coma cluster by Cavaliere et al. (1971) through its X-ray emission due to the thermal Bremsstrahlung mechanism. This gas was heated to the virial temperature by strong accretion shocks and adiabatic compression during the collapse phase of the gas (Gott & Gunn, 1971; Kaiser, 1986), or by the merger activity between galaxy groups (Tucker et al., 1998). Because most of the galaxy clusters at z< 1 appear to be virialized and relaxed, it is possible to study this gas assuming a hydrostatic equilibrium configuration.
- **Galaxies**. Galaxies are the smallest gravitational-bound structures, in a cluster. Clusters can be classified according to the number of hosted galaxies: from groups that host ~10 galaxies to rich clusters containing ~100-1000 galaxies. Furthermore, groups have size of ~1-2 Mpc and mass $\sim 10^{13} M_\odot$, while rich clusters exhibit a size of 5-7 Mpc and a mass of $\sim 10^{15} M_\odot$.

Galaxy clusters are selected and studied via multi-wavelength observations, from radio to X-ray energies. As example, Fig. 4.1 shows three images at different wavelength (i.e. Optical, X-ray and radio) of the galaxy cluster Abell 2744

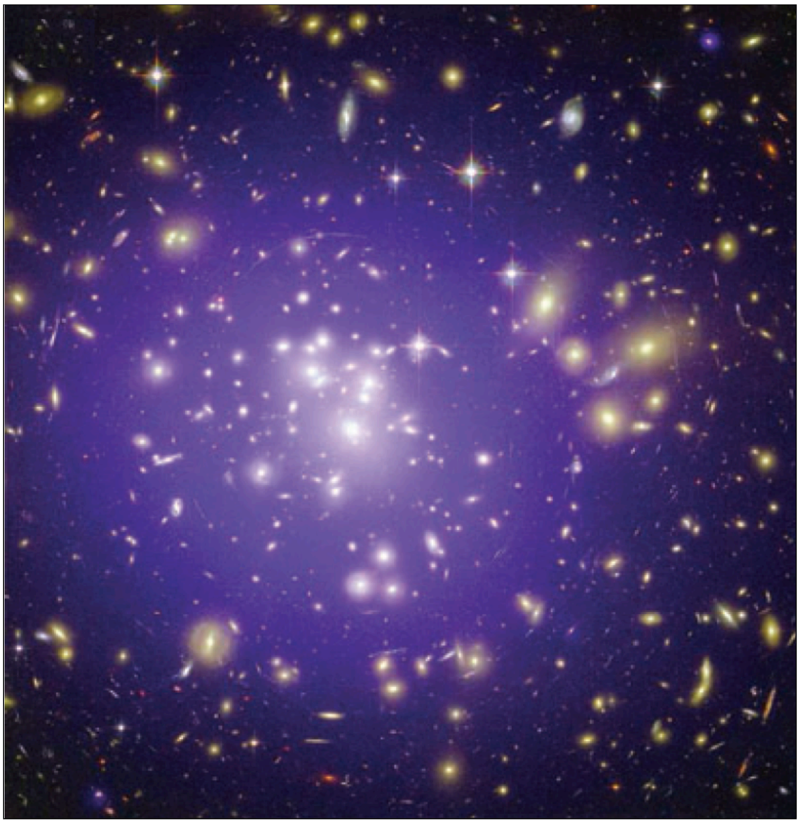

Figure 4.2: Combined optical + X-ray image of the z≈0.2 galaxy cluster Abell 1689. Yellow/black colors report the HST image, while the purple colors indicate the Chandra X-ray emission. The gravitational effects of the DM is clearly visible under the form of gravitational lensing, which produce light arcs in the HST image. Credit: NASA, ESA, E. Jullo (JPL/LAM), P. Natarajan (Yale) and J-P. Kneib (LAM).

(Pearce et al., 2017; van Weeren et al., 2019), in which each emission band indicates a different galaxy cluster component. Specifically, X-ray emission traces diffuse thermal plasma, while galaxies are clearly visible only in the optical band. Finally, radio emission is due to a relativistic electrons population in the intra-cluster magnetic field, which can be attributed both to single radio galaxies and relic sources.

An other example of local galaxy cluster is reported in Fig. 4.2, which shows a composite image of Chandra X-ray and Optical HST observations of the $z = 0.18$ galaxy cluster Abell 1689. This figure shows the three typical components of the galaxy clusters: the Intra-cluster Light (ICL), the ICM (purple colors) and the light arcs due to the lensing gravitational effects of the DM halo.

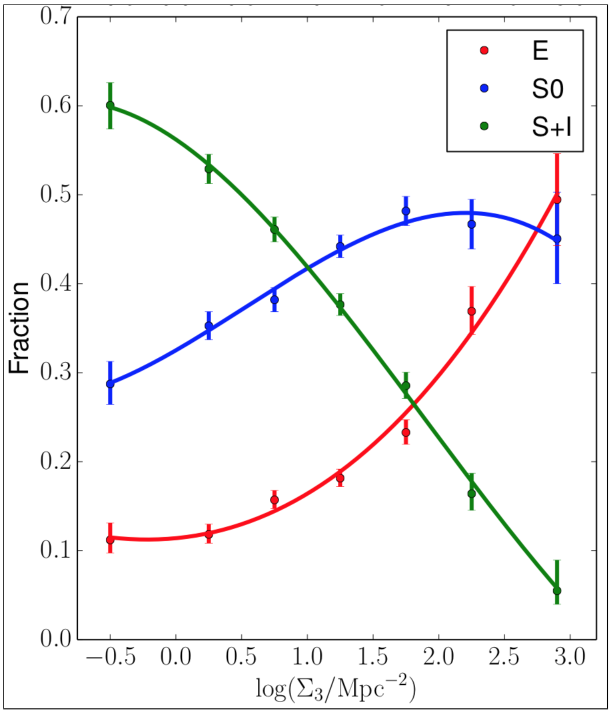

Figure 4.3: Average projected density versus the fraction of early-type (Elliptical; red), late-type (Spiral + Irregular; green) and lenticular (S0; blue) galaxies (Houghton, 2015).

4.1.1 *The galaxy population in clusters*

Properties of galaxies in clusters are strongly affected by their environment, since their evolution takes place preferentially in dense regions (Blanton & Moustakas, 2009). Observations show that the central regions of local galaxy clusters are characterised by a high percentage of massive galaxies exhibiting red and passive stellar populations (i.e. early-type). On the other hand, galaxy cluster outskirts host spiral and star-forming galaxies (i.e. late-type; Bower et al., 1992; Kauffmann et al., 2004). These observations suggest a correlation between SFR and galaxy density in local clusters. Dressler (1980) was the first to claim a relation between density and morphology (or type-density) for galaxies in clusters. Fig. 4.3 reports the fraction of lenticular (S0), elliptical (Es) and late-type galaxies (LTGs) as a function of the average projected density of the clusters and shows a fraction of E and S0 galaxies higher in cluster denser regions than the lower density ones, which are dominated by late-type galaxies (Houghton, 2015). This type-density relation also appears in other forms, such as a color-density (Blanton et al., 2005) and SFR-density relation (Balogh et al., 1998).

The galaxy Red Sequence: Massive early-type galaxies are found preferentially in the dense environments of local galaxy clusters. Interestingly, these galax-

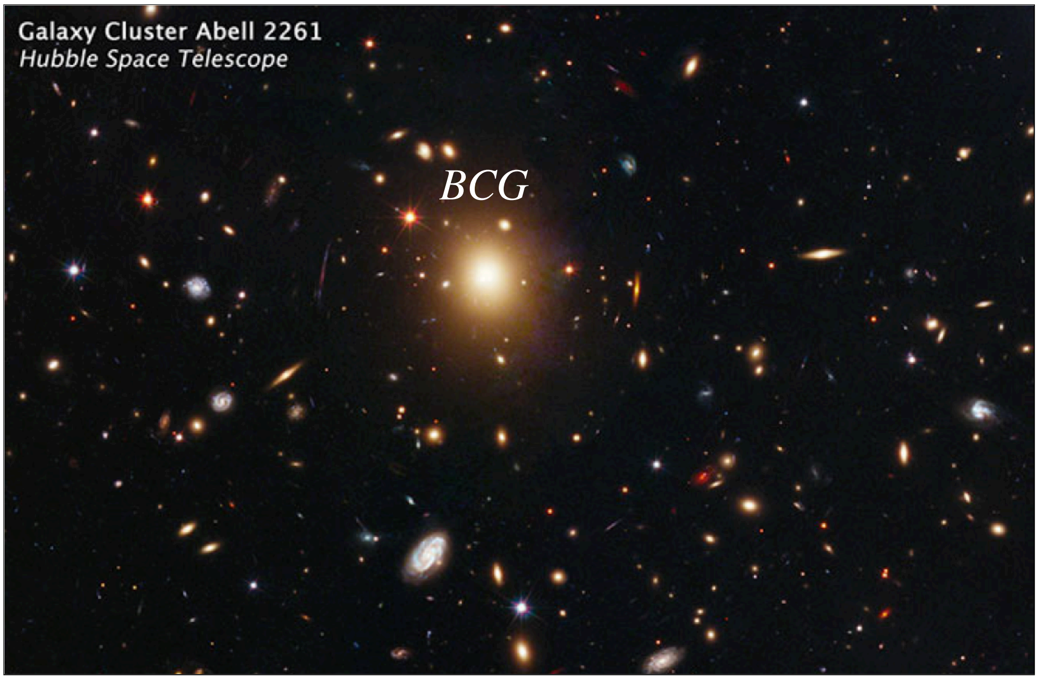

Figure 4.4: HST image of the galaxy cluster Abell 2261. The brightest point source represents the Brightest Cluster Galaxy Image credit: NASA; ESA; M. Postman, STScI; T. Lauer, NOAO, Tucson; CLASH team.

ies have been found to form a tight sequence in the color-magnitude diagram (CMD), the so-called red sequence (RS; see Fig. 1.11b). Bower et al. (1992) reported for the first time the existence of such a positive correlation between galaxy color and luminosity, according to which the brightest galaxies in clusters are the reddest ones. Indeed, brighter galaxies are redder because of their higher metallicity, since more massive galaxies are able to retain more metals, which would otherwise be ejected by stellar winds or tidal forces (Kodama & Arimoto, 1997). Such an explanation was not straightforward because of the age-metallicity degeneracy (Worthey, 1994). Indeed, galaxies could become redder as a consequence of metallicity or age. However, Kodama & Arimoto (1997) by studying the evolution of the RS, showed that the RS slope does not depend on the age of the stellar population, which is on the contrary linked to the RS scatter (Kodama et al., 1998).

The Brightest Cluster Galaxy (BCG): Local galaxy clusters are also characterised by a massive ($M_\star \sim 10^{12} M_\odot$), luminous ($M_v \approx -23$) and giant elliptical galaxy at their centers, i.e. BCG. Fig. 4.4 shows an example of a local BCG in Abell 2261. BCGs exhibit a luminosity ~10 times higher than the normal elliptical galaxies and appear like red, quiescent (up to 100 kpc; Bernardi et al., 2007) elliptical galaxies (Dubinski, 1998). Most of them are classified as cluster Dominant (cD) galaxies, being associated to a large distribution of stars extending beyond the cluster core. Moreover, BCGs show very high velocity dispersions, up to ~400 $km\ s^{-1}$(Newman et al., 2013). BCGs are usually located at the minimum of the cluster potential well, close (~10 kpc) to the peak of the X-ray emission (Lauer et al., 2014). The BCG luminosity seems to be correlated with the cluster X-ray luminosity (Postman & Lauer, 1995), as well as with the mass of the galaxy cluster (Ascaso et al., 2011). Finally, BCGs often show radio nuclear activity and radio jets, which are able to affect the ICM (e.g. Merloni & Heinz, 2007).

4.2 High-z galaxy clusters

In the hierarchical formation scenario of large scale structures, high-z galaxy clusters are expected to be unrelaxed and formed by sub-groups of similar masses. Also numerical simulations (e.g. Cohn & White, 2005) predict higher cluster merger rates as the redshift increases. High-z galaxy clusters are fundamental to explore the early assembly phase of the most massive DM halos and their evolution through the change of their properties, e.g. X-ray emitting hot ICM, galaxy population (Fassbender et al., 2011c).

However, the selection of high-z galaxy cluster progenitors is challenging because some of the features observable at low-z, are not present in the high-z. The first X-ray surveys (e.g. Piccinotti et al., 1982; Abell et al., 1989; Truemper, 1992) were able to collect galaxy clusters up to z$\simeq$ 0.5. Galaxy clusters at z> 1 were largely unexplored due to the flux limits of the surveys. The most recent deep X-ray surveys were able to detect galaxy clusters up to z~ 1.5 (Rosati et al., 2004; Stanford et al., 2006). The epoch beyond z= 1.5 was known as the "redshift desert". Indeed, at z>1.5, it was difficult to detect clusters for many reasons. Firstly, the spectroscopic confirmation of these systems based on the break at 4000Å in the galaxy spectra was challenging since at these redshifts such break is shifted beyond 10000Å, in which sky features heavily contaminate the spectra (Csabai et al., 2003; Webb et al., 2015). Secondly, the X-ray selection works for relaxed systems in which the ICM has had time to relax and virialize, while high-z clusters typically are unrelaxed. Therefore, only very massive galaxy clusters can be easily detected at high-z, due to the relation between X-ray luminosity and ICM mass (Arnaud et al., 2005). We know few exception of very luminous galaxy clusters at z>1.5. For example, in the XMM-Newton Distant Cluster Project (XDCP), Fassbender et al. (2011a) discovered 47 spectroscopically confirmed galaxy clusters at 0.8<z<1.6. Moreover, a relevant number of individual massive galaxy clusters at z> 1.5 have been detected in the last years: ClG 0218.3-0510 at z$\simeq$ 1.62 (Papovich et al., 2010), XMMU J105324.7+572348 at z$\simeq$ 1.75 (Henry et al., 2010), CL J1449-0856 z$\simeq$ 2.01 (Gobat et al., 2011), XMMU J1007.4+1237 at z$\simeq$ 1.56 (Fassbender et al., 2011c), XDCP J0044.0-

2033 at z$\simeq$ 1.58 (Fassbender et al., 2014).

In addition to the X-ray surveys, the last optical and IR facilities enables the discovery of candidate galaxy clusters also by selecting over-density of red galaxies, whose emission peaks at $\sim 2\mu m$ (e.g. Papovich et al. 2008). Therefore, larger samples of candidated high-z galaxy clusters have begun to be identified from deep multi-band photometric surveys with different strategies. For example, (i) Castellano et al. (2007) and Papovich et al. (2010), identified and confirmed massive galaxy clusters beyond z$\sim$ 1.5 through photometric and spectroscopic optical and near-IR data, (ii) Andreon et al. (2009) detected a z$\sim$ 1.9 galaxy cluster by successfully using the red sequence technique, (iii) Goto et al. (2008) detected 16 galaxy clusters at redshifts 0.9<z<1.7 by using the deep near-IR ($2 - 24\mu m$) imaging with the AKARI satellite and (iv) Chiaberge et al. (2010) revealed 3 candidated galaxy clusters at redshifts 1.7<z<2 in the COSMOS field by exploiting the detection of FRI sources and photometric and spectroscopic optical data.

Finally, other methods to reveal high-z clusters are the use HzRGs as signposts for proto-clusters and the detection of an abundance of Lyα emitters, which indicates the presence of a dense environment probable site of a galaxy cluster at z> 2 (Venemans et al., 2007; Cucciati et al., 2014).

4.2.1 The galaxy population of high-z clusters

Galaxy populations of high-z clusters show different properties compared to those in local clusters. First of all, no single BCG is found in the core of high-z galaxy clusters, which on the contrary host multiple normal galaxies exhibiting disturbed morphologies (Zhao et al., 2017). This is also valid for the whole galaxy population in clusters. Indeed, while local clusters hosts mainly early-type galaxies in the core, leading to a SF-density (SFD) relation and a RS in the CMD, as seen in Sect. 4.1.1, high-z galaxy clusters have been found to host more star-forming galaxies with blue colors. This enhancement of blue galaxies in cluster cores as the redshift increases is known as the Butcher - Oemler effect (Butcher & Oemler, 1978). Specifically, a rapid increase in the SF activity is observed in cluster core galaxies at z$\sim$1.5 (Fassbender et al., 2011c; Santos et al., 2015). Indeed, some works on individual galaxy clusters at z>1.4 found strong ongoing SF activity in cluster cores, and no tight RS in the CMD (e.g. Hilton et al., 2010; Gobat, 2010). However, such growing SF activity in cluster cores at z$\sim$ 1.5 could be related to the $z = 1 - 2$ peak of the global SFR history (Madau et al., 1996), rather than a different evolution of galaxies in high-z cluster cores. Some studies (e.g. Popesso et al., 2012; Alberts et al., 2014) analysed the SF history in both clusters and field finding that the evolution of the SF for cluster core galaxies is much faster ($\sim (1 + z)^{6-7}$ Shimakawa et al., 2014; Ma et al., 2015) than the evolution of the SF in the field galaxies ($\sim (1 + z)^4$ Ilbert et al., 2015).

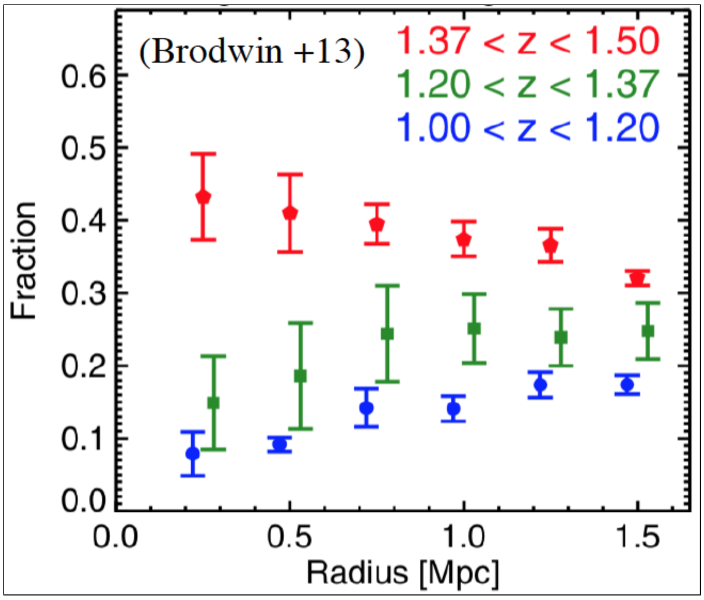

Figure 4.5: Fraction of cluster star-forming galaxies, with $L_{IR} > 10^{11.5} L_{\odot}$, with respect to the distance from the galaxy cluster center and for three redshifts bins: 1<z<1.2 (blue), 1.2<z<1.37 (green) and 1.37<z<1.5 (red) (Brodwin et al., 2013).

This finding confirms the excess of SF activity in high-z cluster cores compared to the field, highlighting the peculiarity of galaxy evolution in these high-density regions of the Universe in which one or more mechanisms are able to efficiently trigger and quickly quench SF.

Elbaz et al. (2007) investigated the SFD relation at higher redshift in clusters and field and discovered a reversal SFD relation at z>1, while Hilton et al. (2010) revealed a reversal SFD relation in galaxy clusters at z~1.5. Unfortunately, the epoch of this transition is still debated and several works found different results, probably depending on differences in the SFR measurement, AGN contamination and quality of the data (e.g. Muzzin et al., 2012; Darvish et al., 2016). However, the transition epoch is considered to be approximately z~ 1.4 – 1.5 (Fassbender et al., 2011c; Brodwin et al., 2013). Brodwin et al. (2013) analysed 16 IR-selected, spectroscopically confirmed galaxy clusters at 1<z<1.5 and found a reversal SFD relation occurring in clusters at z~ 1.4, as shown in Fig. 4.5. The latter shows that the fraction of star-forming galaxies in the cluster cores is higher than in the outskirt regions. This is consistent with the observed fraction of post-starburst galaxies in galaxy clusters at z~ 1, which increases towards the cores (Muzzin et al., 2012). In this scenario, the interval time between z~ 1.5 and z~ 1 is sufficient to allow a transition from star-forming galaxy to post-starburst galaxy.

4.3 AGN activity in galaxy clusters

Several studies have investigated AGN activity as a function of the environment, e.g. by studying the fraction of AGN in clusters compared to the field. Gisler (1978) and Dressler et al. (1985) found that, at low redshift, galaxy clusters host a lower fraction of AGN with respect to the field. Specifically, AGN hosted in early-type galaxies follows such a trend, while the fraction of AGN in late-type galaxies appears to be homogeneous in cluster and field (Hwang et al., 2012). On the other hand, several authors (Galametz et al., 2009; Martini et al., 2013; Alberts et al., 2016) show that the number of AGN in galaxy clusters increases as the redshift increases. Interestingly, Martini et al. (2013) measured the AGN fraction in a sample of 13 massive ($> 10^{14} M_{\odot}$) galaxy clusters at 1<z<1.5 from the Spitzer/IRAC Shallow and Distant Cluster Surveys (ISCS) and found that this fraction increases by two orders of magnitude from z=0 to z~1.5. Moreover, this increase of AGN is higher in clusters than in the field. The rapid growth of the X-ray and IR selected AGN fraction within high-z galaxy clusters, up to z~2, is reported in many other works (Fassbender et al., 2012; Bufanda et al., 2017). As an example, Fig. 4.6 shows the evolution of the X-ray AGN fraction in the field (open symbols), clusters (solid symbols), and proto-clusters (green hexagons), for AGN with hard X-ray luminosity $L_{X,H} \geq 10^{43}\ erg\ s^{-1}$ (red circles) and $L_{X,H} \geq 10^{44}\ erg\ s^{-1}$ (blue circles) (Martini et al., 2013). Fig. 4.6 demonstrates that, at z<1.25, the fraction of low-luminosity AGN in the field is 6 times higher than in clusters, while the fraction of high luminosity AGN in the field is consistent within 3σ to the cluster one and the fraction of AGN in proto-clusters at z>1.25 exceeds the field one.

Moreover, the fraction of AGN seems to depend also on galaxy cluster morphology and velocity dispersion. Indeed, Martini et al. (2007) found an excess of AGN in local galaxy clusters exhibiting lower velocity dispersion and a larger number of substructures. Finally, the AGN fraction has been also studied as a function of the distance from the X-ray centroid of galaxy clusters. Ruderman & Ebeling (2005) and Fassbender et al. (2012) indeed found an excess of X-ray sources (i.e. AGN) between ~2 and 3 Mpc from the cluster core at z≃0.3-0.7 and z≃0.9-1.6, respectively.

4.4 Evolution of the galaxy population in clusters

The observed change in the SF-density relation at high-z (z~1.4) compared to low-z highlights two trends in the evolution of galaxies in clusters (see Fig. 4.5 in Sect. 4.2.1):

- (a) an increase in the SF activity in the whole galaxy population as redshift increases;

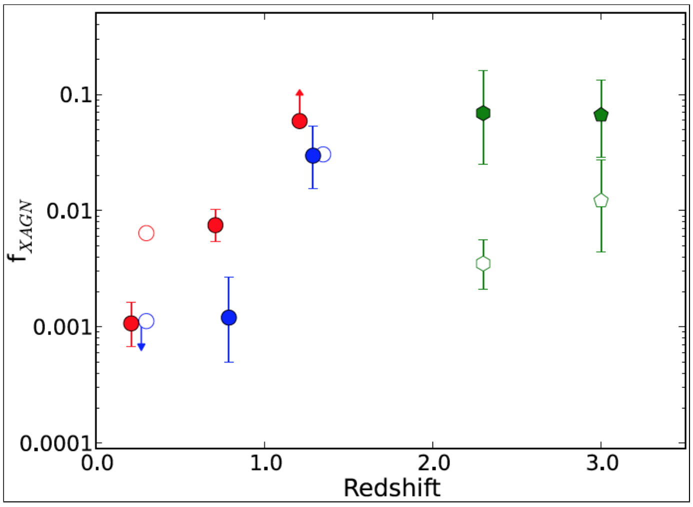

Figure 4.6: X-ray AGN fraction observed in galaxy clusters (solid circles), proto-clusters (green hexagons) and in the field (open symbols), as a function of the redshift from 0.3 to 3 (Martini et al., 2013). The X-ray AGN with hard X-ray luminosity $L_{X,H} \geq 10^{43}$ $erg\ s^{-1}$ (red circles) and $L_{X,H} \geq 10^{44}$ $erg\ s^{-1}$ (blue circles) are from Haggard et al. (2010), while the two proto-clusters and neighbouring fractions at z~2.3 and 3.09 are from Digby-North et al. (2010) and Lehmer et al. (2009), respectively. The error bars correspond to 3σ Gaussian errors.

- (b) a quick drop of the SF in the central region compared to what happens at larger distance in local clusters.

These trends suggest that the cluster galaxy populations undergo one or more processes able of affect the SF activity in a relatively short time. The most popular scenarios predict that the origin of the reversal SFD relation can be solved considering (a) the high rate of merger activity expected in these dense environments (Sect. 4.4.1) and (b) some processes, such as AGN feedback, ram-pressure stripping and/or strangulation, which allow SF to be prevented or abruptly stopped in the center of massive galaxies (Sect. 4.4.2).

4.4.1 Mergers as star formation and AGN triggers

According to most theoretical models, galaxy mergers can induce SF activity. suggesting that the evolution of the merger rate is linked to the evolution of the SF (e.g. Hopkins et al., 2010). Indeed, semi-analytical models, hydrodynamical and N-body simulations (e.g. Hopkins et al., 2010; Rodriguez-Gomez et al., 2015) predict an enhancement of merger activity in galaxy clusters as the redshift increases. This is confirmed by several studies which found pieces of evidences of a larger merger rate in high-z galaxy clusters than in low-z systems and field ones. For example, Mei et al. (2015) and Santos et al. (2015) found that a significant fraction of star-forming galaxies and early-type galaxies in galaxy clusters at z>1.5 with disturbed morphologies. Moreover, statistical evidence of merger activity has been provided by Fassbender et al. (2011b) and Mancone et al. (2012), who found that the luminosity function of high-z galaxy clusters shows a deficiency of massive members at z≥1.4 and interpreted such deficiency as a proof that massive galaxies form mainly through mergers. However, other papers do not confirm such trends. For example, Delahaye et al. (2017) studied four massive ($\sim 10^{14} M_{\odot}$) galaxy clusters at 1.59<z<1.71 and found that the fraction of mergers in the central region of the cluster is comparable to the field one. Nonetheless, this discrepancy could be attributed to the different methods used for identifying galaxy mergers or, as suggested by Brodwin et al. (2013), to the galaxy cluster properties (e.g. halo mass), which may also play a role in the number of mergers seen at a given redshift, i.e. more massive clusters are expected to assemble mass at later epochs. Recently, Watson et al. (2019) combining a variety of selection methods to identify galaxy clusters and galaxy - galaxy interaction have confirmed that the merger fraction in these clusters is enhanced compared to the field.

According to semi-analytic models, the number of interactions that a galaxy experiences within a cluster can be written as follows (Mihos, 2004):

$$N \approx 4\left(\frac{n}{250\ Mpc^{-3}}\right)\left(\frac{r_p}{20\ kpc}\right)^2\left(\frac{\sigma_v}{1000\ km\ s^{-1}}\right)\left(\frac{t}{10\ Myr}\right) \tag{4.2}$$

where n is the number density of galaxies, t is the age of the cluster, r_p is the maximum distance between two galaxies for merger to occur and σ_v is the galaxy cluster velocity dispersion. However, analytic arguments suggest that the dynamical friction scales as v^{-2}, where v represents the relative velocities of the galaxies (Binney & Tremaine, 1987). Therefore, merger events are favoured in overdense regions, where galaxies have moderate relative velocities. Indeed, in case of very low relative velocities ($v_{rel} < 500\ km\ s^{-1}$) the encounters between galaxies would take place at a longer time than the Hubble time. On the other hand, high relative velocities between two nearby galaxies would reduce the interaction time, decreasing the probability to have a merger. Indeed, in the local Universe, even if clusters are populated by a large number of galaxies (Zwicky, 1957), their internal velocity dispersions can reach values of the order of ~1000 $km\ s^{-1}$, so that the galaxy interactions are rare (Aarseth & Fall, 1980; Cordero et al., 2016).

These results seem to match the scenario in which mergers also drive AGN activity. Indeed the AGN fraction reaches a peak at distances from the center of the cluster where the combination of both low velocity dispersion and high-density of galaxies may favour merger events and a AGN activity (Fassbender et al., 2012; Ruderman & Ebeling, 2005) . Moreover, the evolution of the AGN activity shows a similar trend compared to the fraction of star-forming galaxies in

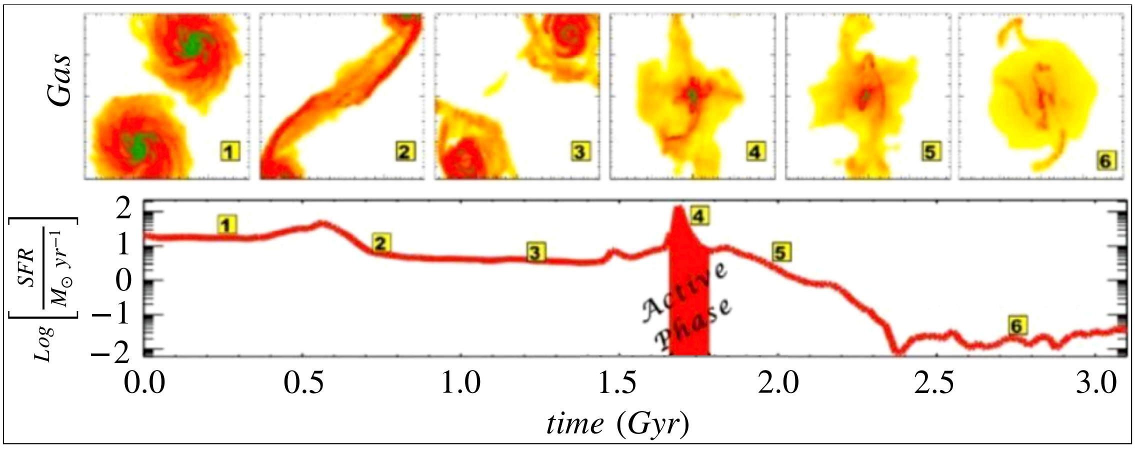

Figure 4.7: Projected gas density of two disc-galaxies during a major merger in the hydrodynamic GADGET simulation performed by Cox et al. (2006). The plot below shows the evolution of the SFR in the merger system at different stages. The red area indicates the merger-phase in which an AGN activity is triggered.

clusters. The latter indeed follows an evolution proportional to $(1+z)^{5.7}$ (Haines et al., 2009) while the AGN fraction in galaxy clusters increases as $(1+z)^{5.3}$ up to z~1.3 (Martini et al., 2009). Finally, Alberts et al. (2016) suggested a co-evolution between SF, AGN and merger activity, by studying the SF and AGN activity in 11 galaxy clusters with masses higher than $10^{14}M_\odot$ and 1<z<1.75. These evidences are in agreement with semi-analytic models and simulations, which predict a scenario in which galaxy major mergers induce starbursts and also fuel BH accretion, triggering an AGN phase (e.g. Hopkins et al., 2006).

Cox et al. (2006) performed hydrodynamic simulations of disc-galaxy "wet" major mergers, including the feedback activity, in order to investigate the SFH as a function of time. Fig. 4.7 reports different steps of the merger activity as a function of the SF occurring in galaxies. This simulation shows how the interaction between galaxies triggers SF (e.g., phases 2 and 4 in Fig. 4.7). Moreover, in the intermediate phase (4) of the interaction, in which a final galaxy begins to shape, the gas is destabilised and triggers also BH accretion.

Observations reveal that the AGN is heavily obscured by dust and gas (Ricci et al., 2017). This obscuration peaks in the late stage of the merger, when the galaxies are very close. In particular, Koss et al. (2018), by analysing a catalogue of 1711 active and inactive galaxies at z<0.075, found that luminous obscured AGN have an excess of merger activity if compared to unobscured or low luminosity AGN and inactive galaxy samples (Fig. 4.8). This excess seems to be larger in a late-stage mergers, i.e. when the two galaxies nuclei are separated by a distance of <3 kpc.

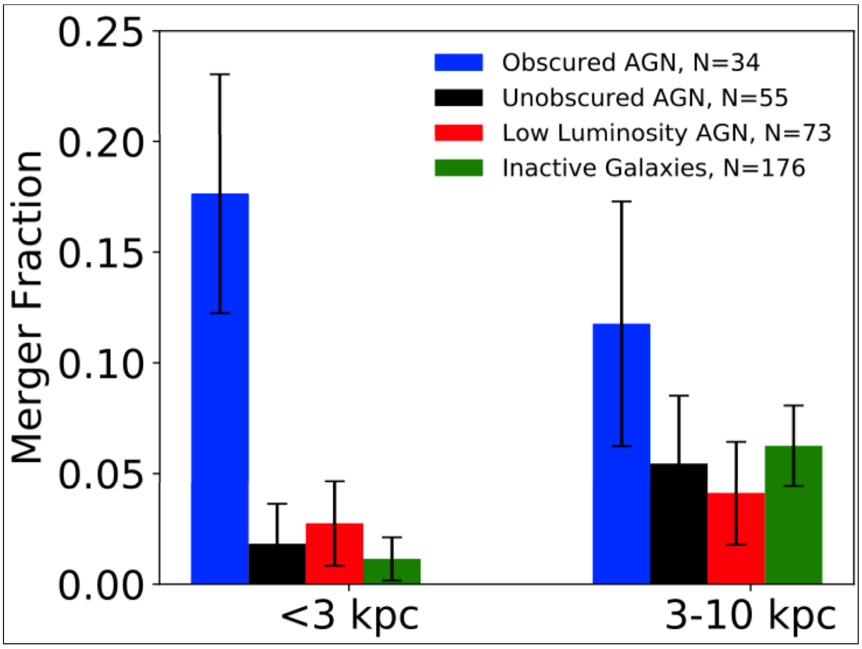

Figure 4.8: Fraction of mergers in early (3-10 kpc) and late (<3 kpc) -phase, which are observed for different type of objects, i.e. obscured, un-obscured and low luminosity AGN and inactive galaxies (Koss et al., 2018). Error bars correspond to a confidence level of 1σ.

4.4.2 *Star formation quenching in central massive galaxies*

Brodwin et al. (2013) report a decreasing of the fraction of massive star-forming galaxies in the center of galaxy clusters as the redshift falls at z< 1.4 (Fig. 4.5). This implies a very quick quenching of the SF activity in massive galaxies residing in high-density regions.

Several processes can be invoked as responsible to quench SF in these galaxies at different timescales and physical lengths:

- **the ram-pressure stripping** (Gunn & Gott, 1972; Kenney et al., 2004), in which the hot ICM gas induces an external force on the ISM gas of a galaxy. This external pressure depends on both the density of the ICM and the relative velocity between the galaxy and ICM (Vollmer et al., 2001). Specifically, the gas is ripped off from the galaxy if the ram-pressure is larger than the gravitational pressure holding back the gas bound to the disk, i.e.:

$$\rho_{IGM} v_{gal}^2 > 2\pi G \Sigma_{gas} \Sigma_{star} \tag{4.3}$$

where, ρ_{IGM} is the IGM density, v_{gal} is the velocity of the galaxy and Σ is the surface density of stars and gas (Boselli & Gavazzi, 2006);

- **strangulation**: a slow SF quenching process in which the supply of cold gas onto the galaxies is halted. In this case, the galaxy can continue to form stars using only the available gas (Peng et al., 2015);

- **tidal interactions** which can affect gas, dust and stars of the interacting galaxies. These tidal forces act as $1/r^3$, therefore, if the two galaxies are separated by a distance r which is not too wide compared to their radius, the interaction can efficiently remove gas from the galaxy halos (Mihos, 2004; Conselice, 2006; Boselli & Gavazzi, 2006);
- **supernovae or AGN driven outflows** which can remove a large amount of gas available to form stars (see Bischetti et al., 2019a, Sect. 1.4). In particular, AGN feedback is predicted by some semi-analytic models and simulations (Springel et al., 2005; Di Matteo et al., 2005; Hopkins et al., 2006, 2008; Narayanan et al., 2010) as the most efficient mechanism to quench SF in massive galaxies.

4.4.3 BCG formation

Dubinski (1998) proposed three models in order to explain the BCG formation, i.e.:

- star formation from cooling flows (e.g. Fabian, 1994);
- accretion and/or cannibalism due to dynamical friction and tidal stripping processes (e.g. Ostriker & Hausman, 1977);
- hierarchical formation during the galaxy cluster evolution (Merritt, 1985).

In the cooling flow model, ICM gas gradually condenses, starts to lose energy through thermal bremsstrahlung emission in the high-density cluster core and contracts under the halo gravitational effects, forming a large number of new stars and, therefore the BCG. Therefore, the evolution of BCGs follows that of their host clusters. Several authors (McNamara et al., 1996; Salomé & Combes, 2003) found molecular gas and excesses of UV light in central galaxies in local cluster cores, suggesting the presence of SF activity spatially correlated with the BCGs. However, the presence of a new stellar population and the color gradients of the BCG halos expected in the cooling flow scenario are not observed. Moreover, the X-ray gas is not able to cool enough to form the BCG (Jordán et al., 2004).

Another possible scenario is the accretion and/or cannibalism which predicts that a first galaxy reaches the cluster center and starts to grow in luminosity and mass, cannibalising other galaxies which are attracted to the cluster core.

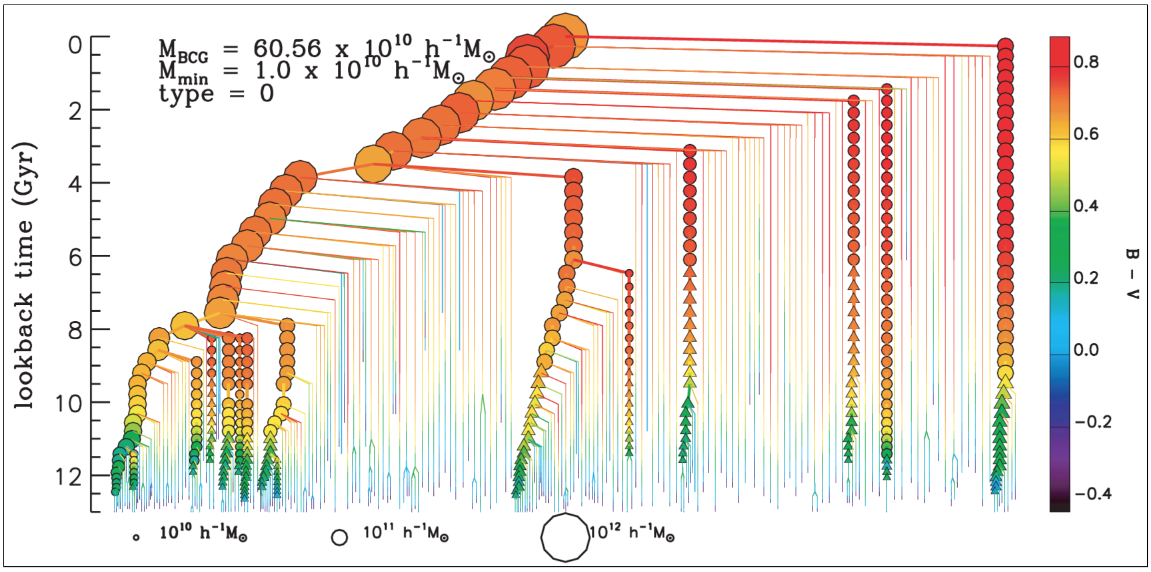

Figure 4.9: BCG merger tree, i.e. the history of the BCG progenitors assembly in a hierarchical scenario. Symbols mark galaxies with mass > $10^{10}h^{-1}M_{\odot}$, whose mass increases as the symbol size increases. The symbol colours indicate the rest-frame B-V colour. The left-most panel is the main branch containing the most massive BCG progenitor, i.e. the main progenitors (De Lucia & Blaizot, 2007).

Finally, the scenario of hierarchical evolution predicts that the BCG is formed through merger events between small galaxies over the time.

Recently, Cooke et al. (2019) analysed FUV and FIR photometric data in the COSMOS field in order to investigate the SF in the BCG progenitor population up to z~3. Their results suggest a scenario for the evolution of BCG progenitors, which should go through three stages:

- the SF phase dominating at z>2.5;
- in situ SF and merger activity up to z~1.25;
- dry mergers and some process able to quench SF in the BCG progenitors at lower-z.

N-body and hydrodynamical simulations for the BCG formation

Hydrodynamical simulations support the scenario of a BCG hierarchical formation through early mergers of few massive galaxies, including physical processes of the baryons (e.g., cooling, SF, AGN feedback). A two-stage BCG formation scenario is usually provided, in which the stellar component of BCGs forms through the collapse of cooling gas, then the BCG accretes through gas-rich mergers at

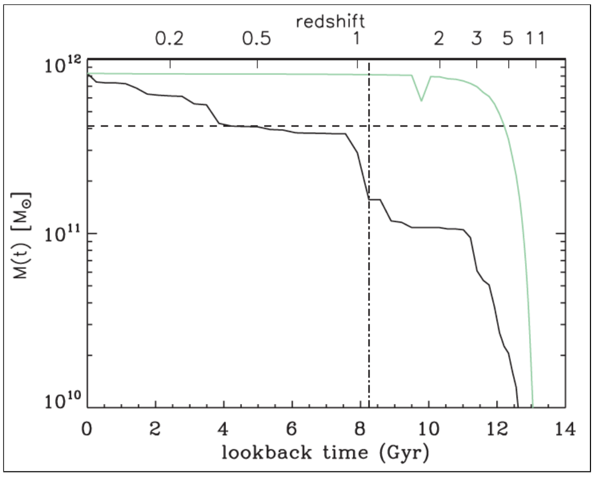

Figure 4.10: History of the star formation and assembly of the main progenitor of the BCG in the case of a hierarchical BCG evolution shown in Fig. 4.9, which is obtained by hydrodynamical (Millennium) simulations and semi-analytic model (De Lucia & Blaizot, 2007). The black lines represents the evolution of the main BCG progenitor assembly, while the green line reports the evolution of the stellar mass summed over all progenitors. The horizontal dashed line indicates half of the final BCG mass and the vertical line marks the identity time (see text for details).

high redshifts and at z<1 continues to grow by dry mergers. For example, De Lucia & Blaizot (2007), through semi-analytic models and hydrodynamical simulations (Millennium), found that in an early phase the formation of small systems occurs. Then these systems start to assembly through a complex merging history. As an example, Fig. 4.9 reports the full merger tree of the BCG progenitors, which will form a BCG with final mass ~ $6.1 \times 10^{11} M_{\odot}$ (De Lucia & Blaizot, 2007). Stellar masses smaller than $10^{10} h^{-1} M_{\odot}$ are shown as lines, while larger symbols represent larger mass. The symbols' color indicates their rest-frame B-V colour. The left-most branch is identified as the main branch, which contains the most massive galaxy of all branches, i.e. the main BCG progenitor. In this example, a rapid cooling at z~2.5 (11 Gyr ago) lead to the formation of massive ($M \sim 10^{11} h^{-1} M_{\odot}$) central galaxies. Major mergers occur at z~1-1.5 (~8-9 Gyrs ago), in which the main BCG progenitor increases its mass. After that, the BCG continues growing by accretion of satellites. Fig. 4.10 reports the mass build-up of the main BCG progenitor (black line) associated to the merger tree in Fig. 4.9 and the evolution of the total stellar mass (green line) formed in the BCG progenitors. It is worth noting that most (~ 80%) of the stars of a local BCG was already in place at z~3 in smaller systems, while z~1-2 seems to be a crucial epoch for the building-up of the main BCG progenitor, which acquires most of the final mass through major mergers.

5. BCG ASSEMBLY AND AGN ACTIVITY IN THE XDCPJ0044.0-2033 CORE

Description: *As introduced in the previous chapter, nearby (z<1), undisturbed galaxy clusters are characterised by a massive and large elliptical galaxy at their center, i.e. the BCG. How these central galaxies form is still under debate. According to most models, a typical epoch for their assembly is z∼1.5. Studying structures at this epoch is therefore crucial to understand the formation process of massive galaxies at the center of clusters and the mechanisms related to it. In order to investigate the main processes responsible for the rapid evolution of galaxies at this epoch, we have performed a detailed multi-wavelength analysis of the core of XDCP J0044.0-2033 (`XDCP0044`), one of the most massive and densest galaxy clusters currently known at redshift $z \sim 1.6$, whose central galaxy population shows high star formation compared to lower-z clusters and an X-ray AGN located close to its center. I have reduced and analysed both SINFONI spatially resolved spectroscopic data in J- and H-band of the cluster central region (∼8"×8") and deep HST photometric data in F105W, F140W and F160W bands of the whole cluster. Archival YJ- and H-band KMOS spectra, X-ray Chandra data, radio JVLA data at 1-2 GHz and ALMA band-6 observations of XDCP0044 have been also used in this study.*

5.1 XDCP0044 galaxy cluster and its core

`XDCP0044` is one of the most massive galaxy clusters discovered at $z > 1.5$ with M_{vir}[1] $\approx 4 \times 10^{14} M_{\odot}$. It has been detected in low-resolution XMM archival data within the XMM-Newton Distant Cluster Project (XDCP, Fassbender et al. 2011b) thanks to its extended X-ray emission (RA=00:44:05.2, Dec = -20:33:59.7), and confirmed by deep Chandra observation to have strong diffuse emission typical of virialized clusters. `XDCP0044` is in a quite advanced state of dynamical relaxation, with no evidence of ongoing cluster-scale major-merger activity (Fassbender et al., 2014) and is a unique laboratory to study the building-up of the BCG and the interplay between galaxies, nuclear activity, and the inter-galactic gas in the core of massive high redshift galaxy clusters.

---

[1] $M_{vir} \equiv M_{200}$, *i.e. the mass which encloses an over-density of 200 times the critical density of the Universe, computed by Tozzi et al. (2015) by modelling the X-ray data of the cluster.*

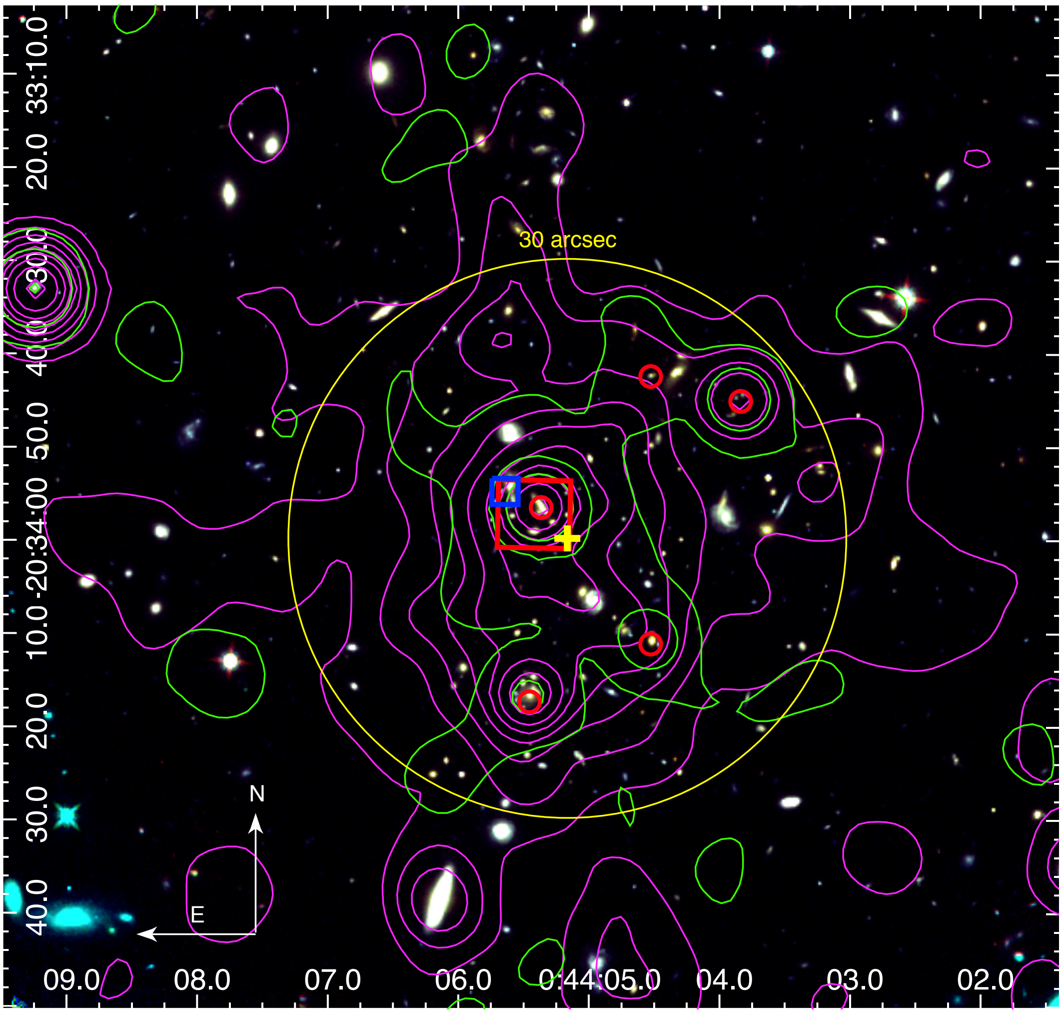

Figure 5.1: HST RGB (F105W + F140W + F160W) image of the galaxy cluster `XDCP0044`. The yellow cross indicates the centroid of the extended X-ray emission (RA 00:44:05.2, Dec -20:33:59.8) while the yellow circle with radius of 30”, which corresponds to a radius of ~250 kpc. The green and magenta contours are the Chandra hard ([2 – 7] keV) and soft ([0.5 – 2] keV) X-ray emissions, respectively while the red circles mark the unresolved X-ray sources as identified by Tozzi et al. (2015). Finally, the red and blue squares delimit the region analysed in this work, corresponding to the SINFONI and the KMOS FOVs.

Fig. 5.1 show the HST RGB (F105W+F140W+F160W) image of `XDCP0044` with overlaid the soft ([0.5-2] keV, magenta) and hard ([2-7] keV, green) bands X-ray contours. Chandra X-ray data analysis performed by Tozzi et al. (2015) pointed out a rather flat density profile, well parameterised by a β-model with $\beta = 0.75$ and core radius $r_c = 99$ kpc, with a rather constant temperature profile around 7 keV out to ~300 kpc. These properties are typically associated with virialized systems and suggest that `XDCP0044` is a non-cool core cluster. Moreover, Tozzi et al. (2015) identified 5 AGN within 30″ (~ 250 kpc) from the cluster center indicated as red circles in Fig. 5.1. Two of these AGN are classified as cluster members and one of them is located in the core of the galaxy cluster, close to the X-ray centroid (~ 17 kpc).

Moreover, Santos et al. (2015) analysed Herschel far-IR (at 100 - 500 μm) data of `XDCP0044` and found a peculiar galaxy population compared to clusters at lower redshifts. Although the virial mass is already significantly developed, the central galaxies in `XDCP0044` are in a very active phase of SF. They found that the total SFR within the projected core area ($r < 250$ kpc; yellow circle in Fig. 5.1) is four times higher than the amount of SF in the cluster outskirts. Contrarily to the local Universe, where star-forming galaxies preferentially live in low density environments, `XDCP0044` shows the opposite behaviour, indicating a possible inversion of the SF-density relation at z~1.6 (Santos et al., 2015). For my PhD Thesis, I have focused on the 8″ × 8″ (i.e. 70 kpc × 70 kpc at z= 1.6) `XDCP0044` central cluster region (Fig. 5.2), for which IFU SINFONI and KMOS observations have been obtained. This region contains two interacting galaxy complexes (A and B) which have been analysed in detail. `Complex A` includes the BCG identified by Fassbender et al. (2014) through HAWK-I images, while `Complex B` consists of the central X-ray AGN found by Tozzi et al. (2015).

Throughout this chapter we will assume a cosmology with $\Omega_\Lambda = 0.6842$ and $H_0 = 67.32\,\mathrm{km\,s^{-1}Mpc^{-1}}$ (Planck Collaboration et al., 2018), and the errors will be quoted at 1σ and upper/lower limits at 90% confidence level, unless otherwise stated.

5.2 Observations and Data Reduction

Several multi-wavelength observations of the inner region of `XDCP0044`, spanning from X-ray to optical, near-infrared (NIR) and radio bands are available. A summary is presented in Table 5.1.
For this study, I have combined and studied the information derived from all the data collected in the central region of the cluster, with particular focus on the new proprietary data (SINFONI and KMOS spectroscopic data, and JVLA observations) and the already available HST and Chandra data.

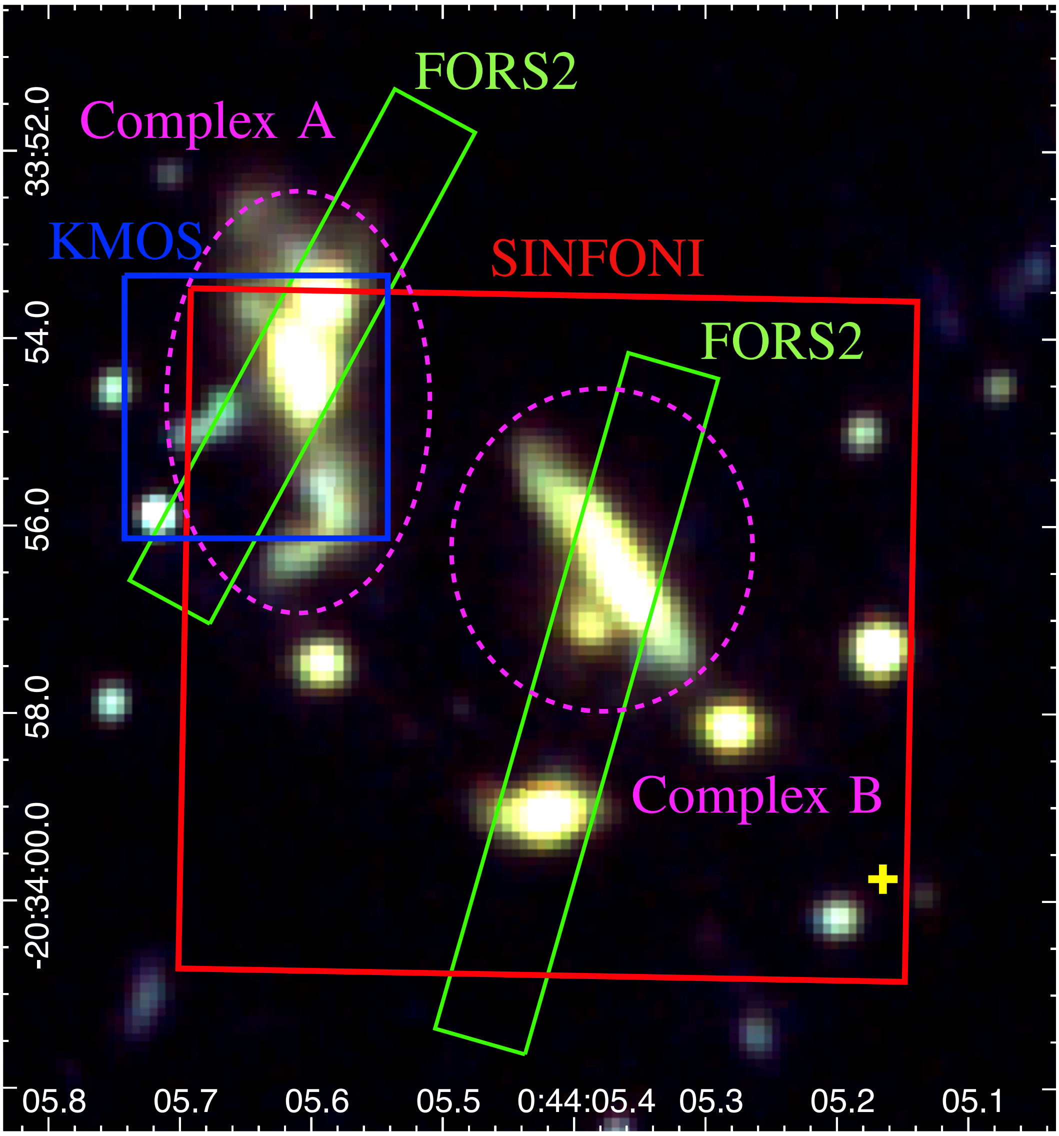

Figure 5.2: Zoom-in of the analysed central region, where two complexes (A and B) are highlighted with the magenta dashed line. The source in the upper left corner is the BCG as identified by Fassbender et al. (2014) while the central source is the X-ray AGN identified by Tozzi et al. (2015). Green rectangles are the FORS2 slits while red and blue squares are the SINFONI and KMOS FOVs.

Table 5.1: List of available photometric and spectroscopic observations in the analysed area. Columns are: (1) Instrument, (2) Band/grating, (3) Exposure time, (4) Program PI, (5) Date of observation and (6) References

Photometric Data					
Name (1)	Band/Grating (2)	t_{exp} (3)	PI (4)	Obs Date (5)	Reference (6)
Chandra/ACIS-S	0.3-8 keV	370 ks	P. Tozzi	10/2013	Tozzi et al., 2015
Subaru/Suprime	V	28 m	G. Smith	09/2009	Fassbender et al. 2014
	i	36 m	G. Smith	09/2009	Fassbender et al. 2014
HST/WFC3	F105W	2 h	S. Perlmutter	7-12/2015	this thesis
	F140W	2 h	S. Perlmutter	6-11/2015	this thesis
	F160W	1 h	S. Perlmutter	8-12/2015	this thesis
	F814W	47 m	S. Perlmutter	5-12/2015	–
VLT/HAWK-I	J	80 m	R. Fassbender	08/2011	Fassbender et al. 2014
	Ks	36 m	R. Fassbender	08/2011	Fassbender et al. 2014
Spitzer/IRAC	3.6μm	270 s	M. Verdugo	08/2011	Fassbender et al. 2014
	4.5μm	270 s	M. Verdugo	08/2011	Fassbender et al. 2014
Herschel/PACS	100/160μm	10.5 h	J. S. Santos	12/2012	Santos et al. 2015
VLA	1.4 GHz		F. De Gasperin	11/2016	Travascio et al. (2019b)
ALMA	221.5 – 240.7 GHz	12.1 m	S. Stuart		Travascio et al. (2019b)
Spectroscopic Data					
VLT/FORS2	Optical	2.2 h	E. Quintana	10/2009	Fassbender et al. 2014 Nastasi et al. 2014
	Optical	2.2 h	F. Romeo	01/2013	Fassbender et al. 2014
VLT/KMOS	JY	4 h 23 m	R. Fassbender	10/2013	Travascio et al. (2019b)
	H	1 h 15 m	R. Fassbender	10/2013	Travascio et al. (2019b)
VLT/SINFONI	J	4 h	A. Bongiorno	9-10/2014	this thesis
	H	1 h 30 m	A. Bongiorno	11/2014	this thesis

5.2.1 SINFONI observations and data reduction

SINFONI IFU observations in J and H-band of the central region of `XDCP0044` (program ID 094.A-0713(A), PI A. Bongiorno), have been obtained in 2014. At the redshift of the cluster, J-band corresponds to the rest-frame [OIII] and Hβ emission lines ($\sim$ 4496 Å - 5230 Å) while H-band samples the Hα emission line with a resolution of R=2000 and R=3000, respectively.
The data have been taken in seeing limited mode (average seeing $\sim 0.8''$) in a $8'' \times$

8″ field of view (FOV) which corresponds to 70kpc × 70kpc. The observed FOV (centered at RA = 00:44:07.755, DEC = −20:34:13.040) is shown in Fig. 5.2. Observations consist of 6 Observing Blocks (OBs) in J-band and 2 OBs in H band. We performed observations of 300 s per frame both on objects (O) and on sky (S), following the scheme "OOSSOOSSOO", in addition to the observations of the standard and telluric stars. The total on target integration time is $\sim 4\ hrs$ in J band and $1\ hr\ 30\ min$ in H band.

SINFONI data reduction has been performed using the ESO pipeline `ESOREX` (Modigliani et al., 2007), with the improved sky subtraction proposed by Davies (2007). After flat-fielding, dark correction, correction for distortions, cosmic rays removal and wavelength calibration, each frame within a single OB is corrected for the sky emission lines, using the IDL routine $skysub.pro$ (Davies, 2007). The science frames within each OB have been combined considering the offsets of the object in each frame and, finally, flux calibrated according to the standard stars. Moreover, a further flux correction in J-band has been applied by rescaling the continuum flux to the HAWK-I J-band photometric point published in Fassbender et al. (2014).

The flux calibrated cubes of the different OBs are then combined together by measuring and applying the relative offset between the peak emissions of the most luminous sources in the fields. The final result of the data reduction procedure is a 3D flux-calibrated data cube, in J- and in H-band, from which we can extract the 2D and 1D spectra at each pixel.

5.2.2 HST observations and data reduction

HST data of the `XDCP0044` galaxy cluster have been obtained in 2015 (Program: 13677, PI S. Perlmutter) in F105W, F140W, F160W and F814W bands, with the following exposure times: 2 hours in F105W and F140W, 1 hour in F160W and 47 minutes in F814W, as listed in Table 5.1. In our analysis we used the images obtained by combining the archival *drizzled* (DRZ) frames, after performing the astrometry and aligning them. Due to the low S/N, the F814W band has not been included in the following analysis. We used SExtractor (Bertin & Arnouts, 1996) to detect and deblend the sources in the relevant region of the images. We chose $WFC3\ F105$ as detection band, identifying a total of 16 sources. Then, we performed aperture photometry in *dual-mode* on the available bands; we did not PSF-match the images, as the FWHMs in all images are comparable (FWHM ~ 0.130", 0.137",0.145" in F105W, F140W and F160W bands, respectively).

We took the isophotal flux (SExtractor `FLUX_ISO`, namely the summation of the fluxes in all the pixel assigned to each object in the segmentation map) as the best photometric estimate, since the severe blending of sources would make photometric measurements in larger areas unreliable. In particular, we do

Table 5.2: List of sources identified in the SINFONI+KMOS analysed area (see Fig. 5.3). Columns are: ID and position in the HST image, and ID in the HAWK-I image as published in Fassbender et al. (2014). For each source, the first column indicates whether it belongs to one of the identified complexes.

	ID_{HST}	RA	DEC	ID_{Hawk-I}
Comp. A	a1	00:44:05.595	-20:33:53.61	BCG
	a2	00:44:05.607	-20:33:54.51	
	a3	00:44:05.680	-20:33:54.92	
	a4	00:44:05.590	-20:33:55.80	
Comp. B	b1	00:44:05.369	-20:33:56.45	QSO
	b2	00:44:05.388	-20:33:57.04	
Other	C	00:44:05.717	-20:33:55.90	#1
	D	00:44:05.594	-20:33:57.46	#2
	E	00:44:05.488	-20:33:57.94	–
	F	00:44:05.423	-20:33:59.04	#3
	G	00:44:05.282	-20:33:58.14	#4
	H	00:44:05.170	-20:33:57.32	#5
	J	00:44:05.151	-20:33:56.48	–
	K	00:44:05.179	-20:33:54.97	#6
	L	00:44:05.299	-20:34:00.40	–
	M	00:44:05.200	-20:34:00.17	#7

not attempt to estimate total fluxes using Kron apertures [1] (`FLUX_AUTO`), as they would be strongly contaminated by light coming from neighbouring sources. Results are presented in Sect. 5.3.

5.2.3 Ancillary data

We also use the following archival data available for `XDCP0044`: (i) YJ- and H-band KMOS IFU data of the cluster central region and, for the whole galaxy cluster, (ii) JVLA L-band (1-2 GHz) data, (iii) ALMA band-6 data, (iv) X-ray data obtained by Chandra, (v) Spitzer/IRAC observations at 3.6 and 4.5μm, (vi) Subaru/Suprime V and I-band, (vii) VLT/HAWK-I J- and K_s-band photometric data and (viii) VLT/FORS2 optical spectroscopy data. Details on these observations are reported in Table 5.1, while data reduction and analysis of some of them is extensively described in Travascio et al. (2019b) A&A submitted.

---

[1] *Elliptical aperture defined by the second order moments of the objectâĂŹs light distribution in SExtractor routine.*

Table 5.3: Multi-wavelength photometry of the identified sources. HST magnitudes are isophotal computed by SExtractor while Subaru V and i-band and HAWK-I J- and Ks-band are 1" aperture magnitude as derived by Fassbender et al. (2014). Magnitudes are given in Vega system.

ID_{HST}	m_{F105W}	m_{F140W}	m_{F160W}	ID_{HwK}	V	i	J	Ks
a1	22.76 ± 0.14	22.09 ± 0.10	21.86 ± 0.16	BCG	24.55 ± 0.004	23.851 ± 0.003	21.576 ± 0.003	19.664 ± 0.003
a2	22.29 ± 0.11	21.60 ± 0.08	21.36 ± 0.13					
a3	23.60 ± 0.21	23.22 ± 0.16	23.21 ± 0.30					
a4	22.47 ± 0.12	21.96 ± 0.09	21.78 ± 0.16					
b1	21.72 ± 0.09	21.01 ± 0.06	20.82 ± 0.10	QSO	25.160 ± 0.007	24.185 ± 0.004	21.738 ± 0.003	19.815 ± 0.003
b2	25.23 ± 0.44	24.34 ± 0.27	24.06 ± 0.45					
C	23.28 ± 0.18	23.12 ± 0.16	23.03 ± 0.28	#1	26.762 ± 0.030	25.915 ± 0.021	23.728 ± 0.018	24.659 ± 0.137
D	23.36 ± 0.19	22.80 ± 0.14	22.62 ± 0.23	#2	26.378 ± 0.021	25.446 ± 0.014	23.049 ± 0.010	21.382 ± 0.014
E	25.97 ± 0.65	25.44 ± 0.48	25.30 ± 0.82	–	–	–	–	–
F	22.47 ± 0.12	21.57 ± 0.08	21.37 ± 0.13	#3	26.706 ± 0.028	25.114 ± 0.010	21.947 ± 0.004	19.951 ± 0.004
G	23.37 ± 0.19	22.49 ± 0.12	22.29 ± 0.20	#4	27.240 ± 0.046	25.833 ± 0.020	22.643 ± 0.007	20.705 ± 0.007
H	23.05 ± 0.16	22.44 ± 0.12	22.25 ± 0.20	#5	26.410 ± 0.022	25.325 ± 0.012	22.530 ± 0.006	20.831 ± 0.008
J	27.05 ± 1.03	27.04 ± 0.98	26.67 ± 1.50	–	–	–	–	–
K	24.16 ± 0.27	23.76 ± 0.22	23.51 ± 0.35	#6	26.448 ± 0.022	25.995 ± 0.023	24.048 ± 0.024	22.880 ± 0.053
L	26.19 ± 0.70	25.83 ± 0.57	25.49 ± 0.88	–	–	–	–	–
M	24.11 ± 0.26	23.68 ± 0.21	23.55 ± 0.36	#7	25.988 ± 0.015	25.458 ± 0.014	23.795 ± 0.019	22.419 ± 0.035

5.3 Optical/NIR source identification

The photometric analysis of the Subaru and HAWK-I images performed by Fassbender et al. (2014) allowed to identify 9 sources (see left panel of Fig. 5.3) in the SINFONI and KMOS fields. Table 5.2 and Tab. 5.3 list their coordinates (RA, DEC), the 1″ aperture magnitudes from Fassbender et al. (2014). Given the PSF FWHM of the data in the different bands (~ 0.51″ in Ks, ~ 0.53″ in J, ~ 0.77″ and 0.72″ in V and i bands, respectively), the 1” aperture magnitude corresponds to 1.3 to 2 times the FWHM (2-to-4.7 σ), although these estimates are affected by the objects' morphology.

In particular, two of the sources identified with HAWK-I have been recognised to be composed of several sources:

- `Complex A` in the top-left corner of the central region of `XDCP0044` (see right panel of Fig. 5.3) was detected in the HAWK-I image by Fassbender et al. (2014) as a single source and identified as the BCG, although with several extensions, interpreted as sign of ongoing or recent mergers. Thanks to the higher resolution of the HST data ($\mathrm{PSF_{HST}/PSF_{HAWK-I}} \sim 0.4$), we have now been able to distinguish 4 different galaxies using SExtractor (`a1`, `a2`, `a3` and `a4`) but the complex might be formed by even more galaxies not identified by SExtractor (see left panel of Fig. 5.4), i.e. `a2` might consist of 2 sources (`a2_1` and `a2_2`) while `a4` has an additional tail (`a4` is therefore made of `a4_1` and `a4_2`).

- `Complex B` is located in the central region of the SINFONI field and includes the X-ray AGN discovered by Tozzi et al. (2013) (source `b1` in the right panel of Fig. 5.3). The HST photometric analysis revealed the presence of a second source (`b2`) very close to the central one. `Complex B` consists indeed of two objects, i.e. `b1` and `b2`.

Moreover, 3 additional faint sources have been identified using HST data (i.e. `E`, `J` and `L` in Fig. 5.3). In total, the analysed region includes therefore 16 photometric sources identified by SExtractor.

Magnitudes in F105W, F140W, and F160W bands of this objects have been computed from the derived isophotal flux (see Sect. 5.2.2), i.e.

$$m = -2.5\log(f_{\rm iso}) + zp$$

where f_{iso} is the isphotal flux and zp=(26.2, 26.4, 25.9) are the zero points in (F105W, F140W, F160)-bands [1]. Table 5.3 lists the identified source ID, the Subaru V and i-band magnitudes, the HAWK-I J and Ks-band magnitudes derived

---

[1] *http://www.stsci.edu/hst/wfc3/ir_phot_zpt*

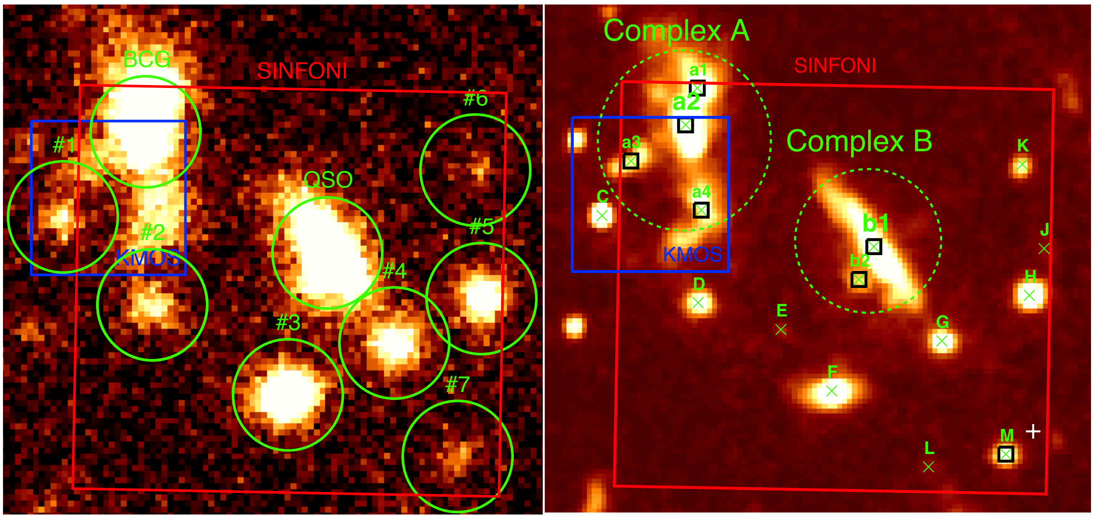

Figure 5.3: *Left Panel:* HAWK-I J-band image of `XDCP0044` centered on the SINFONI FoV. Red and blue squares correspond to SINFONI and KMOS observations, respectively. Green circles mark the 9 sources identified in this image by Fassbender et al. (2014). *Right Panel:* HST F105W image of the same region. Here the green crosses mark the sources identified in the HST images (see Sect. 5.2.2) and listed in Tables 5.2 and 5.3. Black squares mark the sources for which a redshift has been measured while the white cross is the X-ray centroid. The area of the SINFONI FOV corresponds to ~ 70 kpc×70 kpc.

by Fassbender et al. (2014) and the newly derived HST F105W-, F140W, and F160W-band magnitudes.

Additionally, two objects belonging to `Complex A`, i.e. `a2` and `a4`, seem to be constituted by two different sources identified by eye. We have computed also the magnitudes of each component by performing aperture photometry (apertures are shown with yellow regions in Fig. 5.4, left panel). The latter values (reported in Table 5.4) have to be considered as lower limits since the source profile is not properly fitted.

5.4 NIR IFU spectroscopy

In this section, we present the spectroscopic analysis of VLT/SINFONI and KMOS data.

A first extraction of the spectra of the sources identified in HST has been performed using a fixed aperture diameter of 7 pixels in SINFONI (0.875", i.e. PSF $\sim 0.7''$ in J-band and $\sim 0.6''$ in H-band) and 5 pixels in KMOS (1", i.e. PSF $\sim 0.8''$ in JY-band and $\sim 0.9''$ in H-band).
For 7 out of the 16 galaxies, a clear H$\alpha\,\lambda$6563Å line, one of the strongest line expected, has been identified, together with few other lines (e.g. [OIII]$\lambda\lambda$4959Å5007Å

Table 5.4: HST F105W, F140W and F160W magnitudes of the different components of the sources in `Complex A`, extracted as indicated by the yellow circles in Fig. 5.4 (left panel). Magnitudes have to be considered as upper limits (see text for details).

ID_{HST}	F105W	F140W	F160W
a2_1	23.88 ± 0.37	23.32 ± 0.26	23.13 ± 0.18
a2_2	24.72 ± 0.55	24.14 ± 0.37	23.96 ± 0.25
a4_1	23.37 ± 0.29	22.96 ± 0.22	22.77 ± 0.15
a4_2	24.15 ± 0.41	23.74 ± 0.30	23.60 ± 0.21

doublet, H$\beta\lambda$4861Å, [OII]λ3727Å and [NII]$\lambda\lambda$6550Å, 6585Å, marked in red in Fig. 5.6) which confirmed the redshift. The redshifts range from z=1.556 to z=1.589 ($\Delta z \simeq 0.033$), consistently with the redshift of the cluster. All 7 galaxies (shown with a black square in the right panel of Fig. 5.3) are therefore spectroscopically confirmed cluster members and their redshifts are listed in Table 5.5. Moreover, as detailed later, in two of the analysed sources, `a2` in `Complex A` and `b1` in `Complex B`, the Hα emission line is broad ($FWHM > 1500\ km\ s^{-1}$). These sources have been therefore classified as broad line AGN (BL-AGN).

Given the low quality of the data, for these 7 sources, we have built the integrated Signal to Noise Ratio (SNR) of the Hα emission lines. The result is shown in Fig. 5.4 where we over-plot the contours of the SINFONI and KMOS SNR map on the HST F105W image with levels corresponding to SNR >3 with $\Delta(SNR) = 1$. These maps allow us to a) spatially locate the observed Hα emission and b) extract the spectrum of each source at the position that maximise the SN of the Hα line. For what concerns the first aspect, although a mismatch may be possible due to the lower resolution and lower quality of SINFONI and KMOS data compared to HST, especially at the edge of the field (i.e., source `a1`), the contours indicate the source associated to the observed Hα emission, e.g. the Hα line observed in the `a2` spectrum is centered in the souther region (i.e., `a2_2`). Moreover, we note that both broad Hα line emissions are spatially unresolved, confirming therefore their nuclear origin.

The final extraction of the spectra has been performed by using a region centered on the peak of the Hα emission line, with a radius of ~0.4”. Fig. 5.5 shows a zoom-in of the wavelength range where Hα is observed, together with its best-fit model (red line) consisting of a power law + a single Gaussian component.

Finally, for all 7 galaxies for which a redshift has been measured, we have estimated the rest-frame luminosity at 5100Å (L_{5100}) and the V-band absolute magnitudes from the flux measured by interpolating the HST photometric points (i.e., F150W and F140W). The values, reported in Table 5.5, indicate that such galaxies have high luminosities, i.e. `a2` and `b1` are the most powerful sources with $logL_{5100\text{Å}} > 44.4$ and $M_V < -23.5$, in agreement with the fact that they host

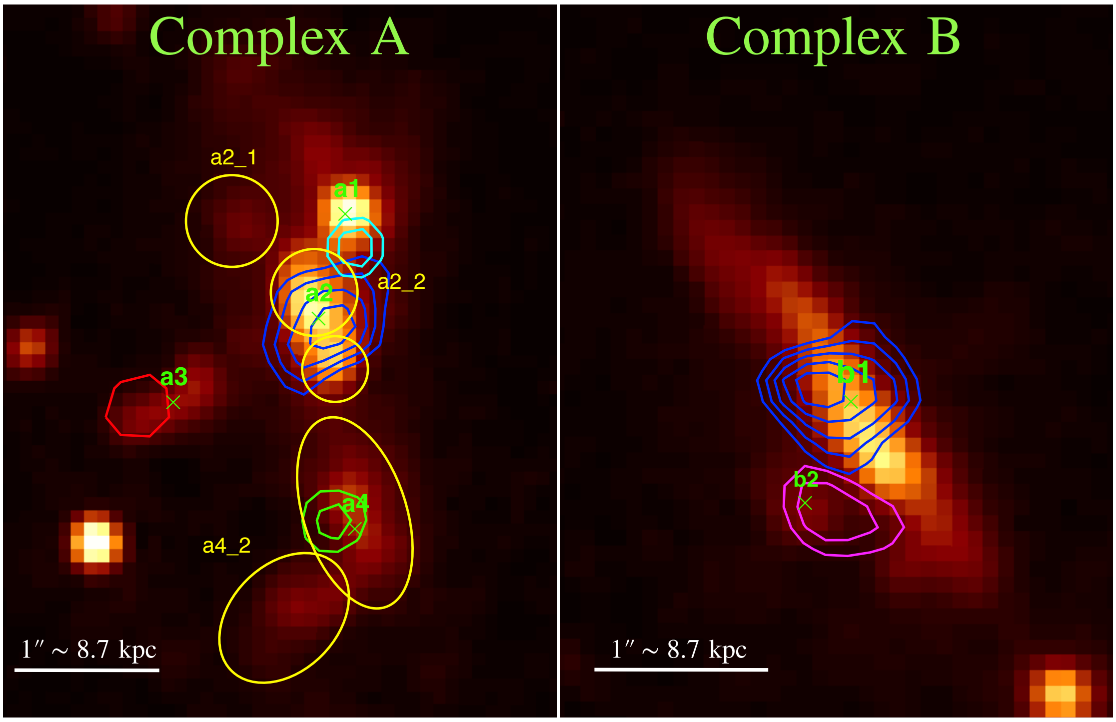

Figure 5.4: Zoom-in of `Complex A` (*l*eft) and `Complex B` (*r*ight) in the HST F105W-band. Yellow ellipses mark the identified sources (not separable by SExtractor). We report the contours at SNR≥3 (with $\Delta(SNR) = 1$) derived from the SNR maps of the Hα emission lines etected for the sources: `a1` (cyan), `a2` (blue), `a3` (red) and `a4` (green) in the left panel, and `b1` (blue) and `b2` (magenta) in the right panel.

an AGN. All other sources show slightly lower luminosities, brighter than typical normal galaxies but consistent with what found for galaxies in high redshift ($z > 1.0$) clusters (i.e. close to the knee of the cluster galaxy luminosity function, Martinet et al. 2015). Table 5.5 lists the properties derived for each source.

5.5 SINFONI, KMOS and FORS2 full spectra of the cluster members

Figs. 5.6 and 5.7 show SINFONI, KMOS and FORS2 spectra of each galaxy in the field of interest classified as cluster members. The expected location of the emission lines is marked. In all galaxies we detect the Hα emission line.

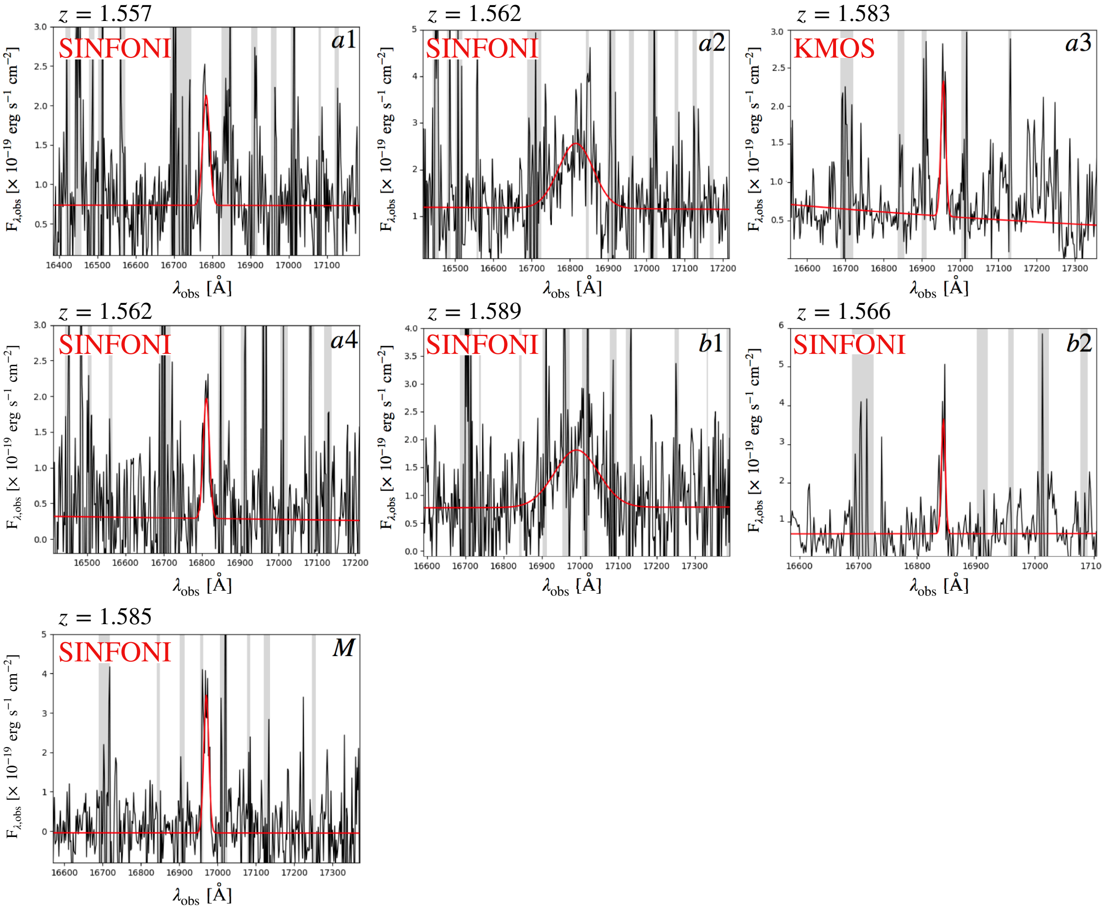

Figure 5.5: Zoom-in of the SINFONI and KMOS spectra around the Hα line of the 7 confirmed cluster members. In red we show the gaussian+power-law best fit of the emission line and the continuum. The derived spectral properties are listed in Table 5.5.

Table 5.5: Results of the SINFONI and KMOS spectral analysis. Properties of the galaxies for which the redshift has been measured. (1) source ID; (2) redshift; (3) signal-to-noise and (4) FWHM of the Hα emission line; (5) instrument and (6) grism used for the Hα emission line detection; (7) 5100Å monochromatic luminosity and (8) absolute magnitudes at λ =5005 Å.

ID_{HST}	z	S/N [Hα]	$FWHM$ [Hα] $[km\,s^{-1}]$	Instrument	grism	$log(L_{5100})$ $[erg\,s^{-1}]$	M_V [mag]
a1	1.557	4	374 ± 89	SINFONI	H	44.25 ± 0.21	-23.1
a2	1.562	6	1911 ± 289	SINFONI	H	44.45 ± 0.17	-23.6
a3	1.583	3	260 ± 92	KMOS	H	43.83 ± 0.36	-22.1
a4	1.562	4	341 ± 89	SINFONI	H	44.31 ± 0.20	-23.2
b1	1.589	7	2389 ± 484	SINFONI	H	44.71 ± 0.13	-24.2
b2	1.566	4	138 ± 30	SINFONI	H	43.35 ± 0.71	-20.8
M	1.585	6	278 ± 61	SINFONI	H	43.65 ± 0.47	-21.6

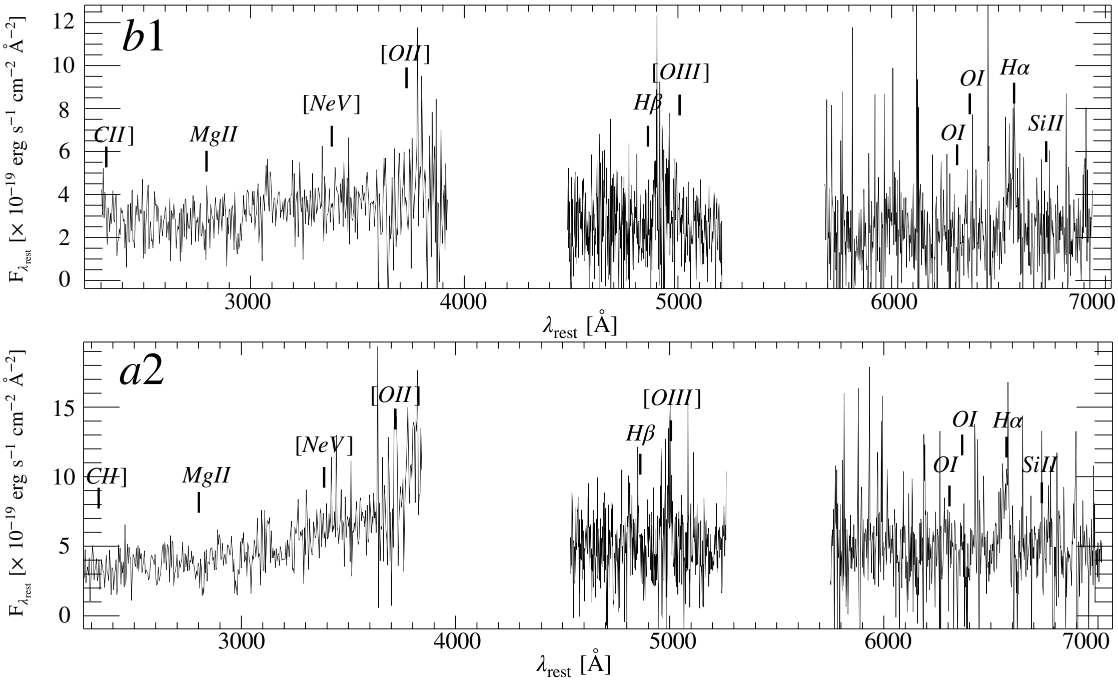

Figure 5.6: SINFONI (J and H) and FORS2 spectra of the two AGN, confirmed cluster members, `a2` and `b1`.

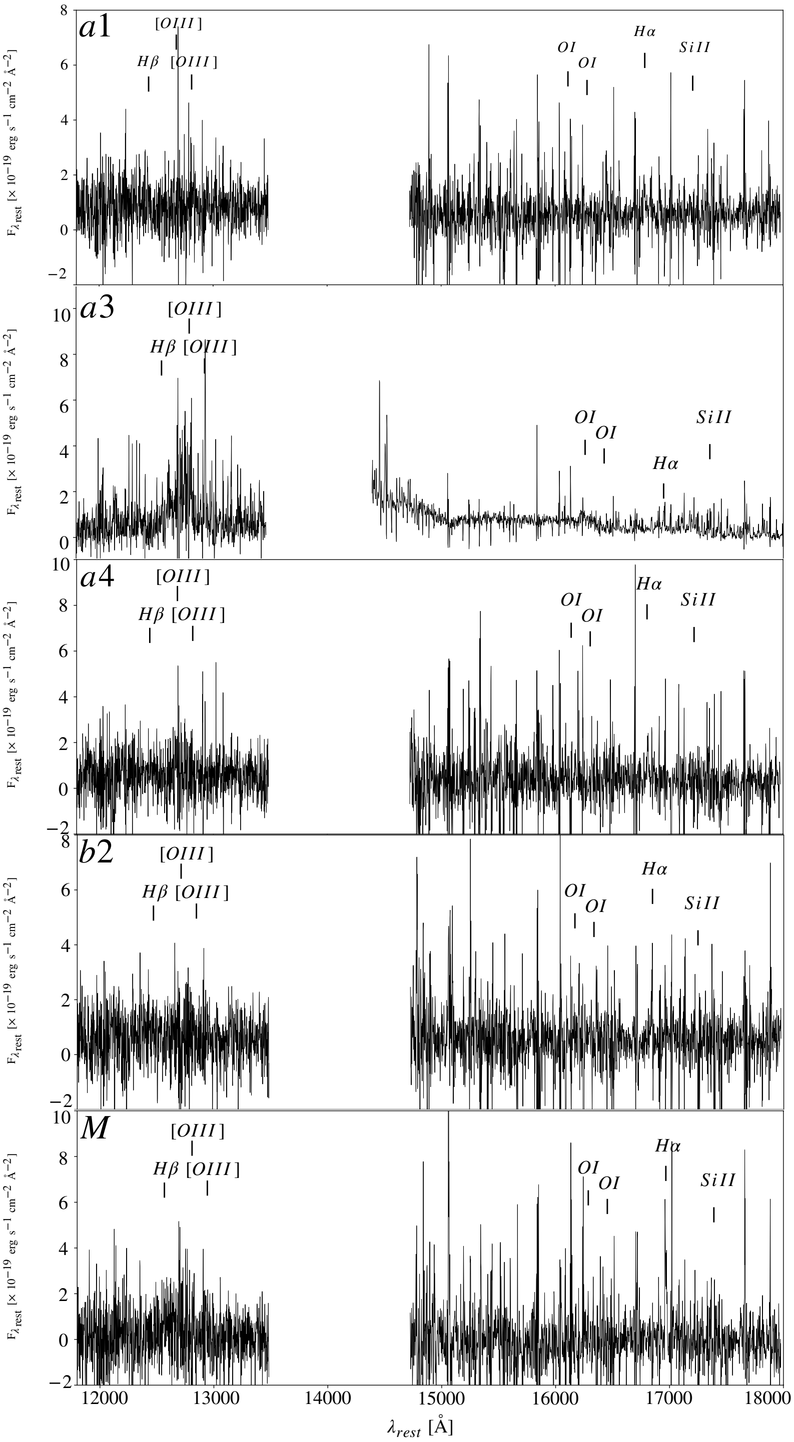

Figure 5.7: KMOS (JY and H) spectra for the source `a3` and SINFONI (J and H) spectra of the other confirmed cluster members in the area of interest, except `a2` and `b1` spectra, which are shown in Fig. 5.6.

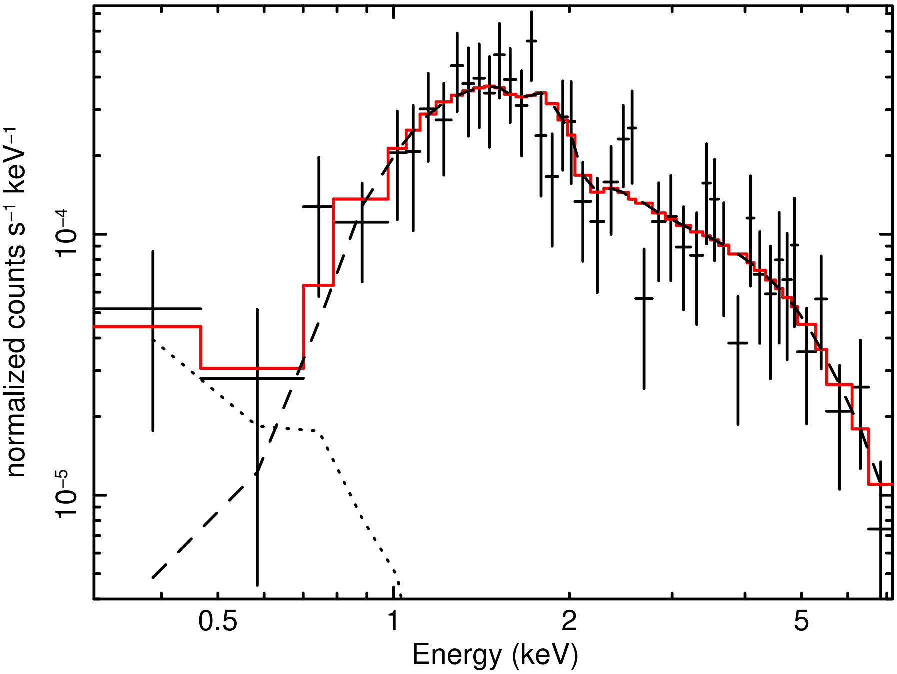

Figure 5.8: X-ray spectrum and best fit model (red) of `b1`. Dotted and dashed lines represent the thermal and absorbed power-law model component, respectively.

5.6 Chandra X-ray spectroscopy

Sources `a2` and `b1` have been spectroscopically identified as AGN, although only `b1` has been detected in the Chandra image, as already reported by Tozzi et al. (2015).

In this Section, I briefly report the X-ray spectral analysis of both sources. Please refer to Travascio et al. (2019b) for a complete description and discussion of the results. The X-ray spectrum of `b1` consists of 268±21 (90% c.l.) background-subtracted counts, in the 0.3-8 keV energy band and is shown in Fig. 5.8. It has been modeled with an intrinsically absorbed power-law (dashed line) with a thermal emission (APEC model in XSPEC, dotted line) at low energies (<0.6 keV) to account for residual excess at low-energy. The latter component can either parametrise a possible hot thermal corona associated with the QSO-host galaxy or may account for the improper background subtraction at these energies due to inhomogeneous distribution of the intra-cluster medium in the spectral extraction regions. The best-fit model ($C - stat/dof = 125/173$) gives a $\Gamma = 1.4 \pm 0.2$ and $N_H = 5.4^{+1.9}_{2.0} \times 10^{22} cm^{-2}$ with a best-fit $kT \approx 0.7$ keV (assuming Solar abundance). The latter is unconstrained given that the thermal component affects a restricted spectral region at energies $< 0.6 - 0.7$ keV of low signal-to-noise ratio. A fit with a canonical $\Gamma = 1.9$ requires slightly higher column densities of $N_H = (10.4 \pm 2.6) \times 10^{22} cm^{-2}$. The resulting unabsorbed 2-10 keV luminosity is $L_{[2-10]keV} = 1.2^{+0.6}_{-0.5} \times 10^{44}\ erg\ s^{-1}$ ($1.5 \times 10^{44}\ erg\ s^{-1}$ for $\Gamma = 1.9$).

As for the a2 source found to have AGN typical broad lines, we do not find any significant X-ray counterpart, for this source we derived a 2σ observed luminosity upper limit $log[L_{[2-10]keV}/erg\ s^{-1}] < 42.7$, assuming an unabsorbed power-law with typical $\Gamma = 1.9$. From a2 bolometric luminosity as derived from $L_{5100Å}$ (i.e. $log[L_{bol}/erg\ s^{-1}] \simeq 45.3$; see Sect. 5.7.1 and Tab. 5.6), by applying $k_{bol,[2-10keV]} \simeq 18.96 \pm 0.24$ (Duras et al. submitted), we expect an intrinsic luminosity $log[L_{[2-10]keV}/erg\ s^{-1}] \sim 44.01$. This is more than 1 dex higher compared to the derived upper limit, thus suggesting a high level of X-ray obscuration. To reproduce the expected X-ray luminosity, a N_H of at least $8 \times 10^{23}\ cm^{-2}$ is required. These derived X-ray properties are reported in Table 5.6. Alternatively, this AGN could belong to the class of intrinsically X-ray weak QSOs (i.e. L_X down to 0.05% L_{bol}, Teng et al., 2014), typically associated to $\lambda_{Edd} \sim 1$ sources, which would explain the non-detection in the Chandra data.

In summary, the analysis of the X-ray data allowed us to measure the nuclear X-ray properties of the b1 QSO, revealing a source with high luminosity ($log[L_{[2-10]keV}/erg\ s^{-1}] = 44.1$) and moderate obscuration ($log[N_H/cm^{-2}] \sim 22.7$). For a2, assuming the bolometric luminosity, as derived from $L_{5100Å}$, we find again a luminous QSO ($log[L_{[2-10]keV}/erg\ s^{-1}] = 44.0$) with a very high level of X-ray obscuration ($log[N_H/cm^{-2}] > 23.9$). This is not at odd with the rest-frame optical properties. The source b1 has an Hα emission line clearly broad $FWHM(H\alpha) > 2000\ km\ s^{-1}$ while a2 has a FWHM which is close to the typical value used as threshold to distinguish between Type-1 and Type-2 AGN. This might suggest the presence of obscuring material formally classifying a2 as an intermediate type AGN.

5.7 AGN and star formation activity in the cluster core

5.7.1 Bolometric luminosity, BH masses and Eddington ratios

Bolometric luminosities have been computed by applying the bolometric correction by Runnoe et al. (2012) to the 5100Å luminosity reported in Table 5.5, estimated from the linear interpolation of the F105W and F140W HST magnitudes. In particular,

$$\log(\mathrm{L_{bol}}) = (4.89 \pm 1.66) + (0.91 \pm 0.04)\log(\lambda \mathrm{L}_\lambda) \tag{5.1}$$

with $\lambda = 5100Å$.

The values obtained for the bolometric luminosity are of the order of $10^{45} - 10^{46}$ erg s^{-1} (see Tab. 5.6).

Table 5.6: Physical properties derived for the two identified AGN, i.e. `b1` and `a2`.

AGN	$logL_{bol}$ $[erg\ s^{-1}]$	$logM_{BH}$ $[M_\odot]$	λ_{Edd}	$\log L^{(*)}_{[2-10]\mathrm{keV}}$ $[erg\ s^{-1}]$	$logN_H$ $[cm^{-2}]$	Γ
a2	45.3 ± 3.4	$7.51^{+0.57}_{-0.34}$	$0.54^{+0.71}_{-0.42}$	44.0	> 23.9	1.9
b1	45.6 ± 3.5	$7.93^{+0.59}_{-0.33}$	$0.35^{+0.47}_{-0.26}$	44.1	22.7	1.4 ± 0.2

(*) the values of $logL_{[2-10]keV}$ reported are intrinsic (unabsorbed). This value has been computed from the X-ray spectrum for `b1` while for `a2` has been derived from the bolometric luminosity.

For source `b1`, we could also estimate the bolometric luminosity from the [2-10]keV band by assuming the bolometric correction from Duras et al. (submitted). The derived value is log(L_{bol})=45.4 $erg\ s^{-1}$, very close to the one computed from the 5100Å luminosity, i.e. log(L_{bol})=45.6 $erg\ s^{-1}$. Moreover, from the broad Hα line, we estimated their BH masses using the virial formula by Greene & Ho (2005):

$$\mathrm{M_{BH}} = 2.0^{+0.4}_{-0.3} \times 10^{6} \left(\frac{\mathrm{L_{H\alpha}}}{10^{42}}\right)^{0.55\pm0.02} \left(\frac{\mathrm{FWHM}}{1000\ \mathrm{km\ s^{-1}}}\right)^{2.06\pm0.06} \mathrm{M_\odot} \tag{5.2}$$

with $L_{H\alpha}$ defined as:

$$\mathrm{L_{H\alpha}} = (5.25 \pm 0.02) \times 10^{42} \left(\frac{\mathrm{L_{5100}}}{10^{44}\ \mathrm{erg\ s^{-1}}}\right)^{1.157\pm0.005} \tag{5.3}$$

We found that both `a2` and `b1` host relatively massive SMBHs of $\sim 3-8\times10^{7}M_\odot$. From these values we could also derive their Eddington ratios, finding $\lambda_{Edd} = L_{bol}/L_{Edd} \sim 0.4-0.5$.
`a2` and `b1` are therefore luminous, massive, highly accreting and obscured AGN. Bolometric luminosities, black hole masses and Eddington ratios are reported in Table 5.6.

5.7.2 Star formation activity

As anticipated in Sect. 5.1, Santos et al. (2015) derived the SFR of the cluster galaxies through Herschel far-IR data, finding for the central region of `XDCP0044` (red contour in Fig. 5.9, which includes all sources studied here plus an additional very bright object on top of the studied region) a SFR $\simeq 452 \pm 58\ M_\odot\ yr^{-1}$. Unfortunately, given the SPIRE point spread function ranging from 17.6″ at 250 μm to 35.2″ at 500 μm, we cannot distinguish the single sources in the Herschel images to know how such SFR is distributed among them. On the contrary, ALMA observations provide sufficient resolution to distinguish the single sources but unfortunately the observed field (shown in cyan in Fig. 5.9) covers only partially the area of interest (see Travascio et al., 2019b, for further details). The only source detected through ALMA angular resolution ($0.59'' \times 0.77''$) observation is the X-ray AGN `b1`. The ALMA continuum map observed at ~230 GHz with a rms sensitivity of 0.13 mJy/beam (magenta contours in Fig. 5.9) reveals cold dust emission from the host galaxy detected at 5σ significance with a flux density of $f_\nu = 0.80 \pm 0.15\ mJy$, and unresolved by the ALMA beam.

Assuming a typical QSO SED, i.e., the Mrk231 template, and normalising it at the observed ALMA flux, we derived a SFR~ 490 $M_\odot\ yr^{-1}$ (by integrating from 8 to 1000μm and then converting such value into SFR, using Kennicutt et al. 1998). This value is consistent with the SFR derived from IR Herschel data by Santos et al. (2015) for the entire central region, suggesting that most of the IR emission, and therefore of the SF, is associated to `b1`. However, if we consider a different modelization for the dust emission and we assume i.e. a simple Blackbody template normalised to the ALMA flux, the SFR we obtain is lower, i.e. ~150 $\mathrm{M}_\odot\ yr^{-1}$. The true value might be somewhere in between. Unfortunately, without additional ALMA observation of the whole field, it is not possible to fully characterise the SF distribution in the central region of `XDCP0044`. For example, given the partial coverage of the ALMA observation, we do not know whether `Complex A`, associated to radio emission (see Sect. 5.7.3), also hosts SF.

5.7.3 Radio properties

In the central region of `XDCP0044` (Fig. 5.9), an extended radio emission associated to `Complex A` has been detected with a luminosity of $L_{1.5\ GHz} = 3.6 \pm 0.5 \times 10^{24} W/Hz$ (see Travascio et al., 2019b, A&A submitted, for a complete presentation of the results obtained from the JVLA observations of `XDCP0044`). Under the assumption that the radio signal is produced by a single source, its power ($logP_{1.5GHz} = 23.45$) would be just above the threshold at z~1.6, introduced by Magliocchetti et al. (2014, $logP_{cross}$(z)=21.7+z), to discriminate SF processes from AGN, suggesting therefore an AGN powered radio emission. On the contrary, if we assume that the observed radio emission is due to SF processes, according to the relation by Brown et al. (2017), the measured radio luminosity would translate into a SFR~ 100 $M_\odot\ yr^{-1}$, which would be consistent with the SFR ($\simeq 452 \pm 58\ M_\odot\ yr^{-1}$) derived from IR Herschel data by Santos et al. (2015) for the entire central region of the cluster (red contours in Fig. 5.9), considering also the contribution from `b1`, as derived through ALMA continuum observations (see Sect. 5.7.2).

Higher resolution observations (frequencies > 2 GHz or using VLBI techniques) would be important to disentangle the different scenarios, i.e. emission generated by a discrete number of compact objects associated to galaxy cores, or smooth diffuse emission mainly associated to SF.

5.8 Dynamics of XDCP0044 galaxies

Together with the 7 galaxies belonging to the galaxy cluster found through KMOS and SINFONI data in this work, there are additional 10 known cluster members whose redshift has been determined through FORS2 optical slit spectroscopy in period P84 and P89 (Nastasi et al., 2013). Their ID, coordinates and redshifts are reported in Table 5.7. Altogether, `XDCP0044` has therefore 17 confirmed cluster members with redshifts in the range $1.557 < z < 1.600$. The central redshift of the cluster, defined as the mean redshift of all member galaxies, is $z_c = 1.578$ (in agreement with the value $z_c = 1.579$ published by Santos et al. 2011). For each galaxy member, we estimated the radial component of the peculiar velocity following Harrison (1974):

$$v_{los} = \frac{(z_i - z_c)}{(1 + z_c)} \cdot c \tag{5.4}$$

where $1 + z_c$ accounts for the cosmological correction for the cluster Hubble flow and z_i is the redshift of each galaxy belonging to the galaxy cluster (see Table 5.7). Fig. 5.10a reports the velocity-radius diagram (left) and the histogram of the velocity shifts of galaxies (right) binned at 500 $km\ s^{-1}$. The velocity distribution peaks at $v \sim 0$ with absolute values up to $\sim 2600\ km\ s^{-1}$. We estimated the velocity dispersion of `XDCP0044` to be $\sigma \approx 1520 \pm 210\ km\ s^{-1}$, in which the uncertainty is computed by adopting the bootstrapping statistic[1]. Such value is higher than expected ($\sim$1000 $km\ s^{-1}$) from the velocity dispersion - temperature relation (Lubin & Bahcall, 1993; Girardi et al., 1996) assuming $kT \sim 7$ keV, as derived by Tozzi et al. (2015).

A Gaussian profile peaked at the average velocity and with FWHM equivalent to the velocity dispersion is also shown in the right panel: although the number of sources is low, the distribution of the velocity shifts do not seem to follow a gaussian profile. In particular there seems to be an excess at the extreme velocities around $v \sim -2000\ km\ s^{-1}$.

However, there are more accurate statistical methods to establish the gaussianity in the distribution of the line of sight velocity, which is usually associated with relaxed systems (Chincarini & Rood, 1977; Łokas et al., 2006), while signatures of unrelaxed dynamic or merging are given by non-Gaussianity velocities distribution (Colless & Dunn, 1996; Girardi et al., 2005). For example the Hellinger Distance (HD) method, proposed by Ribeiro et al. (2013) which is based on the distance between the empirical and theoretical distributions. Following the recipe described in Ribeiro et al. (2013) and de Carvalho et al.

---

[1] *a robust estimator when dealing with small samples* ($N < 50$)

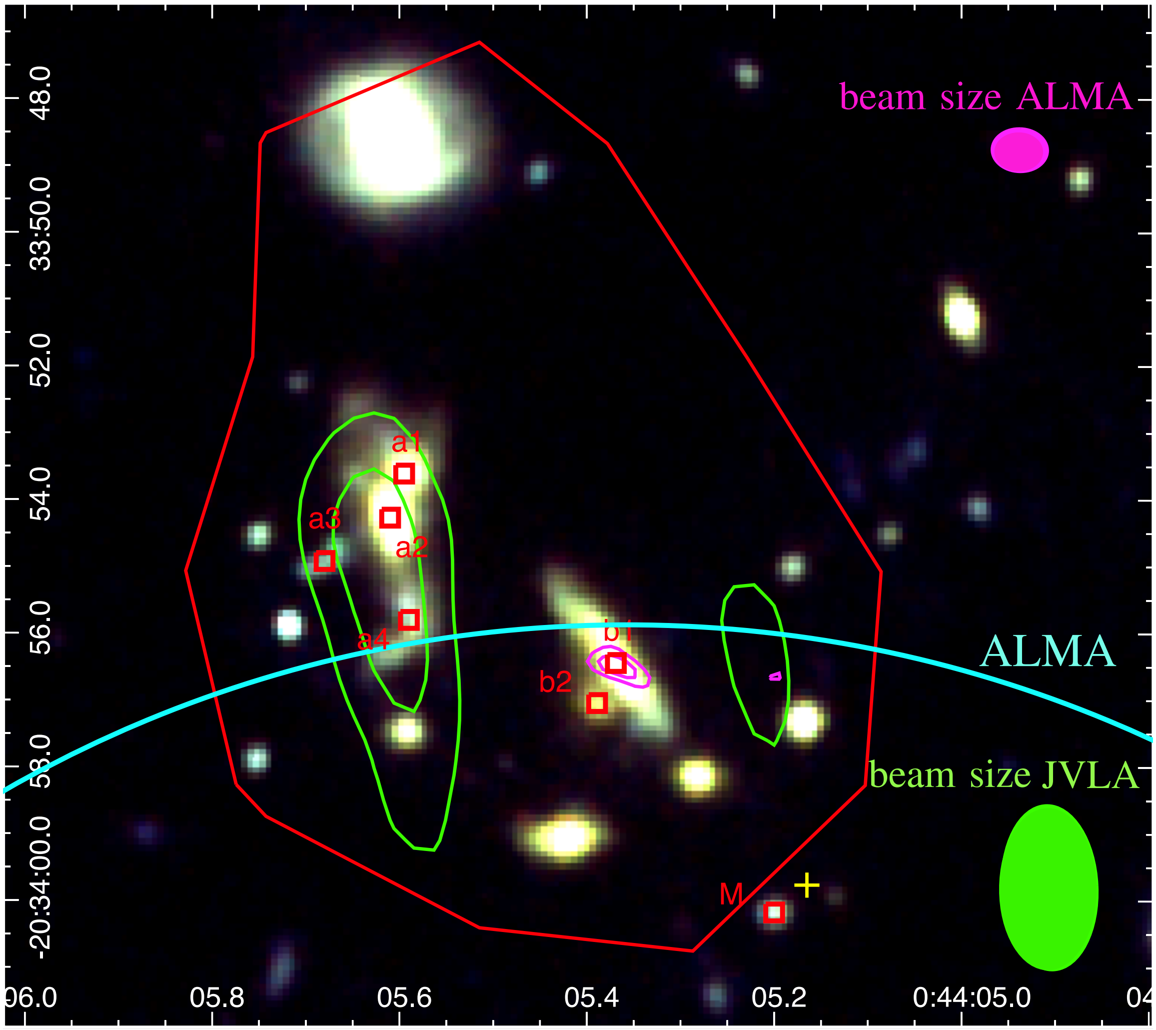

Figure 5.9: HST RGB image of the central region of `XDCP0044`, with over-plotted the 3σ 1–2 GHz JVLA radio contours (green), the Herschel IR 3σ detection (red) and the 230 GHz ALMA continuum at 5σ. The cyan line indicates the ALMA field of view while the green and magenta ellipses are the JVLA and ALMA beam, respectively.

Table 5.7: `XDCP0044` cluster members available whose redshift has been determined through FORS2 optical slit spectroscopy in period P84 and P89 (Nastasi et al., 2013). IDs from 2 to 6 are from Fassbender et al. (2014) (ID=1 in Fassbender et al. (2014) has not been reported because it corresponds to a2 in Table 5). IDs from 7 to 10 are new additional FORS2 cluster members from P84 and P89 but not yet published. Only redshifts with confidence levels higher than 50 % have been included.

ID	RA	DEC	z	$v[km\ s^{-1}]$
SINFONI and KMOS data				
a1	00:44:05.595	-20:33:53.61	1.557	-2494
a2	00:44:05.607	-20:33:54.51	1.562	-1913
a3	00:44:05.680	-20:33:54.92	1.583	530
a4	00:44:05.590	-20:33:55.80	1.562	-2029
b1	00:44:05.369	-20:33:56.45	1.589	1344
b2	00:44:05.388	-20:33:57.04	1.566	-1448
M	00:44:05.200	-20:34:00.17	1.585 sl	762
FORS2 Data				
2	0:44:04.737	-20:34:09.43	1.5936	1880
3a	0:44:05.450	-20:34:16.78	1.5699	-855
3b	0:44:05.531	-20:34:16.78	1.5716	-680
4	0:44:05.325	-20:33:14.28	1.5787	146
5	0:44:05.611	-20:32:58.55	1.5778	41
6	0:44:03.015	-20:32:31.84	1.5986	2460
7	0:44:05.073	-20:33:54.48	1.5789	169
8	0:44:05.826	-20:33:17.28	1.5762	-145
9	0:44:05.257	-20:32:38.23	1.6001	2635
10	0:43:59.311	-20:33:39.49	1.5740	-401

(2017), we used the publicly available "distrEx" package under the R language and environment and we obtained a value HD<0.05 which indicates that the velocity distribution is well described by a single Gaussian distribution. Since we deal with low statistic numbers (N<20), we have also performed the Dip test (Hartigan & Hartigan, 1985) which quantify the maximum distance between the cumulative distribution of the data and the best fitting unimodal distribution. This test is insensitive to the assumption of Gaussianity and has been found to be best suited for clusters with <20 galaxy members (Ribeiro et al., 2013). The R-code "diptest" applied to our data confirms that the data can be described by a unimodal distribution. As a final test, we also used the approach of Dressler & Shectman (1988) (D-S test) to evaluate if the cluster exhibits signatures of sub-structures. The D-S test uses both spatial and velocity information and is calculated for each individual galaxy based on its N_{DS} = 4 nearest neighbours, where $N_{DS} = \sqrt{N_m}$ with N_m the total number of galaxies, as suggested by Pinkney et al. (1996) and Biviano et al. (2002):

In particular, we performed the same procedure reported by Einasto (2012), by using the following formula:

$$\Delta = \sum_{\mathrm{i}}^{\mathrm{N_m}} \sqrt{\frac{\mathrm{N_{DS}} + 1}{\sigma_{\mathrm{c}}^2}[(\mathrm{v_{loc}} - \mathrm{v_c})^2 + (\sigma_{\mathrm{loc}} - \sigma_{\mathrm{c}})^2]} \qquad (5.5)$$

where v_{loc} and σ_{loc} are the mean velocity and velocity dispersion of the closest N_{DS} galaxies, while v_c and σ_c are the same quantity computed for the whole galaxy cluster. Δ_{obs} is the cumulative deviation, which will be $> N_m$, if the system contains substructures. To decrease the probability to obtain false positive and negative, we run multiple Δ_{MC} through Monte Carlo simulation with 25000 iterations, in which the velocity shifts with respect to their initial positions is randomly shuffled each time. The presence of substructures is quantified by the $p - value$ defined as N($\Delta_{MC} > \Delta_{obs}$)/$N_{tot}$. Indeed, if the distribution around the average values for each individual galaxy is Gaussian, we expect the cumulative deviation estimated in any other configuration (Δ_{MC}) to be lower than Δ_{obs}. Hou et al. (2012) found that if $p - value < 0.01$, 99% of their mock groups are correctly classified. Our analysis reports a $p - value \simeq 0.16$. This value does not allow us to firmly claim that the local variations in the velocity distribution are due to the presence of sub-structures (Hou et al., 2012; Dressler & Shectman, 1988), as there is a not negligible probability that these are random fluctuations.

From all these statistical tests we cannot conclude that `XDCP0044` has clear sign of large substructures, although the presence of small-scales clumpy structures cannot be ruled out.

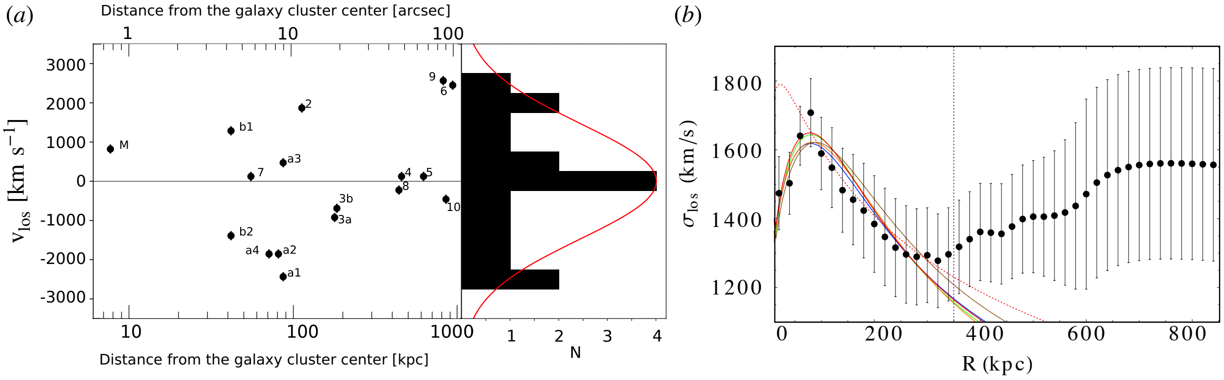

Figure 5.10: Panel (a): on the left, the velocity shift of the individual cluster members (computed as in eq. 5.4) as a function of the distance from the galaxy cluster center. On the right, the histogram of the velocity shifts binned at 500 $km\ s^{-1}$. The red curve shows the best Gaussian fit which approximates the distribution. Panel (b): galaxy VDP ($\sigma_P(R)$) computed as in eq. (5.6) with black dots. The colored lines are the VDPs modelled for a cluster DM corresponding to different models, i.e. (green Duffy et al., 2008), (blue, Amodeo et al., 2016) and (orange, Ragagnin et al., 2019), (brown, T15), (red, 'Free'), see text for details. The vertical dashed purple line labels the maximum R value used in the fit, while the dotted red ones is the result of the fitting in the 'Free' case excluding the first three rising points in the inner region.

5.8.1 Velocity Dispersion Profile of the galaxies in XDCP0044

A powerful tool to study the dynamics of galaxy clusters is the velocity dispersion profile (VDP). It allows us to identify the presence of substructures and to trace the galaxy cluster dynamical state (Struble, 1979). Indeed, the shape and trend of the VDP (e.g. decreasing and increasing) depend on the equilibrium between the DM distribution and the galaxy interactions (Menci & Fusco-Femiano, 1996). Fig. 5.11 reports some examples of VDPs estimated for galaxy clusters which do (top panels) or do not (bottom panels) exhibit merging sub-structures (Bilton & Pimbblet, 2018). VDPs of merging systems show a rising profile in the inner region. Indeed, mergers of sub-groups of galaxies cause a dissipation of the orbital energy as suggested by Menci & Fusco-Femiano (1996).

To obtain the VDP we measured the velocity dispersion at different distances R from the cluster center (i.e. X-ray centroid) and weighted using a Gaussian window function ($\sigma_p(R)$) centered at R. Following Bergond et al. (2006) and Pimbblet et al. (2014), $\sigma_p(R)$ is defined as:

$$\sigma_p(R) = \sqrt{\frac{\sum_i \omega_i(R)(v_i - v_c)^2}{\sum_i \omega_i(R)}} \tag{5.6}$$

where v_i is the velocity of each galaxy (v_{los}), v_c is the mean cluster velocity, and

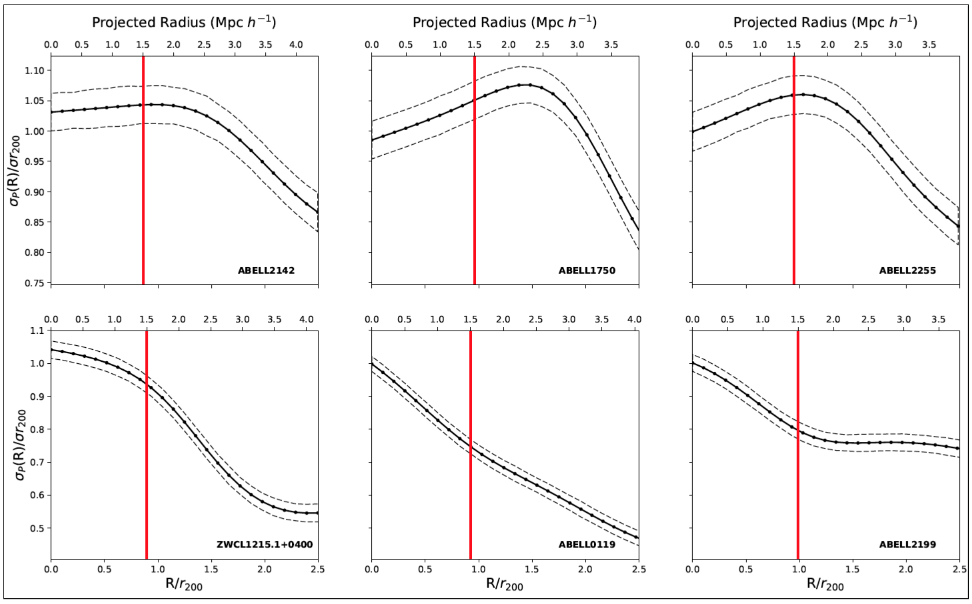

Figure 5.11: VDPs as a function of the radius (r/r_{200}) reported in Bilton & Pimbblet (2018) for a sub-samples of merging (top row) and non-merging (bottom row) galaxy clusters. Red vertical line signs the distance 1.5 $Mpc\ h^{-1}$ from the cluster center within which Δ test is performed to determinate the presence of sub-structures and mergers within galaxy clusters.

$\omega_i(R)$ is the moving window function, defined as:

$$\omega_i(R) = \frac{1}{\sigma_R} exp\left[-\frac{(R-R_i)^2}{2\sigma_R^2}\right] \tag{5.7}$$

with R_i the distance of each galaxy from the X-ray centroid and σ_R the width of the Gaussian profile window chosen, at each R, in order to include 4 galaxies within 1σ.

In Fig. 5.10b, we report the VDP $\sigma_p(R)$ as measured from the data with its errors, and we superimpose the best fit predictions $\sigma_{DM}(R)$ obtained modelling the cluster halo with a NFW (Navarro et al., 1997) profile. Following Mamon & Łokas (2005) and skipping all intermediate steps, we finally end up with the following expression for the velocity dispersion profile projected along the line of sight of a NFW halo

$$\sigma_{los}^2(R) = \frac{GM_{vir}}{R_{vir}} \frac{c_{vir}}{g(1, c_{vir})} \frac{\tilde{\sigma}_{los}^2(R)}{\tilde{\Sigma}(R)} \tag{5.8}$$

where M_{vir} is the mass within the radius R_{vir} where the mean mass density equals 200 times the critical density at the cluster redshift, $c_{vir} = R_{vir}/R_s$ is the halo concentration with R_s the characteristic radius of the NFW model, and we have defined the following auxiliary functions

$$g(x, c_{vir}) = \log\left(1 + c_{vir}x\right) - c_{vir}x/(1 + c_{vir}x)\ , \tag{5.9}$$

$$\tilde{\Sigma}(\eta) = \begin{cases} \dfrac{1 - |c_{vir}^2\eta^2 - 1|^{-1/2}\mathrm{arcosh}(1/c_{vir}\eta)}{c_{vir}^2\eta^2 - 1} & \eta < 1/c_{vir} \\ \dfrac{1}{3} & \eta = 1/c_{vir} \\ \dfrac{1 - |c_{vir}^2\eta^2 - 1|^{-1/2}\mathrm{arcos}(1/c_{vir}\eta)}{c_{vir}^2\eta^2 - 1} & \eta > 1/c_{vir} \end{cases}\ , \tag{5.10}$$

$$\tilde{\sigma}_{los}^2(R) = \int_\eta^\infty \mathcal{K}_{OM}\left(\frac{\xi}{\eta}, \frac{\eta_{OM}}{\eta}\right) \frac{g(\xi, c_{vir})}{\xi^2(1 + c_{vir}\xi)^2} d\xi\ , \tag{5.11}$$

with $\eta = R/R_{vir}$, $\xi = r/R_{vir}$, and $\mathcal{K}_{OM}(u, u_{OM})$ given in Appendix of Mamon & Łokas (2005). It is worth stressing that Eq.(5.8) has been derived under the assumption that the galaxies used to trace the velocity dispersion profile are spatially distributed according to the same density profile as the cluster halo. Recent simulations (see, e.g., Bose et al. (2019)) show that this is indeed the case so that we will keep on using Eqs.(5.8) - (5.11) to compute the cluster $\sigma_{los}(R)$.

To this end, we assume that the galaxy distribution traces the DM one, and take an Osipkov - Merritt profile, i.e., $\beta_{OM}(r) = r^2/(r^2 + r_{OM}^2)$, to model the anisotropy $\beta_{ani}(r)$ of the tracer orbits. The model $\sigma_{DM}(R)$ is then a function of three parameters $(\log M_{vir}, c_{vir}, \log \eta_{OM})$, with M_{vir} the virial mass, c_{vir} the concentration, and we set $\eta_{OM} = r_{OM}/R_{vir}$. We fit for $\log \eta_{OM}$ in order to efficiently explore a wide range for η_{OM} thus being able to approach also the limiting cases of perfect isotropy ($\beta_{ani} = 0$ for $r_{OM} \rightarrow \infty$) and fully radial orbits ($\beta_{ani} = 1$ for $r_{OM} \rightarrow 0$). Ideally, we could determine these quantities by fitting to the full $\sigma_p(R)$ dataset. However, we noted that the whole $\sigma_p(R)$ cannot be modelled with a $\sigma_{DM}(R)$ profile because of their different trends at large distances from the galaxy cluster center. In particular, the change in the logarithmic slope of the $\sigma_p(R)$ for $R > R_U = 340\ kpc$ cannot be matched by any halo profile. We therefore limited the fit to the data to the left of the dashed purple line ($R < R_U$), as shown in Fig. 5.10b.

Given the limited radial range which makes it harder to break the mass - concentration - anisotropy degeneracy, we first fit for $(\log M_{vir}, \log \eta_{OM})$ only setting c_{vir} as:

$$c_{vir}(M_{vir}, z) = A_M \left(\frac{M_{vir}}{M_{piv}}\right)^{B_M} \left(\frac{1 + z}{1 + z_{piv}}\right)^{C_M} \tag{5.12}$$

Model	A_M	B_M	C_M	M_{piv}	z_{piv}
D08	5.72	-0.084	-0.47	$2 \times 10^{12} h^{-1}$ M$_{\odot}$	0.00
A16	1.15	-0.50	0.12	10^{14} M$_{\odot}$	0.00
R19	6.02	-0.12	-0.16	10^{13} M$_{\odot}$	0.47

Table 5.8: Fiducial parameters of the mass - concentration relations. Models are Duffy et al. (2008, D08), Amodeo et al. (2016, A16), and Ragagnin et al. (2019, R19).

with (M_{piv}, z_{piv}) reference values for mass and redshift. We considered three different mass - concentration (MC) relations, whose parameters are listed in Table 5.8. Note that the Amodeo et al. (2016, hereafter A16) one is derived by fitting eq. 5.12 to the mass and concentration of clusters as derived by X - ray data, while both Duffy et al. (2008, hereafter D08) and Ragagnin et al. (2019, hereafter R19) are inferred from simulations with the remarkable difference that D08 uses dark matter only simulations while baryons are added in R19. We use a Monte Carlo Markov Chain algorithm to explore the parameter space defining a Gaussian likelihood $\mathcal{L} \propto \exp(-\chi^2/2)$ with the standard definition of the pseudo - χ^2 merit function, i.e.,

$$\chi^2(\mathbf{p}_{DM}) = \sum \left[\frac{\sigma_p(R_i) - \sigma_{DM}(R_i, \mathbf{p}_{DM})}{\varepsilon(R_i)} \right]^2 \tag{5.13}$$

with $\mathbf{p}_{DM} = \{\log M_{vir}, \log \eta_{OM}\}$ the set of model parameters, $\varepsilon(R_i)$ the error on the i - th measurement, and the sum is over the considered dataset. The best fit model is superimposed to the data in Fig. 5.10b with green, blue, magenta lines for the D08, A16, and R19 MC relations, while the constraints on the model parameters are given in Table 5.9. Note that we also compute constraints on c_{vir} although this is not a fit parameters so that its error comes from the propagation of the one on $\log M_{vir}$ under the assumed MC relation.

Although the fit is quite good for all three models, we nevertheless note that the A16 MC relation predicts a concentration $c_{vir} < 1$ which is meaningless. This is a likely consequence of extrapolating the relation outside the mass range used to infer it so that hereafter we will not discuss this case anymore. Although the constraints are quite weak because of the limited radial range and the large errors on $\sigma_p(R)$, it is worth looking at the fit parameters. First, we note that the mass M_{vir} is significantly smaller than the one inferred by Tozzi et al. (2015) (last row in Table 5.9) from the assumption of hydrodynamical equilibrium. Both the D08 and R19 fits predict a less massive halo as it is also confirmed looking at the masses M_{Δ} within R_{Δ} for both $\Delta = 2500$ and $\Delta = 500$ compared to the Tozzi et al. (2015) estimates (after correcting for the different cosmology). Such a result hints at a possible breakdown of either the assumption in our computation of

$\sigma_{DM}(R)$ or in the Tozzi et al. (2015) mass estimate.

To investigate this issue, we note that the MC relations we have used are actually not deterministic, but probabilistic, i.e., for a given M_{vir}, there is a range of possible c_{vir} values sorted from a lognormal probability distribution centred on the value from Eq.(5.12) and with a non negligible variance. We therefore repeat our fit adding c_{vir} to the model parameters set $\mathbf{p}_{DM}$. In order to better constrain the model parameter, we add a Gaussian prior on the $\log M_{vir}$ with mean and variance given by the Tozzi et al. (2015) estimate. We refer to this model as T15 in Table 5.9 and show the corresponding best fit as the brown curve in Fig. 5.10. Although the fit is still good, we nevertheless note that the model systematically overestimate $\sigma_p(R)$ in the decreasing region predicting the largest $\sigma_{DM}(R)$ values among the all cases we have considered as a consequence of the higher concentration with respect to the D08 and R19 cases. Indeed, for the T15 median M_{vir}, one should get $c_{vir} = 2.52$ using the D08 and 3.76 using the R19 MC relations which are definitely smaller than the values preferred by the fit.

Notwithstanding the prior on M_{vir}, the fit still prefers a mass smaller than the Tozzi et al. (2015) value. We therefore give off this prior and perform the fit leaving all three parameters free to vary. We get the results labeled 'Free' in Table 5.9 and shown as solid red line in Fig. 5.10(b). The fit is now quite similar to the D08 and R19 ones, but the concentration c_{vir} is definitely larger and again in disagreement with both MC relations. Nevertheless, the mass content is still lower than the Tozzi et al. (2015) estimate. However, we find that all the mass estimates we get from fitting the $\sigma_p(R)$ data are consistent with each other within the 68% CL so that we can argue that the cause of the disagreement with Tozzi et al. (2015) should likely not be related to the MC relation. Since the inner regions could be affected by ongoing merging event causing deviations from the NFW profile, we try repeating the 'Free' fit removing the first three points from the $\sigma_p(R)$ dataset. Although the fit to the remaining points improves as shown by the dotted red line in Fig. 5.10b, we find no significant difference in the mass content for all Δ values, while the concentration c_{vir} increases to $c_{vir} = 6.39^{+2.36}_{-2.94}$ and the anisotropy parameter decreases to $\log \eta_{OM} = 0.29^{+1.08}_{-1.34}$. The large errors, however, make these differences statistically meaningless.

The persistent disagreement between VDP and X-ray based estimates of the mass content may be taken as an evidence of a breakdown of the assumptions underlying one of the two methods or both. On one hand, VDP based masses assumes that galaxies trace the DM distribution which is true only if the system is virialized. Should this be the case, however, the orbit distribution is expected to be isotropic, i.e., $\beta_{ani} = 0$ at all r. This is roughly the case over the fitted radial range with $\beta_{ani}(r)$ being no larger than 0.16 (for the D08 case which is the most anisotropic one). However, leaving the concentration free to vary (as in the T15 and 'Free' cases) provides c_{vir} values larger than those expected for virial-

Model	$\log M_{2500}$	$\log M_{500}$	$\log M_{vir}$	$\mathrm{c_{vir}}$	$\log \eta_{OM}$
D08	$13.58^{+0.33}_{-0.28}$	$14.11^{+0.35}_{-0.30}$	$14.32^{+0.36}_{-0.31}$	$2.55^{+0.18}_{-0.16}$	$0.05^{+1.21}_{-0.74}$
A16	$13.03^{+0.09}_{-0.16}$	$13.96^{+0.18}_{-0.37}$	$14.33^{+0.23}_{-0.46}$	$0.88^{+0.61}_{-0.20}$	$-0.59^{+0.79}_{-0.39}$
R19	$13.63^{+0.19}_{-0.25}$	$14.03^{+0.21}_{-0.26}$	$14.19^{+0.21}_{-0.27}$	$3.96^{+0.31}_{-0.23}$	$0.38^{+1.01}_{-0.90}$
T15	$13.55^{+0.28}_{-0.34}$	$13.93^{+0.34}_{-0.37}$	$14.08^{+0.38}_{-0.39}$	$4.76^{+2.81}_{-2.13}$	$0.36^{+1.00}_{-1.03}$
Free	$13.49^{+0.22}_{-0.20}$	$13.82^{+0.28}_{-0.23}$	$13.96^{+0.32}_{-0.24}$	$5.87^{+2.22}_{-2.45}$	$0.42^{+0.97}_{-0.89}$
Tozzi+15	$14.13^{+0.12}_{-0.12}$	$14.55^{+0.10}_{-0.10}$	$14.68^{+0.10}_{-0.10}$	——	——

Table 5.9: Constraints on the NFW VDP parameters ($\log M_{vir}, c_{vir}, \log \eta_{OM}$) for the different cases discussed in the text. Adopting a Bayesian framework, we give the median and 68% confidence range, while the best fit parameters can be slightly different. Note that errors are asymmetric because of the degeneracy in the parameters space. We also reported the mass M_Δ for the typical values $\Delta = (2500, 500)$. As a comparison, we also give M_Δ as inferred in Tozzi et al. (2015) (after correcting for the different cosmology) using X - ray data and the assumption of hydrodynamical equilibrium.

ized systems from simulations. This disagreement could be explained assuming that merging is ongoing in the inner regions thus pushing more matter inside. This would be confirmed by the fact that, in general, a rising galaxy VDP in the inner regions is usually associated with merging processes in the central region (Menci & Fusco-Femiano, 1996). On the other hand, the fact that (Tozzi et al., 2015) values are larger than the ones we infer from VDP fit could be interpreted as a breakdown of the assumption of hydrodynamical equilibrium in the outer regions which is again consistent with a system far from virialization. However, it is also possible that our assumption that galaxies trace DM so that a NFW profile with the same concentration can be used for both components is incorrect. Again, this could be the case if a merging is ongoing in the inner regions. Which hypotheses is the correct one is unfortunately impossible to ascertain with the current VDP dataset.

Moreover, as anticipated, the change in the logarithmic slope of the $\sigma_p(R)$ for $R > R_U$ cannot be matched by any halo profile. Indeed at R > 340 kpc, $\sigma_{DM}(R)$ is always monotonically decreasing (or at most asymptotically constant), while $\sigma_p(R)$ rises. This unusual behaviour might be associated to the presence of distant galaxies with high velocities relative to the galaxy average velocity. Looking at the spatial distribution, this is likely related to a filamentary structure entering into the cluster already reported by Fassbender et al. (2014).

5.9 Discussion

5.9.1 Multiple AGN activity in the cluster core

We confirm that high-z galaxy cluster cores show different properties compared to the z=0 ones. Indeed, no single, early type BCG with low Eddington accretion has been detected. The core of XDCP0044 hosts a large number of interacting star-forming galaxies. Moreover, two luminous, obscured and highly accreting AGN have been captured in two different merger systems ~ 35 kpc away from each other. These two AGN are among the closest AGN pair found at z>1 (De Rosa et al., in prep. and references therein). All these findings underline the rarity and uniqueness of this system that, as it will be discussed, is entirely consistent with the expectation from semi-analytic models and simulations in which the AGN play a leading role in the evolution of the galaxies characterising galaxy clusters.

Few other works have reported multiple AGN activity in the core of high-z galaxy clusters, although not at such small distances (~35 kpc). Hilton et al. (2010) studied the AGN and starburst population within the z = 1.46 galaxy cluster XMMXCS J2215.9-1738, with Chandra X-ray and Spitzer infrared observations, detecting two central X-ray cluster member AGN with a projected distance of ≈90 kpc. Also Casasola et al. (2013) reported the discovery of a radio galaxy and an AGN at a projected distance of ~780 kpc in a galaxy cluster at z~1.4. Stanford et al. (2012) found three AGN, of which one is radio loud, at a minimum projected distance of ~130 kpc from each other, in a z~1.75 galaxy cluster. At z~2.0, Gobat et al. (2013) investigated the AGN population of a fully established galaxy cluster, CL J1449-0856, detecting two X-ray AGN at a projected distance of ~100 kpc.

The discovery of multiple AGN activity is more common in proto-clusters. For example, Digby-North et al. (2010) found five emission-line AGN, two of which X-ray detected, belonging to a z=2.30 proto-cluster in the field of the QSO HS 1700+643, with minimum distance of ~ 500 kpc. The proto-cluster associated to the radio AGN 7C 1756+6520 at z = 1.4156, consists of additional 6 spectroscopical confirmed AGN (Galametz et al., 2010; Casasola et al., 2018) with a minimum projected distance of ~10 kpc and maximum ~3 Mpc. Krishnan et al. (2017) analysed Chandra X-ray imaging data of the Cl 0218.3−0510 proto-cluster at z=1.62 and found a large centrally concentrated over-density of AGN.

In XDCP004, we discover two AGN at a distance of 35 kpc which are merging with other galaxies and their proximity implies a future merger between them. An encounter between two active galaxies is a very rare event and it is much more likely to occur in dense regions of galaxies, as supported by our finding. Our result, together with previous works listed above, suggest that AGN activity is probably triggered during the ongoing formation of the cluster, due to the high number of galaxy encounters established in these dense environments. Simulations suggest that interactions and mergers between gas-rich galaxies can destabilise the gas and cause inflow towards the inner regions, providing potential accreting material for the central BH and triggering starburst activity (e.g., Granato et al., 2004; Hopkins et al., 2008). This scenario is confirmed by several statistical works (e.g. Alberts et al., 2016; Martini et al., 2013) who observed a correlation between AGN and merger activity in both proto-clusters and galaxy clusters, and is also predicted by semi-analytical models (Hopkins et al., 2008; Brodwin et al., 2013; Webb et al., 2015).

Our work seems to agree with this scenario: two obscured and highly accreting AGN caught during an ongoing merger. Moreover, according to semi-analytic models (e.g. De Lucia & Blaizot, 2007) and to several hydrodynamical simulations (e.g. Ragone-Figueroa et al., 2018), it has been proposed that star formation occurs very early in BCG history (mostly before z ~ 3) and is quickly suppressed by AGN feedback in which energy and momentum are released in the form of radiative outflows (e.g. Croton, 2006).

Finally, we also computed the stellar masses of the AGN host galaxies (see next section for more details), finding $log M_{\star} \approx 11.3\ M_{\odot}$ and $11.6\ M_{\odot}$ for `a2` and `b1`, respectively. For both of them, we find that the $M_{BH}/M_{\star}$ ratio is lower than expected at z = 0 (Sani et al., 2011; Häring & Rix, 2004). Such a downward deviation has been also observed for obscured, highly accreting Submillimeter Galaxies (SMGs) at z≈2 (Alexander et al., 2008) and for z < 1 luminous, dust-reddened QSOs by (Urrutia et al., 2012) and might be interpreted as the evidence that in these sources, while the galaxy has grown first and is thus already fully assembled, the BH is catching up and is therefore observed still rapidly growing. According to the different path in the $M_{BH} - M_{\star}$ plane (Volonteri & Bellovary, 2012), these objects will reach the scaling relation at z = 0 from below.

5.9.2 Mass assembly and time scales for the BCG formation

In order to test the scenario which predicts the BCG formation through multiple mergers at this epoch, we estimated the stellar masses of all galaxies resolved with HAWK-I and detected in the SINFONI and KMOS fields (see column 5 in Tab. 5.2). We remind that the HAWK-I images did not allow us to resolve galaxies in `Complex A` and `Complex B`. Masses have been estimated by performing an SED-fitting procedure, by means of the *zphot* code (Fontana et al., 2000), using Bruzual & Charlot (2003) templates, Salpeter (1955) IMF, and Calzetti et al. (2000) extinction. We adopted exponentially declining star formation histories (τ-models) and approximated the redshift of all the sources to $z_c = 1.578$. Assuming that the 7 confirmed cluster members (all 16 galaxies detected by HST) will be forming the BCG, their best-fit masses would sum up to a final stellar mass of $\sim 1.0\,(2.3) \times 10^{12} M_{\odot}$, consistent with the mass range observed for local BCGs (Zhao et al., 2015). For the mass assembly of the BCG, two different scenarios have been analysed.

Following Cavaliere et al. (1992), we considered the case in which `Complex A` and `B` are cluster's sub-clumps, each of which will aggregate to form a cD-like galaxy through a gravitational phase transition. This process is fast and efficient for galaxies with small relative velocities that will form a massive galaxy in a time scale of about $t_{merge} \approx 5 \times t_{cross}$, where $t_{cross} = 2R/v$ is the crossing time, 2R is the size of the system and v is the galaxies' velocity dispersion. In `Complex B`, this process seems to be already in an advanced state, with `b1` dominating the system, while in `Complex A`, several galaxies with similar mass are still visible. However, the resulting merging time (t_{merge}) is similar for both complexes and very short, i.e. $\sim 30\ Myr$ for `Complex A` and $\sim 20\ Myr$ for `Complex B`. This process will lead to the formation of two massive galaxies (galaxy `A` from `Complex A` and galaxy `B` from `Complex B`) at the center of the galaxy cluster which will possibly merge to form the final BCG.

We then consider the two galaxies (`A` and `B`) which have masses as estimated above and velocities given by the mean velocities of the galaxies in the complexes. The time scale for merging galaxy `A` with galaxy `B` and `M` is given by the dynamical friction (Binney & Tremaine, 1987) which describes the time requested by each of them to reach the X-ray centroid, i.e.

$$\mathrm{t_{fric}} = \frac{\mathrm{f}(\epsilon)}{\mathrm{2B(1)log(\Lambda)}} \mathrm{t_{dyn}} \left(\frac{\mathrm{R}}{\mathrm{R_{vir}}}\right)^2 \frac{\mathrm{M_{vir}}}{\mathrm{M_{gal}}} \tag{5.14}$$

with

$$\mathrm{f}(\epsilon) = \frac{\mathrm{v}^2}{\sigma^2}$$

$$B(x) = erf(x) - e^{-x^2} 2x/\sqrt{\pi}$$

$$\mathrm{t_{dyn}} \sim \sqrt{\frac{\mathrm{R}^3}{\mathrm{GM}}}$$

where R_{vir} and M_{vir} are the galaxy cluster virial radius and mass, v the galaxy velocity with respect to the mean redshift of the cluster, σ the cluster velocity dispersion, $log(\Lambda)$ the Coulomb logarithm, M the galaxy mass and R its distance from the X-ray centroid. The t_{fric} computed in this way are $\simeq$ 200 Myr for galaxy `A`, $\sim 30\ Myr$ for galaxy `B` and $\sim 13\ Myr$ for `M`. Putting everything together, according to the first scenario, `XDCP0044` in about $\approx$ 250 Myr could appear as a relaxed cluster with a massive BCG of $\sim 10^{12} M_{\odot}$, located at the center of the X-ray emission.

For the same scenario, we can also include the collision time between a pair of galaxies in a dense system, given by (see for example Aarseth et al., 2008; Vijayaraghavan & Ricker, 2013):

$$t_{coll} = (n\ \Sigma_{coll}\ v_{rel})^{-1} \tag{5.15}$$

in which n is the density of cluster members detected in the SINFONI field, by assuming that all these galaxies are enclosed in a spherical region of diameter $\sim$ 70 kpc, v_{rel} is the velocity shift between two galaxies and Σ_{coll} is their cross section defined as:

$$\Sigma_{coll} \simeq \pi(r_1^2 + r_2^2)\left(1 + \frac{G(M_1 + M_2)}{(r_1 + r_2)v_{rel}^2}\right)\left(\frac{v_{esc}}{v_{rel}}\right)^{2/3} \tag{5.16}$$

with M_i and r_i the mass and the radius of galaxy 1 and 2 and v_{esc} is the escape velocity from the binary system. In this case, the merger between Galaxy A and Galaxy B occurs first, with a collision time of ~200 Myr. After that, Galaxy A+B will incorporate source M in a time of ~100 Myr. The total merger time-scale in this case is therefore ~300 Myr, similar to the friction time.

A second scenario has been analysed in which `Complex A` and `Complex B` do not represent subgroups of the cluster core and therefore all galaxies in the cluster core (i.e. SINFONI field) will directly merge to form the final BCG. Also in this case we computed two different time scales: the binary merging time considering each couple of galaxies (see eq. 5.15) and the dynamical friction time each galaxy needs to reach the X-ray centroid (see eq. 5.14).

For this scenario, we need the stellar masses of each individual galaxy. Since we do not have sufficient photometric coverage for all of them (HAWK-I images do not allow us to distinguish all galaxies), we assumed a constant mass-to-light ratio in K-band (Madau et al., 1998; Bell et al., 2003; Merloni et al., 2010) and derived the masses of the single galaxies using the fluxes in the F160W band, which is the band closest to the K-band, given their redshifts. For the collision time between each couple of galaxies, we find that the central QSO `b1` has very short collision times ($< 0.1\ Gyr$) with all other galaxies, while the time scales computed for all other galaxies are $> 0.2\ Gyr$.

If we consider the case in which all galaxies will merge once they reach the center of the galaxy cluster, assumed to be the X-ray centroid, we find again a dynamical friction time shorter for sources `b1` and `M` compared to other sources. In particular, $t_{fric} \leq 600\ Myr$ for `a2`, $t_{fric} \sim$ 2-3 Gyr for `a4` and `b2`, and $t_{fric} \sim t_H$ for `a1` and `a3`.

From the friction and collisional time scales obtained by assuming this second scenario emerges the importance of the QSO `b1`, the central and most massive galaxy, which will cannibalise all other galaxies in a relatively short time scale (i.e., $\sim$ 100 Myr) reaching first (i.e., $\leq$ 600 Myr) the cluster center (i.e. X-ray centroid).

Concluding, in all considered cases, we find that in a time scale of few hundred Myrs all galaxies observed in the `XDCP0044` cluster core could merge to form a massive central galaxy with $M_{\star} \sim 10^{12} M_{\odot}$. The presence of two AGN also suggests that AGN-driven feedback might play an important role in the BCG formation, by quenching SF and therefore leading to a red and dead galaxy.

6. CONCLUSIONS

The main goals of this Thesis were to better understand (i) the interplay between nuclear activity and the CGM of the host galaxy in a luminous QSO, and (ii) the role of AGN in the early assembly of the BCG. I summarise here the main results of the works presented in Sect. 3 and Sect. 5.

(I) Sect. 3 reports on a VLT/MUSE investigation of the CGM around J1538+08, a z$\approx$ 3.6, broad-line, radio-quiet QSO belonging to the WISSH QSO sample (Bischetti et al., 2017).

- I have discovered a Lyα nebula of ~150 kpc surrounding J1538+08, which is among the most luminous Lyα nebula ($\sim 2 \times 10^{44}$ $erg\ s^{-1}$) reported so far. It appears roughly symmetric on large scales (~several tens of kpc) and exhibits a bright SB peak located at $\sim 10 - 15$ kpc southward of the QSO;
- A CIV nebula has been also significantly ($\sim 5\sigma$) detected with a size of ~75 kpc. This nebula is one of the first discovered around a radio-quiet QSO and exhibits a SB peak and SB profile similar to those found for the Lyα one around J1538+08;
- No significant velocity pattern in the kinematics of Lyα nebula has been found. Remarkably, the $\bar{\sigma_v} \simeq 700$ $km\ s^{-1}$ is higher than the typical values measured so far around radio-quiet QSOs and much more similar to the dispersion observed for Lyα nebulae around HzRGs. Furthermore, Lyα emission regions with $\sigma_v > 1000$ $km\ s^{-1}$ have been revealed at 20-30 kpc from the QSO.
- I have obtained one of the first 2D characterisation via IFU spectroscopy of an ionised outflow at CGM scales (>>10 kpc) around a radio-quiet QSO, by performing the spectral analysis of an extended region with negative skewness value.
    - Specifically, the analysis of the skewness map of the Lyα nebula reveals a banana-shaped region within 30 kpc from the QSO, in which the skewness is negative (see Fig. 3.15) and the Lyα emission profile is significantly asymmetric with a blue tail. This region roughly overlaps

with the SB peak (i.e. within 30 kpc from the QSO) of the Lyα nebula and includes the bulk of the CIV nebula;

- the Lyα spectrum extracted from the region showing negative skewness is well modelled with two Gaussian components (Fig.3.16). This fit results into a systemic narrow ($\sigma_v \sim 500\ km\ s^{-1}$) component and a broader ($\sigma_v \approx 1200\ km\ s^{-1}$) one. The latter is blue-shifted by $v_{shift} \simeq 1500\ km\ s^{-1}$ and is a clear indication of outflowing gas on CGM-scales;

All the reported results clearly suggest the presence of a metal enriched (i.e. non pristine) gas with kinematic features consistent with an outflowing gas component at scales of tens of kpc. Both deeper spatially resolved spectroscopic observations of the CGM around this hyper-luminous QSO and dedicated radiative transfer modellings are necessary in order to confirm and refine this scenario. Specifically, they are needed to accurately characterise the nebulae and outflow physical properties and understand the role of the outflow in transporting metals in the CGM.

(II) In Sect. 5 I have investigated the properties of the galaxy population in the core of `XDCP0044`, one of the most massive galaxy clusters at z~1.6. `XDCP0044` presents a wide multi-wavelength photometric and spectroscopic coverage. Complementary to the already analysed and published Chandra X-ray, optical HAWK-I and IR Herschel data, in this work I have analysed high resolution HST images in F105W, F140W and F160W-bands, integral field spectroscopy obtained with SINFONI in J- and H-band, and KMOS in JY- and H-band. This study also benefits from data taken with ALMA (Band 6) and JVLA (1-2 GHz; see Travascio et al., 2019b, A&A submitted). In particular, I focus on the central core region, ~ 8″ × 8″, corresponding to ~70 kpc × 70 kpc at such redshift. In the following I outline the results of this work.

- High resolution HST F105W, F140W and F160W images reveal the presence of 16 sources in the core of `XDCP0044`. As comparison, previous ground based HAWK-I and Subaru observations allowed to distinguish only 9 of these sources (Fassbender et al., 2014). I find that most of such galaxies are grouped, forming two complexes, i.e. `Complex A` and `Complex B`, as shown in the right panel of Fig. 5.3 and in Fig. 5.4. In particular, `Complex A` includes the BCG identified by Fassbender et al. (2014) through HAWK-I images and consists of 4 to 6 sources at a projected distance of ~20 kpc. `Complex B` consists of 2 galaxies with a projected distance of ~5 kpc, one of which is the central X-ray AGN identified by Tozzi et al. (2015).
- Through IFU SINFONI and KMOS spectroscopy, I have confirmed 7 cluster members. The redshifts range from z=1.556 to z=1.589 ($\Delta z \simeq 0.033$),

consistently with the redshift of the cluster.

- In 2 out of the 7 confirmed cluster members (`a2` in `Complex A` and `b1` in `Complex B`) a broad ($> 2000\ km\ s^{-1}$) Hα emission line is detected. These sources have been therefore classified as BLAGN. They are very luminous ($L_{bol} \sim 10^{45} - 10^{46}$ erg s^{-1}) and host massive ($M_{BH} \sim 3 - 8 \times 10^{7} M_{\odot}$) and highly accreting ($\lambda_{Edd} \sim 0.4 - 0.5$) black holes.

- The Chandra X-ray spectrum of `b1` reveals that it is a moderately luminous and obscured AGN, with X-ray luminosity $L_{[2-10]keV} \sim 1.2 \times 10^{44}\ erg\ s^{-1}$ and $log[N_H/cm^{-2}] \simeq 22.7$. The other AGN (source `a2`), on the contrary, is not detected in the Chandra data. Therefore, its X-ray luminosity is derived from the bolometric luminosity, finding that `a2` is a luminous AGN ($L_{[2-10]keV} \sim 10^{44}\ erg\ s^{-1}$). This implies a very high level of X-ray obscuration ($log[N_H/cm^{-2}] > 23.9$).

- The integrated SFR of the whole central region of `XDCP0044` is $\simeq 452 \pm 58\ M_{\odot}\ yr^{-1}$. This value has been derived by Santos et al. (2015) using Herschel data which however do not allow us to distinguish the different sources. Thanks to the higher resolution ALMA observations, which however cover only half of the field, the SFR of the individual observed sources has been derived. The central AGN `b1` alone contributes to integrated value with a SF ranging from 150 to 490 $M_{\odot}\ yr^{-1}$, depending on the assumed SED. However, additional ALMA observations, covering the whole field, would be necessary to fully characterise the SF distribution among the observed sources.

- JVLA data at 1.5 GHz reveals the presence of a weak radio emission in the `XDCP0044` central region spatially correlated with `Complex A` with a radio power of $L_{1.5GHz} = (3.6 \pm 0.5) \times 10^{24}\ W/Hz$. If associated to a single source, this radio signal would likely be AGN powered. On the contrary, if it is due to SF processes, the measured radio luminosity would translate into a $SFR \sim 100\ \ M_{\odot}\ yr^{-1}$.

- Putting together the 7 cluster members discovered in this work with the 10 already known, `XDCP0044` has in total 17 confirmed cluster members with $1.557 < z < 1.6$. The distribution of the radial velocities is quite large, with values up to $\sim 2600\ km\ s^{-1}$ and a velocity dispersion of $\sigma \simeq 1500 \pm 200\ km\ s^{-1}$. Despite the presence of substructure is not highlighted by the performed statistical tests (HD, dip-test and DS test), the presence of a group of galaxies physically very close with very similar velocities might suggest the presence of substructures in the `XDCP0044` core.

- By comparing the velocity dispersion profile computed for the galaxy cluster members $\sigma_p(R)$ with the dark matter VDP $\sigma_{DM}(R)$, I found a discrepancy at $R > 340$ kpc, which has been interpreted as due to the presence of a substructure, i.e. the known filament at large radii. Moreover, a discrepancy between the VDP and X- ray based mass estimates has been found, which could be explained assuming that merging is ongoing in the inner regions thus pushing more matter inside.

In conclusion, we are witnessing the BCG assembly in one of the densest galaxy cluster core at redshift z∼ 1.6, which is thought to be a crucial formation epoch, when both SF and nuclear activity are at their peak (Madau & Dickinson, 2014; Aird et al., 2015). The core of `XDCP0044` hosts a large number (≥7) of highly star-forming interacting galaxies, grouped in two main complexes, both hosting also AGN activity. These two AGN, at a projected distance of ∼ 35 kpc away from each other, are among the closest AGN pair found at $z > 1$. These results lead to a scenario in which the AGN activity is triggered during the formation of the cluster, when mergers between gas-rich galaxies provide the fuel for the AGN and for triggering starburst activity in galactic nuclei (e.g., Granato et al., 2004; Hopkins et al., 2008). According to these data, I expect to form a typical massive galaxy of $M_\star \sim 10^{12} M_\odot$, hosting a BH with mass $2 \times 10^8 - 10^9\ M_\odot$, in a time scale of few Gyrs.

Additional deep IR, Optical or sub-millimiter observations on the whole field (e.g., Euclid, ALMA) will be crucial to better investigate the properties of this rare system at $z \sim 1.6$, which hosts an over-density of galaxies involved in several processes considered crucial for the BCG formation and galaxy evolution (e.g. mergers, BH accretion and SF activity in dense environment).

REFERENCES

Aarseth S. J., Fall S. M., 1980, ApJ, 236, 43

Aarseth S. J., Tout C. A., Mardling R. A., eds, 2008, The Cambridge N-Body Lectures Lecture Notes in Physics, Berlin Springer Verlag Vol. 760, doi:10.1007/978-1-4020-8431-7.

Abell G. O., Corwin Harold G. J., Olowin R. P., 1989, The Astrophysical Journal Supplement Series, 70, 1

Aird J., Coil A. L., Georgakakis A., Nandra K., Barro G., Pérez-González P. G., 2015, Monthly Notices of the RAS, 451, 1892

Alberts S., et al., 2014, MNRAS, 437, 437

Alberts S., et al., 2016, ApJ, 825, 72

Alexander D. M., et al., 2008, AJ, 135, 1968

Alexander D. M., Swinbank A. M., Smail I., McDermid R., Nesvadba N. P. H., 2010, Monthly Notices of the RAS, 402, 2211

Allen M. G., Groves B. A., Dopita M. A., Sutherland R. S., Kewley L. J., 2008, ApJS, 178, 20

Amodeo S., Ettori S., Capasso R., Sereno M., 2016, A&A, 590, A126

Andreon S., Maughan B., Trinchieri G., Kurk J., 2009, Astronomy and Astrophysics, 507, 147

Antonucci R., 1993, Annual Review of Astron and Astrophys, 31, 473

Arnaud M., Pointecouteau E., Pratt G. W., 2005, Astronomy and Astrophysics, 441, 893

Arrigoni Battaia F., Yang Y., Hennawi J. F., Prochaska J. X., Matsuda Y., Yamada T., Hayashino T., 2015a, ApJ, 804, 26

Arrigoni Battaia F., Hennawi J. F., Prochaska J. X., Cantalupo S., 2015b, ApJ, 809, 163

Arrigoni Battaia F., Hennawi J. F., Cantalupo S., Prochaska J. X., 2016, ApJ, 829, 3

Arrigoni Battaia F., Prochaska J. X., Hennawi J. F., Obreja A., Buck T., Cantalupo S., Dutton A. A., Macciò A. V., 2018a, Monthly Notices of the RAS, 473, 3907

Arrigoni Battaia F., et al., 2018b, A&A, 620, A202

Arrigoni Battaia F., Hennawi J. F., Prochaska J. X., Oñorbe J., Farina E. P., Cantalupo S., Lusso E., 2019, MNRAS, 482, 3162

Ascaso B., Aguerri J. A. L., Varela J., Cava A., Bettoni D., Moles M., D'Onofrio M., 2011, ApJ, 726, 69

Bacon R., et al., 2010, in Proceedings of the SPIE. p. 773508, doi:10.1117/12.856027

Bacon R., et al., 2017, A&A, 608, A1

Balbus S. A., Hawley J. F., 1991, Astrophysical Journal, 376, 214

Baldwin J. A., Phillips M. M., Terlevich R., 1981, PASP, 93, 5

Balogh M. L., Schade D., Morris S. L., Yee H. K. C., Carlberg R. G., Ellingson E., 1998, ApJ, 504, L75

Barnes J. E., Hernquist L. E., 1991, Astrophysical Journal, Letters, 370, L65

Bell E. F., McIntosh D. H., Katz N., Weinberg M. D., 2003, ApJS, 149, 289

Bennert N., Falcke H., Schulz H., Wilson A. S., Wills B. J., 2002, Astrophysical Journal, Letters, 574, L105
Benson A. J., Bower R. G., Frenk C. S., Lacey C. G., Baugh C. M., Cole S., 2003, Astrophysical Journal, 599, 38
Bentz M. C., et al., 2013, ApJ, 767, 149
Berg D. A., Erb D. K., Henry R. B. C., Skillman E. D., McQuinn K. B. W., 2019, Astrophysical Journal, 874, 93
Bergond G., Zepf S. E., Romanowsky A. J., Sharples R. M., Rhode K. L., 2006, A&A, 448, 155
Bernardi M., Hyde J. B., Sheth R. K., Miller C. J., Nichol R. C., 2007, AJ, 133, 1741
Bertin E., Arnouts S., 1996, A&AS, 117, 393
Best P. N., Longair M. S., Roettgering H. J. A., 1998, Monthly Notices of the RAS, 295, 549
Bilton L. E., Pimbblet K. A., 2018, MNRAS, 481, 1507
Binney J., Tremaine S., 1987, Galactic dynamics
Bischetti M., et al., 2017, A&A, 598, A122
Bischetti M., et al., 2019a, arXiv e-prints, p. arXiv:1903.10528
Bischetti M., Maiolino R., Carniani S., Fiore F., Piconcelli E., Fluetsch A., 2019b, A&A, 630, A59
Biviano A., Katgert P., Thomas T., Adami C., 2002, A&A, 387, 8
Blanton M. R., Moustakas J., 2009, ARA&A, 47, 159
Blanton M. R., Eisenstein D., Hogg D. W., Schlegel D. J., Brinkmann J., 2005, ApJ, 629, 143
Blanton E. L., Randall S. W., Douglass E. M., Sarazin C. L., Clarke T. E., McNamara B. R., 2009, Astrophysical Journal, Letters, 697, L95
Blumenthal G. R., Faber S. M., Primack J. R., Rees M. J., 1984, Nature, 311, 517
Blustin A. J., Page M. J., Fuerst S. V., Brand uardi-Raymont G., Ashton C. E., 2005, Astronomy and Astrophysics, 431, 111
Bond J. R., Cole S., Efstathiou G., Kaiser N., 1991, Astrophysical Journal, 379, 440
Borisova E., et al., 2016, ApJ, 831, 39
Bose S., Eisenstein D. J., Hernquist L., Pillepich A., Nelson D., Marinacci F., Springel V., Vogelsberger M., 2019, arXiv e-prints, p. arXiv:1905.08799
Boselli A., Gavazzi G., 2006, PASP, 118, 517
Bouché N., et al., 2016, ApJ, 820, 121
Bournaud F., Combes F., Jog C. J., Puerari I., 2005, Astronomy and Astrophysics, 438, 507
Bowen D. V., Chelouche D., Jenkins E. B., Tripp T. M., Pettini M., York D. G., Frye B. L., 2016, ApJ, 826, 50
Bower R. G., Lucey J. R., Ellis R. S., 1992, Monthly Notices of the RAS, 254, 601
Boyle B. J., Terlevich R. J., 1998, Monthly Notices of the RAS, 293, L49
Brandt W. N., Hasinger G., 2005, ARA&A, 43, 827

Brinchmann J., Charlot S., White S. D. M., Tremonti C., Kauffmann G., Heckman T., Brinkmann J., 2004, Monthly Notices of the RAS, 351, 1151
Brodwin M., et al., 2013, ApJ, 779, 138
Brown M. J. I., et al., 2017, ApJ, 847, 136
Bruni G., et al., 2019, arXiv e-prints, p. arXiv:1908.09673
Bruzual G., Charlot S., 2003, MNRAS, 344, 1000
Bufanda E., et al., 2017, Monthly Notices of the RAS, 465, 2531
Butcher H., Oemler A. J., 1978, The Astrophysical Journal, 219, 18
Cai Z., et al., 2017a, ApJ, 837, 71
Cai Z., et al., 2017b, Astrophysical Journal, 837, 71
Cai Z., et al., 2019, arXiv e-prints, p. arXiv:1909.11098
Calzetti D., Armus L., Bohlin R. C., Kinney A. L., Koornneef J., Storchi-Bergmann T., 2000, ApJ, 533, 682
Cantalupo S., Porciani C., Lilly S. J., Miniati F., 2005, Astrophysical Journal, 628, 61
Cantalupo S., Lilly S. J., Haehnelt M. G., 2012, Monthly Notices of the RAS, 425, 1992
Cantalupo S., Arrigoni-Battaia F., Prochaska J. X., Hennawi J. F., Madau P., 2014, Nature, 506, 63
Cantalupo S., et al., 2019, Monthly Notices of the RAS, 483, 5188
Casasola V., Magrini L., Combes F., Mignano A., Sani E., Paladino R., Fontani F., 2013, Astronomy and Astrophysics, 558, A60
Casasola V., et al., 2018, A&A, 618, A128
Castellano M., et al., 2007, The Astrophysical Journal, 671, 1497
Cavaliere A. G., Gursky H., Tucker W. H., 1971, Nature, 231, 437
Cavaliere A., Colafrancesco S., Menci N., 1992, ApJ, 392, 41
Chen H.-W., et al., 2019, Monthly Notices of the RAS, 484, 431
Chiaberge M., Capetti A., Macchetto F. D., Rosati P., Tozzi P., Tremblay G. R., 2010, The Astrophysical Journal, 710, L107
Chincarini G., Rood H. J., 1977, ApJ, 214, 351
Chung A. S., Dijkstra M., Ciardi B., Kakiichi K., Naab T., 2019, MNRAS, 484, 2420
Cicone C., Feruglio C., Maiolino R., Fiore F., Piconcelli E., Menci N., Aussel H., Sturm E., 2012, Astronomy and Astrophysics, 543, A99
Cicone C., et al., 2014, Astronomy and Astrophysics, 562, A21
Cicone C., et al., 2015, Astronomy and Astrophysics, 574, A14
Cohn J. D., White M., 2005, Astroparticle Physics, 24, 316
Colless M., Dunn A. M., 1996, ApJ, 458, 435
Conselice C. J., 2006, ApJ, 638, 686
Conselice C. J., Rajgor S., Myers R., 2008, MNRAS, 386, 909
Cooke K. C., Kartaltepe J. S., Tyler K. D., Darvish B., Casey C. M., Le Fèvre O., Salvato M., Scoville N., 2019, ApJ, 881, 150
Cordero J. P., Campusano L. E., De Propris R., Haines C. P., Weinzirl T., Jogee S., 2016, ApJ, 817, L6
Costa Tiago S. D. H. M. G., 2014, MNRAS, 444, 2355

Cowie L. L., Songaila A., Kim T.-S., Hu E. M., 1995, Astronomical Journal, 109, 1522
Cowie L. L., Songaila A., Hu E. M., Cohen J. G., 1996, Astronomical Journal, 112, 839
Cox T. J., Jonsson P., Primack J. R., Somerville R. S., 2006, MNRAS, 373, 1013
Crenshaw D. M., et al., 2003, Astrophysical Journal, 594, 116
Cresci G., Maiolino R., 2018, Nature Astronomy, 2, 179
Cresci G., et al., 2015, ApJ, 799, 82
Croton D. J., 2006, MNRAS, 369, 1808
Croton D. J., et al., 2006, Monthly Notices of the RAS, 365, 11
Csabai I., et al., 2003, The Astronomical Journal, 125, 580
Cucciati O., et al., 2014, Astronomy and Astrophysics, 570, A16
Darvish B., Mobasher B., Sobral D., Rettura A., Scoville N., Faisst A., Capak P., 2016, ApJ, 825, 113
Davé R., et al., 2001, Astrophysical Journal, 552, 473
Davies R. I., 2007, MNRAS, 375, 1099
De Lucia G., Blaizot J., 2007, MNRAS, 375, 2
Dekel A., Birnboim Y., 2006, MNRAS, 368, 2
Dekel A., Sari R., Ceverino D., 2009, Astrophysical Journal, 703, 785
Delahaye A. G., et al., 2017, ApJ, 843, 126
Di Matteo T., Springel V., Hernquist L., 2005, Nature, 433, 604
Digby-North J. A., et al., 2010, MNRAS, 407, 846
Dijkstra M., 2017, arXiv e-prints, p. arXiv:1704.03416
Dijkstra M., Haiman Z., Spaans M., 2006, Astrophysical Journal, 649, 37
Draine B. T., 2011, Physics of the Interstellar and Intergalactic Medium
Dressler A., 1980, The Astrophysical Journal, 236, 351
Dressler A., Shectman S. A., 1988, AJ, 95, 985
Dressler A., Thompson I. B., Shectman S. A., 1985, Astrophysical Journal, 288, 481
Dubinski J., 1998, ApJ, 502, 141
Dubinski J., Carlberg R. G., 1991, The Astrophysical Journal, 378, 496
Duffy A. R., Schaye J., Kay S. T., Dalla Vecchia C., 2008, MNRAS, 390, L64
Duras F., et al., 2017, A&A, 604, A67
Einasto M., 2012, arXiv e-prints,
Elbaz D., et al., 2007, A&A, 468, 33
Elvis M., 2000, New Astronomy Reviews, 44, 559
Elvis M., Maccacaro T., Wilson A. S., Ward M. J., Penston M. V., Fosbury R. A. E., Perola G. C., 1978, MNRAS, 183, 129
Erb D. K., Pettini M., Shapley A. E., Steidel C. C., Law D. R., Reddy N. A., 2010, Astrophysical Journal, 719, 1168
Fabian A. C., 1994, ARA&A, 32, 277
Fabian A. C., 1999, Monthly Notices of the RAS, 308, L39
Fabian A. C., 2012, ARA&A, 50, 455
Fabian A. C., Nulsen P. E. J., 1977, Monthly Notices of the RAS, 180, 479
Fabian A. C., et al., 2000, Monthly Notices of the RAS, 318, L65

Fanaroff B. L., Riley J. M., 1974, MNRAS, 167, 31P
Fassbender R., et al., 2011a, New Journal of Physics, 13, 125014
Fassbender R., et al., 2011b, New Journal of Physics, 13, 125014
Fassbender R., et al., 2011c, Astronomy and Astrophysics, 527, L10
Fassbender R., Šuhada R., Nastasi A., 2012, Advances in Astronomy, 2012, 138380
Fassbender R., et al., 2014, A&A, 568, A5
Faucher-Giguère Claude-André & Kereš D., 2011, Monthly Notices of the RAS, 412, L118
Ferrarese L., Ford H., 2005, Space Science Reviews, 116, 523
Feruglio C., Maiolino R., Piconcelli E., Menci N., Aussel H., Lamastra A., Fiore F., 2010, Astronomy and Astrophysics, 518, L155
Feruglio C., et al., 2013, Astronomy and Astrophysics, 549, A51
Feruglio C., et al., 2015, Astronomy and Astrophysics, 583, A99
Fiore F., et al., 2017, A&A, 601, A143
Fischer J., et al., 2010, Astronomy and Astrophysics, 518, L41
Fluetsch A., et al., 2019, MNRAS, 483, 4586
Fontana A., D'Odorico S., Poli F., Giallongo E., Arnouts S., Cristiani S., Moorwood A., Saracco P., 2000, AJ, 120, 2206
Ford A. B., Davé R., Oppenheimer B. D., Katz N., Kollmeier J. A., Thompson R., Weinberg D. H., 2014, Monthly Notices of the RAS, 444, 1260
Frenk C. S., White S. D. M., 2012, Annalen der Physik, 524, 507
Fukumura K., Kazanas D., Contopoulos I., Behar E., 2010, ApJ, 715, 636
Fumagalli M., O'Meara J. M., Prochaska J. X., 2011, Science, 334, 1245
Galametz A., et al., 2009, ApJ, 694, 1309
Galametz A., Stern D., Stanford S. A., De Breuck C., Vernet J., Griffith R. L., Harrison F. A., 2010, A&A, 516, A101
Gallazzi A., Brinchmann J., Charlot S., White S. D. M., 2008, Monthly Notices of the RAS, 383, 1439
Gebhardt K., et al., 2000, Astrophysical Journal, Letters, 543, L5
Gibson R. R., et al., 2009, ApJ, 692, 758
Gilli R., Comastri A., Hasinger G., 2007, A&A, 463, 79
Ginolfi M., Maiolino R., Carniani S., Arrigoni Battaia F., Cantalupo S., Schneider R., 2018, Monthly Notices of the RAS, 476, 2421
Girardi M., Fadda D., Giuricin G., Mardirossian F., Mezzetti M., Biviano A., 1996, ApJ, 457, 61
Girardi M., Demarco R., Rosati P., Borgani S., 2005, A&A, 442, 29
Gisler G. R., 1978, Monthly Notices of the RAS, 183, 633
Gitti M., Brighenti F., McNamara B. R., 2012, Advances in Astronomy, 2012, 950641
Gobat R., 2010, OT1_rgobat_1: Unveiling the nature of strong galaxy activity in an X-ray detected galaxy cluster at z=2.07, Herschel Space Observatory Proposal
Gobat R., et al., 2011, A&A, 526, A133
Gobat R., et al., 2013, ApJ, 776, 9

Gonzalez A. H., Sivanandam S., Zabludoff A. I., Zaritsky D., 2013, Astrophysical Journal, 778, 14
Goto T., et al., 2008, Publications of the Astronomical Society of Japan, 60, S531
Gott J. Richard I., Gunn J. E., 1971, Astrophysical Journal, Letters, 169, L13
Granato G. L., De Zotti G., Silva L., Bressan A., Danese L., 2004, ApJ, 600, 580
Green J. C., et al., 2012, Astrophysical Journal, 744, 60
Greene J. E., Ho L. C., 2005, ApJ, 630, 122
Gronke M., Dijkstra M., 2016, ApJ, 826, 14
Gruppioni C., et al., 2015, Monthly Notices of the RAS, 451, 3419
Gunn J. E., Gott III J. R., 1972, ApJ, 176, 1
Gunn J. E., Peterson B. A., 1965, Astrophysical Journal, 142, 1633
Hafen K., Wheaton J. M., Macfarlane W., 2016, in AGU Fall Meeting Abstracts. pp H53E–1745
Haggard D., Green P. J., Anderson S. F., Constantin A., Aldcroft T. L., Kim D.-W., Barkhouse W. A., 2010, Astrophysical Journal, 723, 1447
Haines C. P., et al., 2009, ApJ, 704, 126
Häring N., Rix H.-W., 2004, ApJ, 604, L89
Harrison E. R., 1974, ApJ, 191, L51
Harrison C. M., 2017, Nature Astronomy, 1, 0165
Hartigan J. A., Hartigan P. M., 1985, Ann. Stat., 13, 70
Heckman T. M., Best P. N., 2014, Annual Review of Astron and Astrophys, 52, 589
Heckman T. M., Lehnert M. D., Miley G. K., van Breugel W., 1991, Astrophysical Journal, 381, 373
Hennawi J. F., Prochaska X., 2007, Quasars Probing Quasars: Shedding Light on the Environments, Emission Geometry, and Lifetimes of Quasars, NOAO Proposal
Hennawi J. F., Prochaska J. X., 2013, ApJ, 766, 58
Hennawi J. F., Prochaska J. X., Cantalupo S., Arrigoni-Battaia F., 2015, Science, 348, 779
Henry J. P., et al., 2010, The Astrophysical Journal, 725, 615
Hernquist L., 1989, Nature, 340, 687
Hernquist L., Mihos J. C., 1995, Astrophysical Journal, 448, 41
Hewett P. C., Foltz C. B., 2003, Astronomical Journal, 125, 1784
Hilton M., et al., 2010, ApJ, 718, 133
Hobbs A., Read J., Nicola A., 2015, Monthly Notices of the RAS, 452, 3593
Holt J., Tadhunter C. N., Morganti R., 2008, Monthly Notices of the RAS, 387, 639
Hopkins P. F., Hernquist L., Cox T. J., Di Matteo T., Robertson B., Springel V., 2006, ApJS, 163, 1
Hopkins P. F., Richards G. T., Hernquist L., 2007, Astrophysical Journal, 654, 731
Hopkins P. F., Hernquist L., Cox T. J., Kereš D., 2008, ApJS, 175, 356
Hopkins P. F., et al., 2010, ApJ, 724, 915
Hou A., et al., 2012, MNRAS, 421, 3594

Houghton R. C. W., 2015, Monthly Notices of the Royal Astronomical Society, 451, 3427
Humphrey A., 2019, MNRAS, 486, 2102
Humphrey A., Villar-Martín M., Fosbury R., Vernet J., di Serego Alighieri S., 2006, MNRAS, 369, 1103
Hwang H. S., Park C., Elbaz D., Choi Y. Y., 2012, Astronomy and Astrophysics, 538, A15
Ilbert O., et al., 2015, A&A, 579, A2
Johnson S. D., Chen H.-W., Mulchaey J. S., 2015, Monthly Notices of the RAS, 449, 3263
Jordán A., Côté P., West M. J., Marzke R. O., Minniti D., Rejkuba M., 2004, AJ, 127, 24
Kaiser N., 1986, Monthly Notices of the Royal Astronomical Society, 222, 323
Kaspi S., Smith P. S., Netzer H., Maoz D., Jannuzi B. T., Giveon U., 2000, ApJ, 533, 631
Kaspi S., et al., 2001, ApJ, 554, 216
Kauffmann G., et al., 2003a, Monthly Notices of the RAS, 341, 54
Kauffmann G., et al., 2003b, MNRAS, 346, 1055
Kauffmann G., White S. D. M., Heckman T. M., Ménard B., Brinchmann J., Charlot S., Tremonti C., Brinkmann J., 2004, Monthly Notices of the RAS, 353, 713
Kellermann K. I., Sramek R., Schmidt M., Shaffer D. B., Green R., 1989, Astronomical Journal, 98, 1195
Kenney J. D. P., van Gorkom J. H., Vollmer B., 2004, AJ, 127, 3361
Kennicutt Jr. R. C., Schweizer F., Barnes J. E., Friedli D., Martinet L., Pfenniger D., eds, 1998, Galaxies: Interactions and Induced Star Formation
Kereš D., Katz N., Weinberg D. H., Davé R., 2005, MNRAS, 363, 2
King A., 2003, Astrophysical Journal, Letters, 596, L27
King A., 2005, Astrophysical Journal, Letters, 635, L121
King A. R., 2010, in Maraschi L., Ghisellini G., Della Ceca R., Tavecchio F., eds, Astronomical Society of the Pacific Conference Series Vol. 427, Accretion and Ejection in AGN: a Global View. p. 315
King A. R. Z. K. P. C., 2011, Monthly Notices of the RAS, 415, L6
King A. R., Pounds K. A., 2014, MNRAS, 437, L81
King A., Pounds K., 2015, ARA&A, 53, 115
Kodama T., Arimoto N., 1997, A&A, 320, 41
Kodama T., Arimoto N., Barger A. J., Arag'on-Salamanca A., 1998, A&A, 334, 99
Kormendy J., Richstone D., 1995, Annual Review of Astron and Astrophys, 33, 581
Koss M. J., et al., 2018, Nature, 563, 214
Kravtsov A. V., Borgani S., 2012, Annual Review of Astron and Astrophys, 50, 353
Krishnan C., et al., 2017, Monthly Notices of the RAS, 470, 2170
Krolik J. H., McKee C. F., Tarter C. B., 1981, Astrophysical Journal, 249, 422
Kuo C. Y., et al., 2011, Astrophysical Journal, 727, 20

LaMassa S. M., et al., 2015, ApJ, 800, 144

Landoni M., Falomo R., Treves A., Scarpa R., Farina E. P., 2016, Monthly Notices of the RAS, 457, 267

Lauer T. R., Postman M., Strauss M. A., Graves G. J., Chisari N. E., 2014, ApJ, 797, 82

Laursen P., Sommer-Larsen J., Andersen A. C., 2009, ApJ, 704, 1640

Lehmer B. D., et al., 2009, ApJ, 691, 687

Lehner N., Wotta C. B., Howk J. C., O'Meara J. M., Oppenheimer B. D., Cooksey K. L., 2019, arXiv e-prints, p. arXiv:1902.10147

Levenson N. A., 2014, in Mickaelian A. M., Sanders D. B., eds, IAU Symposium Vol. 304, Multiwavelength AGN Surveys and Studies. pp 112–118, doi:10.1017/S1743921314003512

Liu C., Hao L., Wang H., Yang X., 2019, ApJ, 878, 69

Łokas E. L., Wojtak R., Gottlöber S., Mamon G. A., Prada F., 2006, MNRAS, 367, 1463

Lotz J. M., et al., 2017, The Astrophysical Journal, 837, 97

Lubin L. M., Bahcall N. A., 1993, ApJ, 415, L17

Luminari A., Piconcelli E., Tombesi F., Zappacosta L., Fiore F., Piro L., Vagnetti F., 2018, A&A, 619, A149

Lynden-Bell D., 1969, Nature, 223, 690

Lynds R., 1971, Astrophysical Journal, Letters, 164, L73

Ma C. J., et al., 2015, ApJ, 806, 257

Madau P., Dickinson M., 2014, Annual Review of Astron and Astrophys, 52, 415

Madau P., Ferguson H. C., Dickinson M. E., Giavalisco M., Steidel C. C., Fruchter A., 1996, MNRAS, 283, 1388

Madau P., Pozzetti L., Dickinson M., 1998, ApJ, 498, 106

Madejski G. G., Sikora M., 2016, ARA&A, 54, 725

Magliocchetti M., et al., 2014, MNRAS, 442, 682

Maiolino R., et al., 2012, MNRAS, 425, L66

Mamon G. A., Łokas E. L., 2005, MNRAS, 363, 705

Mancone C. L., et al., 2012, ApJ, 761, 141

Marconi A., Capetti A., Axon D. J., Koekemoer A., Macchetto D., Schreier E. J., 2001, Astrophysical Journal, 549, 915

Marconi A., Risaliti G., Gilli R., Hunt L. K., Maiolino R., Salvati M., 2004, Monthly Notices of the RAS, 351, 169

Marino R. A., et al., 2019, ApJ, 880, 47

Martin C., 2019, Bulletin of the AAS, 51, 510

Martinet N., et al., 2015, A&A, 575, A116

Martini P., Mulchaey J. S., Kelson D. D., 2007, Astrophysical Journal, 664, 761

Martini P., Sivakoff G. R., Mulchaey J. S., 2009, ApJ, 701, 66

Martini P., et al., 2013, ApJ, 768, 1

McNamara B. R., Nulsen P. E. J., 2012, New Journal of Physics, 14, 055023

McNamara B. R., Wise M., Sarazin C. L., Jannuzi B. T., Elston R., 1996, ApJ, 466, L9

Medezinski E., Umetsu K., Okabe N., Nonino M., Molnar S., Massey R., Dupke R., Merten J., 2016, The Astrophysical Journal, 817, 24
Mei S., et al., 2015, ApJ, 804, 117
Menci N., Fusco-Femiano R., 1996, ApJ, 472, 46
Merloni A., Heinz S., 2007, MNRAS, 381, 589
Merloni A., Heinz S., 2013, Evolution of Active Galactic Nuclei. p. 503, doi:10.1007/978-94-007-5609-0_11
Merloni A., et al., 2010, ApJ, 708, 137
Merritt D., 1985, ApJ, 289, 18
Mihos J. C., 2004, in Mulchaey J. S., Dressler A., Oemler A., eds, Clusters of Galaxies: Probes of Cosmological Structure and Galaxy Evolution. p. 277
Modigliani A., et al., 2007, ArXiv Astrophysics e-prints,
Morganti R., 2017, Frontiers in Astronomy and Space Sciences, 4, 42
Morganti R., Frieswijk W., Oonk R. J. B., Oosterloo T., Tadhunter C., 2013, Astronomy and Astrophysics, 552, L4
Mukhanov V. F., Feldman H. A., Brandenberger R. H., 1992, Physics Reports, 215, 203
Muzzin A., et al., 2012, ApJ, 746, 188
Narayan R., Yi I., 1994, Astrophysical Journal, Letters, 428, L13
Narayanan D., et al., 2010, MNRAS, 407, 1701
Nardini E., et al., 2015, Science, 347, 860
Nastasi A., Scodeggio M., Fassbender R., Böhringer H., Pierini D., Verdugo M., Garilli B. M., Franzetti P., 2013, A&A, 550, A9
Nastasi A., et al., 2014, A&A, 564, A17
Navarro J. F., Frenk C. S., White S. D. M., 1995, Monthly Notices of the Royal Astronomical Society, 275, 56
Navarro J. F., Frenk C. S., White S. D. M., 1997, ApJ, 490, 493
Nesvadba N. P. H., Lehnert M. D., Eisenhauer F., Gilbert A., Tecza M., Abuter R., 2006, Astrophysical Journal, 650, 693
Newman A. B., Treu T., Ellis R. S., Sand D. J., 2013, ApJ, 765, 25
Nicastro F., et al., 2018, Nature, 558, 406
Oppenheimer B. D., Davé R., Kereš D., Fardal M., Katz N., Kollmeier J. A., Weinberg D. H., 2010, Monthly Notices of the RAS, 406, 2325
Ostriker J. P., Hausman M. A., 1977, ApJ, 217, L125
Padovani P., 2017, Nature Astronomy, 1, 0194
Papovich C., et al., 2008, Survey of IRAC-Selected Galaxy Cluster Candidates at z>1.3, NOAO Proposal
Papovich C., et al., 2010, ApJ, 716, 1503
Pearce C. J. J., et al., 2017, The Astrophysical Journal, 845, 81
Peng Y.-j., et al., 2010, ApJ, 721, 193
Peng Y., Maiolino R., Cochrane R., 2015, Nature, 521, 192
Peterson B. M., 1997, An Introduction to Active Galactic Nuclei

Peterson B. M., 2004, in Storchi-Bergmann T., Ho L. C., Schmitt H. R., eds, IAU Symposium Vol. 222, The Interplay Among Black Holes, Stars and ISM in Galactic Nuclei. pp 15–20 (`arXiv:astro-ph/0404539`), doi:10.1017/S1743921304001358

Piccinotti G., Mushotzky R. F., Boldt E. A., Holt S. S., Marshall F. E., Serlemitsos P. J., Shafer R. A., 1982, The Astrophysical Journal, 253, 485

Piconcelli E., Jimenez-Bailón E., Guainazzi M., Schartel N., Rodríguez-Pascual P. M., Santos-Lleó M., 2005, Astronomy and Astrophysics, 432, 15

Pimbblet K. A., Penny S. J., Davies R. L., 2014, MNRAS, 438, 3049

Pinkney J., Roettiger K., Burns J. O., Bird C. M., 1996, ApJS, 104, 1

Planck Collaboration et al., 2016, Astronomy and Astrophysics, 594, A13

Planck Collaboration et al., 2018, arXiv e-prints,

Popesso P., Biviano A., Rodighiero G., Baronchelli I., Salvato M., Saintonge A., 2012, A&A, 537, A58

Postman M., Lauer T. R., 1995, ApJ, 440, 28

Pounds K. A., Reeves J. N., 2009, Monthly Notices of the RAS, 397, 249

Prescott M. K. M., Martin C. L., Dey A., 2015, Astrophysical Journal, 799, 62

Prochaska J. X., Hennawi J. F., 2009, Astrophysical Journal, 690, 1558

Prochaska J. X., Lau M. W., Hennawi J. F., 2014, Astrophysical Journal, 796, 140

Ragagnin A., Dolag K., Moscardini L., Biviano A., D'Onofrio M., 2019, MNRAS, 486, 4001

Ragone-Figueroa C., Granato G. L., Ferraro M. E., Murante G., Biffi V., Borgani S., Planelles S., Rasia E., 2018, MNRAS, 479, 1125

Rakshit S., et al., 2019, arXiv e-prints, p. arXiv:1910.02412

Ramos Almeida C., Ricci C., 2017, Nature Astronomy, 1, 679

Rauch M., et al., 2008, Astrophysical Journal, 681, 856

Reichard T. A., et al., 2003, AJ, 125, 1711

Ribaudo J., Lehner N., Howk J. C., Werk J. K., Tripp T. M., Prochaska J. X., Meiring J. D., Tumlinson J., 2011, Astrophysical Journal, 743, 207

Ribeiro H. V., Antonio F. J., Alves L. G. A., Lenzi E. K., Mendes R. S., 2013, EPL (Europhysics Letters), 104, 69001

Ricci C., et al., 2017, MNRAS, 468, 1273

Risaliti G., Elvis M., 2010, A&A, 516, A89

Risaliti G., Maiolino R., Salvati M., 1999, Astrophysical Journal, 522, 157

Risaliti G., Elvis M., Fabbiano G., Baldi A., Zezas A., Salvati M., 2007, ApJ, 659, L111

Rodriguez-Gomez V., et al., 2015, MNRAS, 449, 49

Rosati P., et al., 2004, The Astronomical Journal, 127, 230

Ruderman J. T., Ebeling H., 2005, Astrophysical Journal, Letters, 623, L81

Runnoe J. C., Brotherton M. S., Shang Z., 2012, MNRAS, 422, 478

Rupke D. S. N., Veilleux S., 2013, Astrophysical Journal, Letters, 775, L15

Russell H. R., Sanders J. S., Fabian A. C., Baum S. A., Donahue M., Edge A. C., McNamara B. R., O'Dea C. P., 2010, Monthly Notices of the RAS, 406, 1721

Salim S., et al., 2007, Astrophysical Journals, 173, 267

Salomé P., Combes F., 2003, A&A, 412, 657
Salpeter E. E., 1955, ApJ, 121, 161
Salpeter E. E., 1964, Astrophysical Journal, 140, 796
Sani E., Marconi A., Hunt L. K., Risaliti G., 2011, MNRAS, 413, 1479
Santini P., et al., 2009, Astronomy and Astrophysics, 504, 751
Santos J. S., et al., 2011, A&A, 531, L15
Santos J. S., et al., 2015, MNRAS, 447, L65
Sarazin C., 2001, Merger Shocks in Clusters of Galaxies, Chandra Proposal
Schaye J., Aguirre A., Kim T.-S., Theuns T., Rauch M., Sargent W. L. W., 2003, Astrophysical Journal, 596, 768
Schechter P., 1976, Astrophysical Journal, 203, 297
Schmidt M., Green R. F., 1983, Astrophysical Journal, 269, 352
Seyfert C. K., 1943, Contributions from the Mount Wilson Observatory / Carnegie Institution of Washington, 671, 1
Shakura N. I., Sunyaev R. A., 1973, Astronomy and Astrophysics, 500, 33
Shankar F., Weinberg D. H., Miralda-Escudé J., 2009, Astrophysical Journal, 690, 20
Shankar F., et al., 2016, Monthly Notices of the RAS, 460, 3119
Shen Y., Liu X., 2012, Astrophysical Journal, 753, 125
Shen Y., Greene J. E., Strauss M. A., Richards G. T., Schneider D. P., 2008, Astrophysical Journal, 680, 169
Shen S., Madau P., Aguirre A., Guedes J., Mayer L., Wadsley J., 2012, Astrophysical Journal, 760, 50
Shen Y., et al., 2016, ApJ, 831, 7
Shimakawa R., Kodama T., Tadaki K. I., Tanaka I., Hayashi M., Koyama Y., 2014, MNRAS, 441, L1
Silk J., Rees M. J., 1998, Astronomy and Astrophysics, 331, L1
Silva M., et al., 2018, Monthly Notices of the RAS, 474, 3649
Soltan A., 1982, Monthly Notices of the RAS, 200, 115
Somerville R. S., Hopkins P. F., Cox T. J., Robertson B. E., Hernquist L., 2008, Monthly Notices of the RAS, 391, 481
Spergel D. N., et al., 2003, Astrophysical Journals, 148, 175
Spinoglio L., Malkan M. A., 1989, Astrophysical Journal, 342, 83
Springel V., 2005, Monthly Notices of the RAS, 364, 1105
Springel V., Di Matteo T., Hernquist L., 2005, MNRAS, 361, 776
Stanford S. A., et al., 2006, ApJ, 646, L13
Stanford S. A., et al., 2012, ApJ, 753, 164
Steidel C. C., Erb D. K., Shapley A. E., Pettini M., Reddy N., Bogosavljević M., Rudie G. C., Rakic O., 2010, Astrophysical Journal, 717, 289
Steidel C. C., Bogosavljević M., Shapley A. E., Kollmeier J. A., Reddy N. A., Erb D. K., Pettini M., 2011, Astrophysical Journal, 736, 160
Stewart K. R., 2017, in Fox A., Davé R., eds, Astrophysics and Space Science Library Vol. 430, Gas Accretion onto Galaxies. p. 249 (`arXiv:1612.00513`), doi:10.1007/978-

3-319-52512-9_11
Stewart K. R., Brooks A. M., Bullock J. S., Maller A. H., Diemand J., Wadsley J., Moustakas L. A., 2013, Astrophysical Journal, 769, 74
Stinson G. S., Bailin J., Couchman H., Wadsley J., Shen S., Nickerson S., Brook C., Quinn T., 2010, Monthly Notices of the RAS, 408, 812
Stone M., Veilleux S., Meléndez M., Sturm E., Graciá-Carpio J., González-Alfonso E., 2016, Astrophysical Journal, 826, 111
Struble M. F., 1979, Ap&SS, 64, 319
Swinbank A. M., Chapman S. C., Smail I., Lindner C., Borys C., Blain A. W., Ivison R. J., Lewis G. F., 2006, Monthly Notices of the RAS, 371, 465
Tadhunter C., 2016, A&ARv, 24, 10
Teng S. H., et al., 2014, ApJ, 785, 19
Thorne K. S., 1974, Astrophysical Journal, 191, 507
Tombesi F., Sambruna R. M., Reeves J. N., Braito V., Ballo L., Gofford J., Cappi M., Mushotzky R. F., 2010, Astrophysical Journal, 719, 700
Tombesi F., Cappi M., Reeves J. N., Braito V., 2012, Monthly Notices of the Royal Astronomical Society, 422, L1
Tozzi P., Santos J. S., Nonino M., Rosati P., Borgani S., Sartoris B., Altieri B., Sanchez-Portal M., 2013, A&A, 551, A45
Tozzi P., et al., 2015, ApJ, 799, 93
Travascio A., et al., 2019b, Astronomy and Astrophysics, Submitted
Travascio A., et al., 2019a, Astronomy and Astrophysics, Submitted
Tremonti C. A., Moustakas J., Diamond-Stanic A. a. M., 2007, Astrophysical Journal, Letters, 663, L77
Tripp T. M., et al., 2011, Science, 334, 952
Truemper J., 1992, Quarterly Journal of the Royal Astronomical Society, 33, 165
Tucker W., et al., 1998, Astrophysical Journal, Letters, 496, L5
Tumlinson J., 2012, COS-Halos: New FUV Measurements of Baryons and Metals in the Inner Circumgalactic Medium, HST Proposal
Tumlinson J., et al., 2011, Astrophysical Journal, 733, 111
Tumlinson J., Peeples M. S., Werk J. K., 2017, Annual Review of Astron and Astrophys, 55, 389
Turner M. L., Schaye J., Crain R. A., Theuns T., Wendt M., 2016, Monthly Notices of the RAS, 462, 2440
Ueda Y., Akiyama M., Hasinger G., Miyaji T., Watson M. G., 2014, Astrophysical Journal, 786, 104
Urrutia T., Lacy M., Spoon H., Glikman E., Petric A., Schulz B., 2012, ApJ, 757, 125
Urry C. M., Padovani P., 1995, Publications of the ASP, 107, 803
Vanden Berk D. E., et al., 2001, Astronomical Journal, 122, 549
Veilleux S., et al., 2013, Astrophysical Journal, 776, 27
Venemans B. P., et al., 2007, Astronomy and Astrophysics, 461, 823
Verhamme A., Schaerer D., Maselli A., 2006, Astronomy and Astrophysics, 460, 397

Véron-Cetty M. P., Véron P., 2003, Astronomy and Astrophysics, 412, 399
Vestergaard M., 2002, Astrophysical Journal, 571, 733
Vietri G., et al., 2018, A&A, 617, A81
Vijayaraghavan R., Ricker P. M., 2013, MNRAS, 435, 2713
Villar-Martín M., Tadhunter C., Morganti R., Axon D., Koekemoer A., 1999, MNRAS, 307, 24
Villar-Martín M., Vernet J., di Serego Alighieri S., Fosbury R., Pentericci L., Cohen M., Goodrich R., Humphrey A., 2003, in Avila-Reese V., Firmani C., Frenk C. S., Allen C., eds, Revista Mexicana de Astronomia y Astrofisica Conference Series Vol. 17, Revista Mexicana de Astronomia y Astrofisica Conference Series. pp 260–261
Villar-Martín M., et al., 2006, Astronomische Nachrichten, 327, 187
Villar-Martín M., Humphrey A., De Breuck C., Fosbury R., Binette L., Vernet J., 2007a, Monthly Notices of the RAS, 375, 1299
Villar-Martín M., Sánchez S. F., Humphrey A., Dijkstra M., di Serego Alighieri S., De Breuck C., González Delgado R., 2007b, MNRAS, 378, 416
Villar-Martín M., Sánchez S. F., Humphrey A., Dijkstra M., di Serego Alighieri S., De Breuck C., González Delgado R., 2007c, Monthly Notices of the RAS, 378, 416
Vollmer B., Cayatte V., Balkowski C., Duschl W. J., 2001, ApJ, 561, 708
Volonteri M., Bellovary J., 2012, Reports on Progress in Physics, 75, 124901
Watson C., et al., 2019, ApJ, 874, 63
Webb T. M. A., et al., 2015, ApJ, 814, 96
Weilbacher P. M., Streicher O., Urrutia T., Pécontal-Rousset A., Jarno A., Bacon R., 2014, in Manset N., Forshay P., eds, Astronomical Society of the Pacific Conference Series Vol. 485, Astronomical Data Analysis Software and Systems XXIII. p. 451 (`arXiv:1507.00034`)
Weymann R. J., Morris S. L., Foltz C. B., Hewett P. C., 1991, Astrophysical Journal, 373, 23
White D. A., Fabian A. C., 1995, Monthly Notices of the Royal Astronomical Society, 273, 72
White S. D. M., Frenk C. S., 1991, ApJ, 379, 52
White M., et al., 2012, MNRAS, 424, 933
Wilman R. J., Johnstone R. M., Crawford C. S., 2000, MNRAS, 317, 9
Wisotzki L., et al., 2016, A&A, 587, A98
Wisotzki L., et al., 2018, Nature, 562, 229
Wolf C., Meisenheimer K., Rix H. W., Borch A., Dye S., Kleinheinrich M., 2003, Astronomy and Astrophysics, 401, 73
Worthey G., 1994, ApJS, 95, 107
Wotta C. B., Lehner N., Howk J. C., O'Meara J. M., Oppenheimer B. D., Cooksey K. L., 2019, Astrophysical Journal, 872, 81
Zhao D., Aragón-Salamanca A., Conselice C. J., 2015, MNRAS, 453, 4444
Zhao D., Conselice C. J., Aragón-Salamanca A., Almaini O., Hartley W. G., Lani C., Mortlock A., Old L., 2017, MNRAS, 464, 1393

Zubovas K., King A. R., 2012, in Chartas G., Hamann F., Leighly K. M., eds, Astronomical Society of the Pacific Conference Series Vol. 460, AGN Winds in Charleston. p. 235 (`arXiv:1201.3540`)
Zwicky F., 1933, Helvetica Physica Acta, 6, 110
Zwicky F., 1957, PASP, 69, 518
de Carvalho R. R., Ribeiro A. L. B., Stalder D. H., Rosa R. R., Costa A. P., Moura T. C., 2017, AJ, 154, 96
van Ojik R., Roettgering H. J. A., Carilli C. L., Miley G. K., Bremer M. N., Macchetto F., 1996, Astronomy and Astrophysics, 313, 25
van Ojik R., Roettgering H. J. A., Miley G. K., Hunstead R. W., 1997, Astronomy and Astrophysics, 317, 358
van Weeren R. J., de Gasperin F., Akamatsu H., Brüggen M., Feretti L., Kang H., Stroe A., Zandanel F., 2019, Space Science Reviews, 215, 16
van de Voort F., 2017, in Fox A., Davé R., eds, Astrophysics and Space Science Library Vol. 430, Gas Accretion onto Galaxies. p. 301 (`arXiv:1612.00591`), doi:10.1007/978-3-319-52512-9_13
van den Bosch R. C. E., 2016, Astrophysical Journal, 831, 134
van der Marel R. P., Cretton N., de Zeeuw P. T., Rix H.-W., 1998, Astrophysical Journal, 493, 613